Performance Evaluation of the FASTPIX Silicon Pixel Sensor Technology Demonstrator for High-Precision Tracking and Timing

Dissertation
zur Erlangung des Doktorgrades
an der Fakultät für Mathematik, Informatik
und Naturwissenschaften
Fachbereich Physik
der Universität Hamburg

vorgelegt von

Justus Braach

Hamburg
2024

Gutachter der Dissertation:	Dr. Dominik Dannheim Prof. Dr. Elisabetta Gallo
Vorsitzender der Prüfungskommission:	Prof. Dr. Dieter Horns
Zusammensetzung der Prüfungskommission:	Dr. Dominik Dannheim Prof. Dr. Elisabetta Gallo Prof. Dr. Dieter Horns Dr. Axel Lindner Prof. Dr. Geraldine Servant
Datum der Disputation:	03.06.24

Vorsitzender des Fach-Promotionsausschusses PHYSIK:	Prof. Dr. Markus Drescher
Leiter des Fachbereichs PHYSIK:	Prof. Dr. Wolfgang J. Parak
Dekan der Fakultät MIN:	Prof. Dr.-Ing. Norbert Ritter

Eidesstattliche Versicherung

Hiermit versichere ich an Eides statt, die vorliegende Dissertationsschrift selbst verfasst und keine anderen als die angegebenen Hilfsmittel und Quellen benutzt zu haben. Sofern im Zuge der Erstellung der vorliegenden Dissertationsschrift generative Künstliche Intelligenz (gKI) basierte elektronische Hilfsmittel verwendet wurden, versichere ich, dass meine eigene Leistung im Vordergrund stand und dass eine vollständige Dokumentation aller verwendeten Hilfsmittel gemäß der Guten wissenschaftlichen Praxis vorliegt. Ich trage die Verantwortung für eventuell durch die gKI generierte fehlerhafte oder verzerrte Inhalte, fehlerhafte Referenzen, Verstöße gegen das Datenschutz- und Urheberrecht oder Plagiate.

Hamburg, den 16.05.24 Unterschrift: 

Zusammenfassung

Fortschritt im Feld der Teilchenphysik wird durch aktuelle und zukünftige Kollisions-Beschleuniger treibt die technologische Entwicklung in der Instrumentierung voran. Experimente bei höchsten Energien und Intensitäten konzentrieren sich auf hochpräzise Messungen der Standardmodell-Physik und der Suche nach Physik jenseits des Standardmodells. Die physikalischen Fragestellungen und Betriebsbedingungen zukünftiger Beschleuniger erfordern anspruchsvolle Verbesserungen in allen Detektor-Komponenten. Detektoren in den inneren Lagen zukünftiger Experimente unterliegen besonders anspruchsvollen Anforderungen. Sie müssen einzelne ionisierende Teilchen mit kleinen ($< 25\,\mu$m) Pixeln nachweisen, mit einer Ortsauflösung von $< 3\,\mu$m, einer Zeitauflösung von < 100 ps, bei einem minimalen Materialbudget und eine extremer Strahlenhärte.
Diese Dissertation konzentriert sich auf die Entwicklung von Silizium-Vertex- und Spur-Detektoren für zukünftige Hochenergiephysik-Detektoren und demonstriert die Leistungsfähigkeit des monolithischen Silizium-Pixel-Sensor-Demonstrators FASTPIX wurde in einem modifizierten 180 nm CMOS-Prozess für bildgebende Sensoren entwickelt. Das Sensordesign verfügt über kleine Ladungssammlungselektroden auf einer 25 μm dünnen Detektionsschicht mit kleinen Pixelgrößen von 8.66 μm bis 20 μm. Ein großer Parameterraum von 32 Mini-Matrizen mit jeweils 68 Pixeln zeigt Unterschiede in der Leistungsfähigkeit des Detektors je nach jeweiliger Modifikation des Herstellungsprozesses und Designvariation des Sensors. Das Sensordesign umfasst hexagonale Pixel mit Kapazitäten von wenigen Femtofarad und großen Signal-zu-Rausch-Verhältnissen, was die Nachweis-Effizienz und präzise Zeitmessung begünstigt.
Die Leistungsfähigkeit der Detektoren wird in Labor- und Teststrahlmessungen charakterisiert, denen Entwicklungen von Hardware und Software für die verwendeten Testsysteme vorausgegangen sind. Kalibrierungsmessungen ergeben einen nominalen Detektionsschwellenwert von 60 e – 160 e bei ≤15 e Front-End-Rauschen und einer Frequenz von Rauschsignalen von <10 Hz für die jeweilige Matrix. Die Ergebnisse zeigen Ortsauflösungen bis zu 1 μm für die Matrizen der kleinsten Pixelgröße, eine Zeitpräzision von etwa 100 ps für die Matrizen der größten Pixelgröße sowie Detektionseffizienzen von >99 % für die Prozessmodifikation mit verbesserter Ladungssammlung.
Die FASTPIX-Ergebnisse erfüllen oder übertreffen die meisten Anforderungen für zukünftige Pixel-Detektoren. Eine größere Pixel-Matrix und die Integration vollständiger Front-End- und Auslese-Funktionalität für zukünftige Hoch-Energie-Physik-Anwendungen wird durch gegenwärtige Entwicklungen von CMOS-Technologieknoten mit kleineren Strukturgrößen ermöglicht.

Abstract

The advancement of particle physics through current and future collider facilities pushes the boundaries of technology in HEP instrumentation. Experiments at the energy and intensity frontier focus on high-precision measurements of Standard Model physics and searches for physics beyond the Standard Model. The physics programs and operational conditions at future colliders necessitate sophisticated improvements in all detector subsystems. Detectors in the inner layers of future experiments face stringent requirements, needing to detect single ionizing particles with small ($< 25\,\mu$m) pixels, achieving $< 3\,\mu$m spatial resolution, < 100 ps time resolution, minimal material budget, and extreme radiation tolerance.

This dissertation focuses on advancing silicon vertex and tracking detectors for future high-energy physics collider detectors by demonstrating the performance of the monolithic silicon pixel sensor demonstrator FASTPIX, which was implemented in a modified 180 nm CMOS imaging process technology. The sensor features a small collection electrode design on a 25 μm-thin sensitive detection layer with small pixels ranging from 8.66 μm to 20 μm pitch. A large parameter space of 32 mini matrices with 68 pixels each assesses the performance impact of manufacturing-process modifications and sensor-design variations previously optimized in simulations. The sensor design includes hexagonal pixels with capacitances of a few femto-farads and large signal-to-noise ratios, enabling high detection efficiency and precise timing.

The detector performance is characterized in laboratory and test beam measurements with associate developments of hardware and software for the employed test systems. Calibration measurement conclude in a nominal threshold of 60 e – 160 e with $\leq$15 e front-end noise and <10 Hz total noise rate across all matrices. Spatial resolutions down to 1 μm for the smallest-pitch matrices, a timing precision of 100 ps – 150 ps for largest-pitch matrices as well as hit detection efficiencies >99 % are observed in test-beam for samples with process modifications for improved charge collection.

The FASTPIX results match or surpass most analog performance requirements for future pixel detectors. A larger pixel-matrix size and the integration of full front-end and readout functionality can be envisaged for future HEP applications, taking advantage of advancements in smaller feature-size CMOS processes.

Contents

Zusammenfassung iii

Abstract iv

Contents v

1 Introduction 1

2 High Energy Particle Physics 4
2.1 The Standard Model of Particle Physics . . . 4
2.1.1 The Model . . . 4
2.1.2 Physics Beyond the Standard Model . . . 6
2.1.3 Experimental Validation . . . 6
2.2 Benchmark Collider and Detector Technology at CERN . . . 7
2.2.1 The Large Hadron Collider . . . 7
2.2.2 The High-Luminosity Large Hadron Collider . . . 7
2.2.3 The Collider Experiment Concept . . . 8
2.2.4 Vertex and Tracking Figures of Merit . . . 9
2.2.5 HL-LHC detector upgrades . . . 11
2.3 Future Colliders and Experiments . . . 14
2.3.1 The Future Circular Collider . . . 14
2.3.2 Requirements for vertex and tracking detectors . . . 15

3 Principles of Semiconductor Physics 17
3.1 Semiconductors . . . 17
3.1.1 Band Structure . . . 18
3.1.2 Silicon and Doping . . . 19
3.1.3 Charge generation . . . 19
3.1.4 Charge Carrier Motion . . . 20
3.1.5 Carrier density and Doping . . . 21
3.1.6 The p-n Junction . . . 23
3.1.7 Leakage Current . . . 26
3.2 Particle Interaction with silicon . . . 27
3.2.1 Photons . . . 27
3.2.2 Charged Particles . . . 28
3.2.3 Multiple Coulomb Scattering . . . 30

4 Silicon Pixel Detector Concepts 32
4.1 Signal Formation . . . 32
4.2 Position measurement . . . 34
4.2.1 Binary Readout . . . 34
4.2.2 Charge Sharing . . . 34

4.2.3 Analog readout . . . 35
4.2.4 Pixel Geometry . . . 36
4.3 Technology Packaging . . . 36
4.3.1 Hybrid Pixel Detectors . . . 37
4.3.2 Monolithic Pixel Detectors . . . 37
4.4 Frontend Electronics . . . 38
4.4.1 Charge-sensitive Front-end . . . 39
4.4.2 Time of Arrival, Time Walk and Time over Threshold . . . 40
4.5 Noise . . . 41
4.5.1 Equivalent Noise Charge . . . 41
4.5.2 Thermal Noise . . . 41
4.5.3 Shot Noise . . . 41
4.5.4 Flicker Noise . . . 41

5 The FASTPIX Technology Demonstrator 43
5.1 ATTRACT FASTPIX . . . 43
5.2 The Chip . . . 44
5.2.1 Multi-Project Wafer . . . 44
5.2.2 Chip Layout . . . 45
5.3 Wafer-Level Modifications . . . 46
5.3.1 The standard 180 nm CMOS imaging process . . . 47
5.3.2 Sensor Simulation . . . 48
5.3.3 Modification of the 180 nm CMOS imaging process . . . 50
5.4 Pixel-Level Modifications . . . 50
5.4.1 Optimization of the Lateral Field . . . 50
5.4.2 FASTPIX pixel design parameters . . . 51
5.5 Frontend Electronics . . . 53
5.6 Readout Scheme . . . 55
5.7 Powering & Sensor Configuration . . . 57
5.8 Chip parameter space . . . 59

6 Laboratory Setups and Methods 61
6.1 The Caribou Data Acquisition System . . . 61
6.2 The FASTPIX Chip Board . . . 63
6.2.1 Material Budget . . . 64
6.3 Laboratory Setup . . . 65
6.3.1 Setup and Components . . . 65
6.3.2 Environmental Monitoring and Control . . . 66
6.4 Electrical, Noise and Signal Injection Measurements . . . 67
6.4.1 Electrical Characterization . . . 67
6.4.2 Signal response and Noise Characterization . . . 68
6.4.3 Test Pulse Injection Measurements . . . 68
6.5 Calibration Measurements with X-ray Photons . . . 71
6.5.1 The Source Measurement Setup . . . 71
6.5.2 The X-ray Tube Setup . . . 72

7 Laboratory characterization and calibration 74
7.1 Current-Voltage Characteristic . . . 74
7.1.1 Measurement conditions . . . 75
7.1.2 Measurement results . . . 75
7.2 Energy Calibration . . . 79
7.2.1 Time-over-Threshold . . . 79
7.2.2 Discriminator Threshold . . . 90
7.3 Noise Characterization . . . 95
7.3.1 Test Pulse Signal Injection . . . 95
7.3.2 Pixel Noise Scan . . . 99
7.4 Operational Threshold . . . 101
7.5 Summary . . . 103

8 Test-Beam Setup 105
8.1 The CERN SPS North Area Test-Beam Facility . . . 105
8.2 The CLICdp Beam Telescope . . . 107
8.2.1 Material Budget . . . 108
8.2.2 Experimental Setup . . . 108
8.2.3 Data Acquisition . . . 113

9 Test-Beam Reconstruction and Analysis 116
9.1 Corryvreckan . . . 116
9.2 Test-Beam Data Reconstruction . . . 117
9.2.1 Adaptation for FASTPIX campaigns . . . 117
9.2.2 Event Building . . . 118
9.2.3 Clustering . . . 119
9.2.4 Noise . . . 120
9.2.5 Offline Pixel Masking . . . 120
9.2.6 Correlations . . . 121
9.2.7 Track Reconstruction . . . 122
9.2.8 Track-Cluster Association . . . 123
9.3 Alignment . . . 124
9.3.1 Alignment Sequence . . . 124
9.3.2 Pre-Alignment . . . 124
9.3.3 Telescope Alignment . . . 125
9.3.4 DUT Alignment . . . 125
9.4 Cluster Position Reconstruction . . . 126
9.4.1 Charge-Weighted Position Reconstruction . . . 126
9.4.2 Eta Correction for Non-Linear Charge Sharing . . . 126
9.5 Observables . . . 129
9.5.1 Noise . . . 129
9.5.2 Cluster Size . . . 130
9.5.3 Hit-Detection Efficiency . . . 130
9.5.4 Spatial Resolution . . . 131
9.5.5 Time Resolution . . . 132

10 Detector Performance in Test-Beam Measurements 136
10.1 Noise . . . 137
10.1.1 Fake Hit Rate . . . 137
10.1.2 Hit Rate . . . 138
10.2 Charge Sharing . . . 138
10.2.1 Pixel Level . . . 139
10.2.2 Matrix Level . . . 140
10.2.3 Threshold Dependence . . . 141
10.2.4 Sample Level . . . 142
10.3 Signal . . . 145
10.3.1 Matrix Level . . . 145
10.3.2 Sample Level . . . 146
10.4 Hit-Detection Efficiency . . . 147
10.4.1 Matrix Level . . . 148
10.4.2 Sample Level . . . 150
10.5 Spatial Resolution . . . 151
10.5.1 Matrix Level . . . 151
10.5.2 Sample Level . . . 152
10.6 Time Resolution . . . 154
10.6.1 Matrix Level . . . 155
10.6.2 Sample Level . . . 155
10.6.3 High-Statistic Data Set . . . 157
10.7 Summary . . . 159

11 Summary and Prospects 161

References 165

1 Introduction

Particle physics takes a unique role in fundamental research with a notion of revolutionary discovery as the main criterion for realization of its future experimental proposals. Over the course of almost two decades, results from the Large Hadron Collider (LHC) [1] and its experiments at CERN (Geneva, Switzerland) have had a lasting impact on the particle-physics landscape. The discovery of the Higgs boson with a mass of 125 GeV was able to complete the current model, the Standard Model (SM) of Particle Physics, and offered a clean slate for new exploration. Yet, the absence of experimental evidence for new physics beyond the SM casts uncertainty on the field's future facilities. Since the SM sofar can not account for the remaining open questions and clear guidance from theory is yet to come, the prospect of an experimental programme aiming for higher precision SM measurements is a feasible option [2].

At the time of this thesis, CERN prioritizes the upgrade of its accelerator complex to the imminent High-Luminosity (HL) LHC to deliver an up to 10 times higher potential for discoveries to its experiments, which themselves implement associated upgrades [3]. In parallel, CERN and the european High Energy Physics (HEP) community are assembling a vision for the post-HL-LHC future after 2040, with proposals for linear as well as circular collider concepts.
Following the 2021 update of the European Strategy for Particle Physics [4], the Future Circular Collider (FCC) [5] was introduced as an electron–positron collider (FCC-ee) [6] in its first stage, followed by a second-stage hadron collider (FCC-hh) [7] after 30 years of initial lepton-collider operation. The earlier Compact Linear Collider (CLIC) [8] project for the construction and operation of a high-luminosity, high-energy electron–positron linear collider is continued in order to maintain CLIC as an option for a future collider at CERN and to further develop numerous technological innovations [9].
FCC feasibility studies develop designs for the HL-LHC successor, which are expected to conclude in 2025 with a final assessment of the technical and financial viability of the FCC project as well as possible collider experiment proposals.

In parallel to the R&D towards accelerator technologies, detector proposals are being investigated. The projections and simulations of the individual physics case make it clear that advancements in many technologies are necessary to achieve the construction, commission and successful operation of the proposed future colliders. To address these challenges the

CERN Experimental Physics (EP) Department has defined a strategic R&D programme (EP R&D) aimed at advancing the detector technologies in question [10].
The research conducted within this thesis is part of general-purpose pixel detector R&D. It aims to demonstrate the performance of new pixel detector technologies for future high-energy physics collider detector proposals at the next-generation of particle accelerators. Detectors placed in the inner layers of collider detector experiments face stringent requirements in view of their spatial and temporal measurement performance as well as the projected experimental conditions.
The development of monolithic CMOS sensors[1] for the inner-most detector layers for maximum performance is carried out in collaboration with external university groups and research labs, and in close cooperation with industrial partners [10]. A second instrumental link between fundamental research and industrial partners is established by the European ATTRACT project [11], which provides funding to develop breakthrough detection and imaging technologies for scientific and commercial applications.

Within the ATTRACT FASTPIX project a monolithic silicon pixel sensor demonstrator chip has been developed in a modified 180 nm CMOS imaging process technology, targeting a sub-nanosecond timing precision for single ionizing particles [12]. The implemented sensor comprises mini matrices that allow the assessment of manufacturing process modifications and sensor design variations. The 32 matrices feature small signal collection electrodes on a 25 µm-thin sensitive detection layer and consist of a hexagonal pixel grid with pitches ranging from 8.66 to 20 µm.
Small line-width CMOS technologies allow the design of hexagonal pixels with collection electrodes capacitances of a few femtofarad and large signal-to-noise ratios, in favor of detection efficiency and precise timing. Low-field regions, non-uniform electric field configurations and space requirements for complex in-pixel circuits introduce timing variation depending on the in-pixel particle incidence location. In order to face a tradeoff between pixel size and non-uniform timing, various design variations are explored, aiming at accelerating the charge collection and making the timing of the charge collection more uniform over the pixel area. Signal treatment of the analog waveforms, as well as reconstruction of digital position, time and charge information, is carried out off-chip.

The aim of the FASTPIX project is to investigate the potential of targeted sensor process modifications and design optimizations for the detector performance. The conducted research presented by this thesis covers laboratory and test beam characterization measurements as well as the associate development of hardware and software for the employed test systems. After first results from measurements with two matrices of a sample chip presented in [13], and performance highlights from beam tests with minimum-ionizing particles presented in [14], this manuscript accesses the full set of measurement data for a comparison of the various process modifications, sensor layouts and pixel pitches.

The document is organized as follows. After this brief introduction, Chapter 2 introduces High-Energy Physics with an outline of the SM, the theory to be validated and completed/extended further based on observation made in collider experiments. The importance of advancements

[1] A complementary metal oxide semiconductor (CMOS) sensor has a diode and CMOS transistor circuitry inside of each pixel, allowing for individual in-pixel signal processing.

in instrumentation is illustrated by an account of the current state-of-the-art technology and its necessary improvements in future HEP instrumentation. The latter section confines the discussion to pixelated detectors at the inner-most radii of collider detector experiments, the detector type at the heart of this effort.
Chapter 3 introduces the fundamental concepts of semiconductor physics as well as the different interaction mechanisms of charged particles with matter. An explanation of the basic operational principle of silicon pixel detectors, the different detector concepts and the observables at the core of a pixelated detector follow in Chapter 4.
Chapter 5 introduces the ATTRACT programme and locates the FASTPIX project as the main subject of this thesis. The chip layout, applied manufacturing process modifications as well as pixel-level design variations are motivated, discussed and summarized in the final illustration of the chip parameter space. The chapter also discusses relevant aspects of the analogue front-end and digital-logic circuitry of the chip that informs the evaluation, encoding and decoding of hit information.
Chapter 6 introduces the readout systems, the setups, the methodology and analysis strategies for laboratory measurements conducted within the scope of this thesis. The laboratory measurement results are presented in Chapter 7 and provide integral information for the characterization of the novel pixel detector prototype. The basic functionality of the tested FASTPIX samples is assessed in a controlled environment, initially through the examination of the sensor's electrical properties, followed by an energy calibration of detector observables, and tests of the signal gain and noise performance. A summarizing discussion completes the transition towards more advanced experimental setups and measurements.
In test-beam measurements FASTPIX is exposed to a beam of charged high-momentum particles that allow to characterize its performance in an environment that closely resembles the forseen spectrum of applications. The test beam enables to study the sensor response to ionizing particles in reference to particle track information provided by a beam-telescope setup. Chapter 8 explains the experimental approach of detector characterization in test-beam measurement campaigns conducted with FASTPIX. It provides an introduction to the test-beam facility, the mechanical components of the reference beam telescope setup and a detailed discussion on the device integration as well as the electronics hardware used for data acquisition. The methods and strategies applied for reconstruction and analysis of test beam data are presented in Chapter 9. In addition, the chapter provides performance figures of the reference telescope used for the test-beam characterization of FASTPIX.
Chapter 10 presents a detailed performance evaluation of FASTPIX matrices based on test-beam measurements. The chapter aims to extract the performance gained by the large parameter space of improvements to the manufacturing process and pixel cell through an assessment of noise, hit-cluster formation, signal collection, hit-detection efficiency, spatial resolution and time resolution.
Results from laboratory as well as test beam measurements are summarized and brought to conclusion in Chapter 11. Apart from a discussion on the potential of the tested sensor-process modifications and pixel-design optimizations for the detector performance, FASTPIX is evaluated with respect to the detector requirements of tracking detectors in future collider experiments. The encountered limitations as well as possible improvements are put in the context of recently started developments in the smaller 65 nm CMOS technology node.

2

High Energy Particle Physics

This chapter describes the key landmarks of the prevailing present HEP landscape. The underlying theoretical model as well as the experimental facilities tasked with the validation and exploration of the model are introduced, with a focus on collider experiments.
After a summary of the current understanding of fundamental particle physics and the experimentally observed limitations of the SM, the chapter elaborates on the necessity for extensions to the theory. A description of the strategy used in the validation and search for new physics based on experimental observations bridges the model to the purpose-built experimental facilities. After the introduction of a generic collider detector concept, its flavours are exemplified by the concepts behind experiments along the Large Hadron Collider. The quest for a higher discovery potential delivered to the experiments is achieved through coordinated upgrades to the accelerator complex as well as the experiments themselves. For a discussion of the state-of-the-art technologies that comprise currently ongoing detector upgrades, the focus is shifted to the tracking sub-detector systems closest to the particle interaction point. The chapter closes with a discussion of proposed future accelerator facilities in succession of the HL-LHC, their capabilities and the inferred requirements for tracking detectors a future experiments.

2.1. The Standard Model of Particle Physics

The Standard Model (SM) of particle physics represents the theoretical framework for fundamental particles and their interactions [15]. Originating in the 1930s and since marked by theoretical advancements and experimental discoveries, the model continues to predict experimental outcomes with outstanding precision across a broad energy spectrum.

2.1.1. The Model

An overview of the 17 experimentally confirmed elementary particles of the SM is shown in Figure 2.1. The SM encompasses both fermions, which constitute the building blocks of matter, and bosons, which act as the mediators of fundamental forces. Fermions can be further segmented into quarks and leptons. They are characterized by half-integer spins and adhere to the Pauli exclusion principle. Six distinct quarks (up, down, charm, strange, top, and bottom) and six leptons (electron, muon, tau, electron neutrino, muon neutrino, and tau

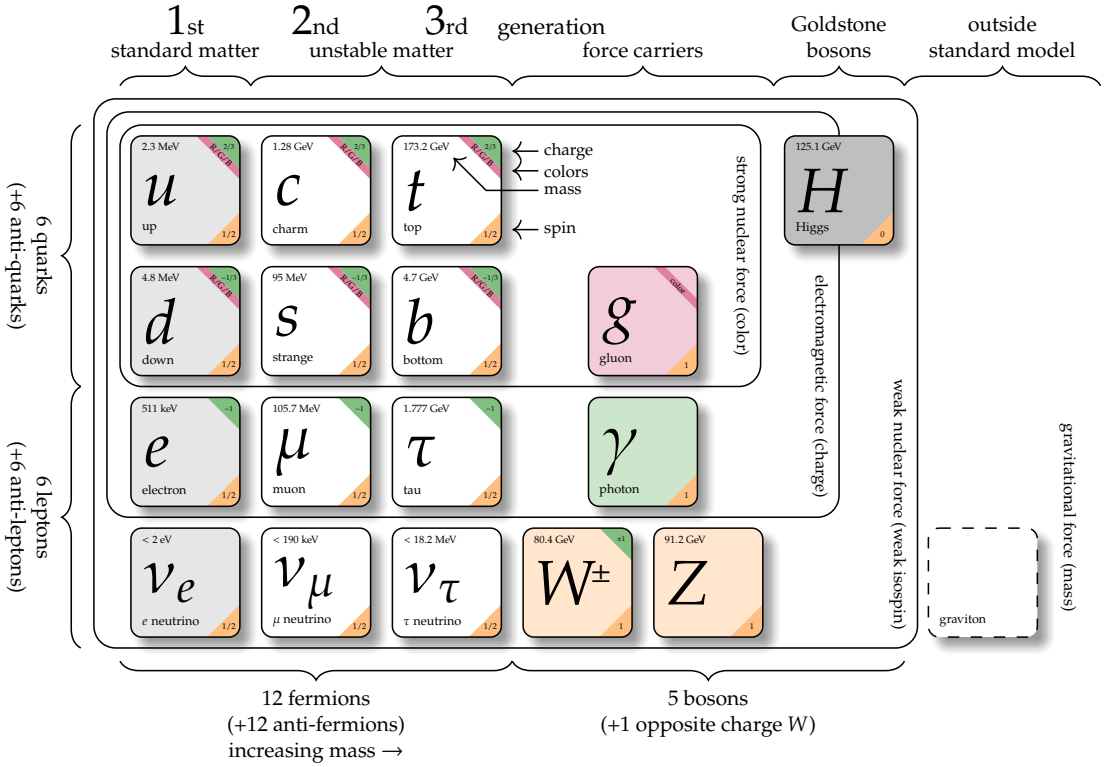

Figure 2.1: Diagram of the Standard Model of particle physics [16].

neutrino) are organized into three generations, with mass generally increasing across the generations. Each generation contains an up and down-type quark with distinct fractional elementary charges of $+\frac{2}{3}$ and $-\frac{1}{3}$ and two leptons, one charged (-1) and one electrically neutral neutrino. With the exception of the electron neutrino, first-generation fermions constitute all visible matter. Each fermion is associated to an antiparticle with opposite quantum numbers. Within the SM, neutrinos are stable and massless.

Bosons carry spin 1 and serve as mediators of three of the four fundamental forces: electromagnetic interactions via the photon, the strong force through gluons, and the weak force via W and Z bosons.

Fermions can interact via the weak force and, if carrying electrical charge, via the electromagnetic interaction. Quarks are affected by all fundamental forces within the SM.

The interactions among these particles are mediated by fields of the SM's gauge theory structure that unifies the electromagnetic and weak forces into the electroweak theory and incorporates Quantum Chromodynamics (QCD) for strong interactions. The SM does not account for gravitation, the fourth fundamental force.

The Higgs boson, the only scalar particle (spin = 0) in the SM, is the excitation of the Higgs field, which plays a crucial role in mass acquisition by particles through the mechanism of spontaneous symmetry breaking in the electroweak sector.

In experimental contexts, the SM has been rigorously tested and confirmed, supporting its applications in predicting particle interactions. The framework not only describes all known matter and radiation, but also continues to guide theoretical and experimental explorations in particle physics.

2.1.2. Physics Beyond the Standard Model

Despite its profound impact and numerous validations, the Standard Model does not represent a complete framework. The model aligns with experimental data, yet fails to account for a range of phenomena that point to fundamental shortcomings.

The observed predominance of matter over antimatter in the universe suggests an asymmetry between the two. Indirect evidence supporting asymmetry is provided by experiments that observe CP violation, which describes a differences in the behavior of particles and their antiparticles [17].

Outside the HEP field, astronomical observations of galaxies conclude in gravitational pulls and lensing effects that can not be accounted for by visible matter alone [18, 19]. The presence of dark energy is inferred from the accelerated expansion of the universe, as observed in the light from distant supernovae and the cosmic microwave background [20]. Still, widely recognized hypothesis regarding the properties of dark matter and dark energy have yet to be put in context of the SM.

The phenomenon of non-zero neutrino masses is concluded from oscillations observed in atmospheric, solar, reactor, and accelerator neutrinos, where neutrinos switch between different flavors [21, 22, 23, 24]. At the same time, existence of three generations of fermions is confirmed by experiments that measure the properties of the Z boson, which can decay into any of these fermions [25]. A fourth light neutrino species, which would alter the Z boson's decay rate, is excluded at the energies accessible for current experiments. In its current form, the SM neither provides a concrete explanation for the existence of exactly three generations of fermions, nor gives a mechanism responsible for the observed neutrino oscillations.

Theories beyond the SM, such as supersymmetry (SUSY) and theories involving extra dimensions, offer potential solutions but have yet to gain empirical support despite intense experimental investigation [26].
Although the search for new particles and interactions is ongoing, no conclusive evidence has been found, which reinforces the notion that our understanding of the universe remains incomplete. Only further theoretical development and rigorous experimental testing of predictions can challenge the current paradigms of particle physics.

2.1.3. Experimental Validation

Experimental confirmation of SM predictions is achieved through the investigation of collisions of high-energy particles with one-another or against fixed targets. Particles are accelerated to an increased energy and steered into collisions, where shares of energy convert to mass ($E = mc^2$) and generate numerous new primary particles. After their creation at the primary vertex, particles of interest usually decay quickly into secondary collision products, created at the secondary vertex. The detection and analysis of secondary particles and radiation produced by rare processes assesses the interactions in the collision and the primary short-lives particles of interest. Modeled data sets, obeying SM-theory, are validated by comparison with the physics observables extracted from the measurement data. Deviations in these findings can hint at new physics phenomena beyond the current model.

Researchers employ the following two approaches to experimentally validate predictions from the theoretical model:

- Direct observations are possible for SM and possible non-SM particles with a rest mass less than the total energy in the particle collision.
- Indirect tests of the model involve searching for small deviations from SM predictions that put focus on extremely rare interactions.

2.2. Benchmark Collider and Detector Technology at CERN

2.2.1. The Large Hadron Collider

The LHC at CERN with its four experiments is the present-day benchmark of circular collider accelerator and detector technology, purpose-built for SM measurements and the discovery of new physics phenomena beyond the SM. The 27 km-circumference synchrotron ring accelerates protons (heavy led ions) up to a center-of-mass (c.o.m.) energy of 14 TeV (5.5 TeV) and is the last stage of the CERN accelerator complex. In the LHC, the accelerated particles are grouped in bunches, spaced in discrete time intervals of 25 ns, and are brought to collision at four Interaction Points (IP).
Figure 2.2 locates the circular collider in its geographic surroundings and illustrates the common coordinate system of the facility.

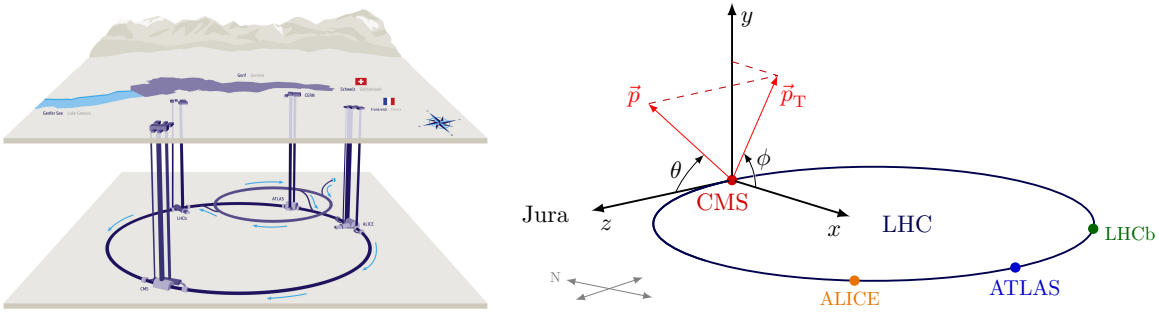

(a) Geographic location/site plan [27].

(b) Machine coordinate system at CMS [28].

Figure 2.2: Geographic overview and machine coordinate system of the LHC.

2.2.2. The High-Luminosity Large Hadron Collider

The LHC has been operational since 2008 and is slated for an upgrade to the High-Luminosity LHC (HL-LHC), which will extend the physics discovery potential through an increased collision rate and its project timeline until 2038 [29].
Besides the c.o.m energy, the rate of particle collisions is the improved figure of merit that characterizes the new HL-LHC configuration of the circular collider. The luminosity L is the interaction rate at the crossing of the beams and is defined as the reaction rate $\frac{dR}{dt}$ per production cross-section σ_p [30]:

$$L = \frac{dR}{dt}\frac{1}{\sigma_p} \tag{2.1}$$

In the simplest case of equal beam profiles with N particles following two-dimensional Gaussian distributions perpendicular to the beam axis, the instant luminosity can be obtained from:

$$L = \frac{N^2}{t \cdot \sigma_{\text{eff}}} \quad , \tag{2.2}$$

where t is the time between bunches and σ_{eff} is the effective cross-section of the collisions.
Retaining its 14 TeV c.o.m. energy, the HL-LHC project aims at instantaneous luminosities 5 to 7.5 times larger than the nominal $1 \cdot 10^{34}\,\text{cm}^{-2}\,\text{s}^{-1}$ of the current accelerator design. By the end of the 12 yr project timeline, the upgraded collider is estimated to deliver an integrated luminosity (total number of collisions) of $3\,\text{ab}^{-1}$ by 2038, an order of magnitude more than the preceding stage during the last 15 years of operation.
The new accelerator configuration relies on key innovations that push accelerator technology beyond its present limits. In a similar way, its experiments need to undergo upgrades to all sub-detector systems in order to take advantage of the imminent unprecedented amounts of collision data.
The LHC hosts four large experiments at four IPs, ATLAS (A Toroidal LHC ApparatuS) [31], CMS (Compact Muon Solenoid) [32], ALICE (A Large Ion Collider Experiment) [33] and LHCb (LHC beauty) [34]. ATLAS and CMS are general-purpose experiments, whereas ALICE and LHCb focus on specific phenomena.

2.2.3. The Collider Experiment Concept

Accelerator as well as experiment upgrades in preparation for the HL-LHC operation span over a decade of dedicated R&D effort conducted on a global scale. In the following subsection the concept of a general-purpose detector poses as a reference for the inner-workings of a common particle collider experiment. Vertex and tracking detectors, the main application of the technology characterized in this manuscript, are located within the setup. HL-LHC vertex and tracking detector upgrades are discussed as a representation of the present-day state of technologies in HEP instrumentation vertex and tracking applications.
Particle detectors in experiments at the LHC typically are magnet spectrometers that track secondary and tertiary particle trajectories in a fixed magnetic field configuration in parallel with the colliding beams. The momenta of charged particles are determined from their trajectories that are curved in the magnetic field and measured by the tracking detector. Their energy is obtained in the calorimeters through a destructive, inelastic interaction with absorber materials and subsequent distribution of its energy onto a shower of tertiary particles.
The symmetric energies of two colliding particle beams of opposite direction cause the laboratory and the centre-of-mass coordinate system to be congruent. Experiments that strive for a complete detection of all reaction products require a 4π solid angle coverage of the volume surrounding the interaction point, typically implemented by a largely cylindrical arrangement of detection layers and two endcaps.
Figure 2.3 illustrates such a general-purpose detector in collider-configuration, with sub-detector system layers that each are designed for a specific task. At the center of the detector, the vertex tracker detects vertices of secondary particles that separate from the primary particle vertex of the particle collision. After the high-granularity pixelated detection layers of the vertex tracker, the number of detection cells and readout channels per unit volume

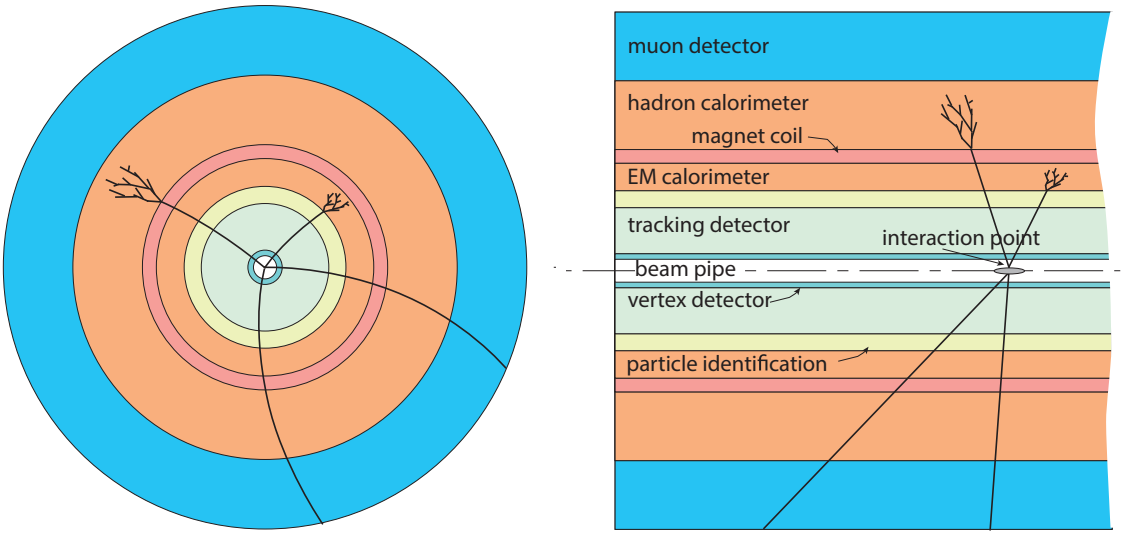

(a) x-/y-plane, cut perpendicular to beams. **(b)** z-/y-plane, cut parallel to the beams.

Figure 2.3: Configuration of detector components in collider experiments. Modified from [30].

decreases with increasing distance from the interaction point. Tracking sub-detectors at larger radii allow to reconstruct the particle track, are able to determine the particle momentum and identify the type of particle based on the curvature of a given trajectory. The electromagnetic calorimeter measures the energy of electromagnetic showers (electrons and photons) that result from the interaction of the traversing particle with an absorber medium. The hadron calorimeter facilitates equivalent detection of hadronic showers. It is either placed outside or inside of the magnet coil, depending on the detector design. The iron yoke returning the magnetic flux often is interweaved with layers of muon tracking devices. As the most penetrating charged particles, muons are identified in the outermost layers of the detector behind the magnet and calorimeters.
Advancements in semiconductor electronics, mainly the increase in transistor count per unit area, allow to equip a given detection volume with increasingly granular particle detection and readout solutions. This development allows modern particle physics experiments to strive for the detection, identification and reconstruction of all collision products in a as much of the 4π solid angle as possible.

The pseudorapidity η is the commonly used relativistically invariant spatial coordinate that describes the angle of a particle trajectory relative to the beam line. It is defined as $-\ln\tan\left(\frac{\theta}{2}\right)$, where θ is the polar angle of the particle measured from the z/beam axis (see Figure 2.2b). It is centered at $\eta = 0$ in the transversal plane with extremes $\eta \rightarrow \pm\,\text{inf}$ for 0° and 180°, respectively.

2.2.4. Vertex and Tracking Figures of Merit

In view of the technology demonstrator characterized in this manuscript, the following discussion of detector technologies will be restricted to vertex and tracking detector applications.

The performance observables used to characterize such detector systems are introduced by the following.

Position Resolution
To measure the space coordinates of a particle trajectory, pixel sensors use the signals registered by a matrix of electrodes in response to the particle intercept. The spatial precision of the measurement is mainly influenced by the distance between adjacent electrodes in the grid, the pixel pitch. Depending on the signal processing strategy and applied algorithms, the position information can be improved beyond the pixel pitch by combining information from simultaneous signals recorded by a group of neighboring pixels.

Multiple Scattering and Material Budget
The interaction of a passing particle with all materials in the detector causes deflections in the trajectory that is to be measured. The concept of multiple scattering describes many small-angle scatters that are mainly caused by Coulomb interactions between particles and nuclei of a medium. The radiation length X_0 is the mean path length over which scattering reduces the energy of a high-energy particle to a fraction $1/e$. The relative thickness x/X_0 of a material in units of radiation length describes the material budget. A large material budget in-path of particle trajectories deteriorates the tracking resolution of the detector. A low material content in detection layers, service and support structures is essential in reducing this adverse effect on the particles trajectory and subsequently on the measurement precision.

Transverse Impact Parameter Resolution
The impact parameter resolution describes the ability of a tracking detector to reconstruct and reliably distinguish vertices. In the evaluation of collision events, a secondary vertex is observed if the extrapolations of a subset of reconstructed tracks arrives offset to the primary interaction point given by the nominal beam position. The projected impact parameter d_0 is the distance in the x/y-plane between the closest approach to the primary vertex at the interaction point. The significance of the observation of a vertex is assessed as the ratio between d_0 and its resolution σ_{d_0}. A good vertex resolution starts at the tracker geometry with a short extrapolation length from the inner-most layers in close proximity to the beam and a large detector diameter for sufficient lever arm. A high single-layer spatial resolution is most-important for the inner-most layers and can be relaxed for larger radii due to multiple scattering limiting the achievable resolution. Similarly, a high number of sensitive layers benefits the spatial resolution of the system but increases the contribution of multiple scattering.

Momentum Resolution
The momentum of a charged particle passing multiple detection layers can be derived from its curvature in the applied magnetic field. For small momenta the resolution is limited by the multiple scattering term, while at high momenta the spatial resolution of the tracker dominates. The number of detector planes is adjusted in order to optimize for a specific momentum range.

Readout Electronics
Tracker geometry and pixel sensor specifications need to be met with adequate readout electronics that amplify the charge generated in particle interactions with the detection

medium, discriminate signals and transmit the acquired data to off-detector processing. Small pixel size promotes tracking resolutions but limits the available area for complex in-pixel circuits. A larger number of readout channels per area only hold feasibility as long as the power consumption per pixel is reduced by at least a similar factor. Aside from operational cost, the power consumption has an influence on the material budget of the full detector, not only through powering services but also through the necessary cooling infrastructure. Dead-time occupied by the processing of an event is benchmarked against expected event rates to prevent data loss. The overlap of signals in consecutive events in a high-occupancy readout scenario is referred to as pile-up. Pile-up is reduced by improvements in time resolution and signal processing time. Smaller pixel pitch as well reduces pile-up by geometrical considerations, where a smaller area is less likely to be hit by a given density of tracks in time and space.

Time Resolution
The time measurement precision of a detector is dependent on contributions from the sensor as well as the readout electronics. In a high track-density and interaction-rate environment the detector time resolution contributes to the impact parameter resolution and mitigation of data-loss through pile-up.

Radiation Damage
Silicon particle detectors experience radiation damage during their exposure to an intense flux of charged and neutral particles as well as γ- and X-rays. Damage of the silicon crystal through non-ionizing energy loss of impinging particles, by convention, is normalized to the damage level caused by 1 MeV neutrons. The particle flux, the fluence Φ_{eq} is quoted in neutron-equivalents per surface area, $\mathrm{n\,eq\,cm^{-2}}$. Total Ionizing Dose (TID) in Gray ($1\,\mathrm{Gy} = 1\,\mathrm{J\,kg^{-1}}$) refers to the amount of ionizing radiation energy absorbed by a material or device over time.

2.2.5. HL-LHC detector upgrades

The state of the art in operational vertex and tracking detectors is reflected by the technologies implemented in present-day detector upgrade campaigns for the near-future HL-LHC operation.
Where possible, substantial margin is included in the design of the upgraded detectors to ensure that experiments retain full performance, even above nominal accelerator performance specifications. Outperforming scenarios comprise up to 200 inelastic proton-proton collisions per bunch crossing, an instantaneous luminosity of $7.5 \cdot 10^{34}\,\mathrm{cm^{-2}\,s^{-1}}$ and an integrated luminosity amounting to $4\,\mathrm{ab^{-1}}$ by 2040.

ATLAS and CMS
ATLAS and CMS have similar aims and largely share the approaches selected to maintain the present tracking performance despite the future high occupancy environment [35, 36]. Priorities are set on pixel detector technologies that reduce the scattering material budget and are capable to operate fully efficient even after the ten-times increased integrated radiation dose at the end of the HL-LHC operation. Both experiments use hybrid silicon detectors that comprise a 130 µm-thick sensor that is interconnected with a 150 µm-thick front-end chip that facilitates the detector readout and control.

The all-silicon detector setups comprise pixel sensors in the innermost radii that reach up to $|\eta| = 4$ and are replaceable after 3000 fb^{-1}, after the first half of HL-LHC runtime, due to the lack of resilient-enough technologies. The innermost pixel layer is expected to experience hadron fluences of $4 \cdot 10^{16}$ n eq cm^{-2} and a total ionizing dose close to 20 MGy, respectively. In order to retain charge collection efficiency the pixel detector technology accepts a high bias voltage up of several 100 V. An increased granularity ensures excellent tracking performance at less than 0.1 % occupancy, despite the high level of pileup.
A large readout bandwidth and deep front-end buffers for higher rate (750 kHz) and longer latency (12.5 µs) allow to process the high readout data rates of up to 5 GB s^{-1}. The readout electronics are designed in 65 nm CMOS technology with a pixel cell size of 50×50 μm^2 and a low detection threshold (below 1000 e).
Larger active surface areas with higher channel density on a larger number of modules calls for efficient and industrial production of components and assemblies.
Both ATLAS and CMS add new sub-detector systems with a focus on high precision time measurement for 4D reconstruction of primary vertices to meet the challenge of high luminosity [37, 38]. Inelastic interactions that probe energies ranging from a few GeV to several TeV are a rare occurrence (in < 1 % of beam crossings) but always are mixed with up to 200 simultaneous pileup interactions per bunch crossings. The resulting spatial overlap of tracks and energy deposits in the detector aggravates the identification and reconstruction performance in these cases. The challenges are the mitigation of falsely identified physics signatures in the detector data in combination with a much higher rate of data to be processed, transmitted and recorded for analysis. Timing information with 30–40 ps (50–60 ps after degradation effects at the end-of runtime) time measurement precision enables to assign charged tracks to the correct interaction vertices. Within the longitudinal extent of the bunches, the interactions are distributed across a time interval of ≈200 ps RMS, which is equivalent to a length of ≈60 mm. Track-vertex association is appended with track-time information that is able to disentangle tracks from spatially associated primary vertex candidates that do not match in interaction time.
For ATLAS, the addition of such timing detectors complements the performance of physics object reconstruction of the inner pixel tracker in the forward region. The CMS upgrades provide timing information with a more hermetic angular coverage (up to $|\eta| = 3$) in the barrel as well as the forward regions of the detector. In both cases Low-Gain Avalanche Silicon Detectors (LGAD), segmented planar Silicon detectors with internal gain, are the technology foreseen for these layers of timing detectors. The internal amplification depends on the doping dose of the implanted multiplication layer which experiences radiation-induced aging effects that accumulate over the course of detector operation.
Similar to the vertex tracker, a replacement of the innermost modules with improved fabrication processes, enhanced radiation tolerance and higher sensor granularity is foreseen at a mid-way point in the HL-LHC programme.

ALICE
Despite its resemblance to the collider detector experiment concept introduced in Section 2.2.3, the ALICE experiment is designed with a focus on the physics of strongly interacting matter. It is purpose-built to probe the properties of the Quark-Gluon Plasma (QGP), a state of matter in which quarks and gluons are not bound in hadrons, that is recreated in collisions of high-energy heavy ions. Similar to the HL-LHC proton-proton collisions, the number of

lead–lead (Pb–Pb) collisions is expected to increase by an order of magnitude with a significant impact on the possible measurement precision of known as well as new phenomena of the QGP medium.
To seize the HL-LHC collisions, the ALICE collaboration has implemented upgrades of multiple sub-detectors, the event readout, online data processing and recording capabilities, matching the Pb–Pb scenario as well as proton–lead (p–Pb) and proton–proton (pp) collisions [39]. Entirely new vertex and tracking detectors address the ability to distinguish secondary vertices from the primary interaction vertex in high-pileup environments, similar to the case of ATLAS and CMS. In addition, the ability to track very low transverse-momentum particles benefits high precision measurements of heavy-flavour hadrons and low-mass di-leptons. Moreover, a three times lower material budget reduces multiple scattering and adds to the tracking performance at low transverse momentum.

With its choice in pixel detector technology, ALICE takes a pioneering role. A $10\,\mathrm{m}^2$ active silicon area and close to 13 billion pixels make the recently installed and operational Inner Tracker System 2 (ITS2) for LHC and HL-LHC the largest pixel detector and the first tracking system based on monolithic active pixel sensors (MAPS).
The monolithic packaging integrates both sensor and readout electronics onto a single detection device, resulting in an advanced CMOS imaging sensor with a minimum feature size of 180 nm. The unification of low-capacitance, small collection-electrode sensor and a read-out based on integrated CMOS circuits meets the required granularity ($27 \times 29\,\mu\mathrm{m}^2$ pixel grid), material budget ($< 1.5\,\%X_0$) and radiation hardness in vertex and tracking detectors. While producing a high number of particles per collision event, the heavy ion collisions, which occur at much lower luminosities and rates as the proton-proton collisions, impose less challenging radiation levels of 700 kGy TID and a fluence of $10^{13}\,\mathrm{n\,eq\,cm^{-2}\,s^{-1}}$.
The availability of full CMOS puts complex readout circuitry directly in the pixel. The operational pixel detector reaches unprecedented single-particle detection performance in terms of signal/noise ratio ($\mathcal{O}(30)$), spatial resolution ($\approx$5 µm), readout speed (> 100 kHz) and power consumption ($< 40\,\mathrm{mW\,cm^{-2}}$).
The detector layout is optimized to achieve the best combined performance in pointing resolution, momentum resolution and tracking efficiency from a barrel-only geometry that covers up to $\eta = \pm 2.5$. In operation at room temperature using water cooling, the tracking system serially transmits zero-suppressed hit data with a bit-rate up to $1.2\,\mathrm{Gb\,s^{-1}}$ to be finally sequenced in continuous $\approx$22 µs intervals.

The experiment continues to advance improvements of the monolithic CMOS technology in its ITS3 vertex detector HL-LHC upgrade [40] and paves the way for the pixel detector technologies of the collider experiments of the future. By exploiting the rapid progress in imaging technology for consumer applications, the possibilities for improvement are manifold. Additional layers implanted into the silicon device, larger-area single devices and the reduction of the sensor thickness to below a tenth of the present standard opens the door for unconventional solutions to the requirements of the inner barrel pixel layers of the experiment. The upgrade innovates with its cylindrical layers of bent wafer-scale stitched $\leq$50 µm-thin 65 nm monolithic CMOS silicon sensors with a $27 \times 29\,\mu\mathrm{m}^2$ pixel grid and unprecedented material budget of $0.07\,\%\ X_0$ per layer.
The rapid growth of CMOS imaging technology introduces a paradigm change in vertex and

tracking detectors with competitive detection performance, added functionality and higher integration density, while at the same time lowering the material budget and the complexity of operational external services.

2.3. Future Colliders and Experiments

In parallel to instrumentation upgrades necessary for the targeted physics yield of the HL-LHC, several proposals for projects beyond the HL-LHC are underway, including the CERN-based linear e^+e^- collider CLIC [8] as well as future circular colliders [5] FCC-ee [6] and FCC-hh [7]. On a global scale the International Linear Collider (ILC) [41] located in Japan and proposals for China's Circular Electron Positron Collider (CEPC) second CERNS's initiatives for further precision measurements of SM physics as well as new discoveries beyond.
Matching the themes already discussed for the HL-LHC, future hadron colliders face challenges in very high luminosities, subsequent severe pile-up, increased track density, heightened radiation exposure, and unprecedented data rates. The integration of high-precision timing data across various sub-detectors offers a viable solution. Future e+e- colliders, on the other hand, have relaxed timing requirements but depend on a high accuracy in vertex detection and tracking, coupled with minimal material budget. All fundamental detector design challenges rely on matching advancements in electronics, mechanical systems, magnets, and cooling systems.

2.3.1. The Future Circular Collider

The Future Circular Collider (FCC) serves as an example for the selection of future projects and is proposed as a two-stage facility with an electron–positron collider (FCC-ee) preceding the final hadron collider (FCC-hh) upgrade after 30 years of initial lepton-collider operation. The initial FCC-ee operations is foreseen to cover a c.o.m energy range between 90 and 350 GeV, targeting precision measurements of the Higgs boson and the top quark.

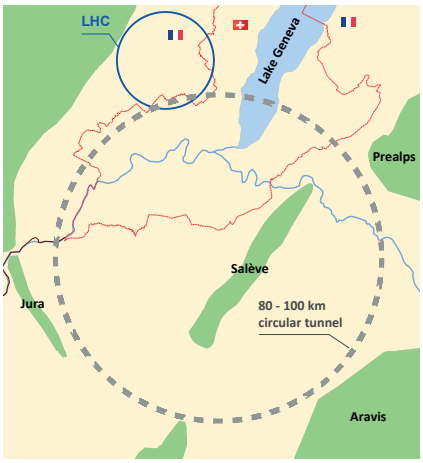

(a) Geographic location/site plan. Modified from [42].

Parameter	HL-LHC	FCC-hh
c.o.m. energy (TeV)	14	100
circumference (km)	26.7	100
peak luminosity ($10^{34}\,\mathrm{cm}^{-2}\,\mathrm{s}^{-1}$)	7.5	30
int. luminosity (ab^{-1})	4	30
bunch spacing (ns)	25	25
events/crossing	135	170
bunch population (10^{11})	2.2	1
pile-up	≈ 200	≈ 1000

(b) Comparison of baseline parameters. Modified from [43] with additions from [10].

Figure 2.4: Geographic overview and comparison of selected HL-LHC and FCC-hh baseline parameters.

The FCC hadron collider stage matches the machine type of the HL-LHC but trumps the

present-day accelerator in its energy and physics reach. Figure 2.4 provides a comparison between the two CERN-based accelerators with respect to the geographical scale of the facilities and a selection of baseline parameters.
The proposed proton collider features a factor 7 increase in energy and extends the range of particle rest mass in the direct observation of collision products by a similar factor. The measurement precision is drastically increased due to larger cross sections for SM processes and higher luminosity. Compared to the HL-LHC, FCC-hh delivers a 4-times larger peak luminosity and a 7-times larger integrated luminosity. The increase in pile-up by an order of magnitude requires the detectors in FCC-hh experiments to face data rates and radiation levels up to 2 orders of magnitude above the HL-LHC conditions.

Ongoing FCC studies use reference designs to evaluate the scale and the requirements of a general purpose detector at the future collider [44]. The detector concepts combine a 4 T central solenoid with a forward magnet system of smaller solenoids or dipoles in an experiment with dimensions comparable to the ATLAS detector. The reference technologies are silicon vertex detection and tracking, liquid argon electromagnetic and hadron calorimetry with scintillator-based hadron calorimetry in the barrel region.

2.3.2. Requirements for vertex and tracking detectors

The development of new pixel detector technologies is a prerequisite for meeting the challenging requirements of the vertex and tracking detectors at future CERN facilities. The themes in pixel detector performance requirements match the previous discussion of the HL-LHC upgrades, but are far exceeded due to the foreseen operational conditions of the future accelerator facilities. Table 2.1 provides an overview of the requirements for the central tracking detectors at the different circular colliders.

Table 2.1: Requirements for tracking detectors at the HL-LHC and FCC. Modified from [10] with additions from [44, 45].

Parameter	HL-LHC	FCC-hh	FCC-ee
fluence ($\mathrm{n\,eq\,cm^{-2}\,yr^{-1}}$)	10^{16}	10^{16} to $8 \cdot 10^{17}$	$< 10^{10}$
max. hit rate ($\mathrm{s^{-1}\,cm^{-2}}$)	2-4 G	20 G	20 M
surface inner tracker ($\mathrm{m^2}$)	10	15	1
surface outer tracker ($\mathrm{m^2}$)	200	400	200
material budget / detection layer (X_0)	0.1%-2%	1%	0.3%
pixel size inner layers ($\mu\mathrm{m^2}$)	50×50	25×50	$< 25 \times 25$
max. single-point resolution (µm)	10	7	3
hit time resolution (ns)	0.2 to 10^3	$\approx 10^{-2}$	$\approx 10^3$
impact parameter resolution (µm)	< 100	< 50	< 10

The eligibility of technologies for the vertex and tracking detectors of future experiments at hadron colliders depends on their radiation hardness or the feasible replacement frequency of sub-detector assemblies. Improvements of an order of magnitude are necessary, compared to state-of-the-art technologies that are presently developed to endure the HL-LHC conditions at the inner-most radii.

Along with the former, hit-rate capability and data throughput are parameters with significant impact on the suitability of a detector technology in such environments. Both ensure the efficient acquisition and processing of hits and similarly need to be enhanced for applications in high occupancy environments.
In particular, the timing information of individual hits provides timestamps for tracks in support of pattern recognition and enables time-of-flight measurements for particle identification. A jump in pile-up for FCC-hh by an order of magnitude requires high precision timing capabilities down to the 10 ps-level.
The highest rate and timing requirements today are achieved by specialty hybrid pixel sensor developments, followed closely in performance by recent radiation-hard monolithic CMOS sensor developments. The latter technology combines high-rate capabilities and 4D measurement precision with particularly low material-budget and power consumption. The planned increase in sensitive detector surface moves the cost-effectivity of sensor and module technologies into the focus of future R&D.
The few-micrometer position resolution of the proposed future vertex detectors in combination with a material budget below 1 % X_0 per detection layer (including structure and services) yields the foreseen factor 2 improvement in impact parameter resolution with respect to the HL-LHC.
The limits of spatial measurement precision are challenged by tracking detectors for future e^+e^- experiments or for heavy-ion experiments in hadron colliders. Exceptionally high spatial measurement precision achieved with ultra-small pixels and very thin detection layers (down to 0.1 %X_0) allows pile-up to be resolved in a high track density and interaction rate environment while achieving $< 10\,\mu m$ impact-parameter resolution.

The required future detector performance calls for sizeable performance gains in sensor technologies beyond the state-of-the-art. Consequently, significant R&D efforts are needed to develop sensors and readout electronics that retain unprecedented performance in operational pixel detector devices that meet the requirements imposed by the foreseen operational conditions and proposed physics programme.

3

Principles of Semiconductor Physics

The detection of charged particles and photons involves their interactions within a medium, leading to energy loss primarily through electromagnetic mechanisms. Pixel sensors make use of the properties and characteristics of semiconductor materials, mainly silicon, which is the most commonly used sensor medium in modern tracking detectors. Charge carriers are generated, mobilized in an electric field and lead to an electrical signal, which indicates the initial particle interaction.
This chapter describes into the principles of semiconductors, which are central to particle detection in silicon. The advantages of semiconductors are summarized and the decision for silicon as the material of choice is motivated. The generation and motion of charge in a semiconductor as well as the modification of the carrier density through doping is discussed before the diode in reverse bias, the central building block of semiconductor particle detectors, is introduced. A discussion of leakage current and its origins closes the section. The second part of the chapter looks at the interaction of photons and charged particles with silicon in terms of energy loss and multiple Coulomb scattering.
The chapter sources from standard literature on the fundamentals and applications of particle detectors [30, 46, 47].

3.1. Semiconductors

Semiconductors offer several advantages in detecting photons and charged particles through ionization.

Energy Resolution: A low ionization energy allows for the creation of large numbers of free charge carriers per deposited unit of energy, improving the ratio between signal and noise as well as the energy resolution.

Charge Collection Efficiency: Charge carriers can be efficiently collected by applying an electric field. The deposited energy is directly converted into a measurable electric signal.

Compactness and Scalability: Small detector volumes are able to maintain high efficiency and detection granularity.

Speed: Charge collection times $O(1\,\text{ns})$ suite high particle high-rate.

Customization and Integration: Advanced consumer electronics fabrication techniques allow a production of highly customized detector geometries and the integration of complex circuitry directly on the sensor.

These properties make semiconductor detectors invaluable in a wide range of applications, including scientific research, medical imaging and the consumer/industrial sector. The following subsections discuss the basic principles of semiconductor materials.

3.1.1. Band Structure

The fundamental mechanism in semiconductor materials employs quantum mechanical principles, that place charge carriers in discrete energy levels. In crystalline structures lattice orientation and size restricts the disposition of energy levels populated by electrons, creating allowed energy bands separated by vacant energy gaps.

Conduction Band: Electrons are not bound to atoms and conduct electric current.

Valence band: Electrons are bound to the respective lattice atom.

In semiconductor materials the separation between bands is small enough to allow an electron to cross the energy gap following a thermal excitation. The band-gap energy E_g is a measure of the separation between both bands and for semiconductors measures $O(1\,\text{eV})$. Insulators comprise a similar band structure, but require a larger energy for an electron to cross between bands ($E_g > 5\,\text{eV}$). The energy bands of conductors either overlap or the conduction band is partially filled and outermost valence electrons conduct current. A representation of the three types of material is shown in Figure 3.1.

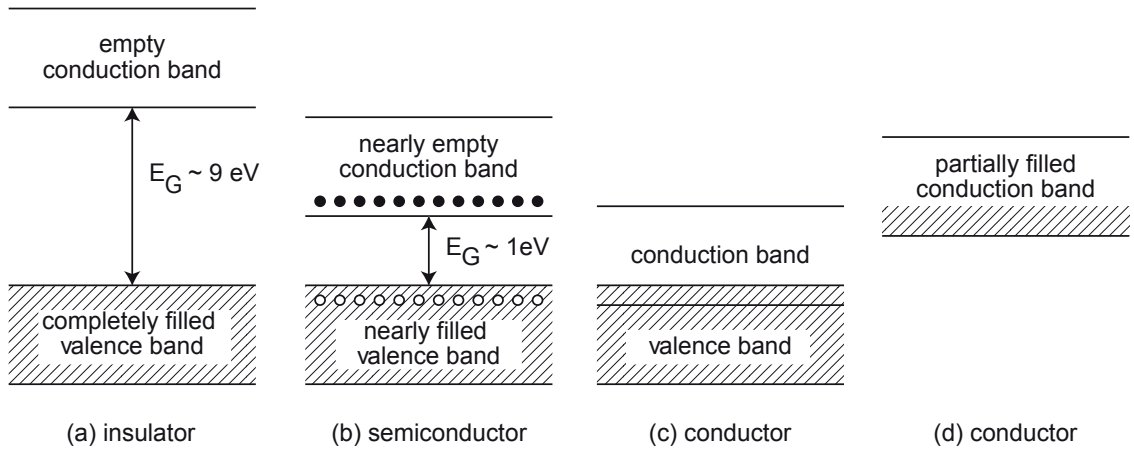

Figure 3.1: Band structure for insulator, semiconductor and conductor materials. Modified from [30].

Vacancies (holes) are created as electrons are excited from their original energy to the higher energy state. Holes are modeled as positively charged particles that move through the bulk and contribute to the conductivity of the material.
The respective lattice momentum of states at the borders with the gap defines the energy input needed to excite an electrons between energy bands. In direct semiconductors the

momenta of both states match. In indirect semiconductor materials a difference in momenta increases the energy requirement for an electron to change states.

Semiconductors exist in intrinsic and extrinsic form. Intrinsic semiconductors consist of Atoms from a singular element. The free charge carriers are generated from thermal excitation. Consequently, at a temperature of 0 K an intrinsic semiconductor holds the properties of an insulator.

3.1.2. Silicon and Doping

Silicon has the atomic number $Z = 14$ which leaves four valence electrons to form covalent bonds with neighboring atoms, making it a semiconductor with a band gap of $E_g = 1.12\,\text{eV}$. Due to its abundance on Earth, processing availability and subsequent wide range of industrial and consumer applications, silicon is utilized in high energy physics (HEP) experiments as an interaction medium for particle detection.
The conduction properties of silicon semiconductors are changed by placing tetravalent or pentavalent atoms inside the lattice, creating n- or p- type silicon through doping. The difference of the covalent bonds is visualized in Figure 3.2 for the example of doping with arsenic (As) and boron (B).

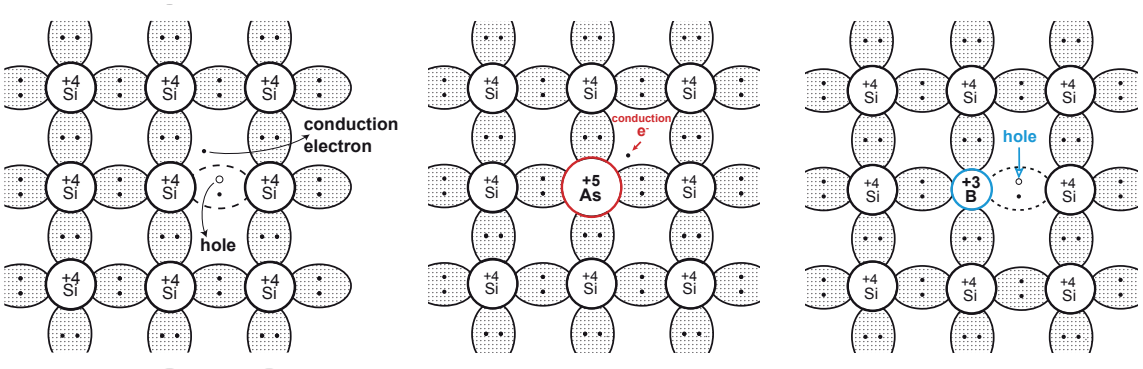

(a) Intrinsic semiconductor. **(b)** n-type semiconductor. **(c)** p-type semiconductor.

Figure 3.2: Intrinsic (a) and extrinsic conduction in n- (b) and p-type (c) semiconductors. Modified from [30]

n-type Dopants with 5 valence electrons provide an extra electron carrier to the conduction band and are referred to as donor impurities.

p-type Dopants with 3 valence electrons introduce a hole carrier into the valence band and are called acceptor impurities.

3.1.3. Charge generation

The interaction of a particle with the lattice of a semiconductor material leads to the generation of electron-hole (e/h) pairs proportional to the released energy. To yield a singular e/h pair in silicon, the introduced energy must exceed the material's indirect band-gap energy. As a semiconductor, silicon has a band-gap energy of $E_g = 1.12\,\text{eV}$ and an excitation energy across its band-gap of about $w_i = 3.6\,\text{eV}$. The average energy w_i for the production of an e/h pair is approximately triple the band-gap energy [47].

This surplus energy is absorbed by the lattice as phonon vibrations, which are emitted in the form of heat. Given a specific energy input E, the formula to calculate the mean count of electron-hole pairs produced is

$$N = E/w_{\mathrm{i}} \quad . \tag{3.1}$$

The expected energy loss of a Minimum Ionizing Particle (MIP) traversing a $O(10\,\mu\mathrm{m})$ thick layer is approximately $\approx 0.28\,\mathrm{keV}/\mu\mathrm{m}$, resulting in about 77 e/h pairs per micrometer [30].

The necessary energy input per generated e/h pair and phonon fluctuates, which leads to a variation in the charge carrier yield

$$\langle N^2 \rangle = F \times N = F \times \frac{E}{w_{\mathrm{i}}} \quad . \tag{3.2}$$

Here, F is the Fano factor [48], with values around 0.1 for commonly used semiconductors. It represents the theoretical limit on energy resolution.

3.1.4. Charge Carrier Motion

The e/h pairs generated through the interaction of particles with matter move freely inside the semiconductor lattice until they recombine. Charge movement within a semiconductor is primarily facilitated through two mechanisms: drift and diffusion [47]. This macroscopic motion of charge carriers is defined as a current density $\vec{J}$, split into the two components

$$\vec{J} = \vec{J}_{\mathrm{drift}} + \vec{J}_{\mathrm{diff}} \quad . \tag{3.3}$$

The mobility is the proportionality factor between the charge propagation speed and a possible externally applied electric field. It depends on the semiconductor material and the electric field itself. For low fields, the mobility is constant, however, for high fields it gradually degrades leading to the charge velocity to saturate.
Drift occurs under an electric field $\vec{E}$, that moves the charges along the field lines while they scatter off lattice phonons and crystal defects. The drift current density is quantified as

$$\vec{J}_{i,\mathrm{drift}} = q_i n_i \vec{v}_i = q_i n_i \mu_i \vec{E} \quad , \tag{3.4}$$

where n_i is the density of charge q_i with the velocity $\vec{v}_i$, defined using charge mobility μ_i and intensity of the electric field $\vec{E}$, indicating the rate of charge movement in response to the electric field. Mobility varies with the semiconductor material, the strength of the applied electric field and with temperature. The velocity increases linearly with the electric field and saturates at $O(1 \cdot 10^7\,\mathrm{cm\,s^{-1}})$. The temperature dependency follows as $\mu_i \sim T^{-2/3}$. The mobility of electrons in the conduction band differs from the slower holes, which rely on the movement of strongly bound charges in the valence band.
Combining both to electron-hole pairs, the Equation (3.4) can be rewritten to

$$\vec{J}_{\mathrm{drift}} = \sum_i \vec{J}_{i,\mathrm{drift}} = q\left(n_{\mathrm{e}}\mu_{\mathrm{e}} + n_{\mathrm{h}}\mu_{\mathrm{h}}\right)\vec{E} = \sigma\vec{E}, \tag{3.5}$$

where e,h denote electrons and holes, respectively. The constant σ represents the conductivity of the material, its inverse value ρ is the resistivity

$$\rho = \frac{1}{\sigma} = \frac{1}{q\,(n_\mathrm{e}\mu_\mathrm{e} + n_\mathrm{h}\mu_\mathrm{h})} \quad . \tag{3.6}$$

The component of diffusion transport describes a motion along a gradient in the concentration of charge carriers $\nabla\vec{n}_i$

$$\vec{J}_{i,\mathrm{diff}} = -q_i D_i \nabla\vec{n}_i = -\mu_i k_\mathrm{B} T \nabla\vec{n}_i \quad , \tag{3.7}$$

D_i representing the diffusion coefficient for the given charge. The Einstein equation allows to substitute

$$D_i = \frac{k_\mathrm{B} T}{q_i}\mu_i \quad , \tag{3.8}$$

where k_B is the Boltzmann constant and T is the absolute temperature. As diffusion originates from random thermal motion, the timescale of diffusion is usually larger than for drift.

The current densities in Equation (3.3) with Equation (3.5) and Equation (3.7) result in the total current density for electron-hole pairs:

$$\vec{J} = \vec{J}_\mathrm{drift} + \vec{J}_\mathrm{diff} = \sigma\vec{E} + k_\mathrm{B} T(\mu_\mathrm{e}\nabla\vec{n}_\mathrm{e} - \mu_\mathrm{h}\nabla\vec{n}_\mathrm{h}) \quad . \tag{3.9}$$

The spatial distribution of the charge collection in perpendicular direction follows as a Gaussian spread $\sigma_{i,\mathrm{charge}}$

$$\sigma_{i,\mathrm{charge}} = \sqrt{2 D_i t_{i,\mathrm{drift}}} = \sqrt{\frac{2 k_\mathrm{B} T x_{i,\mathrm{drift}}}{q|\vec{E}|}}, \tag{3.10}$$

where $t_{i,\mathrm{drift}}$ and $x_{i,\mathrm{drift}}$ represent the drift time and distance, respectively.

3.1.5. Carrier density and Doping

The concentration of free carriers n_i at the energy level E inside an intrinsic semiconductor is

$$n_i = \int_{E_b}^{\infty} N(E) f(E)\,\mathrm{d}E \quad , \tag{3.11}$$

integrating the corresponding density of states $N(E)$ and the Fermi probability distribution $f(E)$ between the lowest energy level in the band E_b and infinity. The density of states is

$$N(E) = 4\pi \left(\frac{2m_i}{h^2}\right)^{3/2} E^{1/2}, \tag{3.12}$$

with the effective mass of carriers m_i in the medium and the Planck constant h. Fermi-Dirac statistics yields the probability distribution

$$f(E) = \frac{1}{\mathrm{e}^{\frac{(E-E_\mathrm{F})}{k_\mathrm{B} T}} + 1}, \tag{3.13}$$

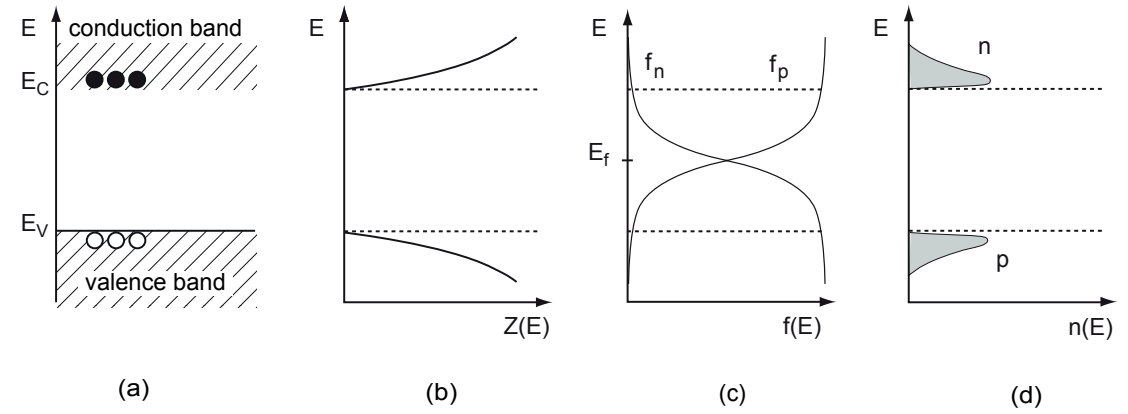

(a) Intrinsic semiconductor.

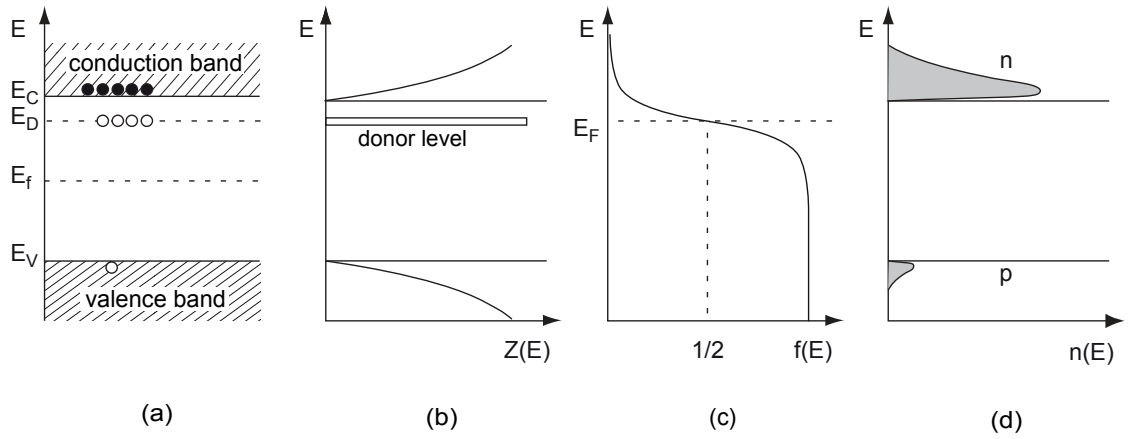

(b) n-type semiconductor.

Figure 3.3: Schematic energy-band model for silicon: (a) band diagram, (b) density of states, (c) occupation probabilities, (d) charge carrier densities in conduction and valence band, respectively. Schematic semiconductor band diagram, density of states $Z(E)$, Fermi-Dirac distribution $f(E)$ and population density $n(E)$. E_C, E_D and E_V represent energy level of the conduction band, the donor impurity energy level and the energy levels of the valence bands, respectively. E_f and E_F represent the intrinsic and doped fermi level, respectively. Modified from [30]

where E_F is the Fermi level, k_B is the Boltzmann constant and T is the absolute temperature. E_F defines the energy where the probability of the carrier occupancy is $f(E) = 0.5$.

Employing the energies of the corresponding conduction E_C and valence E_V bands, the Fermi energy E_I for an intrinsic semiconductor is

$$E_\mathrm{I} \equiv E_\mathrm{F} = \frac{E_\mathrm{C} - E_\mathrm{V}}{2} + \frac{3k_\mathrm{B}T}{4} \ln\left(\frac{m_\mathrm{p}}{m_\mathrm{n}}\right). \tag{3.14}$$

The relation positions the Fermi level is in the middle of the band-gap for $T = 0\,\mathrm{K}$, at higher temperatures a deviation is caused by the different effective masses of electrons and holes.

Industrially produced semiconductor materials, even at the highest possible grade, are extrinsic and commonly get impurities purposefully introduced to modify their properties. Replacing lattice atoms with elements of a different number of valence electrons is changing the balance of charge carriers.
The dopants add a shallow energy level in the band-gap region. Donor impurities introduce additional states close to the conduction band, acceptor impurities cause additional states close to the valence bands. Silicon is doped with both n- and p-types, as well as different concentrations of the same type, that are denoted as n^+ or p^+ type. The energy-band model of intrinsic and n-type semiconductors is visualized in Figure 3.3. In the case of p-doping E_D is replaced by E_A of the acceptor level near the valence band, E_F moves below E_f, and the hole density is larger than the electron density.
At room temperature the majority of atoms are ionized due to the small difference in energy between the added levels and the respective bands. In heavily doped silicon the carrier density $n_{n(p)} \approx N_{D(A)}$ is equal to the concentration of the dopants and N_I is the intrinsic concentration of carriers. For $N_D \gg N_A$, the Fermi level is shifted by

$$E_F = E_I + k_B T \ln\left(\frac{N_D}{N_I}\right) \quad , \tag{3.15}$$

and for $N_A \gg N_D$ the shift amounts to

$$E_F = E_I - k_B T \ln\left(\frac{N_A}{N_I}\right) \quad . \tag{3.16}$$

3.1.6. The p-n Junction

A p-n junction is formed by joining p- and n-doped semiconductor materials along a common interface plane, creating a diode. The inner workings of the interface are illustrated by Figure 3.4a

Built-in Potential
The difference in Fermi levels between both sides of the diode forms a gradient of charge carrier concentration and results in a diffusion current. At the interface, charge carriers recombine and create a depletion region, a zone free of charge carriers. The lattice atoms in the depleted region remain ionized and amount to a space charge. The space-charge density $\rho(x)$ is negative in the p-layer, positive in the n-layer and in combination forms an electric field that causes a drift current opposite to the diffusion.

At equilibrium between diffusion and drift, the Fermi levels match across the junction forcing the energy levels to form a continuous transition. In this case the space-charge region only depends on the doping concentration of the two sides of the diode. The space-charge density is

$$\rho(x) = \begin{cases} -eN_A, & -x_p < x < 0 \\ +eN_D, & 0 < x < x_n \end{cases} \quad , \tag{3.17}$$

with the doping concentration N_A and N_D in the acceptor and donor region, the depths of the space-charge zone x_p and x_n in the p-doped and n-doped parts of the semiconductor and

the elementary charge e.

Charge conservation asks for the number of charge carriers to be equal on both sides of the space-charge region

$$N_A x_p = N_D x_n \quad . \tag{3.18}$$

The electric field $E(x)$ and potential $\phi(x)$ can be derived from Poisson's equation

$$\frac{d^2\phi}{dx^2} = -\frac{\rho(x)}{\varepsilon_0 \varepsilon_r} \quad , \tag{3.19}$$

where ε_0 is the permittivity of vacuum and is ε_r relative permittivity of the material.

Through integration with boundary conditions $E(x) = 0$ outside of the depths of the space-charge zone, Equation (3.19) yields the electric field

$$E(x) = \frac{d\phi(x)}{dx} = \begin{cases} -\frac{eN_A}{\varepsilon_0 \varepsilon_r}(x + x_p), & -x_p < x < 0 \\ \frac{eN_D}{\varepsilon_0 \varepsilon_r}(x - x_n), & 0 < x < x_n \end{cases} \quad . \tag{3.20}$$

The electric potential is derived by integrating Equation (3.20)

$$\phi(x) = \begin{cases} \phi_p + \frac{eN_A}{2\varepsilon_0 \varepsilon_r}(x + x_p)^2, & -x_p < x < 0 \\ \phi_n - \frac{eN_D}{2\varepsilon_0 \varepsilon_r}(x - x_n)^2, & 0 < x < d_n \end{cases} \quad , \tag{3.21}$$

where the potentials at the boundaries of the space-charge region are $\phi_p = \phi(-x_p)$ and $\phi_n = \phi(x_n)$.

The built-in voltage is the voltage drop over the depletion zone and corresponds to the difference in Fermi levels between the two doping types

$$V_{bi} = \phi_n - \phi_p = \frac{1}{q}(E_{F_p} - E_{F_n}) = \frac{k_B T}{q} \ln\left(\frac{N_A N_D}{n_I^2}\right). \tag{3.22}$$

An exemplary band-gap configuration is illustrated by Figure 3.4b I).
By integrating the electric field between the depletion depths x_p and x_n the built-in voltage can be written as

$$V_{bi} = \frac{e}{2\varepsilon_0 \varepsilon_r}(N_A x_p^2 + N_D x_n^2) \quad . \tag{3.23}$$

Silicon has a built-in voltage of approximately 0.6 V.

External bias voltage
An external bias voltage V_{ext} applied across the junction modifies the depletion region. The sign of the external potential distinguishes between two configurations.

Forward Bias is illustrated by Figure 3.4b II). V_{ext} diminishes V_{bi} and forces electron drift from the n-bulk to the p-bulk and causes recombination in the depletion region. For $V > V_{bi}$, current flows through the diode.

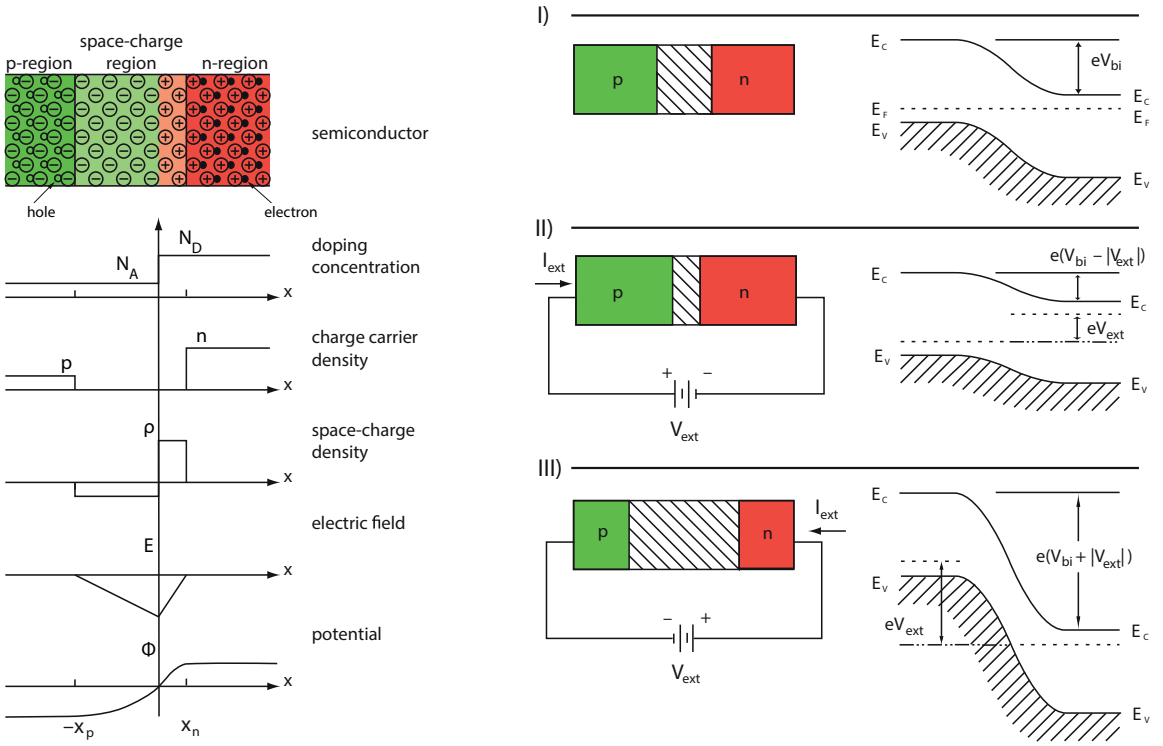

(a) Doping and space charge densities, electric field strength and electric potential at an p-n transition.

(b) External voltage conditions: I) without external voltage, III) with forward voltage applied, III) with reverse voltage applied.

Figure 3.4: Doping, charge, field and potential configuration of a p-n junction and the impact of an external bias voltage. Modified from [30].

Reverse Bias is illustrated by Figure 3.4b III). V_{ext} raises V_{bi} and extracts additional free charge carriers from each side of the diode. The removal of charge carriers leaves an increasing amount of ionized lattice atoms and extends the width of the depletion region.

In reverse biased configuration, the external voltage V_{ext} increases the potential difference of the built-in voltage and based on Equation (3.23) is taken into account as

$$V_{\text{bias}} + V_{\text{bi}} = \frac{e}{2\varepsilon_0\varepsilon_{\text{r}}}(N_{\text{A}}x_{\text{p}}^2 + N_{\text{D}}x_{\text{n}}^2) \quad . \tag{3.24}$$

With the input from Equation (3.18), Equation (3.24) is solved for the depletion width $d = x_{\text{p}} + x_{\text{n}}$

$$d = \sqrt{\frac{2\varepsilon_0\varepsilon_{\text{r}}}{e}\left(\frac{1}{N_{\text{A}}} + \frac{1}{N_{\text{D}}}\right)(V_{\text{bi}} + V_{\text{ext}})} \quad . \tag{3.25}$$

A large doping gradient between both sides of the junction is assumed to be the typical case

for silicon-based particle detection. With $N_A \gg N_D$, a simplification is obtained:

$$d \approx \sqrt{\frac{2\varepsilon_0 \varepsilon_r}{e N_D} V_{ext}} \quad . \tag{3.26}$$

Due to the higher mobility of electrons, the expansion of the depletion originates on the p-type side of the diode and extends towards the n-doped bulk.

The model of a charged capacitor can be used to approximate the depletion region of the reverse-biased p-n junction. The space-charge region similarly holds an electrical potential difference without any free charge carriers. The capacitance per unit area C_A is estimated by

$$C_A = \varepsilon_0 \varepsilon_r \frac{1}{d} = \sqrt{\left(\frac{\varepsilon_0 \varepsilon_r e N_D}{2 V_{bias}} \right)}. \tag{3.27}$$

Capacitance limits the frequency response of the readout circuitry and thereby plays a central role in signal formation and detection. Low capacitance values are beneficial for the overall performance of a detector and are achieved by large widths d of the depleted regions, obtained by high reverse bias voltages and low-doped (high resistivity) junctions.

3.1.7. Leakage Current

Leakage current I_L is observed in reverse biased semiconductor devices and has volume as well as surface contributions that originate from multiple physical sources. Even in ideal diodes, leakage current is present. The depleted region not only affects e/h pairs charges generated by interacting particles but also carriers that originate from thermal excitations or diffusion from un-depleted regions. For thick depletion layers (≤100 µm) the volume contribution to the leakage current is typically dominant.

Volume Contributions
The predominant source of leakage current is thermal generation of e/h pairs in the depletion region. Impurities in the lattice act as generation/recombination centres in the band gap. The observed current is proportional to the depleted depth $d \propto V_{ext}$ underneath the area A of an electrode, $A \times d$.

$$I_L^{gen} = eAd \frac{N_i}{\tau_g} \quad , \tag{3.28}$$

where τ_g is the charge carrier generation lifetime. The strong temperature dependency of $N_i \propto T^{3/2} e^{-E_G/2k_BT}$ propagates to I_L. A parametrization leads to:

$$I_L^{gen} \propto T^2 \exp \frac{-E_a}{2k_BT} \quad , \tag{3.29}$$

where E_a is the activation energy of approximately 1.21 eV in the case of silicon.
A 1 K increase in temperature at room temperature (293 K) results in an approximately 8.5 % increase of the volume leakage current.

Surface Contributions
Surface contributions to the leakage current behave linear with the applied voltage and depend on the geometry of surface structures.
Surface leakage current (I_S) can be parameterized by

$$I_S = 1/2 e s_0 N_i A_s \tag{3.30}$$

where e is the elementary charge, s_0 is the surface recombination velocity, N_i is the intrinsic carrier density, A_s is the depleted surface area. The surface recombination velocity $s_0 = \sigma v_{th} N_{it}$, with the capture cross-section σ, the thermal velocity of the carriers v_{th}, and the interface trap density N_{it}.
The intrinsic carrier density (N_i) and the thermal velocity (v_{th}) are the primary factors that vary significantly with temperature.
The intrinsic carrier density's temperature dependence is given by $N_i(T) \propto e^{-\frac{E_g}{2kT}}$, where E_g is the semiconductor's band-gap energy, k_B is the Boltzmann constant, and T is the temperature in Kelvin. The thermal velocity is proportional to the square root of the temperature, $v_{th}(T) \propto \sqrt{T}$.
Incorporating these temperature dependencies:

$$I_s(T) \propto A_s \sigma N_{it} \sqrt{T} e^{-\frac{E_g}{2k_B T}} \quad . \tag{3.31}$$

The exponential term related to $N_i(T)$ dominates the temperature dependency of I_S, especially for semiconductors with a significant band-gap E_g.
A 1 K change in temperature around room temperature (293 K) results in an approximately 7.6 % increase in surface leakage current.

3.2. Particle Interaction with silicon

The energy deposition from a particle interacting with matter depends on the particle type, its initial energy and the interaction material. The following subsections describe the interaction of photons and charged particles with matter.

3.2.1. Photons

The interaction of photons in matter is described by the photoelectric effect, pair production and the Compton effect. In interactions based on the photoelectric effect or pair production, the photon is completely absorbed. The Compton effect describes the scattering of the photon with a charged particle in the material. The attenuation of a monochromatic photon beam with intensity I_0 is described by

$$I(x) = I_0 e^{-\mu x} \quad , \tag{3.32}$$

which results in the final beam intensity $I(x)$ after a pathlength x in material. The attenuation length μ is a characteristic of the material in combination with the initial photon energy.

The probability of photon absorption in a 300 μm layer of silicon is plotted in Figure 3.5, subdivided into contributions from the three interaction processes. At low photon energies below ≈100 keV, the photoelectric effect dominates.

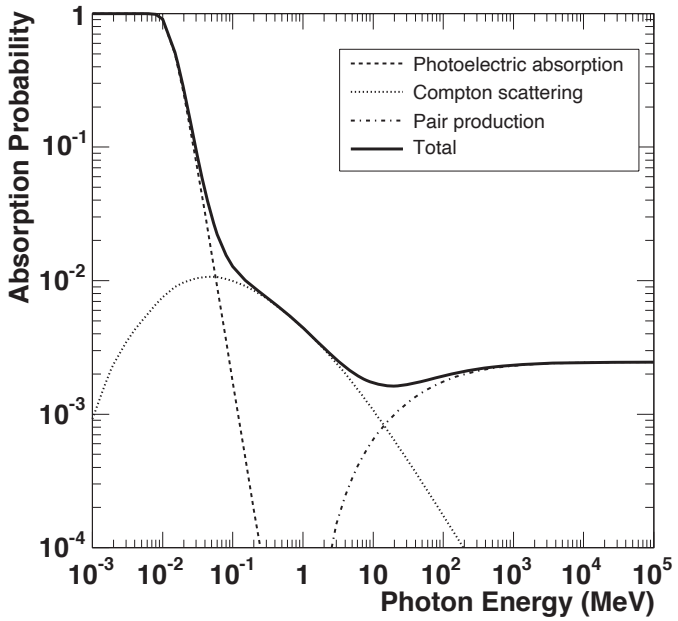

Figure 3.5: Photon absorption probability for a 300 µm layer of silicon as function of the photon energy. The contributions from the different processes are indicated for the case of silicon [47].

At higher energies, scattering processes gain in importance. Pair production contributes at energies $> 2 \times m_e$ and remains relevant even above 10 MeV. The probability of photon interactions is high for energies $\lessapprox 10\,\text{keV}$.

3.2.2. Charged Particles

The energy loss of a charged particle traversing a material is caused by a combination of ionization, atom excitation and bremsstrahlung effects. The mean energy loss also called stopping power, is the lost energy per unit path length and depends on the particle mass and momentum.

The Bethe-Bloch formula describes the energy loss per unit distance $\left\langle \frac{dE}{dx} \right\rangle$ of a charged particle in the range of $1 \cdot 10^{-1} < \beta\gamma < 1 \cdot 10^{3}$, which ionizes the medium as it passes through the lattice.

$$-\left\langle \frac{dE}{dx} \right\rangle = \frac{K}{\beta^2} z^2 \frac{Z}{A} \left[\frac{1}{2} \ln \left(\frac{2 m_e c^2 \beta^2 \gamma^2 T_{\max}}{I^2} \right) - \beta^2 - \frac{\delta(\beta\gamma)}{2} \right] \tag{3.33}$$

The individual variables are listed in table 3.1.
Figure 3.6 shows the stopping power as a function of the normalized momentum $\beta\gamma = p/mc$ for pions interacting with silicon. The interactions are split according to individual underlying processes that cover the low energy region, the Bethe region and the radiative region.

At small incident particle energies, the stopping power decreases with β^{-2} until reaching the minimum at around $\beta\gamma \approx 3$ (corresponding to about $0.94c$). Afterwards, the logarithmic part $\ln(\beta^2\gamma^2)$ slowly increases the value. Particles in this valley with minimal energy loss are called minimum ionizing and deposit the least amount of the energy in the detector.

Table 3.1: Variables for Bethe-Bloch formula.

K	$4\pi N_A r_e^2 m_e c^2$		
N_A	Avogadro's number	c	speed of light
r_e	electron radius	β	particle velocity (as v/c)
m_e	electron mass	γ	Lorentz factor $1/\sqrt{(1-\beta^2)}$
z	incident particle charge	T_{max}	max. kin. energy transfer in single collision
A	atomic mass of absorber	I	mean excitation energy
Z	atomic number of absorber	$\delta(\beta\gamma)$	density correction (high energy particles)

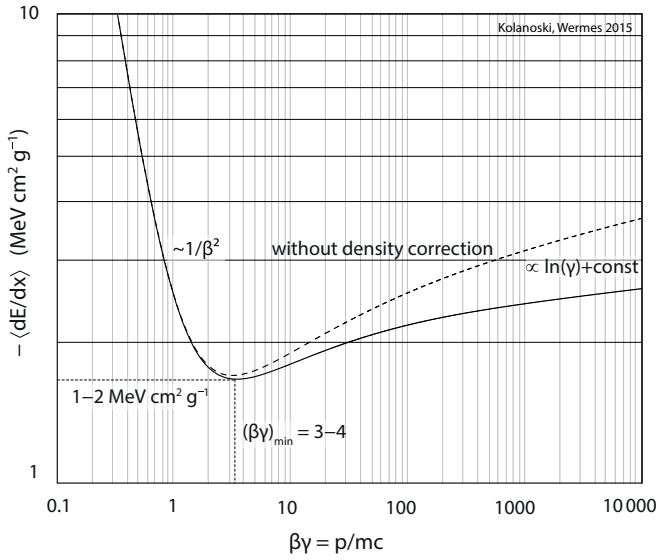

Figure 3.6: Mean energy loss of for charged pions by ionization in silicon as a function of the normalized momentum $\beta\gamma = p/mc$, taken from [30].

While the Bethe region describes kinematic losses which causes excitation or ionization in the atomic electrons, the high energy region is then mostly dominated by radiative losses such as Bremsstrahlung.
Particles with an energy close to the minimum in energy loss rate are called Minimum Ionizing Particle (MIP).

The energy loss probability follows Landau distribution [49]. Figure 3.7 exemplifies the energy loss distributions for 500 MeV pions in silicon samples with four different thicknesses. The most probable energy loss decreases with decreasing thickness of silicon.

Head-on collisions of the incident particle with an electron in the valence band of the lattice transfer large energies. The corresponding electron, called δ electron, is kicked out of its bound state and can create additional electron-hole pairs. This effect deposits a large fraction of energy off track and can lead to a deterioration of the spatial resolution of a segmented silicon sensor.

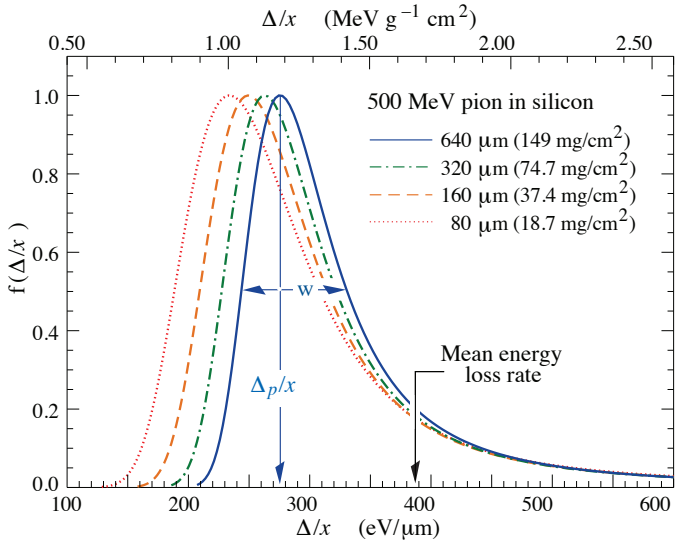

Figure 3.7: Probability density functions $f(\Delta/x)$ of energy loss (Δ) for 500 MeV pions in silicon of different thicknesses (x), normalized to unity at the most probable value [50].

3.2.3. Multiple Coulomb Scattering

The interaction of particles and material do not leave the trajectory unchanged but introduce offsets as well as changes in direction. While the traversing particle loses energy in inelastic scattering, the underlying Coulomb interaction can similarly result in an elastic scattering. Elastic Rutherford scattering impacts the direction of the particle trajectory.
The large number of interactions along the path through a medium allows for approximating the effect using a Gaussian distribution. The standard deviation models the RMS scattering angle $\theta^{\text{RMS}}_{\text{plane}}$

$$\theta^{\text{RMS}}_{\text{plane}} = \frac{13.6\,\text{MeV}}{\beta c p} z \sqrt{\frac{x}{X_0}} \left[1 + 0.038 \ln\left(\frac{x}{X_0}\right)\right] \quad . \tag{3.34}$$

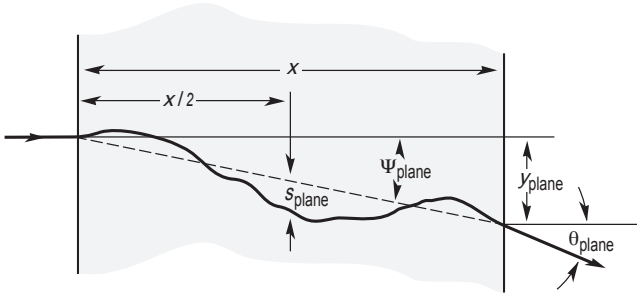

Figure 3.8: Schematic visualization of the Coulomb scattering. Modified from [30].

The material thickness x are given relative to the material radiation length X_0, which is defined as the traveled distance that associates with an energy loss of $(1 - 1/e) \times E_0$.

Multiple scattering interactions are illustrated in Figure 3.8 in a scattering layer perpendicular to the incoming particle. The denoted characteristic quantities are associated with the effects encountered by a particle traversing a layer of material with thickness x. θ_{plane} is the effective scattering angle, ϕ_{plane} is the deflection angle. The vertical offset from the initial position is given by y_{plane} and the offset s_{plane} in the center of the material.
Multiple Coulomb scattering can be reduced by minimizing the amount of detector material along the particle trajectory.

4

Silicon Pixel Detector Concepts

The fundamental working principle of modern pixel sensors is based on the properties of semiconductors, mostly silicon, and the basic concept of the junction between n- and p-doped lattice structures. The general properties and applied concepts are discussed in the previous Chapter 3.
The underlying structure of a silicon detector is the sensitive bulk volume that serves as an interaction volume for traversing particles. A single-sided segmentation of e.g. the n-layer on top of a p-type bulk introduces the possibility to obtain spatial information at a precision far below the dimensions of the sensor silicon die. The n-layer forms an array of pixels on top of the p-doped silicon substrate of a planar silicon sensor.
The energy that is deposited by a charged particle through ionization or by a photon after its absorption results in the generation of e/h pairs which are immediately separated by the applied external electric field. The drift movement of free charge carriers through the sufficiently depleted bulk induces a signal on individual collection electrodes. The signal amplitude and shape is determined by the number of charge carriers, their drift velocity as well as the geometry of the respective electrode.

This chapter outlines the concepts of silicon pixel detectors with a focus on the aspects that are relevant for this thesis. Initially the mechanisms that form an electrical signal on individual collection electrodes of an array of pixels are introduced. The extraction of spatial information from different signal readout approaches is discussed for the common square geometry of the pixel grid before a-typical geometries are considered. Following the signal path of a pixel detector, the basic building blocks of application specific frontend electronics are outlined and motivate the measurement observables acquired by a silicon pixel detector. A discussion on sources of fake signals originating from the front-end circuitry closes the introduction into signal processing.

4.1. Signal Formation

An electric signal is detectable across the duration of charge drift within the depleted volume. Charge generated outside of the depleted sensor diffuses and only partially reaches the depleted region from where it is subsequently collected by drift. The induction of current on an electrode is instantaneous for a charge q that drifts with velocity v. The mechanism is

described by the Shockley-Ramo theorem [51, 52]. The induced current is

$$i = -\frac{dQ}{dt} = q \cdot \vec{E}_w \cdot \vec{v} = q\mu \vec{E}_{\mathrm{w}} \vec{E} \quad , \tag{4.1}$$

where $\vec{E}_{\mathrm{w}}$ is the weighting field, obtained as the electric field when removing the charge q, applying a unit potential to the respective electrode and zero potential to all other conductors. The weighting field describes the interaction between the moving charge and the collection electrode as well as depends on the geometry of a given pixel cell. It affects the strength of the induced signal and not the movement of the charge carriers.
The total collected charge is a time integral of the induced current. The total charge induced on the collection electrode by a carrier q that drifts between time t_1 and t_2 from position x_1 to x_2 follows from

$$Q = \int_{t_1}^{t_2} i(t)\, dt = q \left[\phi_w(x_1) - \phi_w(x_2)\right] \quad , \tag{4.2}$$

where ϕ_w is the weighting potential obtained as the electric potential when removing the charge q, applying a unit potential to the electrode and zero potential to all other conductors.

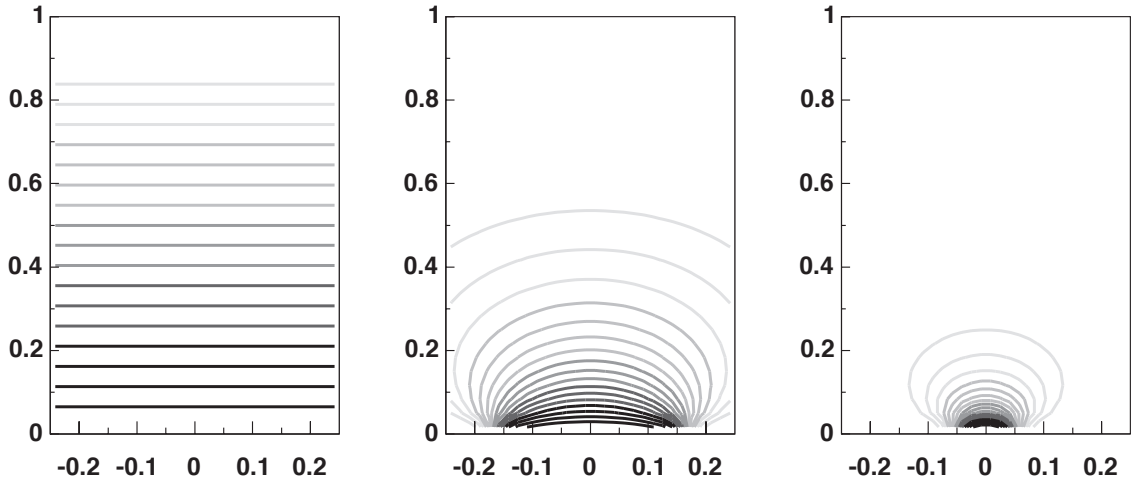

(a) Infinite parallel electrodes in a planar, non-segmented sensor.

(b) Collection electrode 1/3 of the sensor thickness.

(c) Collection electrode 1/10 of the sensor thickness.

Figure 4.1: Illustration of the equipotential lines of the weighting potential for two infinite parallel plates (a), a collection electrode at y = 0 of 1/3 (b) and 1/10 (c) times the unit sensor thickness. Modified from [47].

Figure 4.1 shows the weighting potential for an exemplary sensor thickness of 1 in vertical direction. The illustration is based on a blanket electrode at $y = 1$ and changing collection electrode geometries at $y = 0$. Figure 4.1a shows the case of two infinite parallel planar electrodes. Figure 4.1b and Figure 4.1c exemplify two different aspect ratios between sensor thickness and collection electrode size. The dominant part of the weighting potential moves closer to the collection electrode as the electrode size decreases. The majority of the signal observed by a small collection electrode is induced during the charge carrier drift path in close proximity to the electrode. Upon completion of the drift motion, the induced charge converges to q. The duration of signal induction corresponds to the charge collection time, its integral equals the total charge generated from the particle interaction in the sensor material.

The amount of the induced charge is affected by a modification of the weighting potential that is therefore introduced with the placement of neighboring collection electrodes in a pixelated device.

4.2. Position measurement

The main parameter affecting the spatial resolution of a segmented silicon sensor is the distance between the centers of neighboring collection electrodes, the pixel pitch. Further contributions to the effective spatial detector resolution are found in the amplification, shaping and digitization stages of the application-specific detector frontend electronics. The method applied for the readout of the induced signal (analog or single threshold binary) determines the available information. Finally, the reconstruction algorithm that attributes coordinates in the detector plane to a recorded signal in combination with the amount of charge that is shared between neighboring pixels allows to further improve the precision in hit position reconstruction.

4.2.1. Binary Readout

Binary readout electronics register the particle interaction, a hit, as the signal level crosses a predefined single threshold. This readout strategy is applied for example in detectors that need to cope with very high particle interaction rates and do not prioritize energy resolution.

The theoretical expectation for the 1-dimensional spatial resolution of a pixel detector with pitch p, centered around position 0 is based on a tuned threshold that only yields a hit in a single pixel per impinging particle track. Intercept positions of an incoming uniform density of particles, between $-p/2$ and $p/2$, trigger a signal in the exemplary single pixel. Consequently, the average distance σ_{pos} between the track impact position x_r and the measured impact position $x_m = 0$ (equivalent to the pixel center) is given by

$$\sigma_{\text{pos}}^2 = \frac{\int_{-p/2}^{p/2} (x_r - x_m)^2 dx_r}{\int_{-p/2}^{p/2} dx_r} = \frac{p^2}{12} \quad \text{and} \quad \sigma_{\text{pos}} = \frac{p}{\sqrt{12}} \quad . \tag{4.3}$$

Figure 4.2a shows the registered signal in two neighboring pixels as function of the particle impact position x.

4.2.2. Charge Sharing

In a segmented grid of collection electrodes e/h pairs are regularly generated by a single traversing particle in the volume of two or more neighboring pixels. To employ the full dynamic range of the readout circuitry, the detection threshold is set low, outside of the regime of fake hits from thermally generated e/h pairs (Section 3.1.7) or electronic noise effects (Section 4.5). The group of pixels that shares a signal charge from an interaction of a singular particle is called cluster.
Charge sharing is mostly affected by the position and angle of the track with respect to the sensor surface, as illustrated in Figure 4.3.

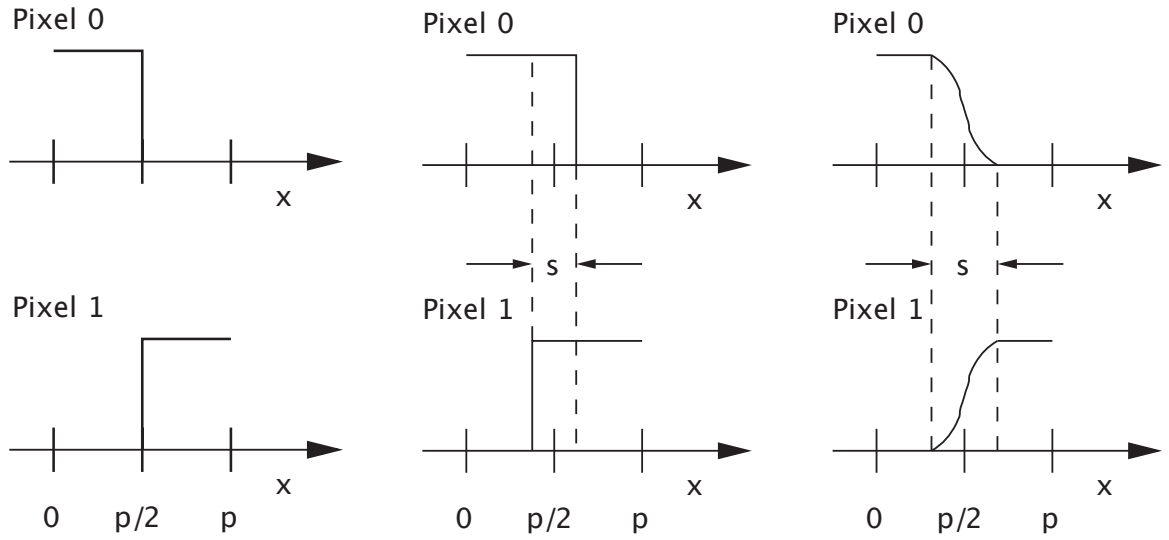

(a) Binary readout, no charge sharing. **(b)** Binary readout, charge sharing. **(c)** Analog readout.

Figure 4.2: Registered signals in two neighboring pixels in relation to the particle impact position x. Modified from [47].

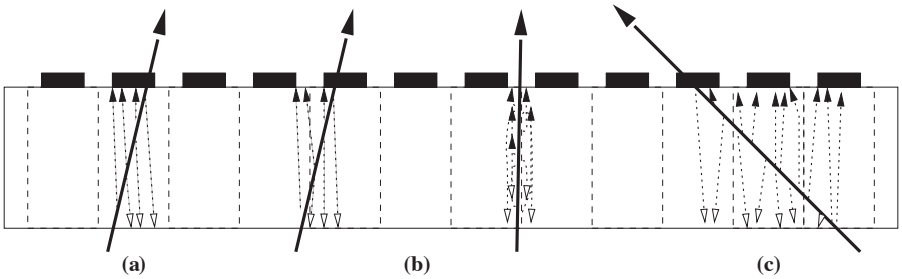

Figure 4.3: Clusters in a silicon detector in the cross section perpendicular to the sensor surface. Solid and hollow arrows on dashed lines denote the different types of charge carriers. Bold arrows indicate particle tracks. (a) size 1, (b) size 2 and (c) size 3 are shown. Modified from [47].

A cluster size > 1 improves the measurement precision due to the spread of spatial information across multiple measurement channels.
The overlap s between a signal recorded by two neighboring pixels is exemplified in Figure 4.2b for a two-pixel cluster between pixel 0 and pixel 1. Particle intercepts that trigger two pixels can be observed with a resolution of $s/\sqrt{12}$. If a singular pixel responds, the resolution is $(p-s)/\sqrt{12}$. The optimal average spatial resolution is reached when $s = p/2$, or when the recorded share of one-pixel and two-pixel clusters is equal.

4.2.3. Analog readout

An improvement of the spatial resolution can be achieved by measuring the signal charge within a cluster.
Through processing of the analog signal shape a readout channel delivers an observable

proportional to the collected charge. Figure 4.2c illustrates two neighboring pixel cells that both register a signal with additional charge information. The added information enables higher fidelity in the transition region between neighboring pixels. A charge-weighted averaging algorithm and corrections for non-linearity in the electric field at the pixel borders are used to achieve a more precise determination of the particle impact point. The algorithm performs best if the spread of the generated charge carrier cloud is of similar dimension as the collection electrode pitch.

By adjusting the detector orientation with respect to the incoming particle track, the region of charge sharing s can be modified to obtain the optimal impact angle and average cluster size. Particle trajectories that differ from the perpendicular case are illustrated in Figure 4.3b and Figure 4.3c. In the tilted configuration, the fraction of two pixel clusters is limited by the smallest possible pixel threshold without significant contributions from fake hits. The optimization of spatial resolution comes with a trade off between cluster size and single-pixel signal. As the signal is shared between multiple pixels, measurement observables that depend on an optimized single-pixel signal amplitude degrade in performance. Consequently subpar signal-to-noise ratio has a negative impact on detection efficiency of larger-size clusters as well as the location of the rising signal edge in timing applications.

4.2.4. Pixel Geometry

A small pixel size is the trivial requirement for a high spatial resolution. A geometrical approach in increasing the spatial resolution without changing the pixel pitch is illustrated by Figure 4.4. In first iteration pixels are arranged in a bricked pattern with a rectangular aspect ratio instead of the usual square footprint. In a rectangular pixel grid aligned with the horizontal axis, a two-pixel cluster across two neighboring rows has an effective pitch of $p/2$, along the horizontal axis. The mean cluster size is reduced by the grid geometry in which at each of the pixel corners only three pixel cells meet.

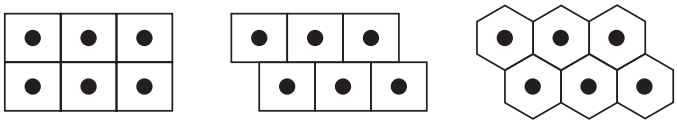

Figure 4.4: A standard rectangular pixels layout, a bricked arrangement and hexagonal pixels of the same pitch. Modified from [47].

The same advantage is obtained from an array of hexagonal pixels. In the case of a particle hit in the corner of a hexagon, the deposited signal charge is shared between the surrounding triplet of pixels. More charge is left per pixel as compared to squares and the mean drift distance across the pixel area is reduced compared to the bricked rectangular design. An even coverage of a given sensor area in both dimensions reduces the inter-pixel capacitance which is responsible for noise and cross talk between pixels.

4.3. Technology Packaging

Pixelated devices can be read out either as a hybrid detector, separating sensor and dedicated readout chip (ASIC) into two devices that are connected in a flip-chip process, or as a

monolithic device that integrates sensor structures and readout in a singular silicon die.

4.3.1. Hybrid Pixel Detectors

Hybrid pixel detectors separate the sensitive sensor layer and the readout electronics in separate silicon dies. This enables the sensor pixel matrix to be produced in a material and manufacturing process independent of the readout chip. The ASIC manufacturing can be facilitated by an industrial-standard, large-volume CMOS process, reducing cost and introducing modularity to the final detector assembly. The sensor and the readout chip can be optimized separately and tailored for individual applications. In both sensor and readout chip the pixel cells are usually arranged in the same grid structure with identical pitch. Both devices are interconnected using flip-chip and bump-bonding techniques, which as well are available in the semiconductor industry.

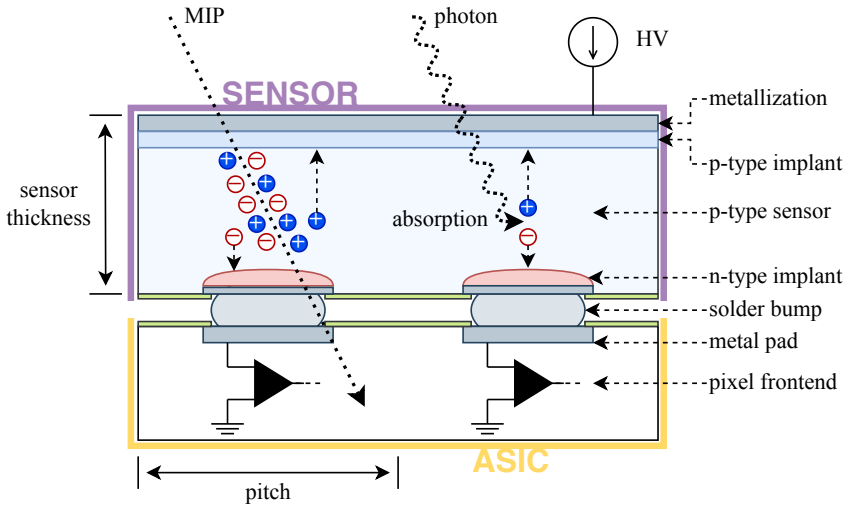

Figure 4.5: Schematic cross-section of a hybrid pixel detector consisting of a depleted silicon sensor on top bump-bonded to a readout ASIC below. The relevant cases of signal generation, induced signal from a traversing MIP as well as from an absorbed photon, are shown.

The interconnection technique used for the hybrid packaging imposes limitations to the pixel detector concept. The available bump-bonding technique enforces a minimum pixel size and increases the sensor capacitance, resulting in a larger power consumption and a larger material budget for the same detection performance. Additionally, the applied hybridization techniques are complex and take up a significant share of the cost for large-area detector systems.

4.3.2. Monolithic Pixel Detectors

Monolithic active pixel sensors (MAPS) integrate both, sensor structures and readout circuitry in a singular silicon die. While initially established for the commercial detection of visible light, pixel detectors based on the monolithic packaging was successfully operated in a particle beam as early as 1992 [53]. The manufacturing process of monolithic chips employs commercial CMOS technologies and with that, offers a cost-effective alternative to hybrid

detectors. The technology realizes smaller pixels at a lower pixel capacitance with reduced power consumption and material budget compared to hybrid detectors. The latter is inherent to the single-layer silicon device.

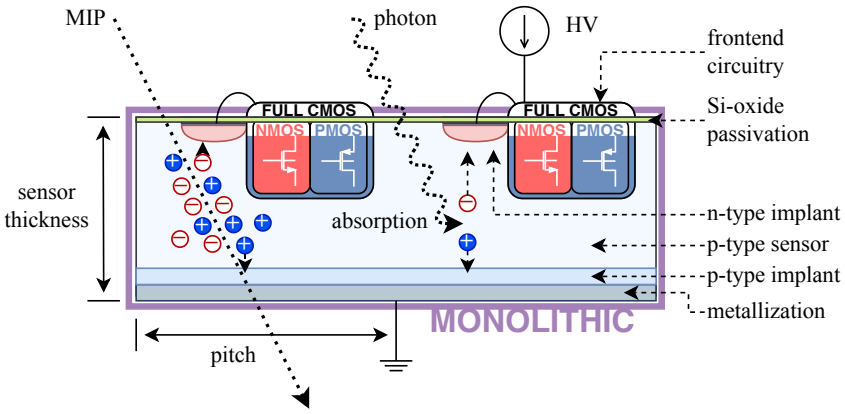

Figure 4.6: Schematic cross section of a CMOS pixel detector cell (MAPS). The charge from a charged particle is collected in an n-well electrode on the p-epitaxial layer.

The simplified MAPS structure in Figure 4.6 shows a n-type collection electrode in a p-type substrate. The full CMOS readout electronics are placed next to the collection electrode inside a p-well which is used to shield the transistors. MIPs generate e/h-pairs along their full path through the sensor thickness and call for fast, uniform charge collection from the whole sensitive sensor volume. Photons are absorbed and locally generate an e/h-pair after penetrating the silicon to a characteristic depth. Compared to diffusion processes, the collection by drift dominates a monolithic sensor concept. Small collection electrodes providing a low sensor capacitance in combination with large-area, complex readout circuitry complicate full sensor depletion over the entire pixel area.
The sensor structures, design concepts and readout circuitry of the monolithic technology demonstrator FASTPIX are introduced and discussed in the following Chapter 5.

4.4. Frontend Electronics

The induced electrode signal is amplified, shaped and digitized by application-specific circuitry. The following subsections discuss general aspects of the electronic circuitry inside a pixel frontend.
In particle physics tracking application the necessary large amount of readout channels and uncompromising reliability asks for a self contained approach to the frontend circuitry design that has to integrate into the data aggregation of a complex detector system. In demonstrator chips or detector prototypes, the readout architecture is implemented for a reduced number of channels, functionality and specification and relies on external equipment to complete a measurement setup.

4.4.1. Charge-sensitive Front-end

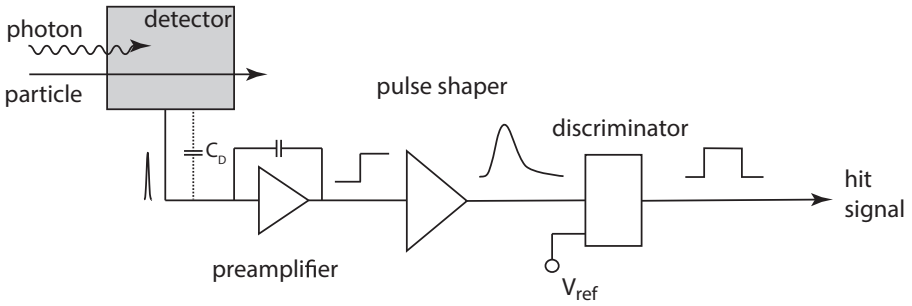

Figure 4.7: Generic front-end readout scheme of a detector including amplification, pulse shaping and discrimination. Modified from [30].

Figure 4.7 shows a diagram of the fundamental blocks that are typically implemented in a front-end readout chain for HEP applications. The charge signal induced on a collection electrode of a silicon pixel detector is of the order of 1 fC and has to be amplified. Each pixel is represented by an effective detector capacitance C_D, a signal current modeled by a current source I_{sig}. The short current signal induced on a collection electrode is connected to a high-gain node with a capacitive feedback. The signal at the input of this charge-sensitive amplifier (CSA) is integrated and transformed into a voltage step proportional to the signal charge. The gain of the CSA is determined by the feedback capacitance C_f.

After the amplifier the voltage step is filtered by a shaper applying a tunable bandwidth limitation to the signal that reduces the electronic noise and the probability of signal pile-up. The output of the shaper is a triangular pulse with a height and width proportional to the input charge and with that also proportional to the energy deposited in a given pixel. A significant impact on the performance of the signal path is the detector capacitance parallel to the preamplifier input. Input capacitance has to be accounted for in the design of the front-end circuitry and determines the noise performance.
The linearity of amplification, shaping and pulse filter stages is another important property for the readout chain. Especially the latter step can only be realized by an electronic circuit block if the shape of the input signal does not change with its amplitude.

The shaper output is proportional to the generated charge and with that also proportional to the energy deposited in a given pixel. A discriminator compares the shaper output voltage to a reference voltage V_{ref}. Whenever the discriminator input exceeds the reference, a digital signal is generated at its output. The width of the discriminator output signal corresponds to the duration for which the input signal exceeds the threshold.
The discriminator charge threshold, has a direct impact on detection efficiency as particles generating a small number of e/h pairs during their interaction in the sensor are likely to induce signals that stay below a certain set threshold.
In order to retain high detection efficiencies, the charge threshold of the discriminator is set to values that yield a small share of fake hits without significantly cutting into the signal range of the observed physics processes. Small variations in circuit components result in a

pixel-to-pixel variation of the threshold response.

Depending on the application, the discriminator output or a pair of digital pulses, marking both intercepts with V_{ref}, is propagated to the periphery for further processing.
Additional features of the in-pixel circuitry include the possibility of injecting a test pulse to the input of the amplifier in order to test the readout chain without a particle beam. Other common feature entail the possibility of pixel masking or tuning DACs for signal response equalization.

4.4.2. Time of Arrival, Time Walk and Time over Threshold

The charge collection time, amplifier rise time, shaper bandwidth, discriminator speed and digital logic delay contribute to the response time of the signal output. The dominant contribution is the signal propagation time from the amplifier to the discrimination stage output.
In applications that depend on precise time measurements, a decrease of the timing performance for smaller input pulse height is observed. Figure 4.8a illustrates how the discriminator stage compares an input pulse with a set voltage threshold and generates a rectangular output pulse.

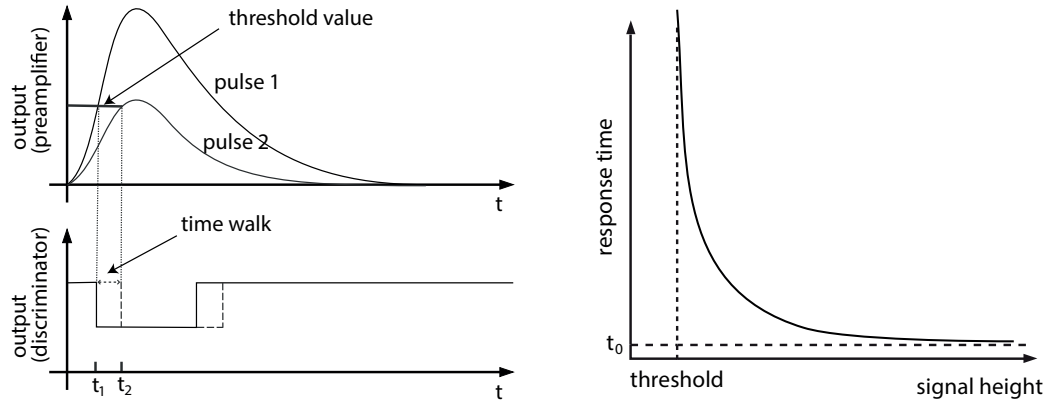

(a) Time walk mechanism.

(b) Response time.

Figure 4.8: Time walk behavior in a readout chain with discriminator. Time delay dependence of the discriminator output on the pulse height; t_0 quantifies the minimal delay caused by the discriminator electronics only. Modified from [30].

Figure 4.8b illustrates the dependency between response time and signal height. Signal height is measurement as time-over-threshold (ToT). The time Δt during which the signal pulse is larger than a given threshold value is proportional to the peak height and the total area of the pulse. The ToT gives an indirect representation of the total deposited charge. In applications demanding high timing precision the response time over signal height is modelled and a correction is applied.

4.5. Noise

Noise from the gain stages of the front-end electronics result in fake hits from voltage fluctuations which limit the detectable charge to a minimum detectable signal above threshold.

4.5.1. Equivalent Noise Charge

The noise is quantified by the equivalent noise charge (ENC) and is defined as the amplitude fluctuation of the input charge that results in the voltage noise observed at the output.
Electronic noise is the result of stochastic fluctuations in the number and velocity of charge carriers. Noise is typically described by means of its power spectral density. Depending on the physical processes, the following noise sources can be identified:

4.5.2. Thermal Noise

Thermal excitation of charge carriers induces fluctuations in a device current. The power spectral density of a current flowing through a conductor with resistance R and temperature T is

$$d\langle i^2\rangle_{\text{therm}} = 4k_B T \frac{1}{R}\, df \quad , \tag{4.4}$$

independent of the frequency (white noise) and current. The thermal noise of a transistor depends on its biasing and size and can be expressed as a voltage in series with its gate. The transistor power spectral density is

$$v^2_{n,th} = 4k_B T \frac{2}{3}\frac{1}{g_m}\, df \quad , \tag{4.5}$$

where g_m is the transconductance of the transistor.

4.5.3. Shot Noise

Statistical fluctuations of carriers emitted independently of each other form a noise contribution as they cross a potential barrier (e.g. p-n junction). The power spectral density is

$$d\langle i^2\rangle_{\text{shot}} = 2qI_0\, df \quad , \tag{4.6}$$

where I_0 is the mean current flowing through the barrier. Shot noise is directly proportional to the current and has a white noise spectrum.

4.5.4. Flicker Noise

The defects at the interface between silicon and the gate oxide are responsible for the capture/release of charge. The fluctuations of carriers from these defects contribute to non-physical signals in a readout channel. The power spectral density of the flicker noise has a $1/f$ behavior and can be expressed as a voltage source in series to the transistor gate.

$$d\langle v^2\rangle_{\text{flicker}} = \frac{k_f}{C^2_{ox} WL}\frac{df}{f} \quad , \tag{4.7}$$

where k_f is a process-specific constant, C_{ox} is the gate oxide capacitance per unit of area and W and L are the transistor width and length respectively.

5

The FASTPIX Technology Demonstrator

A silicon-based pixel detector concept for the detection of ionizing particles that is able to combine fine-pitch pixels (< 20 µm) with a time measurement precision around 100 ps will not only meet the requirements of future HEP experiments but also spark interest in a wide array of other scientific and commercial applications. So far, fine-pitch sensor designs with very small collection electrodes struggle with a limited possible transistor count per area and non-uniformities in the signal response across the sensitive area of a given common pixel design [12]. As commercial silicon manufacturing advances, finer line width technologies become available also for R&D of (ionizing) radiation detection and imaging technologies. The FASTPIX project set out to act as a forerunner for manufacturing process modifications and sensor design optimizations, relying on the tried and tested 180 nm CMOS imaging technology, while developments in finer 65 nm line width technologies are well on their way.

In this chapter the following section will introduce the ATTRACT programme and locate the FASTPIX project within. After a description of the chip layout and geometrical characteristics, wafer-level modifications as well as pixel-level design variations are discussed in detail. Starting with aspects and potential of the standard 180 nm CMOS imaging process, different modifications are motivated, illustrated and qualitatively assessed. Summarizing the previous, the chip parameter space is unfolded and put in context with the extent of samples and measurements presented in this work. Subsequently, the relevant aspects of the analogue front-end and digital logic circuitry of the chip are discussed. An emphasis is put on analog an digital signal processing as well as the evaluation, encoding and decoding of hit information.

5.1. ATTRACT FASTPIX

ATTRACT [11] is integrated in the European Commission (EC) Horizon 2020 funding programme [54] and funds the R&D cycle for new (ionizing) radiation detection and imaging technologies outside of the upgrade cycle of the present physics research facilities and experiments. The programme creates synergies between the detector R&D communities including physics, research, astronomy, space exploration, nuclear engineering, medical imaging, and Small/Medium sized Enterprises.

Starting in 2018, ATTRACT phase 1 supported 170 breakthrough technology concepts across Europe with seed funding intended to create a proof-of-concept, among those is FASTPIX. The ATTRACT FASTPIX project set out to provide an image sensor, advancing not only applications in high energy physics, but also other fields such as imaging Time-of-Flight Mass Spectroscopy, Fluorescence Life-Time Imaging Microscopy, electron microscopy, even commercial Light Detection and Ranging systems.
In late 2020, with the end of phase 1, the FASTPIX demonstrator chip was produced based on the results of detailed research on the motion and collection of signal charge as well as the feasibility of performant, complex in-pixel circuits necessary to propagate the detected information. The characterization of the device in laboratory and test beam measurements allows to assess the impact of the modifications and optimizations applied to the CMOS imaging manufacturing process and the design of the single-pixel cell, respectively. The results provide valuable insight towards an optimized application/combination of improvements and benchmark the obtained performance gain in view of a transfer onto smaller feature-size manufacturing processes.

5.2. The Chip

5.2.1. Multi-Project Wafer

The FASTPIX chip was produced on a 300 µm thin, 8 ″ high-purity single crystal silicon (resistivity $\rho > 1\,\mathrm{k\Omega cm}$) wafer [55] as part of two multi-project submission.
A multi-project wafer describes the combination of multiple designs from different clients onto a single silicon wafer. This fabrication approach is cost-effective, especially for small-scale productions or prototypes, making it feasible to produce advanced sensor technologies without the need for large individual investments. A selection of chip designs is grouped in a rectangular cell arrangement, called reticle, constrained by the dimension and content of the lithography masks. The 180 nm feature size employed for the FASTPIX device indicates the

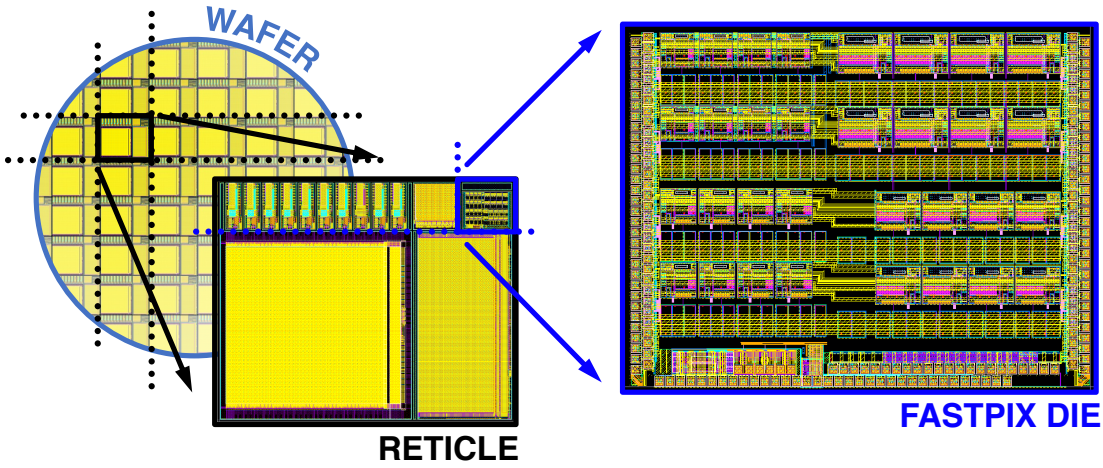

Figure 5.1: Schematic illustration of the wafer, reticle and silicon die for the FASTPIX chip. A wafer is diced along the dotted lines, separating reticles and subsequently single chips.

limit of the smallest feature that can be reliably transferred from the reticle onto the wafer. During wafer processing the reticle is multiplied across the surface of the wafer.
Figure 5.1 illustrates the repeated structures on the surface of a wafer, the reticle and a singular chip die, here FASTPIX. Following the processing, whole wafers are diced by laser cutting in order to separate the individual silicon devices.

5.2.2. Chip Layout

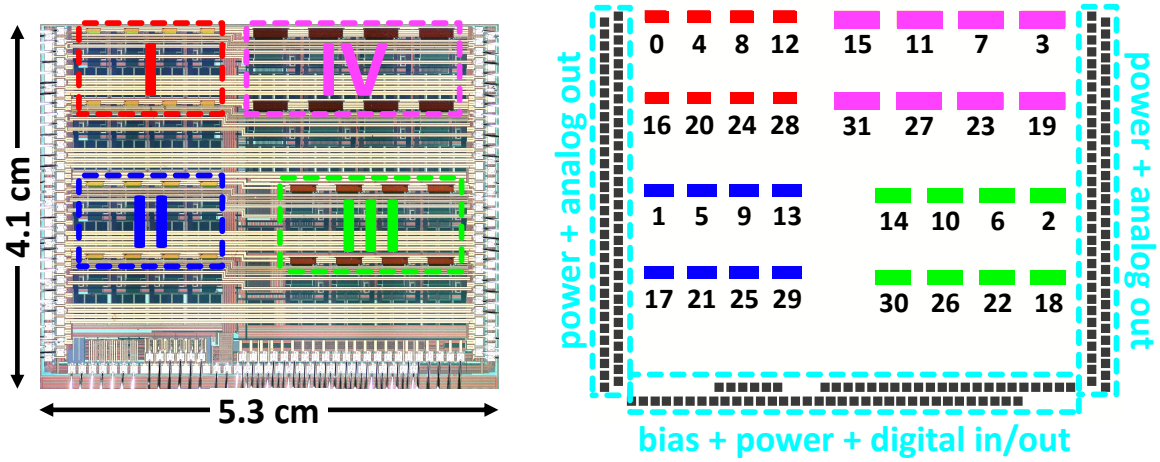

Figure 5.2: Photograph of the FASTPIX chip (left), divided in four quadrants of matrices with pixel pitches I: 8.66 µm, II: 10 µm, III: 15 µm and IV: 20 µm. A reduced illustration of the matrix arrangement and interconnection pads marked in teal boxes (right).

The FASTPIX 5.3 mm × 4.1 mm chip contains 32 mini matrices with pixel pitches ranging from 8.66 to 20 µm. The pixel pitch is the radial distance between two adjacent collection electrodes or equivalent to the diameter of the incircle of a hexagonal pixel. Figure 5.2 illustrates the four quadrants of matrices with I: 8.66 µm, II: 10 µm, III: 15 µm and IV: 20 µm pixel pitch as well as the matrix numbering and the interconnection pads. The specifications of the integrated sensor are summarized in Table 5.1.

Table 5.1: Main parameters of the FASTPIX chip

Parameter	Value			
Chip size	5.3 mm × 4.1 mm			
Matrix count	32			
Matrix size	16 pixel × 4 pixel			
Dimensions	Group	Pitch	Width x Height	Active Area
	I	8.66 µm	139 µm × 35 µm	4800 µm^2
	II	10 µm	160 µm × 40 µm	6400 µm^2
	III	15 µm	240 µm × 60 µm	14400 µm^2
	IV	20 µm	320 µm × 80 µm	25600 µm^2
Readout scheme	Asynchronous			

Rows of wire bonding pads line three out of four edges of the silicon die. Pads along the left and right chip edge receive power and provide the analog outputs associated with the matrices of the respective side of the device. Pads along bottom edge receive bias and power and allow connections to the digital inputs and outputs of the chip.
The local spatial coordinates follow a left-handed cartesian coordinate system where the positive x, y and z axes point right, up and onto the face of the chip, respectively. Positive rotation is clockwise around the axis of rotation.
Each matrix has 68 active hexagonal pixels, of which four pixels transmit an analog output signal and 64 transmit binary hit information. The pixel are arranged on a pointy-topped, staggered hexagonal grid. Pixels in the same row are a pitch apart in y while pixels in the same row are offset in x alternating between 0× pitch and 0.5× pitch witch a distance in y of 1.299× pitch. Columns follow from left to right and rows from bottom to top of a given horizontally aligned rectangular-shaped matrix.
The active matrix area is surrounded by dummy pixels that similarly get biased but lack the readout circuitry.

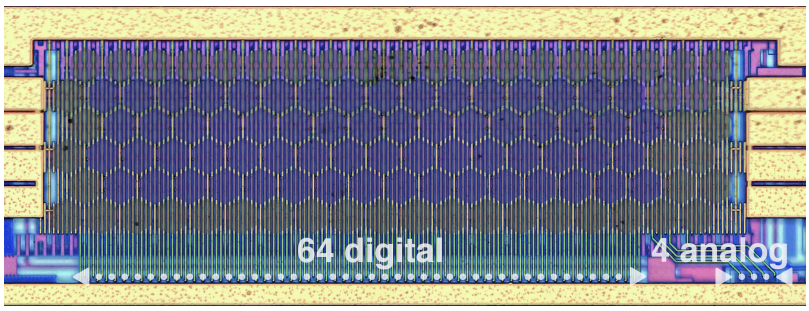

(a) Microscopy image of a 20 µm pitch matrix.

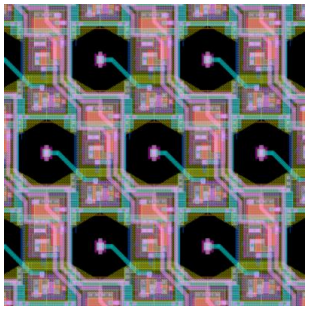

(b) Digital visualization of sensor and metal stack layers for a group of 7 digital pixels.

Figure 5.3: The FASTPIX matrix and the hexagonal pixel grid.

Figure 5.3 shows an edited microscopy photo of a 20 µm pitch matrix and a more detailed representation of a group of seven pixels originating from the design stage of the chip. The hexagonal pixel grid is enhanced to be visible underneath the metal stack distributing power and control to the individual pixels. The 64 vertical transmission lines from the 16×4 pixel grid are routed to the bottom edge of the matrix followed by four test pixels on the right side of the image. A zoom into the hexagonal pixel grid illustrates the placement of 5 PMOS transistors in the area surrounding the n-well collection electrode in the center of each pixel. Matrices from the left and right side of the chip are implemented in a mirrored configuration detailed in Figure 5.4. While on the left side of the chip the quartet of test pixels is placed at the bottom left of the matrix, on the right side they are located on the bottom right - always on the side close to the analog output pads along the vertical edges of the chip. The order of the pixels is similarly mirrored.

5.3. Wafer-Level Modifications

The FASTPIX monolithic pixel sensor demonstrator chip has been developed in a modified 180 nm CMOS imaging process technology [56]. The aim of the development is to achieve

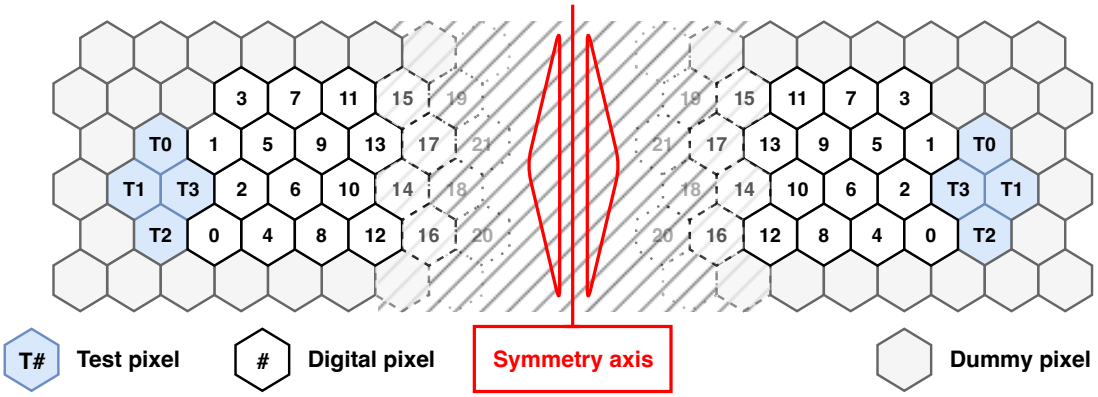

Figure 5.4: Schematic illustration of the left-handed and right-handed matrix flavor implemented on the left and right half of the chip, respectively. An exemplary case would be a comparison of matrix 12 and matrix 15. Individual pixel numbers are placed in the center of every pixel to underline the mirrored order.

fast charge collection, improve timing precision and increase efficiency for very thin sensors by combining advantages from two directions. The monolithic approach comes with a reduced production effort, reduced cost and reduced detector material budget. It is combined with advantages of femto-farad sensor capacitance which are a precise spatial resolution and the reduced power consumption of the analog frontend. The combination of these three key aspects, "monolithic", "small capacitance" and "fast charge collection", opens a large application window for such a technology. Examples are future LHC experiments, future collider experiments or particle tracking detectors at future colliders, medical imaging applications and industrial applications further down the line.

The following two sub-sections qualitatively discuss the modifications of the wafer manufacturing process and its influence on the performance of the sensor.

5.3.1. The standard 180 nm CMOS imaging process

FASTPIX has been produced in multiple versions that are based on two variants of the 180 nm CMOS imaging manufacturing process. The standard process pixel structure is implemented on a 25 µm-thick high resistivity epitaxial layer. The basic building blocks are shown in Figure 5.5. The pixel geometry is shown in symmetry around the corner and edge of the pixel cell, with halves of the collection electrode in its corners.
Figure 5.5a illustrates this epitaxial layer which is grown on a low resistivity substrate. In the applied process the epitaxial layer can reach resistivities $> 1\,\mathrm{k\Omega\,cm}$ [57] essential for sensor depletion and particle detection, but is limited in thickness.
Figure 5.5b introduces a small $2\,\mu\mathrm{m} \times 2\,\mu\mathrm{m}$ n-well collection electrode at the center of the pixel sensing volume with a junction capacitance of $\approx 2\,\mathrm{fF}$ [57]. The small sensor capacitance achieves a high signal to noise ratio and low analog power consumption. However, a small collection electrode directly implies that also the sensor junction initially is similarly small in size.
Full CMOS circuitry is placed in p-wells and n-wells shielded by a deep p-well implant that is located between the collection electrodes and is inversely doped, as illustrated by Figure 5.5c.

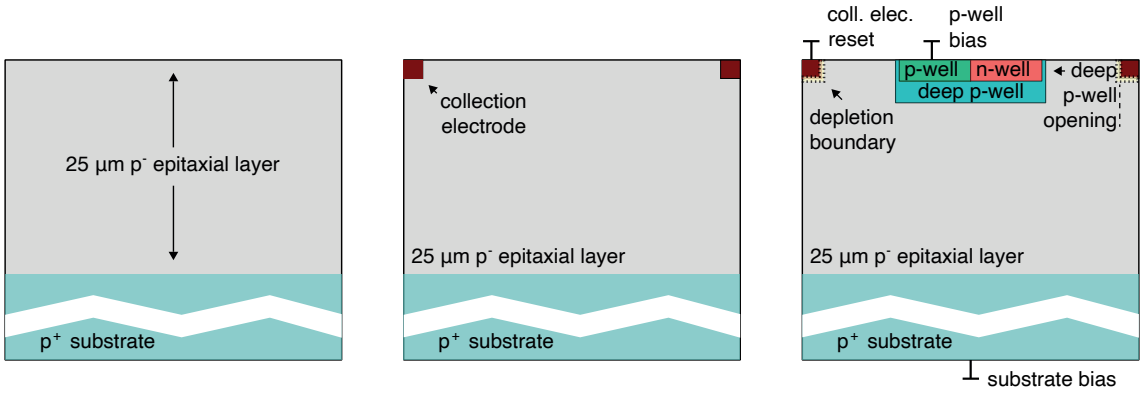

(a) P-doped 25 µm-thick high resistivity epitaxial layer (light teal) on a p^+ substrate (teal).

(b) Introducing collection electrodes in the top corners (dark red). Only the inside half of the electrode is shown.

(c) Addition of collection electrodes in the top corners in dark red. Only the inside half of the electrode is shown.

Figure 5.5: The standard 180 nm CMOS imaging process, showing a cut perpendicular to the sensor surface. The sensor junction is represented by a beige double-dotted line along the implantation geometry.

This has two immediate consequences for the sensor performance. Firstly, placing a doped well within the sensor severely alters or deforms the electric field and the charge collection behavior in the sensor. Secondly, to achieve a sizeable depletion, a bias voltage is applied to the p wells, which is limited by the circuitry inside. As a result, the sensor bias voltage in this type of process is limited to a few volts.

5.3.2. Sensor Simulation

The impact of different designs choices, in first instance, was evaluated by three-dimensional technology computer design (TCAD) simulations. In this domain two central aspects are investigated. Firstly, the inhomogeneous electric field deformation introduced by the p wells results in a variation in field strength up to a factor 10 over the area of the pixel cell [58]. Secondly, the multitude of well structures placed inside the sensor requires a large range of doping which impacts parameters such as charge carrier mobility, drift-velocity and recombination.
An exemplary 3D TCAD simulation of a square single pixel unit cell is shown in Figure 5.6a. The pixel geometry is not shown with the collection electrode in its center, but in symmetry around the corner and edge of the pixel cell. Here, in every corner of the rendered unit cell, a quarter of the collection electrode of four neighboring pixels is shown, motivated by the edge effects being of central importance for this simulation.
The color scale represents the electrostatic potential and the depletion depth is indicated by the white lines. In the presented case the depletion is limited to a small region evolving in a balloon-like shape from the collection electrodes. From a performance perspective this sample will show a lot of diffusion in the non-depleted parts of the pixel volume, ultimately arriving at large charge sharing between neighboring pixels which yields improved spatial detector resolution. The downsides are reduced time measurement precision and efficiency, because the charge shared between pixels by diffusion reduces the single pixel signal and ultimately reduces detection efficiency. This is the case even for very high resistivity epitaxial layer and the maximum applicable sensor bias voltage, still the depletion is incomplete.

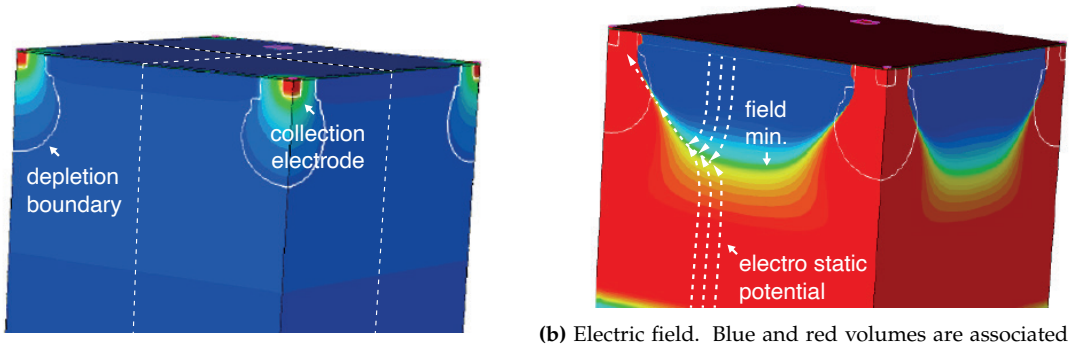

(a) Electrostatic potential. The white dotted lines are the pixel boundaries

(b) Electric field. Blue and red volumes are associated with different signs of the electric field, that crosses a minimum along the green shades of the color scale.

Figure 5.6: 3D TCAD simulation of a square single pixel unit cell in the Tower Semiconductor standard 180 nm CMOS imaging process, showing a 3D cut through the center of adjacent collection electrodes and perpendicular to the sensor surface. Modified from [58].

Another aspect to be considered is the electric field minimum, illustrated in Figure 5.6b with exemplary charge traveling along the white dotted lines to the minimum and finally to the collection electrode. In addition symmetry considerations imply that the lateral part of the electric field needs to be zero at the pixel borders. The electric field minimum present in the exemplary simulation is caused by the p wells, placed along the edges of the pixel cell (center lines of top surface of the simulation unit cell). The path of the signal charge through the sensor is bent at first in the minimum before continuing towards the collection electrode, an elongated path slowing down charge collection.

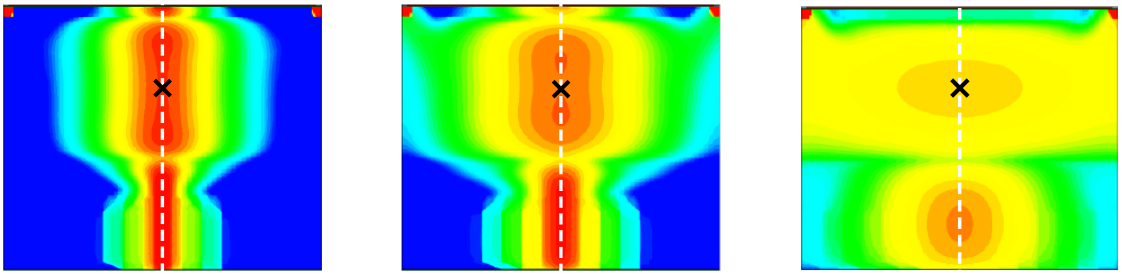

(a) After 0.5 ns. **(b)** After 1.5 ns. **(c)** After 15.5 ns.

Figure 5.7: 3D TCAD simulation of charge collection over time in a square single pixel unit cell of the standard 180 nm CMOS imaging process, showing a cut through the center of diagonally adjacent collection electrodes and perpendicular to the sensor surface. High charge carrier density is illustrated in red, low charge carrier density in blue. The position of the electric field minimum is marked with an X. The dotted white line marks the corner of the pixel cell. Modified from [58].

An initial evaluation of the sensor is done using Monte Carlo simulation frameworks like the Geant4-based Allpix2 framework [59, 60, 61, 62]. Here, a high statistic Monte Carlo simulation of charge carrier motion inside the complex silicon structure is added to the 3D TCAD electrostatic simulation. After the initial deposition of energy by a MIP crossing through the pixel corner (worst case), the Monte Carlo simulation computes the electron density at discrete times after signal generation. The three moments in time presented in Figure 5.7 show the expected diffusion and draw into the field minimum.

5.3.3. Modification of the 180 nm CMOS imaging process

Modifications of the 180 nm CMOS imaging process address and try to overcome the limited depleted region and the effect of the electric field minimum introduced by the small sensor junction and placement of p-well structures, respectively.

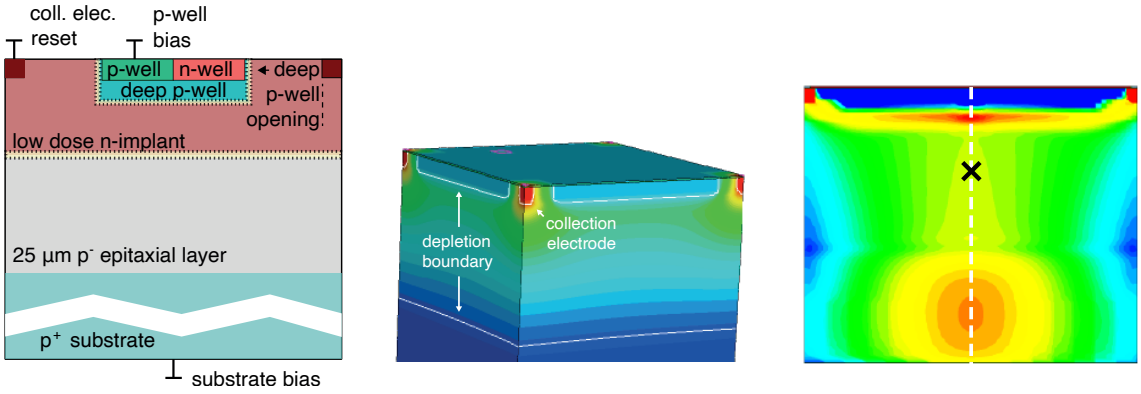

(a) A deep low-dose n-implant is added across the full silicon device. The sensor junction is represented by a beige double-dotted line along the implantation geometry.

(b) 3D TCAD simulation of the electrostatic potential, simulated for −6 V applied to p-wells and substrate. The white lines illustrate the depletion boundaries.

(c) 3D TCAD simulation of electron density after 14.5 ns at −6 V bias in a square single pixel unit cell of the modified process with low-dose n-implant. Marker and colors follow Figure 5.7.

Figure 5.8: Modification of the Tower Semiconductor 180 nm CMOS imaging process and corresponding TCAD simulations. The figures show cuts through the center of adjacent collection electrodes and perpendicular to the sensor surface. (b) and (c) are modified from [58].

The small sensor p-n-junction and the limited depletion is addressed by the addition of a deep low-dose n-implant, illustrated in Figure 5.8a. The built in depletion is now extended to a large U-shaped junction towards the p-well and a planar junction covering the full pixel cell between the deep low-dose n-layer and the high resistivity epitaxial layer (Figure 5.8b). This modification achieves full lateral depletion and isolates the backside from the circuitry in the p-wells, which opens the operation range to higher sensor bias voltages. Figure 5.8c exemplifies how the previous diffusion and concentration of charges inside the field minimum has been altered. Charge carriers now accumulate in the center below the deep p-well implantation, already after 14.5 ns after the injection of a MIP in the corner of the pixel.

5.4. Pixel-Level Modifications

Further process modifications address the diversion of charges caused by the field minimum. The aims is to further bend the electric field towards the collection electrodes at an earlier point in the charge drift path.

5.4.1. Optimization of the Lateral Field

A vertical junction close to field minimum underneath the p-wells significantly increases the lateral electric field and shifts the electric field minimum deeper into the silicon. This junction is implemented either in form of a gap in the deep low-dose n-implant (Figure 5.9a) or as an additional extra-deep p-implant (Figure 5.9c). Both measures reduce the length of

the drift path and mitigate charges getting trapped or pushed inside the field minimum and thereby improve charge collection speed and efficiency.

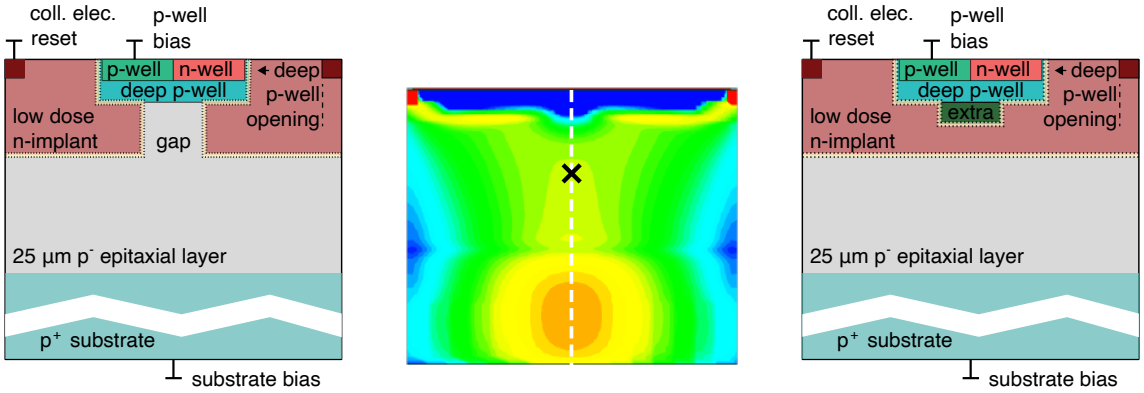

(a) A gap in the deep low-dose n-implant is introduced at the pixel border. The sensor junction is represented by a beige double-dotted line along the implantation geometry.

(b) 3D TCAD simulation of electron density after 14.5 ns in a square single pixel unit cell of the modified process with a gap in the low-dose n-implant. Marker and colors follow Figure 5.7.

(c) An extra deep low-dose n-implant is added below the p-wells along the pixel border. The sensor junction is represented by a beige double-dotted line along the implantation geometry.

Figure 5.9: Pixel-level modification in the 180 nm CMOS imaging process, showing cuts through the center of adjacent collection electrodes and perpendicular to the sensor surface. (b) is modified from [58].

The pixel-level modifications were also validated in 3D TCAD simulation. The case of the deep low-dose n-implant gap is illustrated by Figure 5.9b, 14.5 ns after the injection of a MIP in the corner of the pixel. The electron density map visualizes how the vertical junction guides the charges from the sensor depth towards the collection electrode while the modified process without gap in Figure 5.8c still retains charge below the p-well, above the electric field minimum.

5.4.2. FASTPIX pixel design parameters

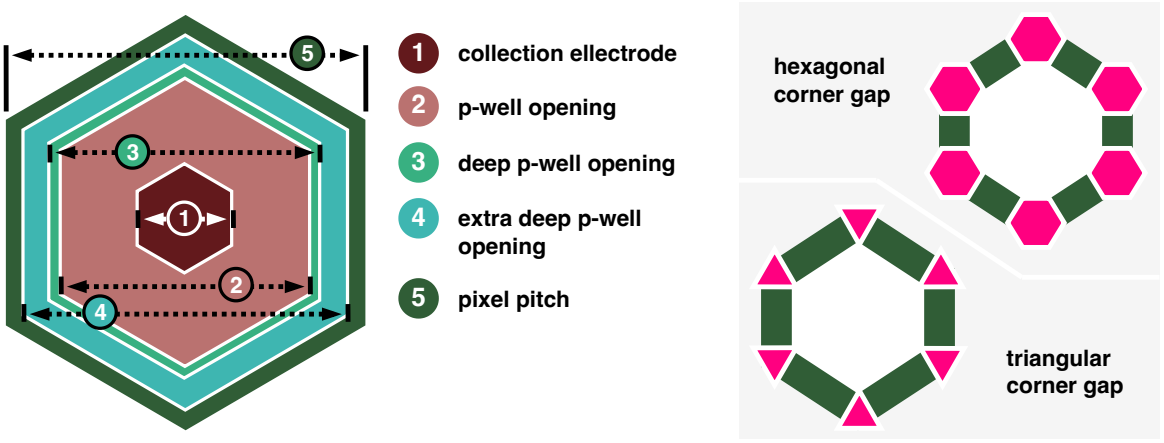

Figure 5.10: Schematic top view onto the geometric structures of a hexagonal pixel cell in the modified process with deep low-dose n-implant gap and additional extra-deep p-implant.

Figure 5.10 marks the dimensions of the features of a FASTPIX pixel cell, which are varied in pixel design optimization.

Pixel pitch
The $O(10\,\mu m)$ pixel pitch of FASTPIX was chosen in view of its impact on the charge collection speed. In case of a pixel pitch of multiple tens of micrometers the charge collection time can reach $O(10\,ns)$ [57]. With decreasing pitch the potential gradient and the electric field along the lateral dimension increases, an effect that reduces the length of the drift path and mitigates charge trapping inside the field minimum.

Collection electrode
Besides the pixel pitch, the size of the collection electrode similarly impacts the strength of the lateral field. The n-well collection electrode size and its distance to the surrounding p-type implants along the edge of the pixel is subject to a tradeoff. A small collection electrode has a small capacitance which is beneficial in view of the analog performance of the frontend circuitry. On the other hand, a larger-size electrode is favorable in the quest for a strong electric field and a good contact to the low dose n-type implant underneath.

P-well opening
The p-well opening describes the region around the collection electrode where the p-well is removed. For a given pixel pitch, a smaller opening is equivalent to a larger area for the in-pixel analog frontend circuitry but limits the lateral electric field, which in turn has a negative impact on the charge collection speed. In addition to its contribution to the strength of the lateral field, a large opening reduces the depletion underneath the collection electrode, increasing the sensor capacitance.

Deep p-well opening
The deep p-well opening size describes a retraction of the well structure below the p- and n-well, as far as the circuitry-shielding quality of p-wells allows. Similar to the p-well opening but without significant impact on capacitance, the lateral electric field around the collection electrode and consequently the charge collection speed is improved.

One key limitation still remains unaddressed at this stage. A spread in the charge collection time across the pixel area is introduced by a difference in charge collection time for a hit near the corner compared to a hit close to the pixel center. The electric field strength in combination with the distance between the point of charge ionization and the collection electrode determines the collection time from interaction that are uniformly distributed over the pixel area. Minimizing the maximum distance between charge generation and collection is a first step in the optimization for timing uniformity and is realized in part by the hexagonal arrangement of collection electrodes. For the same pixel area the maximum distance from the pixel corner to the collection electrode in the square grid is reduced by 12 % in the hexagonal case. In addition, the hexagonal grid comes with only three neighboring pixels instead of four, as it is the case for the previously assumed rectangular geometries. Consequently charge sharing at the pixel corners is reduced and the seed pixel signal is maximized.

Extra-deep p-well opening and corner gaps
For time-measurement applications that require a sub-nanosecond time resolution, optimiza-

tion approaches are combined. By implementing a gap in the deep low-dose n-implant at the pixel corners below the additional extra-deep n-implant along the pixel edge, the shaping of the electric field is maximized. On FASTPIX a hexagonal and a triangular corner gap are implemented within the design as illustrated by Figure 5.10. The triangular gap matches its three sides with the three pixel edges joining up in a given corner. The hexagonal gap provides similar geometry with three of its edges. It creates an increased interruption of the pixel-edge implants in a given pixel corner by exposing one of its remaining three edges towards the center of the hexagon. In the corner region, the pronounced push towards the collection electrode accelerates charge collection by drift, reduces charge sharing, maximizes the seed pixel signal and narrows the spread in timing performance across the pixel area.

The previously discussed TCAD simulations were able to identify promising pixel geometry parameters. Based on this, FASTPIX explores eight pixel design variants and therefore allows for an experimental and quantitative assessment of the impact of individual design parameters on detector performance. The results from FASTPIX will inform the implementation of advanced lateral field components in the current 180 nm CMOS imaging technology node as well as future developments in smaller line width technologies. First measurement results from chips that shared the reticle with FASTPIX could already show improved sensor response in pixel regions with p-well layouts that leads to a higher lateral field [63].

5.5. Frontend Electronics

FASTPIX being a demonstrator chip for sensor concepts requires an on-chip circuitry which is capable to resolve small differences in charge collection time to support a detailed characterization of the timing performance of the sensor. The implemented front end circuitry design prioritizes signal quality and integrity over low power consumption or the implementation of a fully developed data digitization and reduction/concentration stage.
The frontend provides each of the 64 pixels in a given matrix with an amplifier, comparator and digital readout as well as analog buffers for two of four test pixels per matrix. In order to implement pixel pitches between 8.66 µm and 20 µm in a 180 nm CMOS imaging technology, only part of the circuitry is placed in the constrained space available inside the p-wells surrounding the collection electrode. In simulation, in-pixel and periphery circuitry together consume $\mathcal{O}(170\,\mu W)$ per digital pixel and ≈20 mW per analog pixel from a 1.8 V supply. In the digital case the circuit reaches a simulated equivalent noise charge (ENC) of 11 e and a time jitter of ≈20 ps [57].

Figure 5.11 shows a simplified schematic of the FASTPIX frontend sectioned in an in-pixel and periphery part of the circuit as well as the output pads.
The in-pixel circuitry connects the collection electrode of the pixel diode to a reset and leakage compensation stage comprised of three transistors M0, M1 and M2. M0 sets the current IRESET at its gate and determines the rate of the signal return to baseline. VRESET controls the gate of M1 which in turn propagates a signal baseline voltage offset to the reset transistor M2.

For two matrices in every pixel pitch group the PMOS-based reset mechanism is exchanged for a diode reset. A diode receives VRESET on its anode and feeds a reset current that is tuned on the sensor leakage current and signal amplitude from its cathode into the IN net of

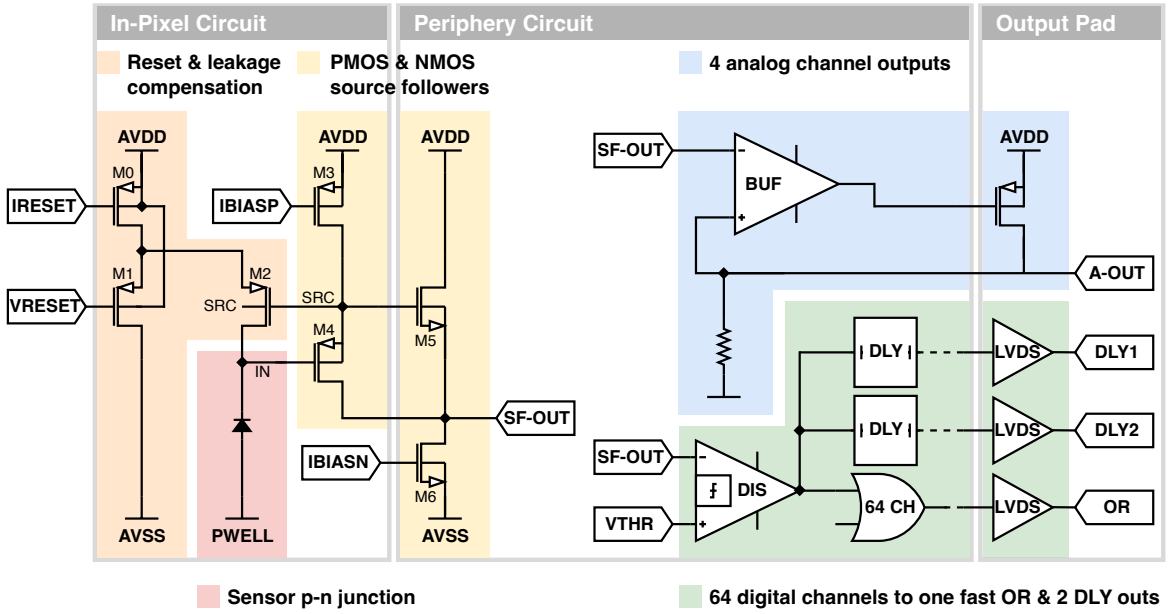

Figure 5.11: The main circuit blocks of the FASTPIX analog and digital frontend grouped, from left to right, into an in-pixel circuit, matrix periphery circuit and the output pads.

the circuit. The continuous reset mechanism holds the collection electrode voltage which is set by VRESET according to the sensor leakage current.

The input capacitance C_{in} is the sum of the capacitance of the sensor diode C_d and the parasitic capacitance C_p of M2. The amplitude of the voltage signal at the IN net is equal to Q_{in}/C_{in} with Q_{in} as the collected signal charge.

At the IN net of four individual test pixels an analog test pulse can be injected into the amplifier stage of the frontend. The pulse originates from a test pulse capacitor above the pixel collection electrode. The capacitor is discharged and charged following the high and low state of a low duty-cycle externally provided differential trigger signal that is routed to one of four test pixels at a time. Two analog test pixels allow to probe the analog signal after the leakage current compensation and shaping stages. The other two feed their signal into the discrimination and digitization stage of the frontend and allow characterization measurements based on the digital test pixel output of the delay lines.

Fast signals need to be buffered to reach the matrix periphery where the discriminators and additional logic is implemented, which imposes the main penalty on the FASTPIX frontend power consumption. Hence, the second, still in-pixel, signal manipulation stage is a PMOS source follower comprised of two transistors that buffer the input voltage signal. M4 serves as the input transistor for the source follower stage while M3 sets the bias current IBIASP.
To compensate the M4 gate-source capacitance, the output SRC follows the IN net in parallel and is fed back to gate and bulk of M2. With this also the M2 gate-drain and bulk-drain capacitance is compensated for at the IN node.
The SRC line connects the in-pixel circuit to the periphery of the pixel matrix. Here transistor

M5 serves as input for the signal while M6 applies the bias current IBIASN. This second NMOS source follower stage marks the end of the fully analog signal path. Similar to before the output node SF-OUT is fed back to the drain of the input transistor M4 of the in-pixel source follower circuit for gate-drain capacitance compensation.

5.6. Readout Scheme

The 4 test pixel channels per matrix are routed to 4 fast analog monitoring channels that buffer the second source follower and as well transmit it off-chip to the A-OUT analog output pad. For every digital pixel an individual connection to the periphery feeds the DF-OUT signal to 64 dedicated discriminators per matrix that compare the received signal to a threshold set by voltage VTHR. Pixel-to-pixel variations of the effective threshold applied during the discrimination of signal can not be corrected by e.g. a local offset tuning DAC.
The discriminated signal is split threefold as shown in Figure 5.12a. One of the three discriminator output signal splits from a given pixel is merged in a fast-OR logic block with the other 63 pixels. The output of the fast-OR passes the signal of the fastest pixel response with minimal latency following e.g. a particle interaction in the sensor and transmits it off-chip via a Low Voltage Differential Signal (LVDS) driver to the OR digital output pad. The other two splits of the discriminator output signal are fed into two delay lines. The resulting signals contain a time-based encoding of position, time and energy of a hit, as shown in Figure 5.12b.

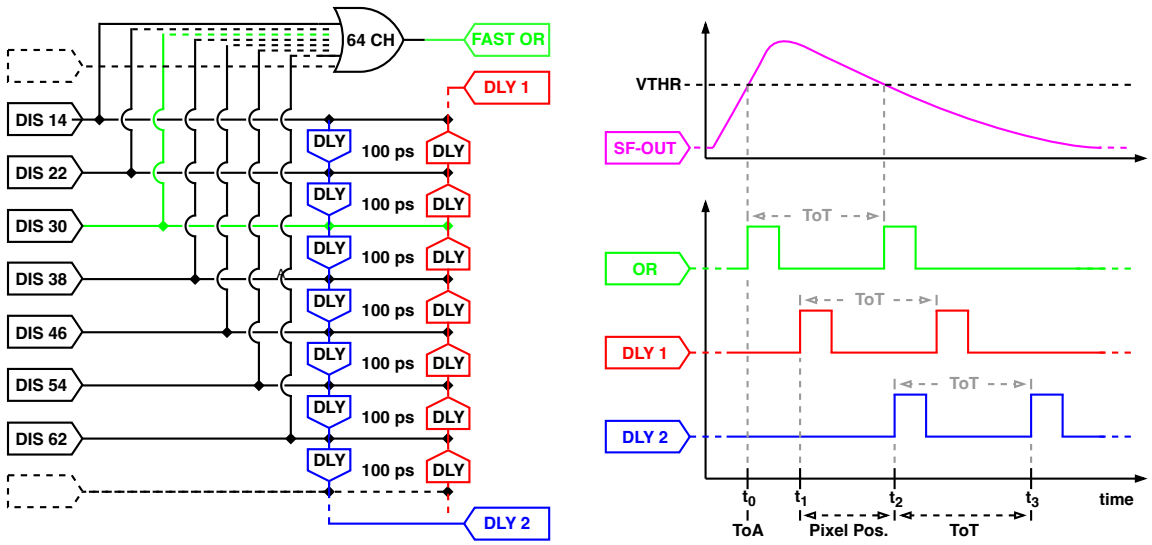

(a) Schematic of the delay line section. An Exemplary signal path is highlighted in bright green for pixel 30.

(b) Single pixel signal at discriminator input (top) and resulting signals at the three digital output pads.

Figure 5.12: Schematic representations of the signal manipulation between the discriminator input and the digital output pad.

Figure 5.12a details the working principle of the delay line section at the end of the digital signal path of each matrix. For every pixel the incoming discriminator output DIS # is split and directed to the fast-OR at the top of the graphic before it gets plugged into the nodes of

the blue DLY 2 as well as the red DLY 1 delay line. Between two consecutive pixel nodes the signal is delayed by ≈100 ps as it propagate through DLY 1 and DLY 2 in opposite directions. Like that the exemplary signal from pixel number 30, which is highlighted in bright green, experiences 500 ps delay while propagating DLY 2 and 200 ps delay while propagating DLY 1.

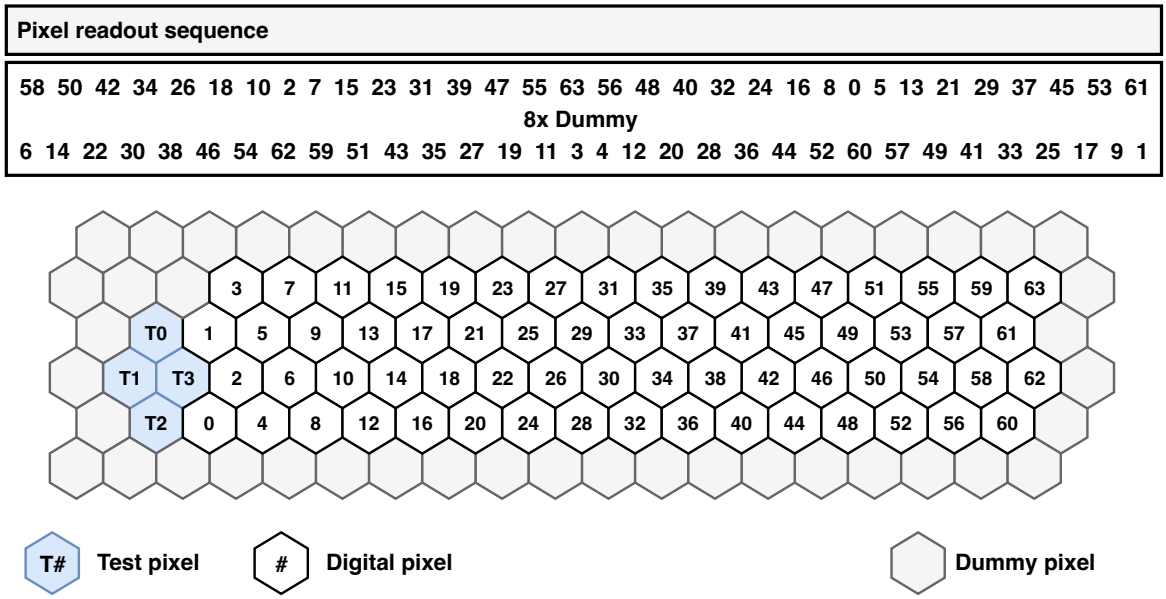

Figure 5.13: Pixel readout sequence of a FASTPIX delay line and associated pixel position arrangement in a left-handed 4×16 hexagonal grid matrix.

The order in which pixel signals are fed into the delay line follows a sequence introduced in Figure 5.13. To allow a time delay between signals from pixels that are neighbors in the spatial domain, these pixels are placed in the time series of the delay line with a gap of at least 16×100 ps. Together with 8 dummy delays included in the middle of the readout chain, this arrangement avoids spatially adjacent pixels to be too close in the delay line, which mitigates signal overlap and ultimately information loss in higher occupancy scenarios.

Figure 5.12b provides a qualitative representation of a single pixel signal at the input of the discriminator (top) as well as at the three digital output pads. The discriminator outputs a pulse whenever the pixel signal rises above or falls below threshold. The time-over-threshold (ToT) of a pixel signal follows as the distance between a pair of rectangular pulses. The time-of-arrival (ToA) is calculated from the first edge of the fastest pixel signal, the fast-OR output of the chip. The pulse pairs on DLY 1 and DLY 2 exhibit the shorter and longer delay associated with the direction of signal propagation, respectively. The position of a pixel is thereby encoded in the time distance between the first edge on both delay lines.

In operation OR, DLY 1 and DLY 2 are read out asynchronously. Signal treatment of the analog waveforms as well as the evaluation and decoding of the digital output signals is carried out off-chip [13]. The temporal positions of the 64 pixels within a delay line are determined from a calibration of a given matrix using single-pixel hits. For decoding, the coordinates of the spatial pixel center are attributed to the designed sequence of pixels in the delay line. The

spatial position of a recorded pixel hit is then found by mapping the measured time value to the calibrated pixel delays on the delay line.
Overlap between signals from pixels simultaneously crossing the threshold poses a challenge for this pixel position en-/decoding scheme. In case of signal overlap the correct position can still be identified, as long as the relative majority of signal combinations from both delay lines indicate the correct pixel position value. Hits that can not be completely decoded are discarded in the data decoding stage.
In every set of three LVDS output signal waveforms that has been recorded upon an injection pulse trigger, its features are extracted from the time-series of signal amplitude data through edge detection.
In an iterative process transitions in the signal are identified based on the threshold value `th` = 100 mV, detecting both, rising and falling edges. The precise timestamp of a threshold transition is found using linear interpolation, which accounts for the fact that the actual signal edge occurs between two sampled points. A rising edge is paired with the corresponding falling edge to define the full extent of a signal pulse in the waveform. The precise detection and pairing of rising/falling edges are crucial for decoding the temporal characteristics of the signals, such as pulse widths and time intervals.
From the detected edges a set of observables is calculated and stored in TTree data structure provided by the CERN ROOT framework.

- **mb:** matrix number
- **pb:** test pixel number
- $\mathbf{v_{pulse}}$**:** applied pulser voltage
- $\mathbf{i_{thr}}$**:** set threshold voltage
- **time:** associated timestamp
- **toT:** time over threshold
- **count:** count of recorded pulses
- **triggers:** number of triggered pulses

5.7. Powering & Sensor Configuration

The application of different reverse bias voltages to sensors in this modified small collection electrode CMOS technology has a strong impact on performance.
Voltage is applied to the p-wells, to the collection electrode and the sensor backside, as previously introduced in Section 5.3.1. Depletion takes place at two different junctions. Between the deep low-dose n-implant and the epitaxial layer it starts already without external potential and is fully formed at a few volts. Around the p wells sizeable depletion needs higher external potential before balloon-shaped undepleted regions around the collection electrodes are reduced to the shape of the electrode. An increase in sensor depletion leads to additional gain from a reduction of sensor capacitance as well as lowered noise.
The introduction of the deep low-dose n-implant adds isolation between the p-wells and the sensor backside and allows for higher reverse bias voltages to be applied to the substrate. The pixel-level modifications "gap" and "extra deep p-well" counteract the extended bias range and enable a high flow of current between p-wells and substrate (punch-through). This punch-through occurs for substrate voltages below the potential of the p-well, while the collection electrode and p-well bias are held at fixed potentials. The small depletion of the interrupted (gap) and/or reduced (extra deep p-well) epitaxial layer does no longer sufficiently isolate the p-wells from the sensor backside.
The maximal reverse bias voltage to be applied to the p-wells while simultaneously retaining full functionality of the frontend is limited to −6 V by the p-well CMOS circuitry in the 180

nm process [64].
Lowering the p-well voltage below −6 V impairs the functionality of the CMOS circuitry and, while the substrate voltage and collection electrode voltage remain at constant levels, reduces the depletion. The optimal depletion is achieved for zero potential difference between the backside and the p-wells. The depletion depth is limited to the 25 µm-thin epitaxial layer after which higher bias voltages no longer increase depletion but exaggerate the vertical field. Lowering the substrate voltage below −6 V reduces the bend of the field lines towards the collection electrode. The lateral field component looses its impact and accentuates a field minimum underneath the p-wells, increasing the charge drift path in the pixel. In this sense, the evacuation of charge carriers from beneath the p-well that was achieved by the pixel-level modifications shown in Section 5.4, can be rendered ineffective to the point of a charge collection performance similar to a bare low-dose n-type implant described in Section 5.3.3.
The nominal bias configuration for FASTPIX is 0.8 V VRESET at the collection electrode and −6 V at substrate and p-wells. The remaining currents and voltages discussed in Section 5.5 are set as follows: 100 pA IRESET, 10 µA IBIASP, 50 µA IBIASN. The full chip configuration treatment is saved as part of the device-specific information inside the control and readout system introduced in Section 6.1.

5.8. Chip parameter space

The FASTPIX monolithic sensor technology demonstrator chip has been produced on 38 wafers with $O(30)$ chips per wafer from two reticle submissions and subsequent production cycles. Since the performance characterization of one FASTPIX sample is in many ways equivalent to the characterization of 32 singular small sensor technology demonstrator chips, only a subset of the available process modifications and design variations have been characterized in this work.
This work focuses on FASTPIX samples from the first reticle submission and wafer production cycle, named *S1*. 12 process splits were implemented from combinations of different doping concentration and two different versions of the two lithographic photomasks that control the feature sizes of n-type and p-type implantation into the epitaxial layer. This thesis covers measurements and results obtained from FASTPIX samples of three wafers: *3*, *15*, *18*.
A sample naming convention has been established by combining the wafer information *W##* with the submission name: *W03S1*, *W15S1* and *W18S1*. In writing the abbreviated version *W03*, *W15* and *W18* is used when highlighting general process specific differences that are uncoupled from differences between two chips from the same wafer.

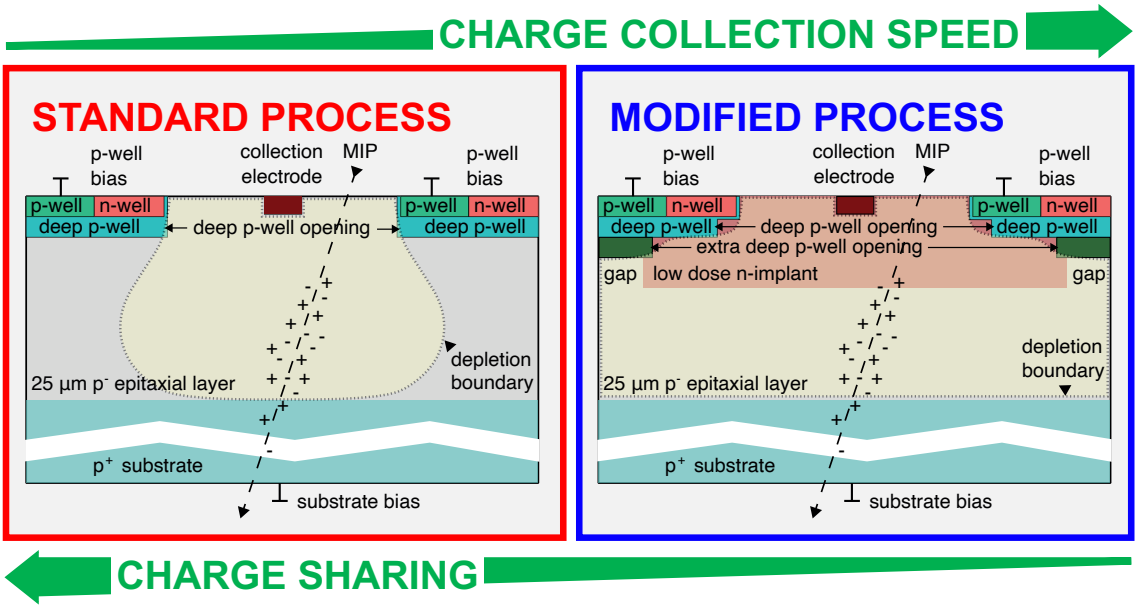

Figure 5.14: Wafer production process variants for FASTPIX represented by schematic cross-sections of the pixel unit cells centered around the collection electrode, showing a cut perpendicular to the sensor surface. The standard 180 nm CMOS imaging process (left) and the modified process variant (right) with added low-dose n-type implant and optimizations such as a gap in the n-implant, retracted deep p-well and additional extra-deep p-well implant.

The three investigated wafers hold FASTPIX samples that are based on two variants of the manufacturing process illustrated in figure 5.14.
W03S1 represents the standard process introduced in Section 5.3.1. It sets the baseline for evaluation as it features no additional measure to accelerate the collection of signal charge and reaches only incomplete lateral depletion of the sensor volume. W15S1 and W18S1 both represent matrix-level modification introduced in Section 5.3.3 as well as pixel-level

modifications discussed in Section 5.4. Matrices on both wafers feature an additional extra-deep p-well implant as well as a gap in the n-implant near the pixel edge. W18S1 sets itself apart from W15S1 with a higher-dose deep n-implant that increases the effect of the added blanket n-layer and is expected to reach the best performance results.

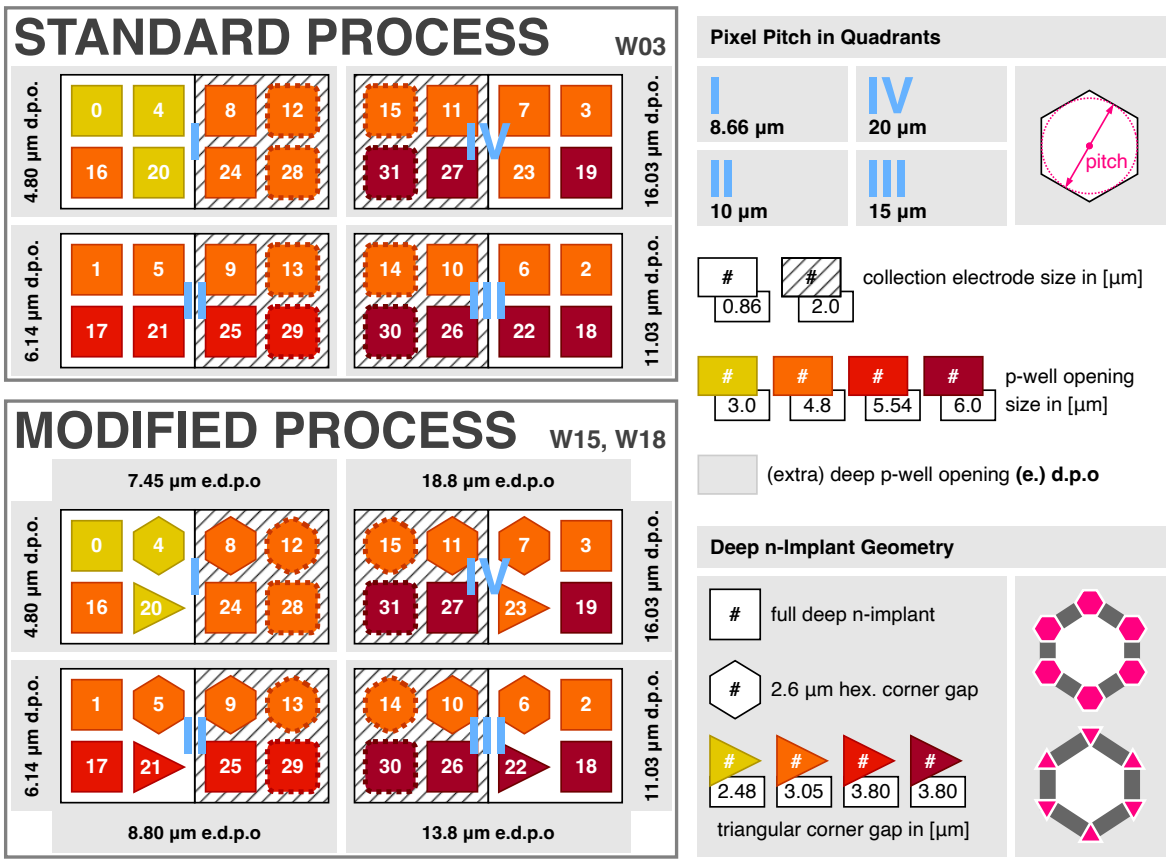

Figure 5.15: Overview of the 32 matrices implemented on a single FASTPIX chip. The top-left scheme illustrates the parameter space of wafers produced using the standard process, below a similar representation of 4×8 matrices on a chip produced in the modified process. The four quadrants are indicated by light blue roman numeral and are attributed their pixel pitch in the table on the top right. Within each quadrant two different collection electrode sizes are represented by white or hatched background. The matrices themselves are illustrated by geometrical icons colored in yellow, orange, red, or dark-red with the respective matrix number in bold white. The colorway indicates the p-well opening size of the pixel cell. The deep p-well opening and extra-deep p-well opening size is written along the outside edges of each quadrant. In case of the modified process different deep n-implant (gap) geometries are represented by the shape of the icon of a given matrix. In both process variants the matrices closest to the chip center line employ a diode instead of a PMOS-based reset circuit, represented by a bold, dotted outline.

On chips from W15S1 and W18S1, different sensor design features are explored in the 8 matrices of each group: size of the collection electrode, p-well opening, deep-p- well and n-type implants geometry. The modified-process samples therefore cover a wide range of optimizations geared towards improved time-measurement performance. Figure 5.15 gives an overview of the large parameter space of layout variations implemented across the 32 matrices on a given FASTPIX chip sample investigated in this thesis.

6

Laboratory Setups and Methods

This chapter introduces the readout systems, the setups, the methodology and analysis strategies for the laboratory measurements conducted within the scope of this thesis. In preparation for test beam measurement campaigns, four FASTPIX samples have been commissioned, tested and calibrated following and developing the methodology first introduced in [13].

6.1. The Caribou Data Acquisition System

During the commissioning, testing, for laboratory as well as for test beam measurements of FASTPIX assemblies, the Caribou Data Acquisition (DAQ) system [65] carries out the powering, slow-control and readout. The central hardware components of Caribou are shown in Figure 6.1, representing the use case for FASTPIX.

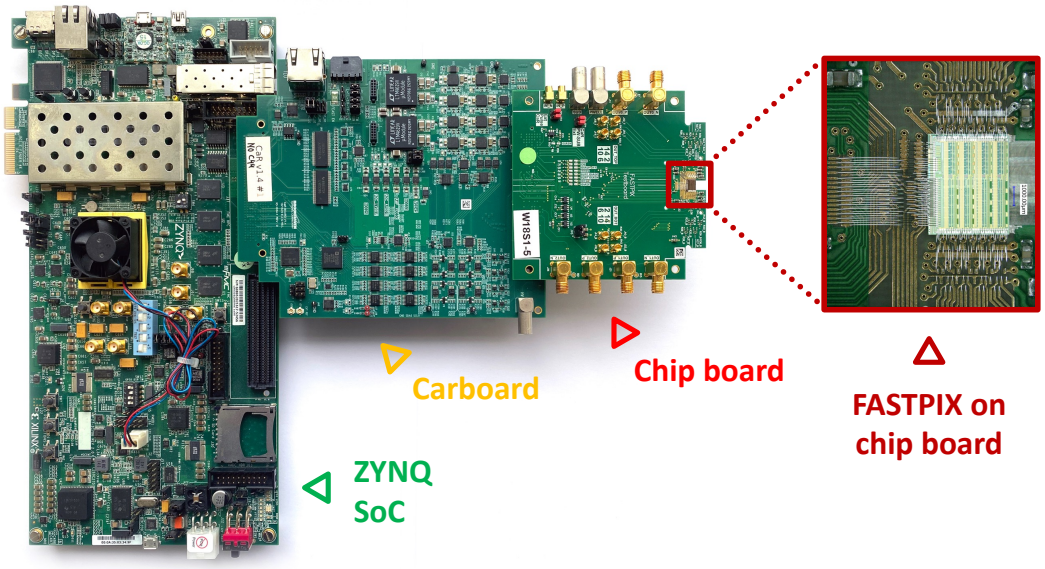

Figure 6.1: Central components of the Caribou data acquisition system. On the left, the System-on-Chip (SoC) evaluation board, the Control and Readout board (Carboard) in the middle and the chip-specific carrier board (chipboard) for FASTPIX towards the right. On the very right, a zoomed-in view details the glued and wire-bonded silicon chip.

The versatile system has been developed to enable a fast integration of new detector prototypes. The Caribou hardware comprises a combination of a System-on-Chip (SoC) evaluation board, the Carboard and a custom Printed Circuit Board (PCB) that houses the detector under test.

The core of the Caribou system is the Xilinx ZYNQ SoC housed on a ZC706 evaluation board (ZYNQ board) [66], powered by an external off-the-shelf 12 V DC supply. It incorporates a Kintex-7 Field Programmable Gate Array (FPGA) [67] and a dual-core ARM Cortex-A9 Central Processing Unit (CPU) [68]. Both, FPGA and ARM processor are linked via an Advanced eXtensible Interface (AXI) [69] bus, establishing a conducive environment for reading and writing FPGA registers within software applications. The ARM CPU supports basic computing tasks and runs a Yocto-based Linux distribution, Poky [70]. It is remotely accessed via Ethernet and a secure shell (SSH) [71] connection, eliminating the need for dedicated computer hardware and retaining the system's compactness.

The Carboard uses an FPGA Mezzanine Card (FMC) [72] connection to interface with the ZYNQ board. Operational flexibility is achieved by incorporating an optional extension cable between the ZYNQ board and the Carboard. Embedded with analogue-to-digital converters (ADC), adjustable voltage/current references and an Inter-Integrated Circuit (I2C) [73] bus, the Carboard offers the supplies and services that are necessary to operate FASTPIX. An RJ45 socket allows the Carboard to receive external clock and trigger signals provided by the Trigger Logic Unit (TLU) of a higher-level DAQ system. The link to a FASTPIX assembly is established through a SEARAY^{TM} high speed, high density open-pin-field array connector [74] at the opposite side of the Carboard.

The detector under test is wire-bonded to a chip carrier PCB (chip board) that securely fixes and interconnects the silicon device to its periphery. The chip board is populated with passive as well as few active components and interconnects with the Carboard through the SEARAY^{TM} connector. In addition, it allows for detector-specific configuration changes through jumpers, gives additional connections for biasing and access to debug signals through surface-mounted connectors.

The Peary DAQ software provides the link between hardware and user. With a Hardware Abstraction Layer (HAL) that creates an interface between hardware and software components, the software implements control and communication with the connected detector and other periphery devices. Peary supports stand-alone applications like laboratory measurements through a Command Line Interface (CLI) and can be integrated into other DAQ systems using an Application Programming Interface (API). CLI is used for laboratory measurements with FASTPIX whereas the API is employed to incorporate detector configuration and readout into the test beam reference telescope setup.

The integration of FASTPIX into the Caribou DAQ system utilizes its flexible hardware and software components, yielding a compact, efficient, and versatile solution for prototype development and testing.

6.2. The FASTPIX Chip Board

For testing and small-scale integration a detector is typically glued and wire-bonded to a dedicated chip board that offers a rigid structure commonly made from multiple conducting copper layers sandwiched between FR-4 [75]. The chipboard facilitates the necessary fan-out of $\mathcal{O}(100\,\mu m)$-pitched wire bond interconnections, signal routing, electronic circuitry for level shifting, amplification and buffering of signals as well as connectors for power control and readout

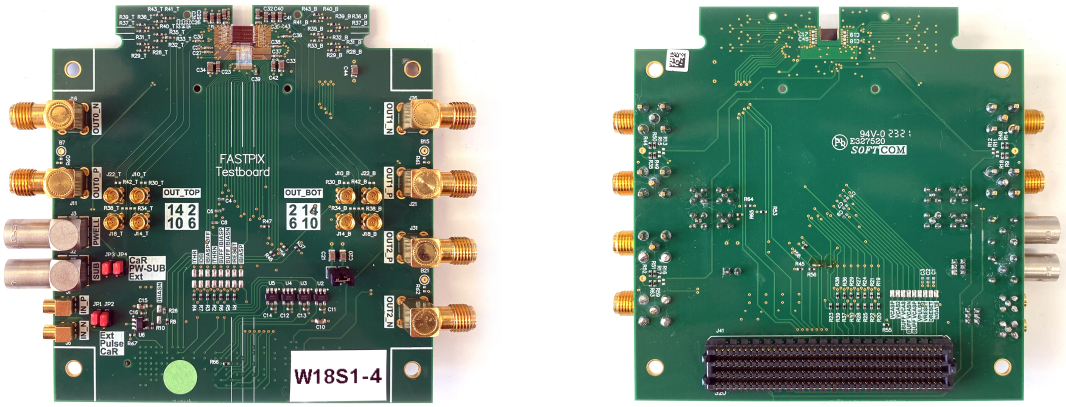

(a) Front **(b)** Back

Figure 6.2: FASTPIX chip board assembly.

The FASTPIX detector prototype is placed at the top edge of the chip board shown in Figure 6.2. The custom PCB provides secure electrical connections and mechanical mounting points for the integration of FASTPIX samples in Caribou test setups.
The chip board comprises five substrate layers of FR-4 and six copper layers. STAYSTIK 571 [76], an epoxy glue containing silver particles, is used to achieve mechanical adhesion and conductive connection with a dedicated pad in the top copper layer. A 8.05 mm by 4.40 mm cut-out behind the chip, centered along the top edge, minimizes the material content that is encountered by a particle beam traversing the assembly.
On the chip board passive as well as active components propagate the communication lines, provide constant current sources and filter supply voltages from the Carboard, necessary to operate the detector frontend circuitry. Sensor bias voltages are applied directly to the PCB via two LEMO connectors [77] on the front left side of the board, designated for sensor p-wells and substrate. Four SMA connectors along the right side and two along the left side provide the connection for differential signal readout of the three output signal lines of the chip, *FAST OR*, *DLY1* and *DLY2*. Two micro SMA connectors are placed on the right side, receiving a differential trigger signal for the analog frontend pulse injection circuitry. Jumpers on the front face of the board select between a Carboard-internal or external supply of the substrate bias voltage and the test pulse injection trigger signal. FASTPIX uses external source meter power supplies for biasing that provide constant voltage at a high accuracy and continuously monitor the leakage current. The SEARAY^{TM} connector on the backside bottom

edge interfaces with the readout and control system.

6.2.1. Material Budget

The material content of a detector assembly is a pivotal characteristic, given its influence on the trajectory of a charged particles via multiple scattering. With particles typically incident perpendicular to the assembly, the material budget is calculated by dividing the thickness of the layers perpendicular to the assembly by the radiation length of the material. The material contribution is expressed as a percentage of radiation length, for the detector and PCB separately, and is given in Table 6.1 for the FASTPIX chipboard. Each layer of the silicon device and the chipboard, from the silicon substrate and metallization to the FR-4 and copper layers, is accounted for, excluding the sensor passivation layer, PCB silk screen and solder mask.

Table 6.1: Estimation of material content X/X_0 of the FASTPIX sensor and the carrier PCB. X_0 is the radiation length of the material and X the thickness of the component. Based on and adapted from [78, 79, 80].

Layer	Material	X_0 [mm]	X [µm]	X/X_0 [%]
Chip			**300**	**0.32**
Sensor	Silicon	93.6	290	0.31
Metal Stack	Aluminum	88.9	10	0.01
PCB			**1744**	**2.16**
Metal layers	Copper	14.3	144	1.0
Substrate	Glass fibre (60% of FR-4)	97.66	960	0.98
Resin	Epoxy resin (40% of FR-4)	349.89	640	0.18
Covers			**1000**	**0.24**
Front cover	ABS plastic	406.4	500	0.12
Back cover	ABS plastic	406.4	500	0.12

The cutout behind the chip removes the PCB from material budget considerations and leaves the contributions from chip and covers of 0.56 % X_0.

6.3. Laboratory Setup

The following section introduces the main components and arrangement of the benchtop setup that was used for all laboratory measurements with FASTPIX.

6.3.1. Setup and Components

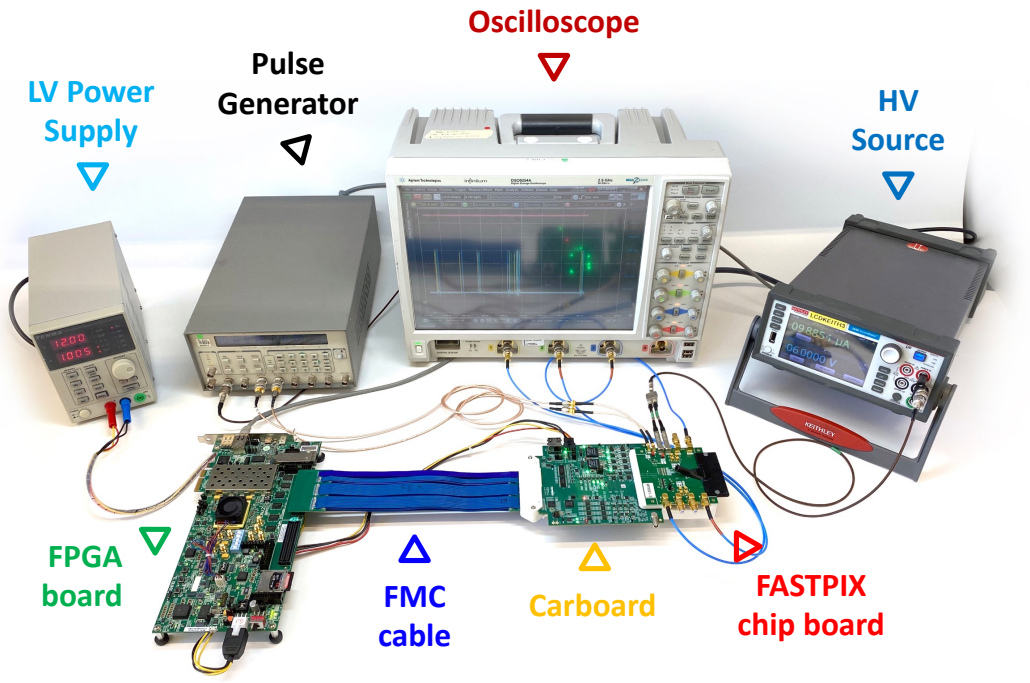

Figure 6.3: Benchtop measurement setup for FASTPIX.

The benchtop setup for laboratory tests with FASTPIX is shown in Figure 6.3. In the foreground on the left side of the lab bench the ZYNQ board is connected to the Carboard via a short FMC cable. On the other end of the FMC cable, towards the right, the Carboard with the attached FASTPIX chipboard are mounted onto a white 3D printed acrylonitrile butadiene styrene (ABS) [81, 82] support structure. The support structure offers additional mounting points in different laboratory setups and relieves the multi-pin array connectors from mechanical strain when changing the arrangement of the hardware components.
The ZYNQ board and Carboard receive 12 V DC from a Tenma 72-2540 low-voltage power supply [83] in the back-left of the setup. A Keithley 2450 SourceMeter [84] in the back-right of the bench applies the FASTPIX reverse bias voltages for p-wells and substrate. The source meter power supply monitors the total chip current and enforces a current compliance typically set to 30 µA, ensuring a non-destructive detector operation.
In the back-center, the Agilent DSO925A oscilloscope [85] is pictured receiving the detector signal outputs during the following measurements. The same applies for the Stanford Research Systems Inc. DG535 digital delay/pulse generator [86], pictured to the left of the oscilloscope, which is used for triggering test pulse injection measurements.

Low-voltage power and control for FASTPIX are executed through the Caribou system. Data readout is performed using the oscilloscope with a 2.5 GHz analog bandwidth and a sampling rate of 10 GS s^{-1}. This oscilloscope-based readout of detector output signals is as well controlled by the Caribou system using a local ethernet connection between both devices. The FASTPIX chip and the oscilloscope are powered and configured during the start up of the Peary command line interface. The applied settings are provided in configuration files, locally saved on the SoC Linux distribution.

6.3.2. Environmental Monitoring and Control

The backside of FASTPIX is insensitive to ambient light due to its aluminum metallization. At the front face of the chip light is partially reflected at the surface, at the interface of the passivation or at the interface of each of the different layers of the metal stack.

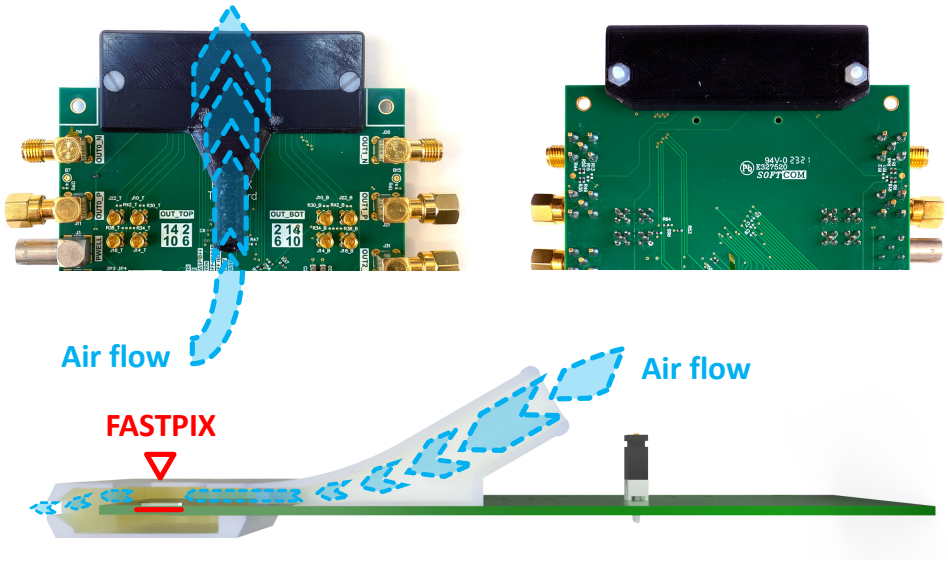

Figure 6.4: ABS plastic 3D printed chip cover. The top left and top right show the installed cover from the the front face and backside of the PCB. The bottom image illustrates the air flow inside of the cover rendered in a light grey material.

To further reduce the introduction of ambient light, a 1 mm thick ABS plastic 3D printed cover was fitted to each assembly. It is fixed with two plastic screws at the far ends of the piece and was used for all of the presented measurements. The printed ABS part is designed with a custom light-tight fit around the front edge of the chipboard and is shown in Figure 6.4. It is produced on demand when a new FASTPIX assembly is commissioned and introduces an additional material budget of 0.5 % X_0. The number of photons entering the active sensor region is largely reduced such that ambient light does not significantly contribute to the measured leakage current and noise. By design, the cover protects the chip against possible mechanical damage during handling.

The laboratory has a controlled climate with an ambient temperature of approximately 22 ± 1 °C, as illustrated by Figure 6.5.

Figure 6.5: Measurmeent of ambient temperature in the laboratory extending over 12 h. The data was taken with a Bosch BME280 sensor [87].

The covered detector lacks convective heat transfer with the ambient air in addition to a reduced heat transfer to the PCB due to the small contact area previously discussed in Section 6.2. To stabilize the device operation in measurement, the cover provides an air inlet to introduce airflow around the chip. Particularly in high particle rate scenarios an ambient-temperature, dried airflow has shown to stabilize the device operation in measurement.

6.4. Electrical, Noise and Signal Injection Measurements

The measurement setups described in the following section comprise basic functional tests and an evaluation of the chip based on observables that do not require external sources of signal.

6.4.1. Electrical Characterization

The electrical properties of the FASTPIX chip are investigated by measuring the sensor leakage current of each assembly as a function of applied bias voltage, its current-voltage (IV) characteristics. Utilizing the Caribou laboratory setup introduced in Section 6.3.1, IV curves are obtained by a series of automated voltage scans. The data is acquired by a lab computer that runs a python-based measurement script and communicates with the HV source via the local network.

The HV source simultaneously connects to the p-well and substrate terminal and ramps the voltage into the reverse bias regime. The on-chip circuitry shares both bias terminals among all matrices and prevents a fully independent IV measurement of a singular matrix.
The IV measurement range of FASTPIX starts at a bias voltage $< 0\,\mathrm{V}$, which is necessary to configure the chip in a stable state.
Between measurement points a waiting time allows the current to stabilize before a series of current measurements is taken for every set voltage V_{set}. The repetition of the current measurement ensures that possible fluctuations in current are represented by the measurement statistics. In order to avoid damage to the device under test, the measurement is stopped once the leakage current surpasses $30\,\mu\mathrm{A}$.
The IV measurements were taken at a controlled room temperature and with a low volume of air constantly flowing through the ABS plastic chip cover.

6.4.2. Signal response and Noise Characterization

The noise in FASTPIX samples can be examined using the laboratory setup introduced in Section 6.3.1. The biased chip is configured through Caribou and read out using the oscilloscope.
Noise data is recorded at various threshold levels, for a predetermined maximum duration or until a maximum amount of triggers has been recorded by the oscilloscope readout. The measurements are conducted under standard operating conditions in the laboratory, at room temperature of approximately 22 ± 1 °C and with the chip shielded from ambient light.
The delay line calibration, previously described in Section 5.6, is applied to the gathered data and links the timing signatures in the recorded waveforms with the pixel indices of the FASTPIX matrix. With this information, the FASTPIX noise performance is assessed on pixel and matrix level as well as for the impact of detection threshold.
An average noise rate is determined as

$$n_{\text{chip}} = \frac{N_{\text{hits}}}{t_{\text{DAQ}}} \quad , \tag{6.1}$$

where N_{hits} is the number of hits during the data taking time t_{DAQ}.

Measurements at nominal detection thresholds, which are also set during test beam campaigns, aid in identifying noisy pixels and asses their impact on the detector performance. Measurements covering a larger threshold range illustrate the dependence of noise rate on detection threshold on matrix and pixel level. From the rate turn-on that occurs as the threshold is lowered into noise the optimal threshold level of a given matrix for more advanced tests with particle beams and reference tracking systems is extracted.

6.4.3. Test Pulse Injection Measurements

To allow a good performance comparison between matrices, the discriminator threshold-to-charge relation as well as the ToT-to-charge relation of each matrix is calibrated using charge injection measurements.

Test Pulse Setup
The possibility on externally injecting a signal of known charge into the analog pixel front-end allows for a calibration of the measured ToT values and the global discriminator threshold.
For FASTPIX the test pulse feature injects externally triggered current signals into two dedicated digital test pixels. The association of the LVDS output with the selected test pixel is predetermined by the FASTPIX configuration and does not involve the delay line calibration.
The laboratory setup used for test pulse injection measurements employs the benchtop setup introduced in Section 6.3.1. The biased chip is configured through Caribou and read out using the oscilloscope. The discharge of an internal capacitor into the pixel frontend is externally switched by a differential pair of pulse generator signals connected to the two micro SMA connectors on the edge of the chipboard.
During the measurement a trigger is sent at a rate of 500 Hz with a pulse width of 500 ns. Inbetween subsequent trigger pulses, the front end returns to zero and the injection capacitor is recharged. The oscilloscope acquires measurement data in-sync with auxiliary trigger

pulses from the pulse generator.

The conversion of the voltage used to charge the injection capacitance follows from the equation

$$n_e = \frac{C}{q_e} \cdot v_{\text{pulse}} \quad , \tag{6.2}$$

where n_e is the number of electrons, C is the injection capacitance, q_e is the electron charge, and v_{pulse} is the test-pulse voltage in V. The associated uncertainty in the number of electrons, considering uncertainties in both the voltage and the conversion factor, can be obtained through error propagation.

$$\Delta n_e = \sqrt{\left(v_{\text{pulse}} \cdot \frac{\Delta C}{q_e}\right)^2 + \left(\frac{C}{q_e} \cdot \Delta v_{\text{pulse}}\right)^2} \quad , \tag{6.3}$$

where Δn_e is the uncertainty in the number of electrons, ΔC is the uncertainty on the capacitance, and Δv_{pulse} is the error in the voltage.

Table 6.2 summarizes the expected injection capacitances and calculated conversion factors that relates the number of electrons to the voltage applied to the test pulse capacitance. Capacitance values and uncertainties are extracted from a post-layout simulation of the chip with a 20 % uncertainty on the value of the injection capacitance [55].

Table 6.2: Conversion factors $k = C/q_e$ for different pixel pitch p, injection capacitances C, and their associated uncertainties [55].

p (µm)	C (aF)	k (e/V)
8.66	57.3 ± 11.5	358.1 ± 71.6
10.0	57.0 ± 11.4	356.3 ± 71.3
15.0	55.5 ± 11.1	346.9 ± 69.4
20.0	54.0 ± 10.8	337.5 ± 67.5

The discriminator threshold and injected pulse amplitude are set by the Caribou system. The largest simulated injection capacitance yields a measurement range that extends up to an injected signal of 650 e.

Time-over-Threshold Calibration

At a given threshold, the ToT calibration connects the time-over-threshold measurement with the injected signal.

For each pulsed pixel and at each discriminator threshold that was set during the measurement, the ToT distribution of a given injected signal is recorded. The ToT spectrum shows the distribution of measured durations for which the signal amplitude was registered above the set discriminator threshold. A Gaussian fit is applied to each peak and yields the mean of the Gaussian fit as the final ToT peak position value.

A surrogate function represents a non-linear trend and is used to fit the data:

$$\mathrm{t}_{\text{ToT}} = a \cdot E_{\text{ToT}} + b + \frac{c}{E_{\text{ToT}} - d} \quad , \tag{6.4}$$

where t_{ToT} is the ToT measurement, E_{ToT} the deposited energy and a, b, c, d are the parameters to be found by the fit.
For high values of deposited energy, a linear relationship between t_{ToT} and E_{ToT} with slope a and intercept b dominates the surrogate function. Towards lower energies, $\frac{c}{E_{ToT}-d}$ takes over, with c defining the curvature and an asymptotic behavior for $E_{ToT} = d$. The intercept with the x-axis $t_{ToT} = 0$ represents the minimum threshold for detecting the injected charge of the set v_{pulse}.

The calibration for each threshold is derived from the fitted range of injected pulse amplitudes over the mean ToT value. Applying a conversion from pulser voltage to injected charge converts the time measurement to the equivalent charge signal.

Discriminator Threshold
For each set threshold value, a range of injection pulse amplitudes is scanned. The efficiency ε as a function of v_{pulse}, is calculated as the ratio between recorded n and N triggered pulse counts $\varepsilon = n/N$. The transition from zero efficiency to $\varepsilon = 1$ follows a saturation curve, called S-curve. The 50 % point of the S-curve is found by fitting the equation

$$\varepsilon(v_{pulse}) = \frac{1}{2}\mathrm{Erfc}\left(\frac{v_{th} - v_{pulse}}{\sqrt{2}\sigma}\right), \tag{6.5}$$

where v_{pulse} denotes the pulser voltage, v_{th} is the pulser voltage at the 50 % point, and σ represents the observed noise. The complementary error function is defined by:

$$\mathrm{Erfc}(x) = \frac{2}{\sqrt{\pi}}\int_x^\infty e^{-t^2}\,dt. \tag{6.6}$$

The function $\mathrm{Erfc}(x)$ represents the probability that a random variable, following a normal distribution with a mean of zero and variance of $1/2$, exceeds x.

The associated errors stem from the statistical uncertainties in the efficiency calculation represented by the confidence intervals calculated using the Clopper-Pearson method. The method utilizes the Beta distribution for a more accurate representation of efficiency uncertainty in cases of small numbers of trials. The lower and upper bounds of the Clopper-Pearson confidence interval for efficiency at confidence level α (commonly 0.68) are calculated using the Beta distribution:

$$\varepsilon_{low} = \mathrm{B}_{\frac{\alpha}{2}}(n, N-n+1) \quad , \quad \varepsilon_{high} = \mathrm{B}_{1-\frac{\alpha}{2}}(n+1, N-n) \quad , \tag{6.7}$$

where $\mathrm{B}_p(a, b)$ represents the p^{th} quantile of the Beta distribution with shape parameters a and b. The Beta function is defined as:

$$\mathrm{B}(a, b) = \int_0^1 t^{a-1}(1-t)^{b-1}dt \tag{6.8}$$

The application of the Clopper-Pearson method is implemented in CERN ROOT's TEfficiency class [88] and applied for every efficiency histogram.
By utilizing a conversion factor from pulser voltage v_{pulse} to injected charge in Table 6.2, the charge threshold values are calculated.

6.5. Calibration Measurements with X-ray Photons

The energy calibration of the global detection threshold and the ToT measurement is critical for a precise sensor performance evaluation. Measurements employing X-ray photons were conducted using two radioactive isotopes as well as X-ray fluorescence from different target materials in a primary X-ray beam. The resulting energy calibration of the detection threshold and the ToT against known photon emission energies allows a comparison to theoretical models, simulations, and other pixel detectors.

6.5.1. The Source Measurement Setup

As part of the inventory of the lab, radioactive sources containing the isotopes ^{55}Fe and ^{109}Cd suggest themselves as an external source of independent calibration signals. Their discrete emission of x-ray photons as monochromatic radiation with sharp energy peaks is optimal for energy calibration.

^{55}Fe, with a 2.737 years half-life, emits X-rays photons at K_{α_1} = 5.9 keV with an intensity of 25 %, K_{α_2} = 6.5 keV with an intensity of 5 % and K_β = 6.7 keV with an intensity of 2.5 %. The remaining emission consists of Auger electrons emitted at energies below 0.6 keV due to internal electron transitions following the decay.
^{109}Cd, with a half-life of 1.264 years, emits gamma rays and X-rays, along with Auger electrons. Gamma rays are produced at 88 keV with an intensity of 3.6 %. X-rays occur at K_α = 22.1 keV with an intensity of 15 % and K_β = 25 keV with an intensity of 5 %. Auger electrons make up the remaining share of emitted particles at energies below 0.6 keV [89].
The calibration relies on the absorption of photons within the sensitive volume of the sensor. In the 25 µm thick epitaxial layer of FASTPIX, the majority of photons emitted from the ^{55}Fe source are absorbed. The higher-energy photons from the ^{109}Cd source, where the absorption depth exceeds the thickness of the epitaxial layer, interact significantly less likely. Measurements with ^{109}Cd therefore require an increase in measurement time in order to acquire statistics of similar magnitude.
Table 6.3 lists the expected most probable absorption depth and expected deposited charge from absorbed X-ray photons in silicon.

Table 6.3: Prominent X-ray photon emission peaks of radioactive isotopes with associated absorption depth and deposited charge in silicon. The calculation is based on interpolated mass attenuation coefficients μ/ρ from the NIST Standard Reference Database 126 [90].

Isotope	Energy of K_α (keV)	Absorption depth (µm)	Deposited charge (e)
^{55}Fe	5.9	29	1640
^{109}Cd	22.1	111	6530

In the energy range of the two γ-sources an energy of approximately 3.6 eV is necessary to generate a single electron-hole pair within the sensor material. Thus, the energy deposited by the absorbed photon can be directly related to a total number of electron-hole pairs created in silicon.

The calibration measurements employ the same Caribou-based setup as the measurements in Section 6.4.2. In addition, a radioactive source is placed approximately 10 mm above the sensor surface.

6.5.2. The X-ray Tube Setup

Compared to an energy calibration measurement with monoenergetic photons from the decay of radioactive isotopes, X-ray fluorescence can be utilized to obtain additional calibration points across a more divers spectrum of energies at higher rate.

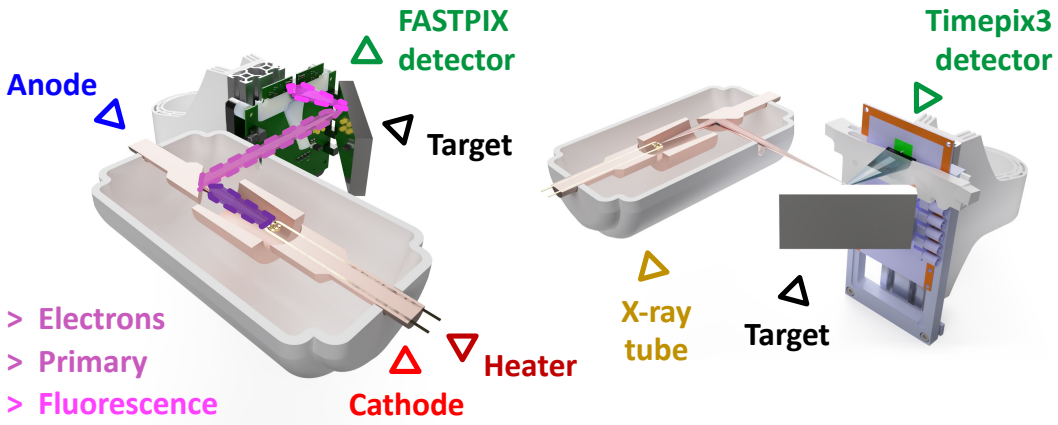

Figure 6.6: Rendering of the main components of the X-ray tube setup. On the left, the acceleration of electrons, generation of primary and secondary X-rays is in focus and shown by a color coded series of arrows. On the right, the arrangement of components is emphasized by the change in perspective.

The Malvern Panalytical EMPYREAN PW3373/10 Ceramic X-ray Tube [91] is at the heart of the X-ray machine used for these measurements. A rendering of the main components of the X-ray tube setup is shown in Figure 6.6. Inside the tube vacuum electrons are emitted from a cathode heater filament and get accelerated towards the anode inside the potential of a high voltage supply. Primary X-ray photons are generated by colliding accelerated electrons with the anode copper target. The interactions of 15–40 keV electrons and copper atoms generate a bremsstrahlung spectrum that is superimposed with the characteristic K_α-lines of copper. The primary beam then interacts with various secondary targets, such as titanium, calcium, iron, and copper, resulting in the emission of secondary fluorescence X-rays with an distinct energy spectrum that is characteristic of the secondary target material. The device under test is irradiated with the secondary X-rays at an intensity that is modulated via the tube cathode current.
The conducted measurements rely on the absorption of photons within the sensitive, depleted volume of the sensor. The approximate most-probable absorption depth and expected deposited charge in silicon is listed in Table 6.4 for X-ray fluorescence emission peaks from a selection of target materials.
The measurements with high energy photons from X-ray fluorescence are conducted using the same setup as the source measurements discussed in Section 6.5.1. The spatial constraints inside the enclosure of the X-ray machine call for a slight adaptation in cable length and support structures.
Based on Table 6.4, the X-ray fluorescent photons emitted from the Ca and the Ti target are

Table 6.4: Absorption depth and deposited charge in silicon for X-ray fluorescence emission peaks from a selection of target materials. The associated absorption depth and deposited charge in silicon are calculated based on interpolated mass attenuation coefficients μ/ρ from the NIST Standard Reference Database 126 [90].

Target	Energy of K_α (keV)	Absorption depth (µm)	Deposited charge (e^-)
Ca	3.7	8	1000
Ti	4.5	14	1220
Fe	6.4	42	1730
Cu	8.1	66	2190
Mo	17.4	570	4830
Ag	22.1	1120	6140
Sn	25.1	1470	6970

fully absorbed within the 25 µm thick epitaxial layer of FASTPIX at full depletion. The same applies for a large share of photons from the Fe and the Cu target. The higher-energy K_α lines of Mo, Ag and Sn exceeds the thickness of the epitaxial layer and interact less likely with increasing emission energy.

7

Laboratory characterization and calibration

Laboratory measurements provide integral information for the characterization of a novel pixel detector prototype. The focus lays on assessing the basic functionality of the tested FASTPIX samples in a controlled environment. Building upon the methodologies outlined in the preceding chapter, this chapter commences with an examination of the sensor's electrical properties through current-voltage characteristic studies. The following sections elaborate on an energy calibration of the global discriminator detection threshold, the time-over-threshold measurement and the signal gain. Later sections in the chapter address the noise observed during the preceding measurements as well as the overall noise performance from an observed fake hit rate in a low signal threshold range. The chapter closes with a summary of results and concludes with a discussion on the impact on the performance in particle-detection measurements with the available FASTPIX samples, setting the stage for its application in more advanced experimental setups.

7.1. Current-Voltage Characteristic

The first step in the laboratory characterization of a silicon sensor is a measurement of sensor leakage current as a function of applied bias voltage. As introduced in section 6.4.1, such a current-voltage (IV) measurement allows to confirm the working state of each FASTPIX assembly and is a first test of its electrical properties.
A central aspect, that is to be confirmed by the following measurements, is whether a stable leakage current is reached for a sufficiently high bias voltage to fully deplete the epitaxial layer. This state is instrumental for a performant and efficient detector operation, where the collected charge and therefore the induced signal is maximized. The punch-through voltage v_{punch} identifies the bias beyond which an abrupt, excessive current occurs between the p-doped substrate and the p-type implant structures at the pixel edge, which can damage the monolithic device. The punch-through point is determined by the change in current exceeding 0.2 µA between two consecutive measurement points in the regime $v_{\text{bias}} < -5\,\text{V}$.

7.1.1. Measurement conditions

IV curves are obtained by a series of automated measurements with the setup previously introduced in Section 6.4.1.
Room temperature fluctuations of 1 °C results in a variation on the measured current. The power spectral density of a current flowing through a conductor was introduced in Section 4.5 and has a relationship with the temperature of the conductor and its resistance. The relative change in the RMS noise current for a 1 °C temperature change at room temperature (approximately 295 K) is about 0.2 %. It is dominated by a relative change in volume generation current of approximately 8.5 % and surface leakage current of approximately 7.6 % at the same room temperature. In the following discussions, an 8 % relative variation in measured current is expected for temperature fluctuations of 1 °C.

The predefined individual voltage points of the presented measurements are scanned by slowly ramping the 0.5 V steps between measurement points. The setting 0 V is excluded since the chip configuration routine is not able to configure an unbiased chip. A waiting time of 10 s allows the current to stabilize before a series of 10 current measurements is taken with a measurement frequency of 1 Hz for every set voltage V_{set}. The ten-time repetition of the current measurement ensures that small fluctuations which are still present during the measurement time can be represented by appropriate errors. Occasional errors in the communication between the measurement script and the source meter power supply cause a wrong assignment of values read out from the measurement device buffer. The collection of multiple current measurements per voltage setting rules out a repetition of the measurement due to missing data points. The analysis of electrical measurement data involves several steps to ensure the accuracy and reliability of the calculated mean values and their corresponding uncertainties (standard deviations).

For each set of data that was taken for a voltage V_{set}, the arithmetic mean and standard deviation of both voltage and current measurements are computed.

The following section presents and discusses IV measurements for standard-process, modified-process and most-modified-process samples. Each plot displays four IV measurements, which differ in the matrix selected during the measurement with a given fully powered and configured FASTPIX sample. The matrices 0, 1, 2 and 3 have been selected for this comparison because of the absence of pixel modifications across all three process modifications. They serve as a set of baseline matrices that only differ in pixel pitch and the process modification applied during the processing of the corresponding wafer. The nominal detection threshold of 820 mV was chosen to ensure a largely noise-free operation.
Furthermore, a comparison between a sample with intensive beam time and a minimally-tested backup sample is given, as well as a qualitative illustration of the impact of ambient temperature air flowing through the ABS plastic chip cover.

7.1.2. Measurement results

Figure 7.1 shows the IV measurement of a standard and a modified process sample. For both samples an onset of current occurs that is completed around −2 V and turns into a slower, more consistent increase for the lower part of the scanned voltage range. Compared to the

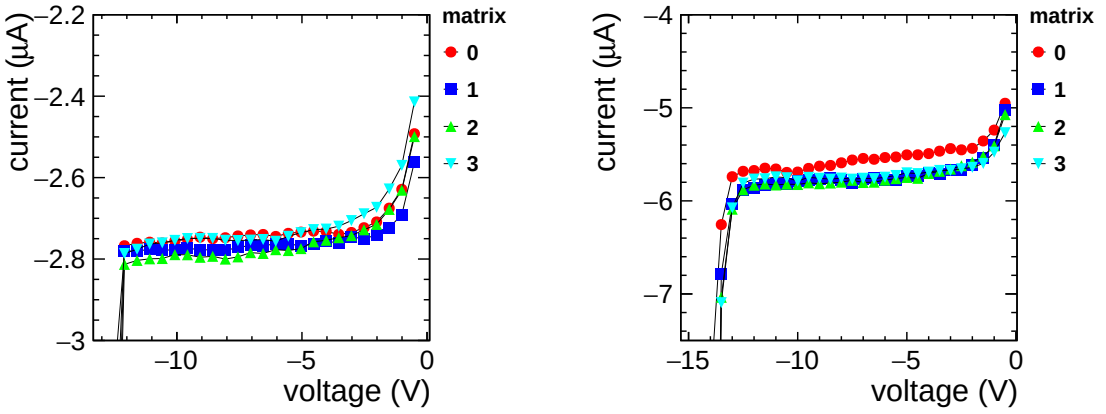

(a) W03S1-1. **(b)** W15S1-1.

Figure 7.1: IV measurements of a standard and a modified process sample. The plots show data for the first four matrices with index 0, 1, 2 and 3.

modified process sample, the standard process sample exhibits an approximately two-times lower current.

At −6 V bias, the standard process yields an average −2.8 µA, while the modified process has already reached −5.7 µA, averaged across the four measured matrices. The standard process sample W03S1 reached punch-through after −12 V, whereas the modified process sample W15S1-1 retains stable currents down to −13 V.
Due to its continuous n-implant acting as an isolation between the p-well and substrate, the W15S1-1 sample can sustain higher substrate voltages. The modified process shows the expected superior isolation with its higher punch-through voltage.
Despite slight differences in current between the four matrices, these do not represent isolated physical differences that can be attributed to the features of individual matrices within the relative error on the current measurement in the laboratory setting. The measured current is influenced by current contributions from other regions of the chip that are simultaneously biased, as discussed in Section 5.7. A dependency on $\sqrt{V}$, which is indicative of a dominant contribution from volume generation current, could not be observed. The measured current is a convolution of volume and surface currents as well as contributions from the front end circuitry inside the p-well along the edge of each pixel.

Figure 7.2 shows the IV measurements for two samples of the most-modified process from wafer W18. The observed trends in current are similar with respect to the measurements with W03S1-1 and W15S1-1.
Both W18S1 samples have measured a current that is of comparable magnitude to the W15S1-1 sample. At −6 V bias a −6.2 µA current is measured with the W18S1-3 sample while the W18S1-4 sample yields a slightly elevated −5.9 µA. The gap in the deep n-implant disrupts the isolating qualities of the blanket structure and results in slightly higher currents compared to the W15 sample. The 0.3 µA difference between both samples is not significant within the uncertainty of the current measurement in the laboratory environment.

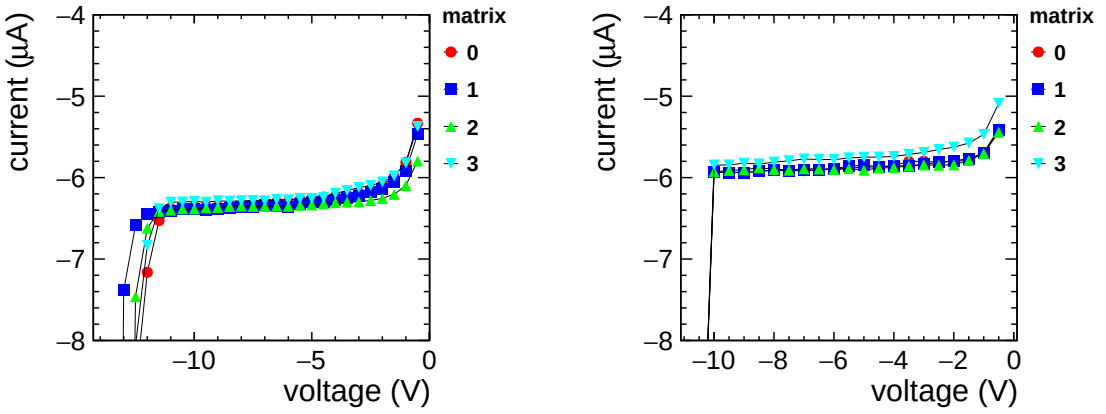

(a) W18S1-3, the test beam sample.

(b) W18S1-4, the backup sample.

Figure 7.2: IV measurements of two most-modified process samples from wafer W18. The plots show data for the first four matrices with index 0, 1, 2 and 3.

The onset of a punch-through is observed after −12 V for sample W18S1-3 and below −10 V for sample W18S1-4. The additional extra-deep p-implant as well has a diminishing impact on the isolation between p-wells and substrate. Inturn the punch-through voltage is decreased, compared to the W15S1-1 sample. This effect is most pronounced for matrices with the gap in the deep n-implant in combination with the increased deep n-layer doping concentration of the W18S1 samples. Compared to the W15S1-1 data, the punch-through of W18S1 samples at lower absolute bias voltages can be observed in measurement data.

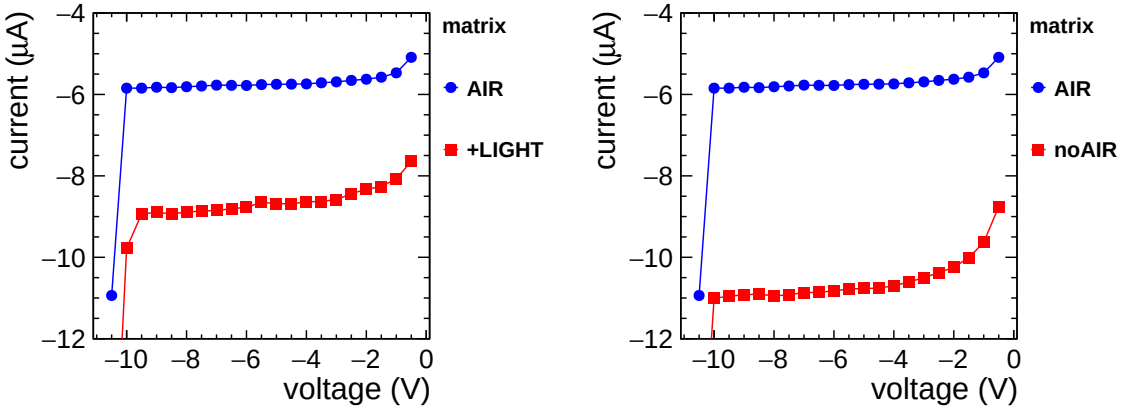

(a) Impact of ambient light on sensor current

(b) Impact of air-flow on sensor current

Figure 7.3: IV measurements of sample W18S1-4 matrix 3 illustrating the impact on ambient light and a low-volume ambient temperature air flow.

The impact of ambient light in a lab environment on the current measurement during a bias voltage scan is illustrated by Figure 7.3a.

The qualitative influence of the low-volume ambient temperature air flow that is introduced to the ABS plastic chip cover can be assessed in Figure 7.3b.
The additional air flow causes a 45 % change in current which is equivalent to approximately 6 °C change in chip temperature. A direct temperature measurement was not attempted due to the small size of the chip.

The presented IV measurements confirm the working state of each FASTPIX assembly as well as a safe operational voltage range. In the following parts of the thesis, if not mentioned otherwise, FASTPIX is operated at −6 V p-well and substrate bias, as intended by the chip design and verified in simulation [92].
The current values measured in the laboratory environment at the nominal designed bias voltage are summarized in Table 7.1 for all available samples.

Table 7.1: Current values and standard error on the mean at -6V substrate and p-well bias for available samples measured in laboratory conditions at 22 °C, with 8 % relative error stemming from the uncertainty on temperature.

Matrix Unit	0 (µA)	1 (µA)	2 (µA)	3 (µA)	Mean (µA)
W03S1-1	−2.7 ± 0.2	−2.8 ± 0.2	−2.8 ± 0.2	−2.8 ± 0.2	−2.8 ± 0.2
W15S1-1	−5.5 ± 0.5	−5.8 ± 0.5	−5.8 ± 0.5	−5.7 ± 0.5	−5.7 ± 0.5
W15S1-3	−5.5 ± 0.5	−5.6 ± 0.5	−5.6 ± 0.5	−5.7 ± 0.5	−5.6 ± 0.5
W18S1-3	−6.3 ± 0.5	−6.4 ± 0.5	−6.4 ± 0.5	−6.3 ± 0.5	−6.3 ± 0.5
W18S1-4	−5.9 ± 0.5	−5.9 ± 0.5	−5.9 ± 0.5	−5.8 ± 0.5	−5.9 ± 0.5
W18S1-5	−5.9 ± 0.5	−5.7 ± 0.5	−5.9 ± 0.5	−5.8 ± 0.5	−5.8 ± 0.5

The measurements reflect the expected and previously discussed qualitative change in current. While the difference in pitch does not cause a significant difference in measured current, an increase can be observed with the introduction of the blanket n-layer between W03S1-1 and W15S1-1 and a change to higher deep n-layer doping between W15S1 and W18S1 samples. Sample-to-sample differences are within the uncertainties of the measurements, with the exception of W18S1-3, the sample heavily tested with ionizing radiation in lab and test beam. As discussed in Section 5.7, higher bias voltages available within the confirmed operational voltage range before punch-through are expected not to improve performance, based on results from simulation.

On chip level, the standard manufacturing process (W03) as well as its modifications (W15, W18) did show the expected behavior. The introduction of the deep blanket n-layer in W15 and W18 samples shows an increase in current and a slight extension of the isolation towards higher punch-through voltages, the latter decreases again for the increased deep n-layer doping concentration of the W18 sample. The nominal p-well and substrate bias voltage of −6 V is within the stable current range of each tested sample without the risk of punch-through or destabilization during advanced measurements wit particle beams.

7.2. Energy Calibration

Calibration measurements with electric test pulses, radioactive photon sources and photons from X-ray fluorescence allow to translate the detector-specific information units acquired by the DAQ system into the physics observable at the heart of a measurement. Detailed detector characterization and calibration in the laboratory environment complement advanced performance measurements with particle beams described in Chapter 10.

7.2.1. Time-over-Threshold

The time during which the analog signal amplitude surpasses a given threshold, is a measure of the collected charge, which itself is proportional to the energy deposited in the detector.

Test Pulse Signal Injection
The injection of electrical test pulses offers the possibility of investigating the response of the analogue circuitry and digital logic of the detector frontend.
The full FASTPIX control and readout chain is used for electrical test pulse signal injection. Section 6.4.3 introduces the measurement setup that enables an energy calibration of measured ToT values. The test pulse injection is configured for the two digital test pixels. The test pixels are independent of the 64 pixels in the matrix and are individually selected for each measurement.

The pulser voltage v_{pulse} is scanned in a discriminator i_{thr}-range between 0.1 V and 1.2 V with a 0.1 V threshold step. The setting $i_{\text{thr}} = 0.0$ V is left out since the threshold current defined by a resistor on the chipboard goes to infinity as the voltage approaches zero and no longer provides a reliable working point. An individual v_{pulse} scan per set threshold covers a range from 0.0 V to 1.8 V v_{pulse} with a step size of 10 mV. At every v_{pulse} step 250 triggered pulses are recorded by the oscilloscope readout before the next test pulse voltage is configured through Caribou.

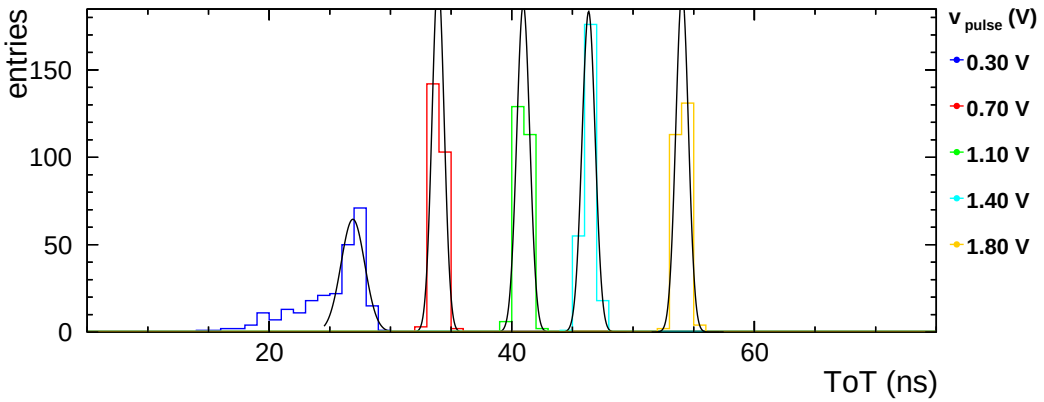

Figure 7.4: Exemplary ToT data and fits for matrix 3 of sample W18S1-3 at a selection of 5 pulse injection voltages v_{pulse}. The data was recorded with test pixel $pb = 3$ at $i_{\text{thr}} = 0.82$.

For all combinations of threshold voltage (i_{thr}), pixel number (pb), and pulse injection voltage (v_{pulse}), the corresponding ToT values are obtained from the measured data. Figure 7.4 presents exemplary ToT distribution histograms and fits for a selection of 5 pulse injection

voltages v_{pulse}. The data was taken with test pixel 3 from the 20 µm-pitch matrix 3 of sample W18S1-3 at a threshold $i_{\text{thr}} = 0.82\,\text{V}$.

A peak processing algorithm is applied to each histogram and identifies the most probable ToT value for a given injected pulse height v_{pulse}. Peaks in the spectrum are found using ROOT's `TSpectrum` class [88], limited to the precision of the histogram bin width. The final peak position and its uncertainty are calculated in two steps. Initially, staring parameters are found for the fit, to increase the reliability of a converging fit result. A subset of five bins surrounding the maximum-content bin is identified to sufficiently enclose the peak.
A Gaussian fit is subsequently applied to each peak, with the peak bin, its amplitude and σ_{calc} as initial parameters. The fit range remains set to ±2 bins. The mean of the Gaussian fit yields the final ToT peak position value with the error on the resulting fit parameter as the error on the peak position. The fit results for the selection of thresholds shown in Figure 7.4 are summarized in Table 7.2.

Table 7.2: Exemplary fit results for matrix 3 of sample W18S1-3 at a selection of 5 pulse injection voltages v_{pulse}. The data was recorded with test pixel $pb = 3$ at $i_{\text{thr}} = 0.82$.

i_{thr}	(V)	0.3	0.7	1.1	1.4	1.8
μ	(ns)	26.90 ± 0.11	33.93 ± 0.03	40.95 ± 0.03	46.34 ± 0.04	54.04 ± 0.03
σ	(ns)	0.98 ± 0.08	0.50 ± 0.03	0.53 ± 0.03	0.54 ± 0.02	0.52 ± 0.03

At a fixed signal detection threshold i_{thr}, the position of the distribution of measured ToT values moves with the set v_{pulse} values. With increasing v_{pulse}, the mean of the distribution moves towards higher ToT, spanning values from around 25 ns up to around 55 ns for the highest possible injection signal at $v_{\text{pulse}} = 1.8\,\text{V}$ and a global detection threshold of $i_{\text{thr}} = 0.82\,\text{V}$.
At a lower pulse injection voltage, here shown for $v_{\text{pulse}} = 0.3\,\text{V}$, the injected signal peak is washed out by a tail forming towards smaller ToT values. While the ToT is registered by the analog front end and the analog signal is being reset to baseline, a later stage determines whether there was a hit. The analog signal is propagated to a high gain inverter node that needs a minimum pulse length to trigger the analog-to-digital conversion stage. Even if the signal is meeting the threshold, the discrimination requires a minimum ToT to be able to propagate the pulse into the delay lines. The transition region around this minimum processable ToT of approx. 27 ns is additionally broadened by thermal noise of the frontend circuit.
The width of the peaks can be attributed to fluctuations of the signal baseline. The extracted standard deviation of the Gaussian fit shows no dependency on the injected signal amplitude, apart from the lower limit on ToT.

When evaluating ToT as a function of signal, the data yields a linear behavior with an initial non-linear shift for small signals, as discussed in Section 6.5.1. For the ToT calibration the pulser signal as a function of measured ToT is assembled from the measurement data.

Figure 7.5 illustrates how the non-linear model in Equation (6.4) manages to approximate exemplary data from 20 µm-pitch matrix 3 of sample W18S1-3.

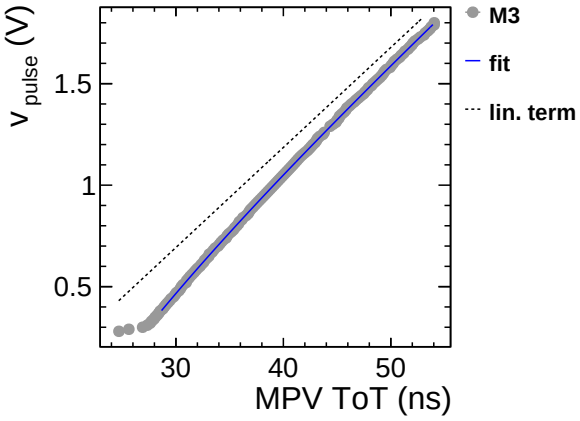

(a) $E_{\mathrm{ToT}}(t_{\mathrm{ToT}})$

Parameter	Value (V)
a	-0.486 ± 0.001
b	0.04693 ± 0.00001
c	-13.69 ± 0.09
d	0.003 ± 0.046
χ^2	0.001
NDoF	137
χ^2/NDoF	0.00001

(b) Fit result

Figure 7.5: Fit of the non-linear model surrogate function to data from sample W18S1-3 matrix 3 test pixel 3 at $i_{\mathrm{thr}} = 0.82\,\mathrm{V}$. The dashed line marks the linear term of the non-linear model.

An asymptotic behavior of the data points is visible around 27 ns most-probable ToT that describes a minimum detectable ToT value and transitions into the non-linear trend. Based on this feature, the fit model is applied with a lower ToT limit of 26.0 ns, 26.5 ns, 27.5 ns and 28.5 ns for 8.66 µm-, 10 µm-, 15 µm- and 20 µm-pitch matrices, respectively. Time-over-threshold distributions in Section 10.3 confirm that setting such a limit for the ToT calibration does not have an impact on the physics content of the ToT spectrum of a given matrix. The non-linear fit is instrumental in extrapolating v_{pulse} to the higher ToT regime during later stages of the energy calibration process.

Figure 7.6 shows the pulser signal over measured and extracted most-probable ToT values for the first 4 matrices of a standard and a modified process sample.

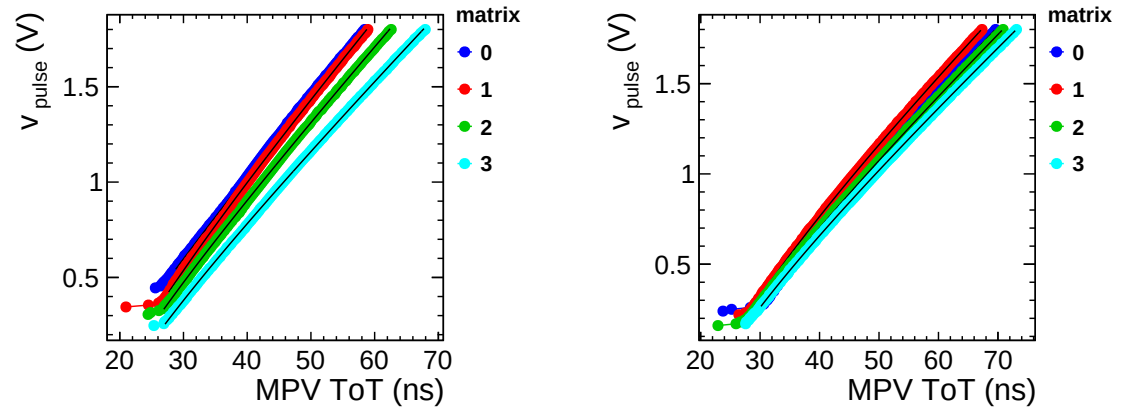

(a) W03S1-1.

(b) W15S1-1.

Figure 7.6: Pulser signal over measured and extracted most-probable ToT for the first 4 matrices of a standard and a modified process sample, operated at $i_{\mathrm{thr}} = 0.82\,\mathrm{V}$.

The fit results encompass the relationship of measured ToT to the injected signal amplitude spanning a range between the lower limit on ToT and the maximum amplitude set with $v_{\text{pulse}} = 1.8\,\text{V}$. The asymptotic behavior that describes a minimum detectable time-over-threshold value can be observed for all presented matrices. Sporadically, ToT spectra are left incomplete or with content that is comprised of artifacts along the data acquisition chain. In these cases the data is filtered and the plotted data shows missing patches or does not extend to the maximum v_{pulse}.

Table 7.3: Slope of the linear term from fit results for the first 4 matrices on a standard and a modified process sample, operated at $i_{\text{thr}} = 0.82\,\text{V}$.

Matrix		0	1	2	3
Pitch	(µm)	8.66 µm	10 µm	15 µm	20 µm
W03S1-1	(mV/ns)	40.6 ± 0.2	39.4 ± 0.2	37.5 ± 0.2	34.2 ± 0.1
W15S1-1	(mV/ns)	33.3 ± 0.1	32.9 ± 0.1	31.4 ± 0.6	30.8 ± 0.5

For the comparison of measurements from the first four matrices of the presented FASTPIX samples, the slopes of the fitted linear term are listed in Table 7.3. It can be used to approximate the basic relationship between ToT and pulser signal, especially for higher ToT regions where the non-linear term looses impact. The observed slope of the linear term of the model decreases with increasing pixel pitch, a trend that is most prominent for the sample W03S1-1.

Within a group of four matrices that share the same pixel design variant, which is the case for matrices 0 through 3, the collection electrode size is constant. The p-well opening size changes from 3 µm to 4.8 µm between 0.86 µm and 10 µm pitch. Stepping up to the 15 µm-pitch and 20 µm-pitch hexagonal grid, the pitch is the only changing parameter. With a constant collection electrode and p-well opening size the decrease in slope between the 10 µm, 15 µm and 20 µm pitch illustrates the impact of the pixel area on the effective pixel capacitance. A increased capacitance leads to higher gain which results in a larger observed ToT value at the same injected signal (v_{pulse}), assuming a similar electron-equivalent signal threshold at $i_{\text{thr}} = 0.82\,\text{V}$. In comparison with the standard process sample W03S1-1, the modified process sample W15S1-1 yields approximately 15 % smaller slope and a reduced dependency between pitch and observed slope.

Figure 7.7 shows the pulser signal over measured and extracted most-probable ToT values for the first 4 matrices of two samples from the same wafer, W18S1-3 and W18S1-4.
The resulting curves and fits for the first four matrices from a most-modified process sample with increased blanket n-layer doping follow similar trends. In these cases the data is filtered and the plotted data shows missing patches or does not extend to the maximum v_{pulse}. While the effect of a minimum detectable ToT can be observed at similar values, the change of slope with regard to the pixel pitch ist still present but manifests in a flipped configuration.
Again, enabling a comparison of the basic relationship between ToT and pulser signal, the slopes of the fitted linear term are listed in Table 7.4 for the first four matrices of the respective sample.

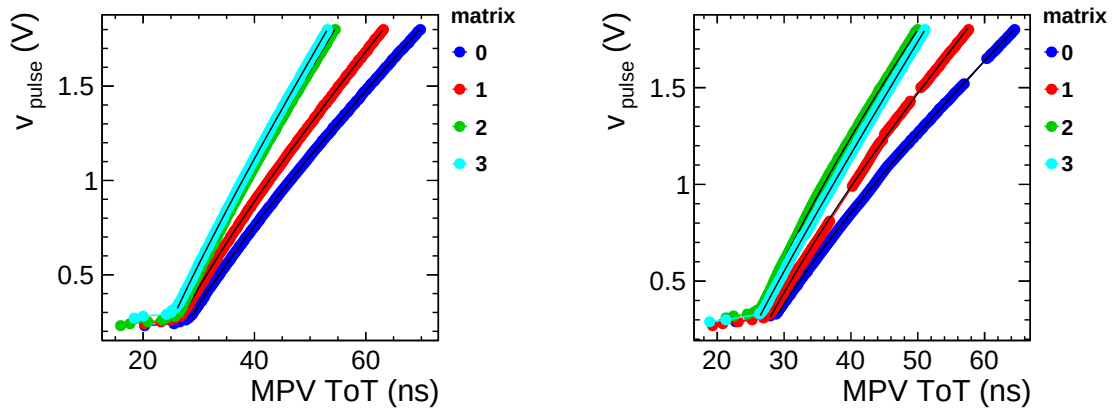

(a) W18S1-4. **(b)** W18S1-3.

Figure 7.7: Pulser signal over measured and extracted most-probable ToT for the first 4 matrices of a sample with minimal exposure to ionizing radiation (W18S1-4) and a sample (W18S1-3) heavily tested with X-ray source and pion beam, both operated at $i_{\text{thr}} = 0.82\,\text{V}$.

Table 7.4: Slope of the linear term from fit results for the first 4 matrices of a sample with minimal exposure to ionizing radiation (W18S1-4) and a sample (W18S1-3) heavily tested with X-ray source and pion beam, both operated at $i_{\text{thr}} = 0.82\,\text{V}$.

Matrix		0	1	2	3
Pitch	(µm)	8.66 µm	10 µm	15 µm	20 µm
W18S1-4	(mV/ns)	30.1 ± 0.1	33.6 ± 0.1	43.5 ± 0.1	47.3 ± 0.1
W18S1-3	(mV/ns)	32.0 ± 0.1	38.1 ± 0.4	44.6 ± 0.1	54.0 ± 0.1

In case of the W18S1 samples and contrary to Table 7.3, the observed slope of the linear term of the model increases with increasing pixel pitch.
Within a group of four matrices that share the same pixel design variant, which is the case for matrices 0 through 3, the collection electrode size is constant. The changes in pixel design variation are equivalent to the previously discussed samples from the standard and modified manufacturing process. During the measurements with W18S1, a smaller ToT value is observed for larger-pitch matrices at the same injected signal (v_{pulse}). In this case the assumption of similar electron-equivalent signal threshold at $i_{\text{thr}} = 0.82\,\text{V}$ is up for question, as the previous discussion of increased effective pixel capacitance and thereby increased gain still holds.

The non-linear function fitted to the data presents a model for the ToT response that covers the range of injected electrical test pulse signals and reaches down to the lowest measurable ToT. At this point of the calibration a precise link between the injected test pulse signal and its equivalent injected charge is obtained from measurements with photon sources.

Signal from Radioactive Sources
Further calibration of the FASTPIX time-over-threshold measurement is using radioactive sources containing the isotopes ^{55}Fe and ^{109}Cd. The measurement setup and methods are introduced in Section 6.5.1.

The calibration measurements rely on the absorption of photons within the sensitive volume of the sensor. The energy deposited by the absorbed photon can be directly related to the total number of electron-hole pairs created in silicon.
Since the expected most probable absorption depth in silicon increases with photon energy, the majority of ^{55}Fe X-ray photons are absorbed in the 25 µm thick epitaxial layer of FASTPIX. The higher-energy photons from the ^{109}Cd source interact significantly less likely. Therefore, the lower-energy source is the preferred choice considering trigger rate during measurement and the closer proximity in ToT to the already modeled set of pulse injection measurements.

Source data was recorded with sample W18S1-3, which was mostly tested in test beam. The ^{55}Fe source was used to cover the large parameter space of 32 matrices and 3 i_{thr} settings 0.3 V, 0.6 V and 0.7 V. The ^{109}Cd source was used for measurements of the first four matrices as well as all 20 µm-pitch matrices in quadrant 4 at the same three threshold settings. The nominal $i_{\text{thr}} = 0.82$ V was not included in the scanned set of threshold, as a noiseless data taking with all matrices on a given sample took a higher priority. Even with the larger share of higher-rate ^{55}Fe source measurements, the combined matrix and threshold scan for the entire FASTPIX sample extended over multiple weeks of continuous data taking.

The delay line calibration is the first step in the data-analysis chain for a newly set up measurement and is previously described in Section 5.6. It allows to attribute the discriminator pulse pairs within a recorded waveform to the pixel indices of the FASTPIX matrix. As long as every pixel of a matrix has recorded an identifiable hit, the delay lines can be calibrated. The ToT values are filtered from the measured data for all combinations of threshold voltage (i_{thr}) and matrix number (mb).

Figure 7.8a and Figure 7.8b show exemplary ToT distribution histograms and fits for a selection of 3 discriminator thresholds i_{thr}. The scanned i_{thr} values were chosen such that noise contributions to the measurement are an order of magnitude lower than the rate collected from the Fe55 source. The presented data was taken with the ^{55}Fe and ^{109}Cd source centrally positioned above the 20 µm-pitch matrix 3 of sample W18S1-3.
Similar to the analysis of the pulse injection data, a peak processing algorithm is applied to each histogram which identifies the most probable ToT value for a given set i_{thr}. The analysis strategy is largely the same, initially using the ROOT's `TSpectrum` class [88] to mark peak position bins, which then serve as a center of a sub-range of bins that provide the basic starting parameters for a Gaussian fit that is applied to each peak. The final ToT peak position value is the mean of the Gaussian fit, with the error on the resulting fit parameter as the error on the peak position.
The fit results for the selection of thresholds shown in Figure 7.8 are summarized in Table 7.5.

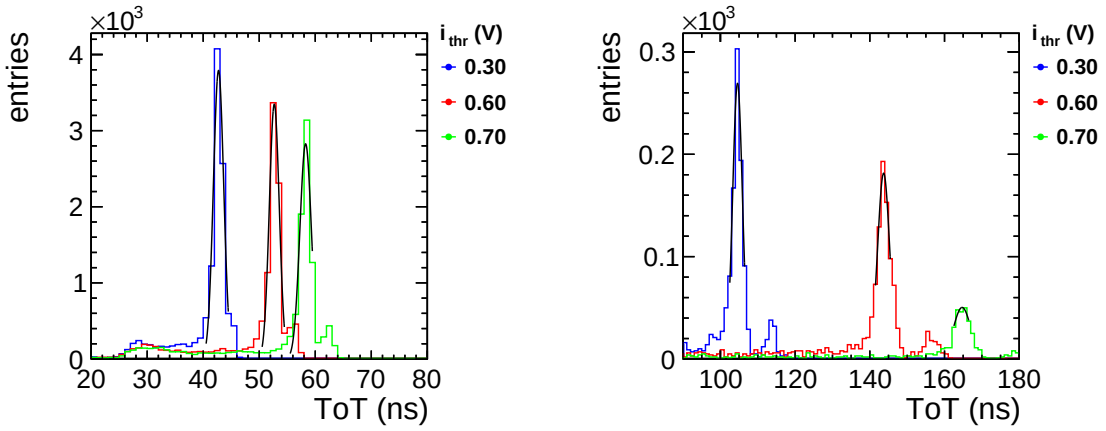

(a) Fe55. **(b)** Cd109.

Figure 7.8: Exemplary ToT data and fits for source measurements with matrix 3 of sample W18S1-3. 3 discriminator threshold settings i_{thr} are selected.

Table 7.5: Fit results for source measurements with matrix 3 of sample W18S1-3 at a selection of 3 discriminator threshold settings i_{thr}, illustrated by Figure 7.8.

(a) Fe55. **(b)** Cd109.

i_{thr}	(V)	0.30	0.60	0.70	0.30	0.60	0.70
μ	(ns)	42.74 ± 0.01	52.69 ± 0.01	58.28 ± 0.01	104.6 ± 0.1	143.7 ± 0.1	164.7 ± 0.3
σ	(ns)	0.92 ± 0.01	0.88 ± 0.01	1.02 ± 0.02	1.3 ± 0.1	1.6 ± 0.1	2.3 ± 0.5

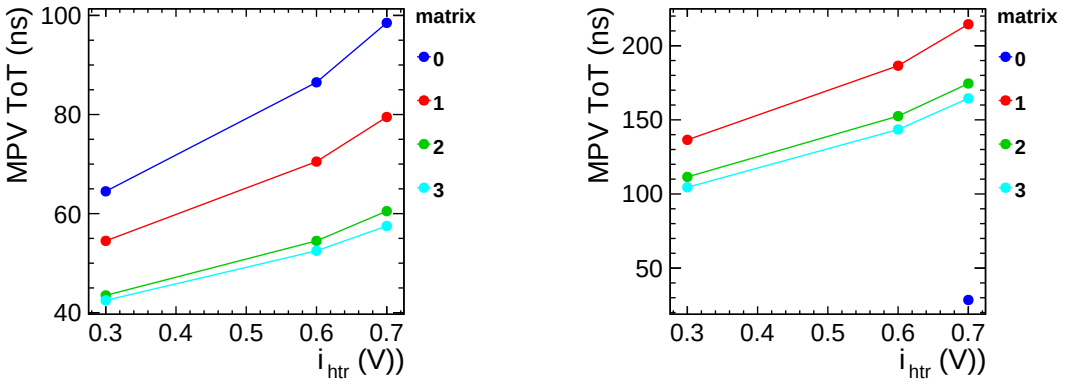

(a) Fe55 **(b)** Cd109

Figure 7.9: Most-probable ToT from irradiation with X-ray photons for the first 4 matrices of sample W18S1-3, predominantly characterized in test beam campaigns. The errors on the mean from the Gaussian fits of peaks in the ToT spectrum (Figure 7.8) are small compared to the scale of the plot.

An increase in i_{thr} corresponds to a decrease of the signal detection threshold at the discriminator stage of the FASTPIX frontend. Along with this, a larger share of the signal remains above threshold, increasing the observed ToT values. The collected data points are shown in

Figure 7.9. The slope represents the gain in measured ToT value per threshold step from a fixed-energy source.
The measured most-probable ToT links the deposited energy to an induced signal and ultimately an energy-equivalent observable. Consequently, a calibration of the ToT response across the range of injected electrical test pulse signals in Section 7.2.1 is possible.

The ToT range observed in pulse injection measurements is limited by the voltage v_{pulse} and results in maximum ToT values between 50 ns and 65 ns. The non-linear fit result can be used to calculate a voltage-equivalent of the most probable ToT value that is obtained from the source measurements. As the ToT response in regions well above 100 ns is not sufficiently represented by the fitted pulse injection data, the ^{55}Fe source is used to provide a point of reference for the energy calibration of the ToT. Dividing the signal expected from the X-ray photon absorption by the non-linear function evaluated at the same ToT value yields a calibration factor with unit e/V.

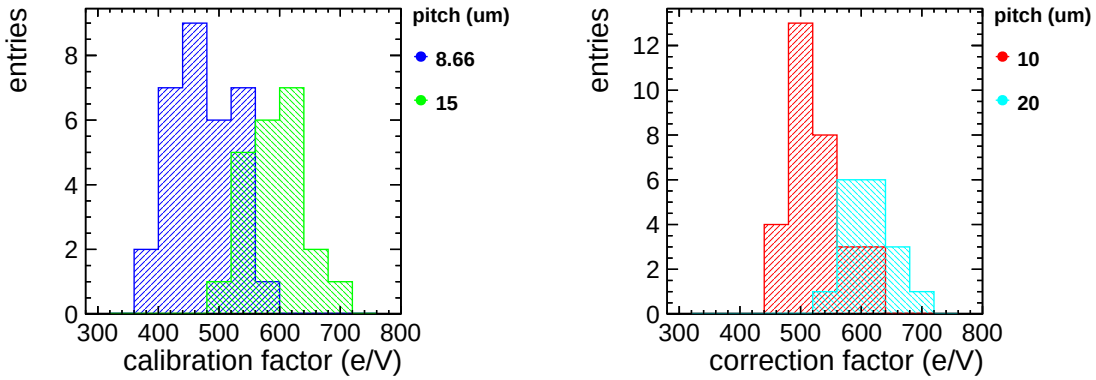

(a) 8.66 µm and 15 µm pitch.

(b) 10 µm and 20 µm pitch.

Figure 7.10: Distribution of test pulse capacitance correction factors k per pixel pitch for the combined measurements of both digital test pixels.

At every i_{thr} value that is share amongst the test pulse injection and the source data a calibration factor is calculated. The calibration factors are filled in histograms following the pitch of the matrices and form the distributions presented in Figure 7.10.

Table 7.6: Calibration factors k obtained as the means from Figure 7.10 and associated injection capacitance for all four pixel pitches. The RMS a measure of the dispersion Δk and is propagated to the capacitance.

Pitch	(µm)	8.66	10	15	20
k	(e/V)	474 ± 52	526 ± 42	595 ± 44	616 ± 43
C	(aF)	76 ± 8	84 ± 7	95 ± 7	99 ± 7

Table 7.6 summarizes the calibration factors and calculated injection capacitances. The calibration factors k are extracted as the mean of the distribution with the RMS as a measure of the dispersion Δk. The associated test pulse capacitance $C = k \times 1.6 \times 10^{-19}$, including the error $\Delta C = \Delta k \times 1.6 \times 10^{-19}$.

Applying the conversion factors to the data presented in Figure 7.6 and Figure 7.7 yields the final time-over-threshold calibration. Figure 7.11 shows the signal in electron over measured and extracted most-probable ToT values for the first 4 matrices of a standard and a modified process sample.

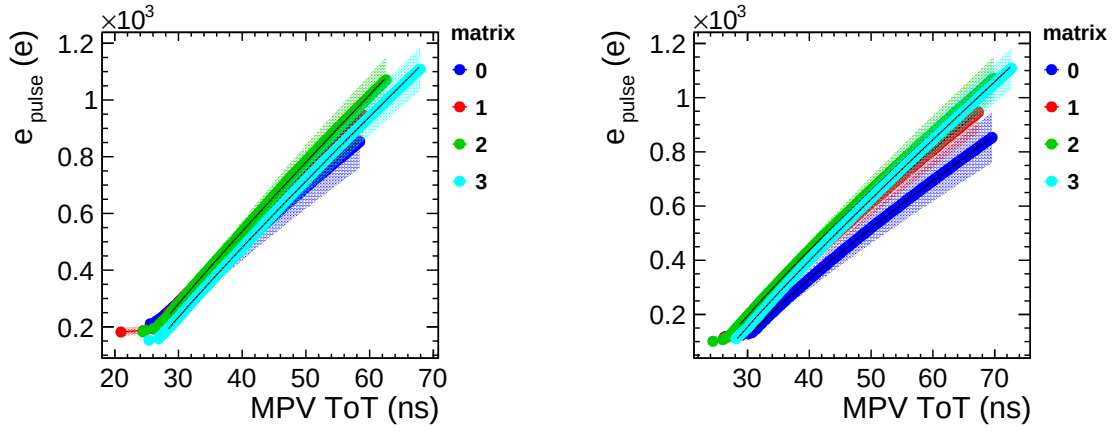

(a) W03S1-1. **(b)** W15S1-1.

Figure 7.11: Injected electrical signal vs. measured and extracted most-probable ToT for the first 4 matrices of a standard and a modified process sample, operated at $i_{\text{thr}} = 0.82\,\text{V}$. The uncertainty bands reflect the uncertainty on the calibration factors k.

Table 7.7: Slope of the linear term from fit results in Figure 7.11 for the first 4 matrices on a standard and a modified process sample, operated at $i_{\text{thr}} = 0.82\,\text{V}$.

Matrix		0	1	2	3
Pitch	(µm)	8.66 µm	10 µm	15 µm	20 µm
W03S1-1	(e/ns)	17 ± 1	18 ± 1	19 ± 1	19 ± 1
W15S1-1	(e/ns)	15 ± 1	17 ± 1	19 ± 1	20 ± 1

Table 7.7 summarized the slope of the linear term from fits in Figure 7.11 as a mean of comparison between both samples. For all scanned i_{thr} settings, the data recorded with either one of the two test pixel indices (pb) is merged. Data points are compared based on common v_{pulse} voltages set during the pulse injection scan. For matching data points, the mean ToT value between both test pixels is calculated with an error propagated as the root mean square of the individual errors.

To quantify the difference in ToT response between both test pixels, the absolute difference in measured ToT between matched v_{pulse} points is plotted. Figure 7.12a present an exemplary distribution with a peak fitted by a Gaussian model. The tails of the distribution originate in different behaviors of the data close to the minimum measurable ToT value as well as a difference in the non-linear term.
The results of similar Gaussian fits are summarized by Figure 7.12b for the first four matrices of most-modified-process sample W18S1-3. The mean of all matrices on the particular sample yields 0.9 ± 0.3 ns.

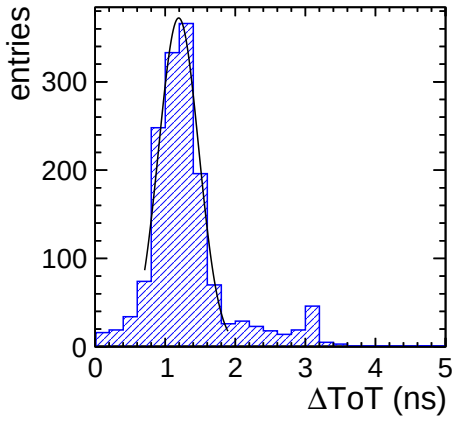

(a) Exemplary distribution for 20 µm-pitch matrix 3

Matrix	μ (ns)	σ (ns)
0	0.81 ± 0.01	0.27 ± 0.01
1	1.03 ± 0.01	0.34 ± 0.01
2	0.58 ± 0.01	0.37 ± 0.01
3	1.19 ± 0.01	0.28 ± 0.01
All	0.9 ± 0.3	

(b) for the first four matrices.

Figure 7.12: Absolute difference in ToT response for matching injection signal v_{pulse} between both test pixels of the first four matrices on most-modified-process sample W18S1-3. The data is combined for all scanned i_{thr} settings. The black line illustrates the fitted Gaussian model.

In case of a malfunctioning or unresponsive test pixel, the data of the remaining, functional pixel is used for further analysis.

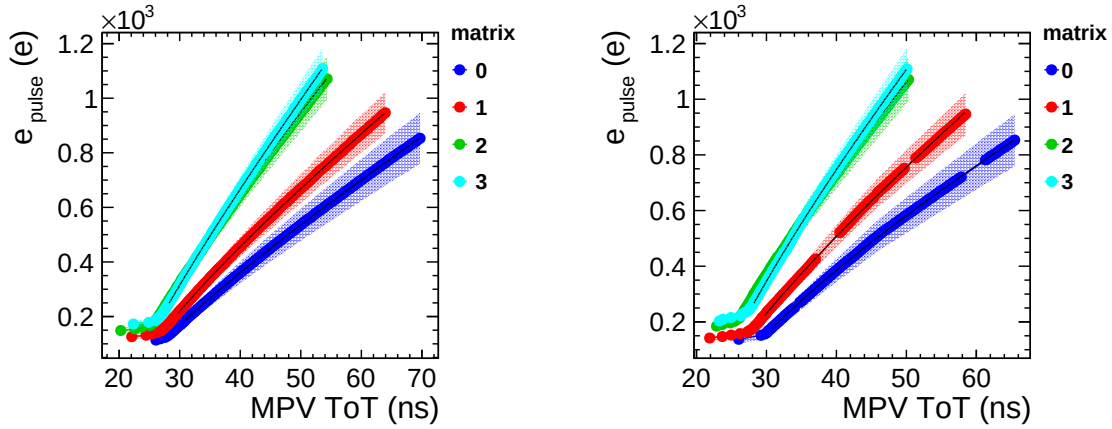

(a) W18S1-4.

(b) W18S1-3.

Figure 7.13: Injected electrical signal over measured and extracted most-probable ToT for the first 4 matrices of a sample with minimal exposure to ionizing radiation (W18S1-4) and a sample (W18S1-3) heavily tested with X-ray source and pion beam, both operated at i_{thr} = 0.82 V.

The merged data is again fitted with the non-linear model from Section 7.2.1. Figure 7.13 shows the signal in electron over measured and extracted most-probable ToT values for the first 4 matrices of a sample with minimal exposure to ionizing radiation (W18S1-4) and a sample (W18S1-3) heavily tested with X-ray source and pion beam.
The fit results encompass the relationship of measured ToT to the injected signal amplitude spanning a range between the lower limit on ToT measurement and the maximum amplitude set with v_{pulse} = 1.8 V.

The slopes of the fitted model are listed in Table 7.8 and can be used to approximate the basic relationship between ToT and pulser signal for higher ToT values that will be observed e.g. in test beam measurements. The observable trends and effects match the discussion for Figure 7.6 and Figure 7.7.

Table 7.8: Slope of the linear term from fit results in Figure 7.13 for the first 4 matrices of a sample with minimal exposure to ionizing radiation (W18S1-4) and a sample (W18S1-3) heavily tested with X-ray source and pion beam, both operated at $i_{\text{thr}} = 0.82\,\text{V}$.

Matrix		0	1	2	3
Pitch	(µm)	8.66 µm	10 µm	15 µm	20 µm
W18S1-4	(e/ns)	15 ± 2	18 ± 2	26 ± 3	29 ± 3
W18S1-1	(e/ns)	15 ± 2	21 ± 3	28 ± 4	30 ± 4

Signal from X-ray Fluorescence

Compared to the limited availability of radioactive sources for an energy calibration measurement, X-ray fluorescence photons can provide additional calibration points across a more divers spectrum of energies at higher particle rate.

The machine as well as the setup used to acquire data from secondary fluorescence X-rays was previously introduced in Section 6.5.2 and, on the side of the FASTPIX DAQ, is equivalent to the setup used for radioactive source measurements. The interaction of a primary beam with various secondary targets results in a distinct energy spectrum that is characteristic of the selected secondary target material. For tests with FASTPIX, target samples made from natrium, aluminum, titanium and iron were placed in the machine.

A selected matrix (mb) is configured to scan a range of global threshold settings (i_{thr}), recording a spectrum of the given fluorescence emission line per i_{thr}. The data analysis approach is inherited from Section 7.2.1.

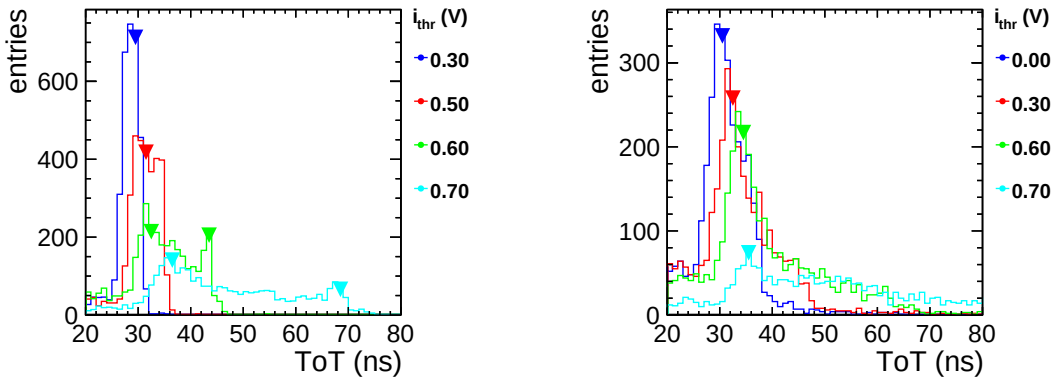

(a) Titanium target. **(b)** Without target.

Figure 7.14: Exemplary ToT spectra from X-ray measurements with matrix 3 of sample W03S1-1. Four discriminator threshold settings i_{thr} are selected, color-coded as assigned by the legend. Triangular markers indicate the identified peaks of the spectra.

The ToT spectrum holds the distribution of measured durations for which the signal amplitude was registered above threshold, exemplified by Figure 7.14.
Both plots present binned ToT values above 20 ns. Peaks in the spectrum are identified by the peak processing strategy that was already previously applied for similar spectra during the analysis of the pulse injection and radioactive source data. The exemplary ToT spectra from X-ray measurements contain triangular markers that indicate identified peak bins.
ToT spectra in both sets of four i_{thr} settings contain two peaks, one dominant peak around 30 ns and lower-statistic peak at higher ToT. For i_{thr} settings below 0.5 V both peaks are merged and appear as a singular dominant peak. The dominant peak at low ToT values is the result of a heightened noise level during the operation of the FASTPIX setup inside the X-ray machine. The noise peak is cut towards low ToT values at 25 ns to 30 ns, depending on the set i_{thr} as a consequence of the minimum-measurable ToT, previously observed during pulse injection measurements.
In a narrow threshold range between 0.5 V and 0.7 V the peaks appear separated and can not be identified reliably within the spectrum. While the dominant peak only moves by approximately 20 ns/V the lower-statistic peak moves towards higher ToT values with 180 ns/V. In the small i_{thr} window where both peaks can be distinguished from each other, the peak positions could not successfully be attributed to emission lines of the individual target materials.

The dominant noise peak remains present in the reference measurement without target. Low-energy background and interference inside the machine could neither be mechanically shielded nor deconvoluted in analysis to a point where a ToT calibration from the acquired data is possible. The decision was made against further calibration efforts with X-ray fluorescence photons in the available machine and setup.

7.2.2. Discriminator Threshold

The determination of the signal-equivalent of a given threshold voltage i_{thr} is part of the energy calibration and enables a comparison of spatial, temporal as well as efficiency observables between the 32 matrixes of a singular FASTPIX sample. The threshold level with respect to the recorded single pixel signal is located by evaluating the detection efficiency as the signal crosses the threshold.

Test Pulse Signal Injection
A laboratory calibration of the discriminator threshold can be achieved by using the injection of electrical test pulses into the FASTPIX frontend circuitry. The associated analysis is based on the same set of pulse injection data that was previously presented in context of the ToT-to-energy calibration. The measurement setup is introduced in Section 6.4.3.

For all combinations of threshold voltage (i_{thr}), pixel number (pb), and pulse injection voltage (v_{pulse}), 250 triggered pulses are recorded by the oscilloscope readout before the next test pulse voltage is configured through Caribou. Contributions from fake hits are filtered up to O(MHz) by the auxiliary trigger signal that is generated by the pulse generator. Compared to a setup that directly triggers on a FASTPIX LVDS output signal, the pulse injection measurement is able to scan an extended i_{thr}-range into lower threshold regimes without over-estimating

detection efficiency at the turn on of the S-curve.

The number of recorded pulses and the number of triggered pulses are filled into the bins of an individual efficiency histogram for each recorded i_{thr}. Figure 7.15 and Table 7.9 present the data and fits for an exemplary set of 5 i_{thr} settings, respectively.

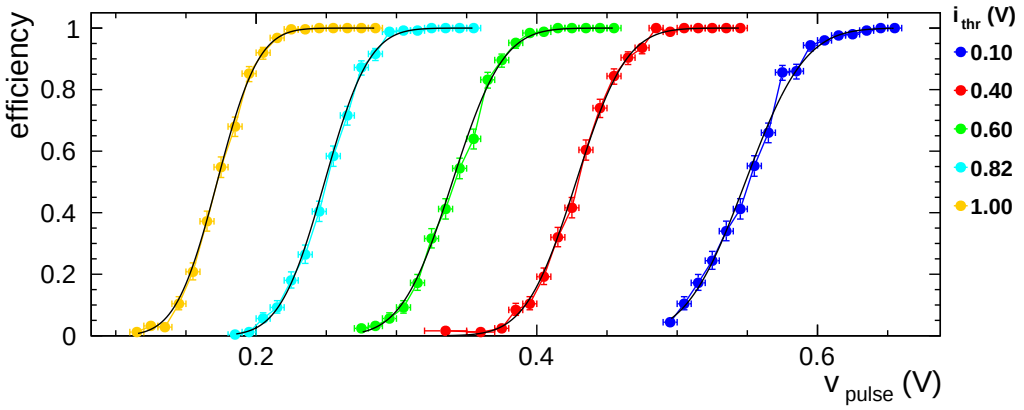

Figure 7.15: Exemplary S-curve data and fits for 20 µm-pitch matrix 3 of sample W18S1-3 at a selection of 5 thresholds i_{thr} (V), color-coded as assigned by the legend. The plotted data was taken with test pulse pixel pb 3.

Table 7.9: Exemplary fit results for 20 µm-pitch matrix 3 of sample W18S1-3 at a selection of 5 thresholds i_{thr} (V). The plotted data was taken with test pulse pixel pb 3.

i_{thr}	(V)	1.0	0.82	0.6	0.4	0.1
μ_{thr}	(V)	0.172 ± 0.002	0.249 ± 0.002	0.340 ± 0.002	0.428 ± 0.002	0.549 ± 0.002
σ_{thr}	(V)	0.023 ± 0.001	0.025 ± 0.001	0.028 ± 0.001	0.028 ± 0.001	0.033 ± 0.002

An S-curve is fitted to all efficiency histograms using an error function model, where μ_{thr} locates the point of 50 % efficiency and σ_{thr} gives a measure of the single-channel frontend noise that broadens the S-curve.
The width of the S-curve increases with decreasing i_{thr}, an approximately 45 % increase in frontend noise across the exemplified range of thresholds. In the FASTPIX frontend the signal gain is not constant but changes with the voltage i_{thr}, which has an impact on the observed noise at a given threshold.
The fit result is consistent with previous observables. Interpolating the values in Table 7.2 the width at i_{thr} equates to a σ_{ToT} of 0.51 ± 0.03 ns. The slope in Table 7.3 provides a $\approx 54.0 \pm 0.1\,\text{mV ns}^{-1}$ conversion from ToT in nanosecond into the equivalent pulser voltage. Finally the width of the ToT peaks equates to $\approx 28 \pm 2$ mV which is in good agreement with the width of the threshold turn-on $\sigma_{\text{thr}} = 28 \pm 1$ mV listed in Table 7.9.
The fast shaping analog frontend reduces noise contribution from leakage current and thermal noise of the frontend therefore dominates the noise on the signal. A more detailed investigation into the noise performance of FASTPIX matrices follows in Section 7.3.

Further graphs are created to visualize the relationship between the pulser signal e_{pulse} and threshold voltage i_{thr}. Figure 7.16 illustrates the data taken with a standard process sample

and a modified process sample.

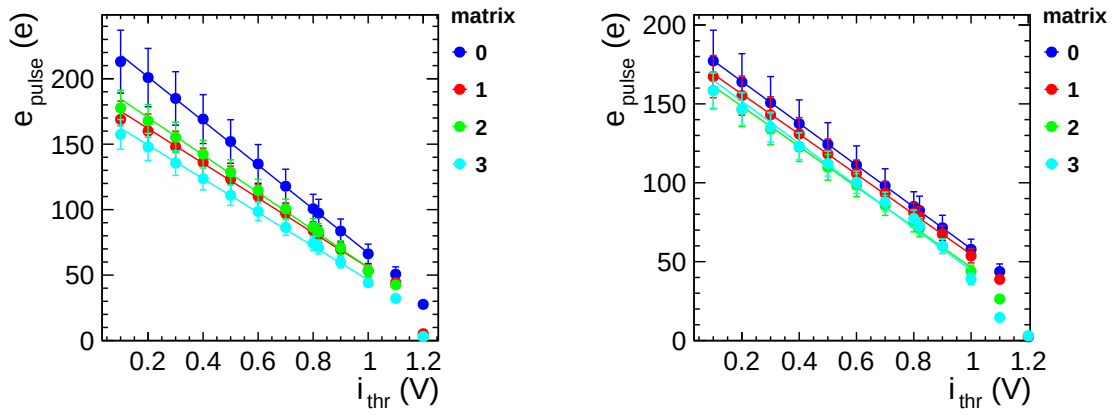

(a) W03S1-1. **(b)** W15S1-1.

Figure 7.16: Pulser signal vs. threshold voltage i_{thr} for the first 4 matrices of a standard and a modified process sample. The plotted data was taken with test pulse pixel pb 3. A linear fit is applied between 0.1 and 1 V i_{thr}. The error bars reflect the uncertainty on the calibration factors k.

The values between 0.1 V and 1 V are fitted with a linear model to asses the relationship between the discriminator threshold level and the injected signal equivalent. The results from these fits in Table 7.10 provide the basis for a threshold calibration in the selected threshold range.

Table 7.10: Fit result for the first 4 matrices of a standard and a modified process sample, illustrated in Figure 7.16.

Matrix		0	1	2	3
Pitch	(µm)	8.66	10	15	20
W03S1-1	(e/V)	-168 ± 16	-133 ± 9	-143 ± 9	-129 ± 7
W15S1-1	(e/V)	-133 ± 13	-130 ± 9	-127 ± 8	-126 ± 7

The conversion of the voltage used to charge the injection capacitance to its equivalent signal in electrons is calibrated in Section 7.2.1. The signal is calculated utilizing the conversion factors in Table 7.6. The errors reflect the propagated uncertainty on the calibration factors k.

For all presented samples, the data is in good agreement with the linear model. At i_{thr} settings above 1 V, noise contributions deform the lower half of the efficiency turn-on and pull the fitted μ_{thr} towards smaller v_{pulse} values. On the standard process sample W03S1-1 as well as the modified process sample W15S1-1, the first four matrices do not exhibit significant differences in slope outside of the uncertainty on the plotted signal. The two samples largely match in their overall threshold signal response.

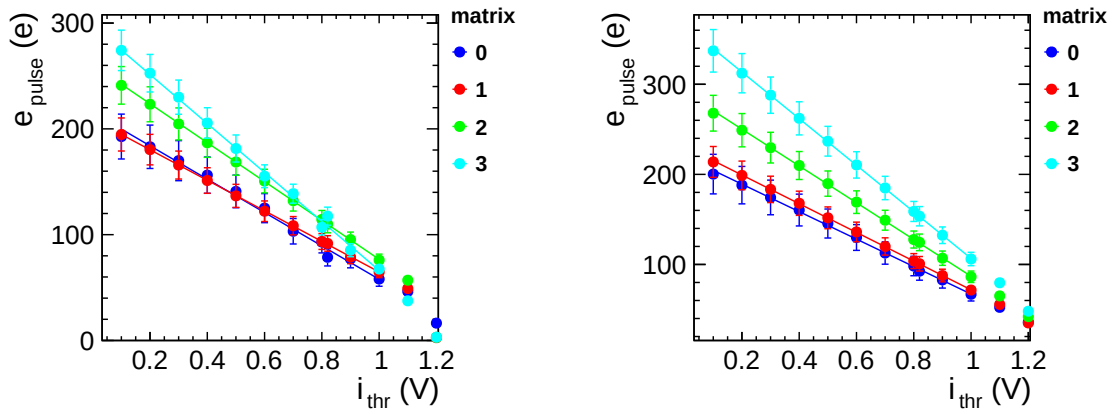

(a) W18S1-4. **(b)** W18S1-3.

Figure 7.17: Pulser signal over threshold voltage i_{thr} for the first 4 matrices of a sample with minimal exposure to ionizing radiation (W18S1-4) and a sample (W18S1-3) heavily tested with X-ray source and pion beam, both operated at $i_{\text{thr}} = 0.82\,\text{V}$.

Table 7.11: Slopes from linear fit results for the first 4 matrices of sample W18S1-4 and sample W18S1-3, illustrated in Figure 7.17.

Matrix		0	1	2	3
Pitch	(µm)	8.66 µm	10 µm	15 µm	20 µm
W18S1-4	(e/V)	-158 ± 14	-150 ± 11	-184 ± 12	-231 ± 12
W18S1-3	(e/V)	-153 ± 15	-159 ± 12	-204 ± 13	-259 ± 17

Figure 7.17 completes the energy calibration of the discriminator threshold by showing data taken with the samples W18S1-3 and W18S1-4. Similar to before, the slopes from linear fit results between 0.1 V and 1 V are listed in Table 7.11 for the selected four matrices. While the 8.66 µm-pitch and 10 µm-pitch match the results from W03S1-1 and W15S1-1 within the uncertainties of the signal conversion, both larger-pitch matrices of this exemplary selection stand out with a significant difference in slope. The 15 µm-pitch matrix 2 yields a ≈40 e/V higher slope, followed by an increase of another ≈50 e/V for the 20 µm-pitch matrix 3.

Signal from Radioactive Sources

A location of the threshold level with respect to the recorded single pixel signal is not possible with either one of the radioactive sources, previously used in Section 7.2.1. Similar to the approach applied for the injected test pulse signal, such a measurement entails a scan of the discriminator threshold surrounding the expected 1640 e and 6530 e signal (Table 6.3) for ^{55}Fe and ^{109}Cd, respectively. In Section 7.2.2 the maximum signal threshold at $i_{\text{thr}} = 0.0\,\text{V}$ was only found to reach signals in the order of 300 e. Based on this result, the FASTPIX threshold range does not extend above the x-ray photon signals.

Signal from X-ray Fluorescence

Similar to Section 7.2.1 X-ray fluorescence can provide additional calibration points at higher particle rate. The X-ray machine as well as the setup used to acquire data from secondary fluorescence X-rays was previously introduced in Section 6.5.2 and discussed during the

evaluation of X-ray fluorescence ToT spectra.

During data taking, the observed hit rate predominantly relies on the probability of photon absorption within the sensitive, depleted volume of the sensor. Based on Table 6.4, the X-ray fluorescent photons emitted from the NaCl and the Al target are expected to be fully absorbed within the 25 µm thick epitaxial layer of FASTPIX.The same applies for a large share of photons from the Ti and the Fe target. The higher-energy K_α lines exceeds the thickness of the epitaxial layer and interact less likely with increasing emission energy.
When starting at a threshold above the signal energy, the hit rate increases as the threshold is lowered into the turn-on that is observed when crossing the K_α line of the installed target. The continuos, trigger-less readout of FASTPIX implies that run time is not constant and changes with the inverse of the hit rate. The oscilloscope readout is setup to define the end of a run after 4000 waveforms are recorded in buffer. For every i_{thr} setting in a range between 0.0 V and 1.2 V the total measurement time is extracted based on the oscilloscope timestamps that are associated with the total number of recorded hits.
The delay line calibration, previously described in Section 5.6, attributes the discriminator pulse pairs within a recorded waveform to the pixel indices of the FASTPIX matrix. Waveforms with only one pair of pulses on each of the three LVDS outputs of FASTPIX are declared as single pixel hits. In these cases the charge deposited by an X-ray photon is collected by a single pixel.

Figure 7.18 examines how the rate of single-pixel hits changes with threshold during the measurements with a given target.

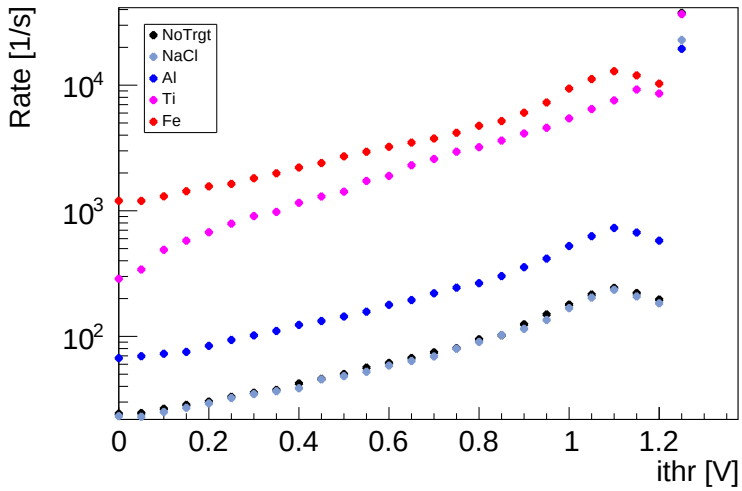

Figure 7.18: Recorded hit rate in x-ray measurements with matrix 3 of sample W03S1-1, scanning the full threshold range.

The observed rates show a clear separation between the data sets from individual targets, except NaCl which does not differ from the rate observed without target. None of the curves show changes in rate that are indicative of the detection threshold crossing the energy of the emitted X-ray fluorescence photons. Neither the evaluation of the derivative nor an additional subtraction of the background measured without a target was able uncover further features.

The deposited charge in silicon from an irradiation with X-ray fluorescence photons is estimated in Table 6.4. None of the available targets provide low enough peak energies that would enable a location of the discriminator threshold level with respect to the recorded single pixel signal. Low-energy targets are covered by the noise observed in the X-ray machine environment.

7.3. Noise Characterization

The few fF collection-electrodes of the FASTPIX sensor design translate to a small frontend input capacitance and result in low noise levels compared to the processed signal amplitude. Consequently, the frontend circuitry poses as the main contributor of the observed signal noise.

7.3.1. Test Pulse Signal Injection

Noise contributions to the signal were first observed as the width of pulse injection efficiency S-curves in Figure 7.15. Figure 7.19 shows the width of the fitted error function model plotted against the set threshold voltage i_{thr} for FASTPIX samples manufactured in the standard CMOS process and the modified CMOS process.

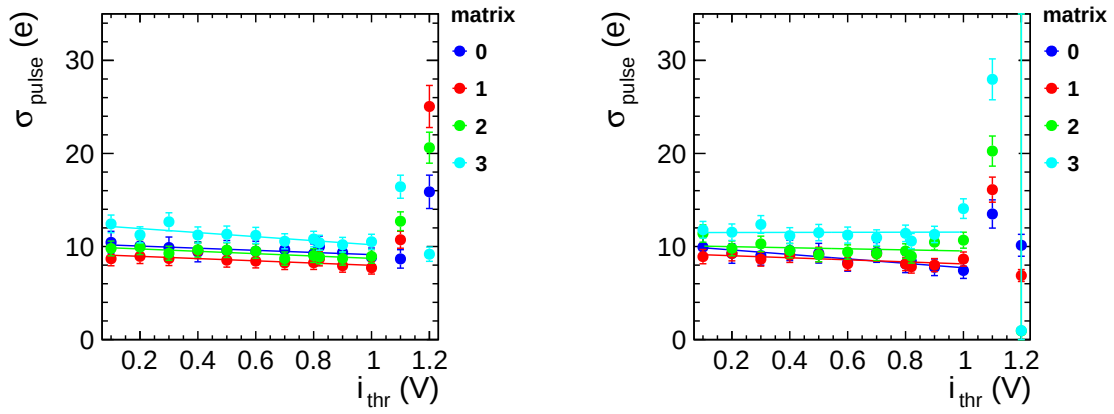

(a) W03S1-1. **(b)** W15S1-1.

Figure 7.19: Noise during test pulse signal injection over threshold voltage i_{thr} for the first 4 matrices of a standard and a modified process sample. The plotted data was taken with test pixel pb 3. A linear fit is applied between 0.1 and 1 V i_{thr}.

Table 7.12: Slope values extracted from fit results in Figure 7.19 for the first 4 matrices of a standard and a modified process sample, illustrated in Figure 7.16.

Matrix		0	1	2	3
Pitch	(µm)	8.66	10	15	20
W03S1-1	(e/V)	-1.1 ± 1.1	-1.2 ± 0.8	-1.3 ± 0.8	-2.2 ± 0.9
W15S1-1	(e/V)	-2.3 ± 1.0	-1.1 ± 0.8	-0.6 ± 0.9	-0.1 ± 1.0

A linear model is fitted to the data and allows an evaluation of trends in gain over the

measured threshold range. The slopes of the fitted linear model are listed in Table 7.12 for samples from the standard process and a modified process wafer.
In both cases, the noise does not exhibit drastic changes between the measurements at i_{thr} values ranging from 0.1 V to 1.0 V. The resulting slope is consistent across all four matrices within the uncertainty on σ_{pulse}, which is dominated by the uncertainty on the conversion factor extracted in Section 7.2.1. The observed noise level is increased for larger pixel pitch and consequently larger collection electrode size. In measurements with either one of the two samples, the noise of the 20 µm-pitch matrix 3 is raised above the three smaller-pitch matrices, that do not show significant differences outside of the uncertainty on σ_{pulse}.
For measurements at $i_{\text{thr}} > 1.0$ V the width of the efficiency turn-on increases. In this threshold range an increasingly high rate of fake hits is registered in addition to the externally triggered LVDS pulse pairs from signal injection.

Figure 7.20 shows the width of the fitted error function model over the set threshold voltage i_{thr} for two FASTPIX samples manufactured in the most-modified process.

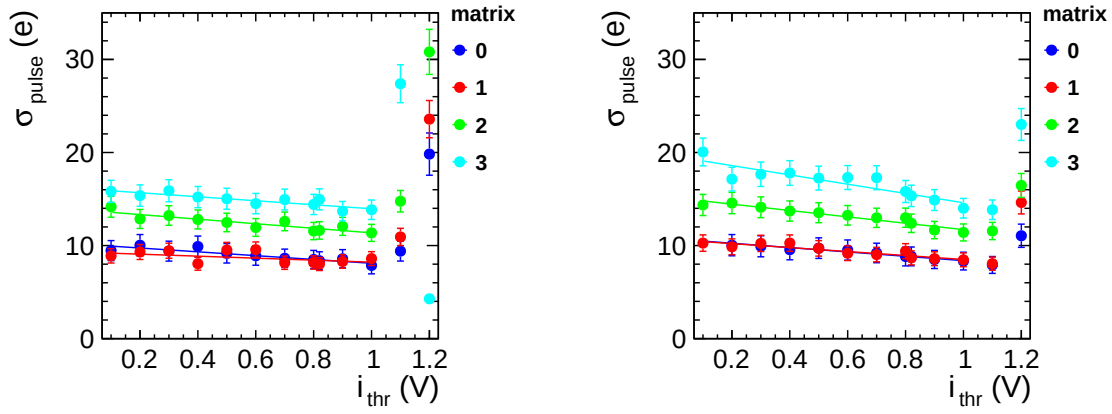

(a) W18S1-4. **(b)** W18S1-3.

Figure 7.20: Noise during test pulse signal injection over threshold voltage i_{thr} for the first 4 matrices of a sample with minimal exposure to ionizing radiation (W18S1-4) and a sample (W18S1-3) heavily tested with X-ray source and pion beam, both operated at $i_{\text{thr}} = 0.82$ V.

Table 7.13: Slope values extracted from fit results for the first 4 matrices of sample W18S1-4 and sample W18S1-3, illustrated in Figure 7.17.

Matrix		0	1	2	3
Pitch	(µm)	8.66	10	15	20
W18S1-4	(e/V)	-2.1 ± 1.1	-1.0 ± 0.8	-2.5 ± 1.0	-2.1 ± 1.2
W18S1-3	(e/V)	-2.3 ± 1.3	-2.1 ± 0.9	-3.4 ± 1.1	-5.0 ± 1.3

The slopes of the fitted linear model are listed separately in Table 7.13. For all matrices on both modified process samples, the noise increases with decreasing i_{thr} values. A change in noise across the scanned i_{thr} is an indicator of changing signal gain. The reason for this dependency is found in the FASTPIX frontend, specifically in the way the threshold is applied, a characteristic that all matrices have in common, independent of the CMOS process. The

signal amplitude is compared to a fixed reference level. In order to set a threshold, the gain of the pulse at the input of the voltage comparator is varied. Reducing the signal gain in order to apply a higher signal threshold gives more weight of the subsequent thermal circuitry noise, an effective increase in noise at lower i_{thr} values.

While a dependency of slope on pixel pitch is not obvious, a difference in noise level between different pixel-pitch matrices can be observed. The similarly sized 8.66 µm-pitch and 10 µm-pitch matrices do not differ in overall noise level. In relation to the two matrices of smaller pitch, 15 µm-pitch matrix 2 and 20 µm-pitch matrix 3 are offset towards higher noise levels by approximately 4 e and 6 e, respectively. The increased noise level goes along with a ≈25 % and ≈50 % higher gain for matrix 2 and matrix 3 of sample W18S1-3 in Table 7.11. The observed increase in noise level with pixel pitch is emphasized by the higher doping of the blanket deep n-layer in the most-modified process, as a comparison of Figure 7.19b and Figure 7.20a shows.

The difference in noise performance between two samples from the same wafer is exemplified in Figure 7.20. In comparison, 8.66 µm-pitch and 10 µm-pitch matrices show similar results. An increased noise of around 2 e is found for the 15 µm-pitch and 20 µm-pitch matrices of W18S1-3. Based on the measurements with W18S1-3, the origin of the higher overall noise share of the electrically injected test pulse signal can not be solely attributed to extensive tests with X-ray sources and in test beams. The conducted laboratory measurement campaign is not able to deconvolute sample-to-sample variations based on the small number of tested samples.

A comparison between all matrices on a standard-process and a modified-process sample is presented by Figure 7.21 at a common threshold setting of $i_{\mathrm{thr}} = 0.82\,\mathrm{V}$. The equivalent threshold in electrons is given in form of a small label above each plotted σ_{pulse} value.

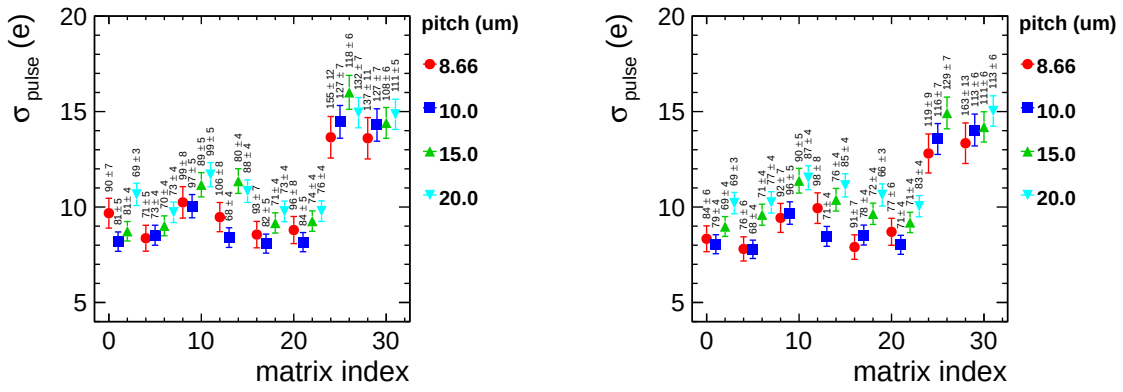

(a) W03S1-1. **(b)** W15S1-1.

Figure 7.21: Mean frontend noise at $i_{\mathrm{thr}} = 0.82\,\mathrm{V}$ for all matrices on a standard and a modified process sample. The mean represents results from both pulsed digital test pixel with propagated error on the mean.

For every group of four consecutive matrix indices a certain pixel design variation is implemented in one of four pixel pitches, as indicated by the color scheme. The overview in

Figure 5.14 illustrates the differences in design parameters and the combinations implemented for all 32 matrices.

Across all 8 pixel variants, the frontend noise agrees with the trends observed in Figure 7.19 and Figure 7.20 for the first four matrices across the whole scanned threshold range.
Within a group of four matrices that share the same pixel design variant, the collection electrode size is constant. The p-well opening size changes between 0.86 µm and 10 µm pitch, which in most pixel design variants has no significant effect on the observed noise within its uncertainty. During the steps to the 15 µm-pitch and 20 µm-pitch hexagonal grid, the pitch is left as the only changing parameter. With a constant collection electrode and p-well opening size the increase in noise between the 10 µm, 15 µm and 20 µm pitch illustrates the impact of the pixel area on gain and ultimately on the noise performance.

The observed noise performance at nominal threshold divides the matrices in two groups. Matrices 0 to 23 at a lower level and matrices 24 to 31 at a raised level of frontend noise despite a larger signal threshold in electrons. The latter group of matrices is characterized by a larger 2.0 µm collection electrode size, the largest p-well opening size implemented in their pitch-quadrant and a full deep n-implant geometry without corner gaps. The increased p-well opening size in combination with a full deep n-implant geometry in combination with a 0.86 µm collection electrode is implemented in matrices 16 to 19, all measuring a low level of frontend noise. Increasing the collection electrode size by approximately a factor 2 equally doubled the observed noise for the respective matrices.
Matrices 8 to 11 also show increased noise due to a similar effect. In comparison with 24 through 27, only collection electrode size is increased while the other parameters are unchanged with regard to the preceding pixel design variant.

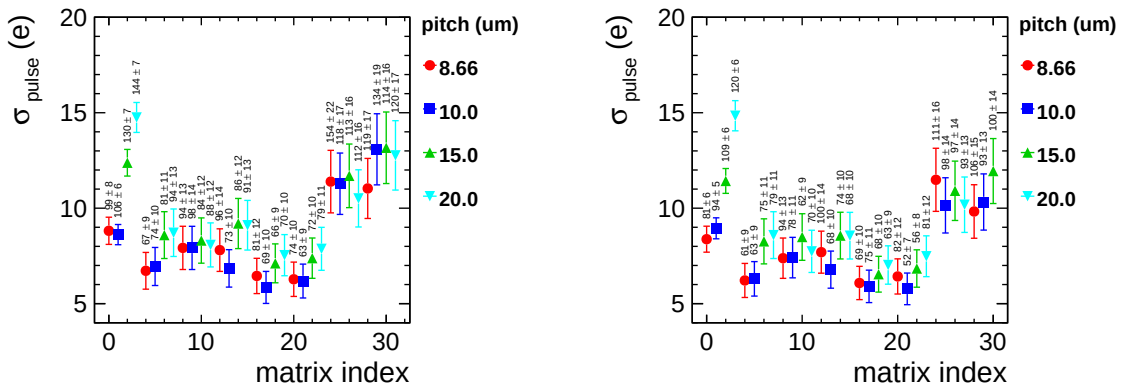

(a) W18S1-3. **(b)** W18S1-4.

Figure 7.22: Mean frontend noise at $i_{\mathrm{thr}} = 0.82\,\mathrm{V}$ for all matrices on two samples from most-modified process wafer W18. The mean represents results from both pulsed digital test pixel with propagated error on the mean.

The introduction of a higher doped blanket n-layer in sample W18S1-3 reduces the overall frontend noise by approximately 2 e. The characteristics found within the results for W03S1-1 and W15S1-1 also translate to the most-modified process sample W18S1-3, within the uncertainties on the extracted noise values.

7.3.2. Pixel Noise Scan

Another approach to the characterization of the noise behavior of a FASTPIX matrix uses the setup and methods discussed in Section 6.4.2. Without the detector being exposed to a direct source of signal, the observed count of fake hits per measurement time is equivalent to the noise rate. The rate increases as i_{thr} is increased and the threshold for the discriminated signal is lowered.

Fake hits are recorded at 20 i_{thr} settings between 0.7 V and 1.2 V, where up to 0.8 V the voltage is increased in steps of 0.1 V, followed by two finer steps of 0.04 V and eventually 0.02 V for the remaining range. The data acquisition is stopped either after a 10 min measurement duration or as soon as 4000 triggers have been recorded by the oscilloscope readout for a given matrix. The measurements are conducted under standard laboratory conditions.
As long as every pixel has registered a signal at one of the scanned thresholds, the delay line calibration, previously described in Section 5.6, is applied to the data and successfully links the extracted waveform observables to the pixel indices of the FASTPIX matrix. Singular missing, unresponsive pixels either are malfunctioning or experience fake hits outside of the scanned threshold range. To an extend, missing pixels are filled in by using symmetries between the two halves of the series of 100 ns delays in a delay line. If $\mathcal{O}(5)$ unresponsive pixels are observed, the delay line calibration fails to correctly link the full series of pixels with the measured delays.

Noise rates and associated uncertainties are investigated per threshold for the full matrix as well as the single pixels from subsets of measurement data. The noise rate is calculated from the number of events within the elapsed measurement duration. The statistical error dominates the uncertainty on the rate.
Measurements covering a larger threshold range illustrate the dependence of noise rate on detection threshold. The calibrated delay line pixel index allows to isolate singular pixels during the rate calculation.

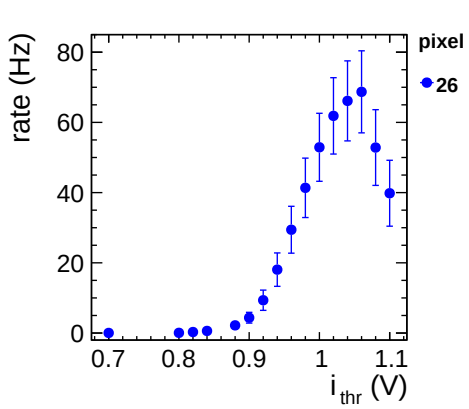

(a) Pixel 26: noise rate over i_{thr}.

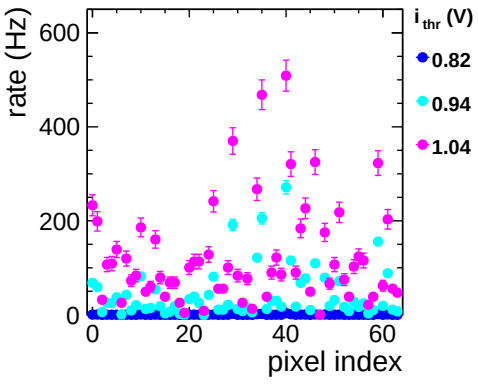

(b) Noise rate over pixel index for a selection of three i_{thr} settings.

Figure 7.23: Single pixel noise rate of matrix 3 on samples W18S1-3. The error bars correspond to the statistical uncertainty of the rate measurement.

The increase in noise rate with decreasing signal detection threshold is exemplified by

Figure 7.23a for the centrally located pixel number 26 of a 20 µm-pitch matrix.
Noise remains undetected as long as the detection threshold is above the amplitude of fluctuations at the output of the analog amplification stage. As the threshold is lowered towards the noise, the rate of fake hits increases and eventually starts to saturate towards the end of the scanned threshold range. The FASTPIX comparator and digitization logic requires a signal transition across threshold for a pair of pulses to be propagated onto the delay lines. By moving the system into the noise a majority of pixels will no longer cross below the threshold and the observed count rate decreases.

Figure 7.23b shows the noise rate for each pixel index across a matrix in ascending order, allowing for the identification of pixels with anomalously high or low noise rates.

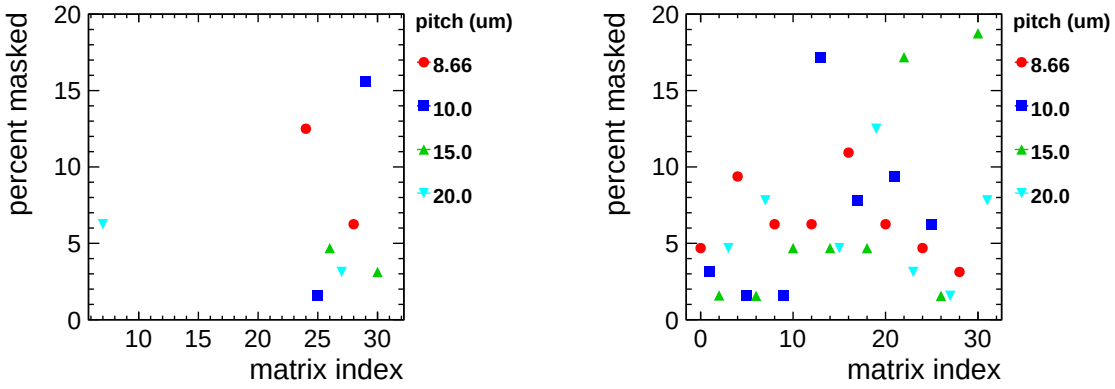

(a) W03S1-1. **(b)** W15S1-1.

Figure 7.24: Percentage of masked pixels per matrix on a standard and modified process samples from W18S1 at a threshold of $i_{\text{thr}} = 0.82\,\text{V}$.

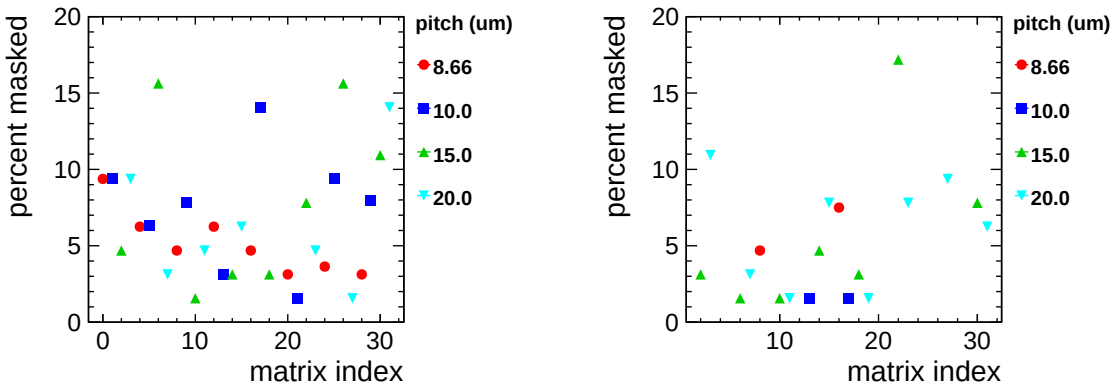

(a) W18S1-3. **(b)** W18S1-4.

Figure 7.25: Percentage of masked pixels per matrix on two sample at a threshold of $i_{\text{thr}} = 0.82\,\text{V}$.

Pixels that experience a fake hit rate more than an order of magnitude above the mean noise rate of the full matrix get flagged as noisy and are entered into a masking file which is later

applied during alignment of the beam telescope data.
Figure 7.24 and Figure 7.25 give an overview of the percentage of masked pixels in a matrix for matrices on a standard sample, a modified sample and two samples from the most-modified process.

7.4. Operational Threshold

Operating FASTPIX matrices at low detection thresholds without registering a substantial rate of fake hits from noise has a positive impact on detection efficiency, spatial as well as time measurement precision. In practice a low detection threshold setting for a matrix under test has to be balanced against fake hits from single pixel noise, pixel-to-pixel variations in the signal response of the discriminator as well as occasional noisy pixels with a noise rate heightened by an order of magnitude. Since the FASTPIX frontend does neither enable pixel masking nor an equalization of the signal response of individual pixels, an operational threshold is found by evaluating the rate of fake hits observed from the full matrix.

The increase in noise rate with decreasing signal detection threshold calculated from the combined fake hit rate is exemplified by Figure 7.26 for the first four matrices of sample W18S1-3.

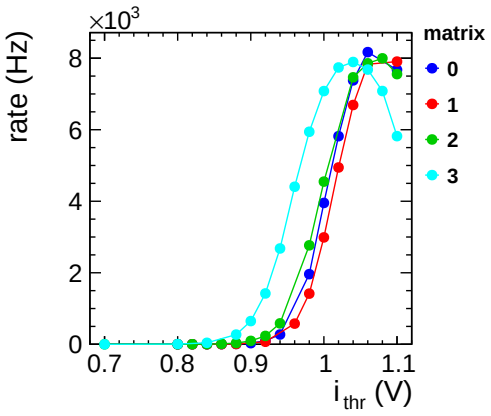

Figure 7.26: Fake hit rate over i_{thr} for the first 4 matrices of sample W18S1-3. The error bars correspond to the statistical uncertainty of the rate measurement.

The ideal operational threshold of a matrix is determined by the point in threshold at with the rate surpasses 10 Hz. The estimated $O(100\,\text{Hz})$ hit rates during more advanced measurements with ionizing particle beams call for a fake hit rate that is an order of magnitude below the expected physics rate. Otherwise the share of recorded noise dominates during the continuous data acquisition and reduces the efficiency of the test beam measurement campaigns in terms of data volume and dead time in read out during data transfer.

Figure 7.27 summarized the resulting operational threshold values for a standard-process and a modified-process sample. Figure 7.28 presents an equivalent overview for two samples from W18S1, the most-modified version of the manufacturing process.

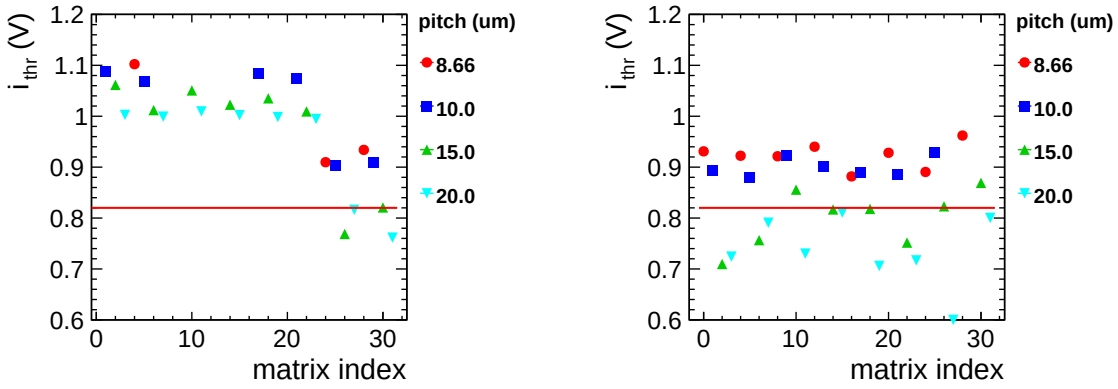

(a) W03S1-1.

(b) W15S1-1.

Figure 7.27: Operational threshold for all matrices on a standard and a modified process sample. The red horizontal line represents the nominal threshold for FASTPIX during test beam data taking.

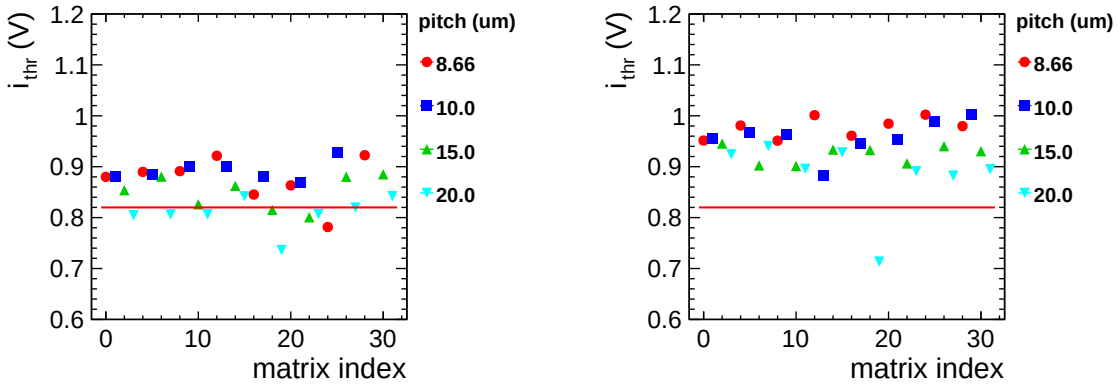

(a) W18S1-3.

(b) W18S1-4.

Figure 7.28: Operational threshold for all matrices on two samples from most-modified process wafer W18. The red horizontal line represents the nominal threshold for FASTPIX during test beam data taking.

The introduction of the blanket deep n-layer raises the capacitance configuration of the W15S1-1 samples and results in an increased mean operational threshold. A similar effect can be observed for the most-modified-process sample W18S1-3. Differences in input capacitance due to pixel pitch place the larger-pitch matrices at higher charge thresholds, compared to the smaller 8.66 µm and 10 µm matrices. While the collection electrode size manages to separate the last eight matrices of the standard-process samples W03S1-1 towards larger operational threshold, this effect is annulled on the modified-process samples.

In test beam measurement campaigns the FASTPIX threshold was set manually, also targeting $\mathcal{O}(10\,\mathrm{Hz})$ matrix noise. The settings differ slightly due to the change in measurement setup and environment. A lower operational threshold and moderately higher fake hit rates do not compromise the measurement and are filtered through track matching in reconstruction and analysis stages.

7.5. Summary

Initial studies of the current-voltage characteristic of individual samples confirm the working state of the sensor and its expected electrical properties. The previously simulated range of bias voltage is reached by the physical detector samples within a stable current. The nominal bias voltage of −6 V for p-well and substrate leaves sufficient margins of approximately ±4 V without drastic changes in current destabilizing detector operation. With the introduction of the blanket n-layer in the modified CMOS process, the absolute punch-through voltage is increased by approximately 10 %. The total current increases with the introduction and subsequent increase in blanket n-layer doping between standard-process, modified-process and most-modified-process samples.

The ToT response to electrically injected signal pulses exhibits a minimum detectable ToT value around 27 ns before transitioning into a non-linear trend. The non-linear term of the model is found to be essential for an approximation and extrapolation of the measured data. In comparison with the standard-process sample, the modified-process sample yields approximately 15 % smaller gain and a less-pronounced dependency on pitch. The dependency on pitch is inverse for the most-modified-process sample.
A calibration of the electrically injected signal is found through a comparison of signal from X-ray photons with the pulse injection voltage at common most-probable ToT values. The calibration factor and associated test pulse injection capacitance are calculated per pitch. The calibrated test pulse capacitance is approximately 60 % higher than the values extracted from a post-layout simulation of the chip that was carried out before the time frame of this thesis. Still, the calibration yields values in the capacitance range considered during the chip design stage [55] with an improvement in uncertainty by a factor of two.

The ToT allows to cross-check laboratory calibrations with the first test beam measurements that were conducted in parallel at the CERN SPS North area test beam.
As discussed in Section 3.2, the minimum ionizing 120 GeV pions, create charge carriers along their path through the silicon bulk, with a most probable generation of 76 electron-hole pairs per micrometer. The measured FASTPIX signal at a given threshold is collected from the sensitive volume of the 25 µm depleted epitaxial layer. Combining both metrics, the resulting signal from perpendicular particle tracks is estimated to correspond to approximately 1900 e. In test beam a most probable ToT of 95 ns and 67 ns was measured at a threshold i_{thr} of 0.82 V for 10 µm-pitch matrix 1 and for 20 µm-pitch matrix 3, respectively [13]. Applying the calibrated signal conversion to the ToT observed in test beam amounts to 2.0 ± 0.3 ke and confirms the calibration to be in agreement with the estimated signal from minimum ionizing particles.

The discriminator detection threshold is calibrated using the test pulse injection data in combination with the confirmed signal-to-energy conversion factors. The discussed exemplary matrices exhibit a gain between 120 e/V and 260 e/V.

Noise contributions to the test pulse signal are first obtained as the width of pulse injection efficiency S-curves. A small decrease in width with decreasing threshold is found as a result of a gain dependency on threshold, caused by the electrical implementation of the discriminator

threshold adjustment. The fast shaping analog frontend reduces the noise contribution from leakage current. Across all samples, the dominant thermal noise of the frontend yields values between 5 e and 15 e with clear trends following pixel pitch and collection electrode size.
In addition, the rate of fake hits in a low charge threshold range is used to identify noisy pixels. The created masking files are later applied during the alignment of the beam telescope data. The combined evaluation of all pixels as an effective matrix rate is the basis for operational threshold values. The threshold-equivalent of a fake hit rate of 10 Hz is defined as target operational threshold as it retains enough hit rate headroom for test beam measurements without jeopardizing the efficiency of the DAQ. For samples with increased deep n-type implant doping levels, increased pitch or enlarged collection electrode, the input capacitance as well as the operational threshold increases as an effect of increased gain.

8

Test-Beam Setup

In test-beam measurements, the device under test is evaluated against a combination of measurements taken in synchronization by well defined and fully characterized reference detectors. To characterize a prototype detector, a beam of minimally ionizing particles (MIPs) is aimed at and passes through an array of reference pixel detector planes, a setup commonly called beam telescope, with the device under test (DUT) at its center.
The measurement data stream from all detector planes of the beam-telescope setup is acquired, synchronized and reconstructed to form digital representations of the particle tracks, the trajectories of the initial beam of MIPs. The collected track information is used to evaluate the performance of the DUT from a comparison between the recorded DUT measurement in space and time to matching information available from track reconstruction. Performance observables like the spatial and temporal resolution as well as the hit detection efficiency of the DUT are accessible from such measurements. The measured data set enables a suppression of falsely identified hits from noise by discarding DUT responses without a matching reconstructed track.

The following chapter explains the general approach of detector characterization in test-beam measurements in the context of the measurement campaigns conducted with FASTPIX at the CERN Super Proton Synchrotron (SPS) North Area test-beam facility. After a brief description of the test-beam facility, the focus shifts towards the Timepix3 reference beam telescope, situated in the H6B beam area test stand along the H6 beam-line. Dedicated sections discuss the mechanical components of the telescope, the integration of the DUT as well as aspects of the electronics hardware used for data acquisition (DAQ).

8.1. The CERN SPS North Area Test-Beam Facility

Test-beam facilities offer an access to particle beams with configurable particle composition, energy range, particle rate, polarities and spill pattern. At the host research lab CERN, facilities, equipment, dedicated technical as well as managerial staff are deployed to uphold the test beam operation and provide beams to users under well defined conditions.
Figure 8.1 shows schematic drawings of the accelerator complex and the beam line used for the FASTPIX measurements. The primary particles used for test-beam operation are protons that receive initial acceleration in the Linear Accelerator 4 (up to 160 MeV), pass the

Proton Synchrotron Booster (up to 2 GeV) and the Proton Synchrotron before entering the Super Proton Synchrotron (SPS) at an energy of 26 GeV. With its 7 km circumference, the SPS accelerates protons to 450 GeV and predominantly serves as a pre-accelerator for the Large Hadron Collider. Besides the LHC injection, SPS particles are distributed to multiple multi-year large-scale experiments such as NA61/SHINE and NA62, COMPASS, ProtoDUNE and AWAKE [93]. In addition, six beam lines in the EHN1 building host test stand areas designated for irradiation studies, detector and accelerator R&D [94].
The particles are delivered in bunched structures, with 4.8 s spills occurring approximately every 30 to 60 s, adhering to the duty-cycle requirements of the experiments utilizing protons from the SPS.

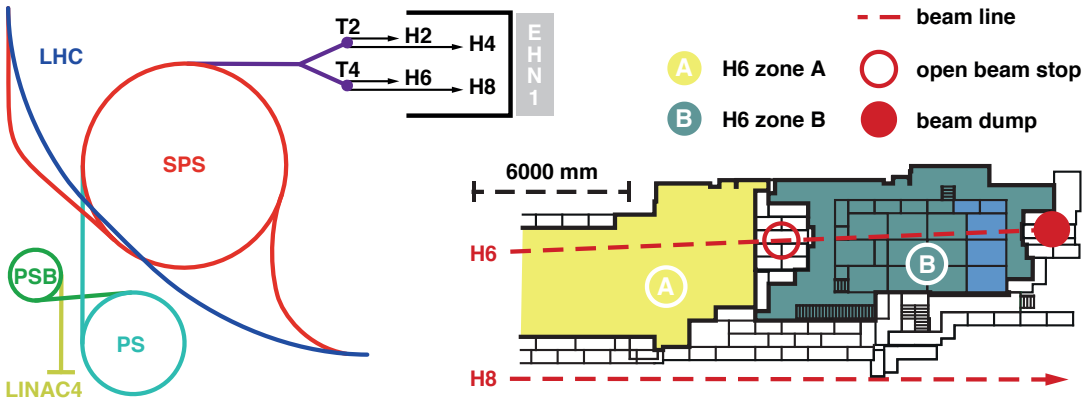

Figure 8.1: Schematic diagram of the primary particle acceleration chain and the secondary beam delivery (left). The SPS particle beam is split delivered simultaneously to target stations, illustrated as dots at the end of the tree-like particle extraction. T2 and T4 are marked as they are the origin of secondary particles for test beam use. On the right, a site plan of the experimental beam areas along beamline H6 in EHN1, the back half of zone H6A and the full zone H6B (modified from [95]).

Secondary particles are created by colliding protons with fixed beryllium or lead targets of varying dimension. After passing through different collimation and magnet-based selection stages secondary particle beams from target T2 and T4 are steered towards the experimental area beam lines.
The CERN SPS North Area test beam hall (EHN1) houses four beam lines ≈0.6 km upstream from the target station [94]. The operation of the hall follows a schedule that coordinates collaborations running big experiments together with small user setups that change with a typical turn-around time of 1-3 weeks. Smaller-scale setups, most of them using beam telescopes, are setup in series along two of the four beam lines in EHN1, called H6 and H8. The beam line H6 is operated as a high-energy, high-resolution secondary mixed hadron (10 to 205 GeV c^{-1}) beam line [94] and hosts the test campaigns associated with this work.
Per scheduled week, users get attributed a status (main user, parallel user or parasitic user) that grants them varying levels of control over the beam makeup, the cross section, position and interruptions of the particle beam of a beam line. Beam position and focus are set using dipole and quadrupole magnets installed upstream of the user experiments. The beam intensity is controlled using collimators further upstream, limiting it to levels permissible under the ionizing radiation standards restricting the parasitic muon flux. An initial beam setup is found in cooperation with a beam line liaison physicist at the beginning of a user

measurement campaign and will undergo only small changes by the user.
Figure 8.2 presents a top view into the empty zone H6B with the closed beam stop in the back wall and the volume to be taken up by the telescope installation.

Figure 8.2: Downstream view along the H6 beamline into zone B. The photograph of the empty zone B was taken from above the open beam stop of H6A, as marked in Figure 8.1. A yellow cross on the red metal block marks the position of the impinging beam, the red arrow. The placement of the telescope setup is traced by a light blue cube.

8.2. The CLICdp Beam Telescope

The test beam measurements presented and discussed in the following chapters were exclusively conducted with the CLICdp Timepix3 reference telescope [96, 97, 98]. The setup is installed in zone B of the H6 beam line in the CERN SPS North Area EHN1 experimental hall. Here FASTPIX assemblies were tested using a mixed hadron, primarily $\pi^{\pm}$, beam with a momentum of 120 GeV c^{-1}, configured to deliver $1 \cdot 10^6$ to $5 \cdot 10^6$ particles per 4.8 s spill on an area of $\approx 1\,cm^2$.

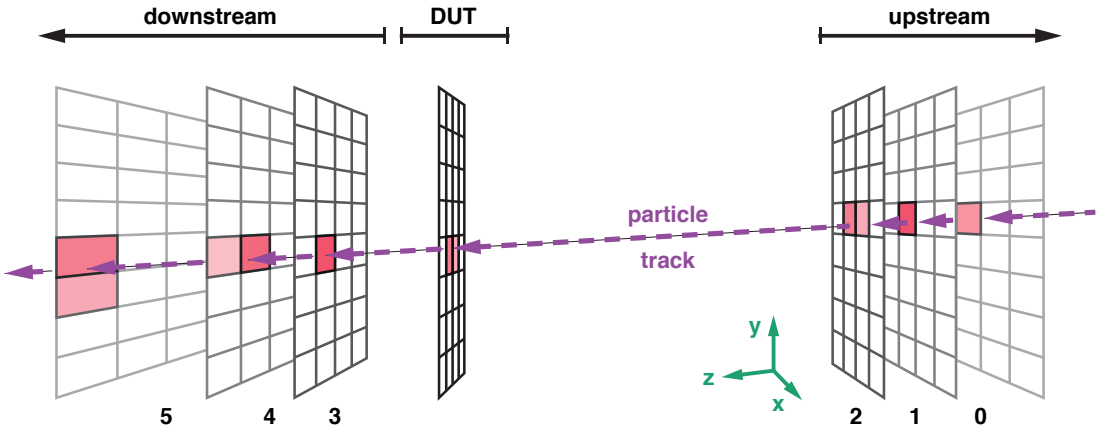

Figure 8.3: Working principle of a beam telescope and its core components: a DUT in the center of 3 upstream and 3 downstream pixelated reference planes. All detectors show hits (red pixels) from the passing particle.

Figure 8.3 shows a simplified illustration of the beam telescope and its core components in a narrowly-spaced configuration. The global coordinate system is a right-handed Cartesian

coordinate system where the beam particles traverse the setup along the positive z-axis. The positive x-axis points to the right when looking upstream into the incoming beam, the y-direction points vertically upwards. Each telescope plane measures the time and position of an incidence particle. The combination of measurements from all 6 pixel detector planes is used to reconstruct the particle trajectory.

The CLICdp Timepix3 reference beam telescope is a particle tracking system based on a similar telescope developed for detector R&D within the LHCb collaboration [96]. The current setup consists of 6 fully characterized Timepix3-based pixel detector reference planes placed along the particle beam axis. The reference planes are arranged for optimal tracking resolution while obeying mechanical limitations and constraints imposed by multiple scattering at the given beam energy.

8.2.1. Material Budget

The material content of a detector assembly and its influence on the trajectory of a charged particles was introduced in Section 2.2.4. Like the material budget of FASTPIX in Section 6.2.1, the material content of Timepix3 hybrid silicon pixel detector assemblies has an important impact on the performance of the reference beam telescope and is summarized in Table 8.1. The PCB consists of eight layers of copper with an average fill factor of 75 % interlaced with an epoxy laminate (Isola IS410). On the backside of the PCB, an additional copper layer is used for the cooling of the chip. In front of the hybrid detector an ABS plastic cover shields the assembly against ambiens light and mechanical influences. The total material of a telescope plane is estimated to correspond to ≈3.8 % X_0.

Table 8.1: Estimation of material content X/X_0 of the Timepix3 hybrid pixel detector assembly and the carrier PCB. X_0 is the radiation length of the material and X the thickness of the component. Based on and adapted from [78, 97, 80].

Layer	Material	X_0 [mm]	X [µm]	X/X_0 [%]
Detector assembly			**1000**	**1.07**
Sensor	Silicon	93.7	300	0.32
ASIC	Silicon	93.7	700	0.75
PCB + Cover			**2700**	**2.69**
Metal layers	Copper	14.4	125	0.87
Substrate	Glass fibre (60% of FR-4)	100.56	885	0.53
Resin	Epoxy resin (40% of FR-4)	67.04	590	0.35
Backside cooling layer	Copper	14.4	100	0.69
Front cover	ABS plastic	406.4	1000	0.25

8.2.2. Experimental Setup

Telescope exterior and periphery

The main mechanical structure is made from 40 mm × 40 mm aluminum extrusions that provide mounting points for subordinate structures, periphery mechanics, mechatronic

and electronic hardware. Visible to the outside, sheet aluminum panels enclose the inside components from course dust and light ingress from the environment of the experimental hall.

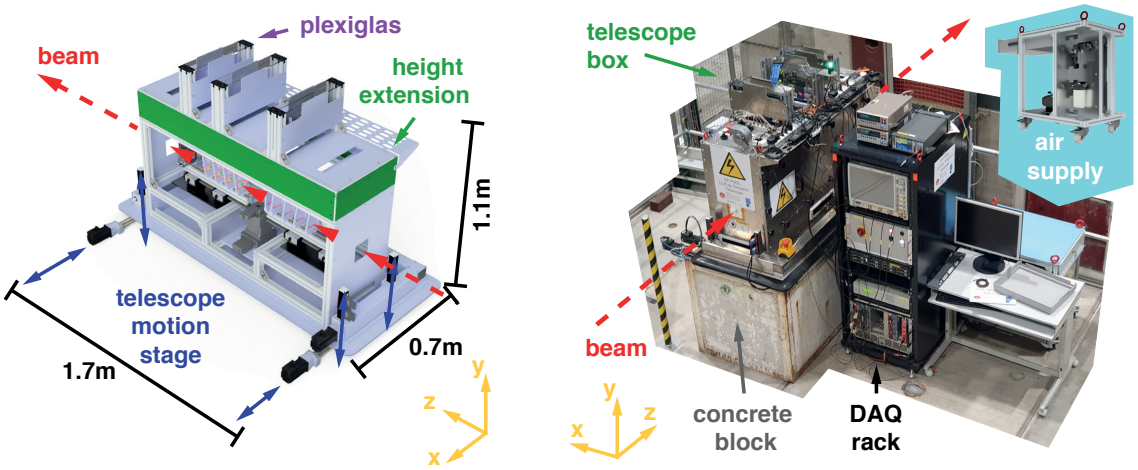

(a) CAD rendering of the main telescope structure showing the beam axis in red, the main motion stage axes in blue, the height extension of the enclosure in green and the Plexiglas covers in violet.

(b) Photograph of the full setup with the main telescope structure on the left resting on a concrete block, traversed by the beam in red. The 19 ″ DAQ rack is placed to the right of the telescope, the air compressor cart behind the server workstation table.

Figure 8.4: CLICdp Timepix3 telescope exterior setup and periphery.

The setup was re-commissioned in summer of 2021 after the restructuring of the H6 beam line over the course of the preceding long shutdown. In that process the height of the telescope enclosure was increased by 15 cm as shown by the rendering in Figure 8.4a. The extension in height allows to fit taller DUT readout and control hardware setups inside the telescope while not sacrificing the range of possible DUT positions and y-rotation angles during measurement scans. To accommodate the increase in height, the position and mounting of data acquisition electronics was adjusted. Additional covers from transparent engineering plastic (Plexiglas) protect the telescope DAQ boards on top of the enclosure.

The main telescope structure rests on a remote-controlled motorized motion stage that allows a first rough alignment of the telescope with the beam and enables to follow movements in beam position over the course of a measurement campaign. During the initial positioning of the telescope in the test area the particle beam line is aligned approximately in parallel to the telescope axis, congruent in the x/y plane.

A 19 inch rack placed on the right side of the telescope enclosure holds power supplies, the trigger logic unit, an oscilloscope, the controllers for motion stages, the measurement server, and a NIM crate for swap-able hardware units.

If necessary, an air compressor cart placed next to the setup delivers a continuous filtered and dried stream of ambient-temperature air to the telescope reference detector planes and/or the DUT. While active cooling solutions using liquid media oftentimes need to match the environment inside an existing upgraded sub-detector system, future detector concepts for e^+e^- colliders foresee air cooling as a solution for heat dissipation. Consequently the CLICdp

beam telescope is reverting to ambient temperature air flow to stabilize the operational conditions of tested prototype pixel detectors. As introduced in Section 6.3.2, the air cooling solutions for devices inside the telescope enclosure introduces directed air flow for convection cooling. Off-axis fans and compressor-fed air guides built into new chip covers mitigate an introduction of additional material into the particle beam and the associated increased scattering.

Telescope interior

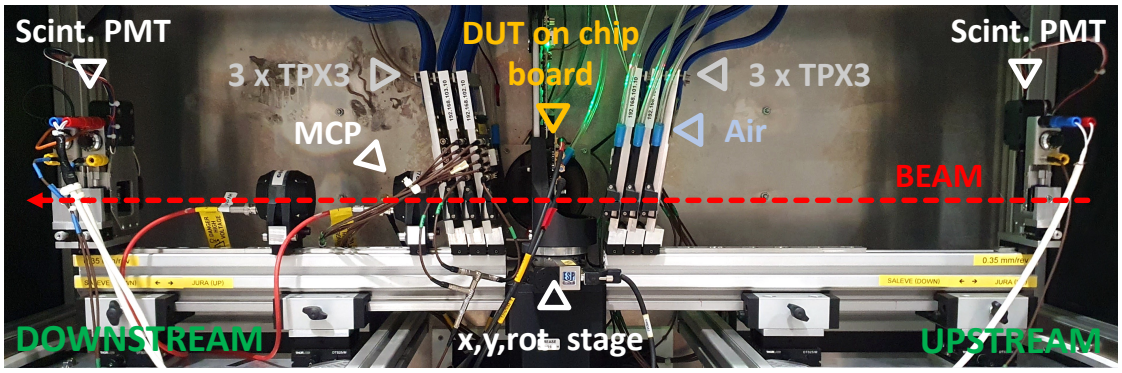

Figure 8.5: Photograph of the telescope interior. The DUT is installed in the center on the x/y/rot. stage, 3 reference planes follow on either side. Two MCP-PMTs are added after the left-most Timepix3 plane (Tpx3). Scintillator PMTs are mounted on the outside ends of the telescope arms. Clear hoses with light blue couplers deliver air flow to the DUT and telescope planes.

Inside the telescope enclosure two triplets of pixel detector reference planes are mounted on a telescope arm on either side, upstream as well as downstream of the DUT. Figure 8.5 presents a photograph of the telescope interior.
The arms of the telescope are constructed from aluminum extrusions that are supported by adjustable precision linear rails and non-adjustable, free-floating rotational stages. The stack of two stages allows the feet underneath the telescope arms to adjust a singular arm in translation along the x-axis as well as in rotation around the y-axis. The newly introduced adjustment range is illustrated by Figure 8.6.
With these mechanical additions the telescope arms can be fine-adjusted for an improved parallelism in their alignment with respect to each other, following the trajectory of the beam particles.

A single-chip carrier board is the central element of the hybrid pixel detector reference planes. It holds a hybrid pixel detector assembly which is glued and wire-bonded onto a PCB that provides secure electrical interconnections and mechanical mounting points. An aluminum frame adapts the PCB of a given reference plane to an aluminum block that tilts the detector by 9° around the x and y axes. This modification of detector orientation increases the observed mean cluster size and thereby increases the amount of pixels that are available for signal-charge-weighted position reconstruction (see Section 4.2.3), ultimately improving the spatial resolution of the system. The tilt around y is implemented in clockwise rotation for all reference planes. Around the x-axis the tilt is implemented in clockwise and counter-clockwise rotation for planes of the downstream and upstream arm of the telescope, respectively. In tilted orientation, a precision rail receives the dovetail mounting base on

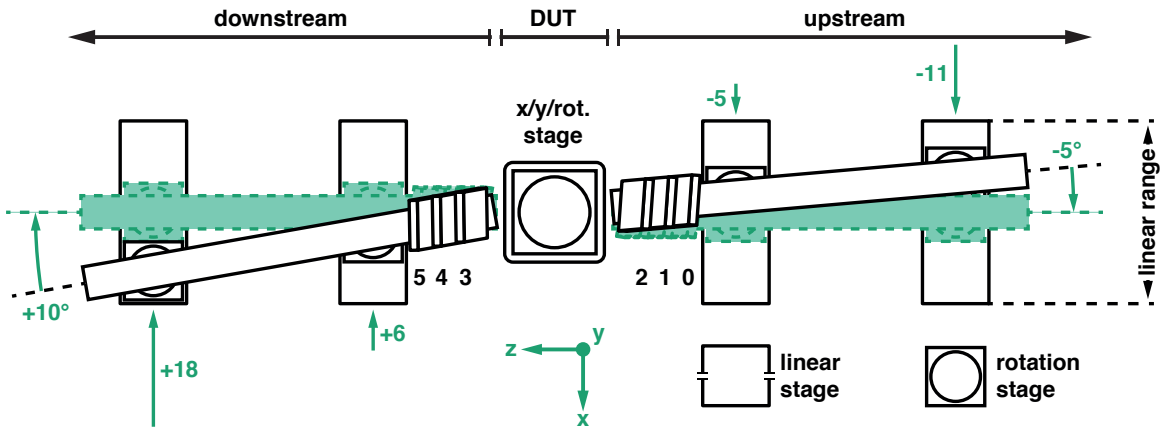

Figure 8.6: Illustration of the added mechanical adjustment of the telescope arms. The DUT is not sketched, merely the x/y/rot. stage in the telescope center. The 3 upstream and 3 downstream pixelated reference planes are numbered 0 to 5 and shown in their tilted orientation. The black telescope arms are misaligned and can be moved into alignment (dashed green) by applying the green adjustment values in x-direction.

the bottom of a given telescope plane assembly and enables a secure and sturdy mechanical placement of planes along the telescope arm. The mounting solution ensures that the devices do not move significantly over time. The relative x/y-offset between reference detector planes caused by manufacturing tolerances of the custom machined aluminum parts are minimized by manually adjusting the plane placement within the wiggle-room of the manufacturing tolerance. The z-axis position of the telescope planes is as well set manually depending on e.g. mechanical constraints introduced by the size of the DUT that require a larger spacing between upstream and downstream planes.
No mechanical structure, except the carrier PCBs and covers, extends into the path of the beam. The protective light-tight ABS plastic cover is optimized for stability and minimal scattering. Apart from shielding the sensitive sensors from external light, a direct ambient air flow introduces heat exchange by convection and prevents electronics noise. Measurement tabs on the outside vertical edges of the telescope planes project the center line of the tilted pixel matrix onto a plane that is well-accessible for the telescope operator. The tabs allow a manual measurement of plane positions along the z-axis.
Table 8.2 summarizes the plane positions from the FASTPIX test campaigns with a measurement precision of 0.5 mm.

The Micro-Channel-Plate Photomultiplier Tube (MCP-PMT) HPK R3809U-50 [99] has been added to the telescope setup for single-digit picosecond precision reference time measurements [100] during test beam campaigns that set out to characterize devices with high precision time measurement capabilities.
In order to minimize the amount of material in the telescope acceptance, the MCP-PMT is positioned after the downstream set of telescope planes. The cylindrical device depicted in Figure 8.7 is adapted to an upright and square aluminum mounting block using a 3D-printed ABS plastic housing. Similar to the telescope reference planes it is mounted to the precision rail with a dovetail mounting base. In the rendering, the front lid of the MCP-PMT housing is pulled away revealing the $\approx$1 cm^2 photocathode window in the front of the device.

Table 8.2: Measured z-position of telescope planes and the FASTPIX DUT relative to the sensor center of the first telescope plane. The measurement with 0.5 mm precision uses the sensor center of the first upstream telescope plane as reference. The MCP position is logged with a global low-precision value for all test beam seasons, as it is not used for reconstruction or analysis of FASTPIX runs.

Detector	ID	Reference	Position (mm)			
			2021	5-7 2022	8-11 2022	2023
Plane 0	D4	Sensor center	0.0	0.0	0.0	0.0
Plane 1	E3	Sensor center	22.0	22.0	21.5	21.0
Plane 2	G2	Sensor center	45.0	43.0	42.5	42.5
DUT	FASTPIX	Chip surface	119.0	116.5	114.0	113.0
Plane 3	G3	Sensor center	193.5	187.5	186.5	185.5
Plane 4	J5	Sensor center	214.5	208.5	208.5	207.5
Plane 5	L9	Sensor center	237.5	232.5	230.0	229.0
MCP-PMT	1449/1776	Front edge	250 ± 10			

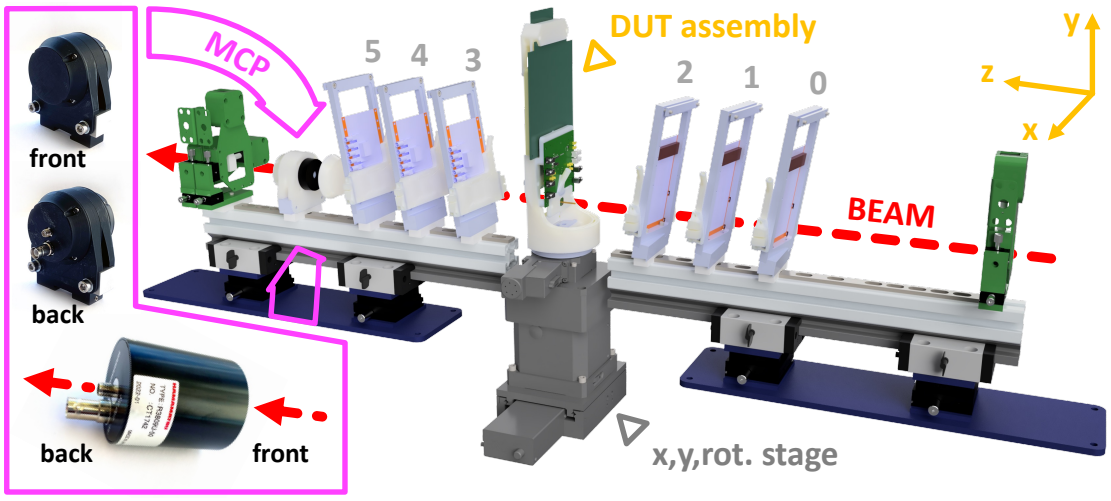

Figure 8.7: CAD rendering of the telescope interior. FASTPIX with Carboard installed as DUT in the center of the setup on the x/y/rot. stage. The MCP-PMT is placed behind the downstream-most Timepix3 reference plane, detailed photographs are found on the left. For the purpose of illustration, 3D printed ABS parts (DUT structure, Timepix3 covers, MCP-PMT housing) are rendered in an off-white translucent material, the Scintillator-PMT planes are colored green, the parts for the telescope arm adjustment are colored dark blue.

At the most-upstream end of the upstream telescope arm and the most-downstream end of the downstream telescope arm a scintillator petal is mounted and read out by a photomultiplier. Here as well, additional degrees of adjustment were added over the course of this work. Two linear stages, one along the global x-axis and one along the global y-axis allow to tune the overlap of the active area of the scintillators. The signals from particles crossing the scintillating volume can be used as a gate-keeper to the telescope, only selecting particles that cross both scintillators and cause a coincidence between signals from the very front and very back of the telescope setup.

While for FASTPIX the scintillators are merely used for debugging and monitoring during data taking, their alignment is crucial for DUTs that are of a similar size as the Timepix3 hybrid detector reference planes. Maximizing the overlap allows to probe a larger DUT area with efficient particle detection and nominal tracking accuracy.

For every DUT the experimental setup is adapted, balancing the need for precision measurements with the mechanical constraints of the physical environment. The main DUT is placed in the centre of the telescope reference system between the upstream and downstream arm of the telescope. Here, the spatial track-reconstruction precision of the reference measurement system is best.

As introduced in Section 6.2, also the FASTPIX chip is glued and wire-bonded to a custom circuit board that provides secure electrical connections and mechanical mounting points for the integration of samples. Detector control and readout is facilitated by the Caribou system that was previously outlined in Section 6.1. Together with the Carboard, the FASTPIX DUT is positioned on a movement stage that is able to perform x/y translations (precision 1 µm) [101, 102] and y-axis rotations (precision 0.02°) [103]. This flexibility is essential for aligning the DUT with the particle beam and the surrounding, fixed telescope planes. A 3D-printed ABS plastic structure receives the chip board, positions the Carboard and allows a fast as well as safe sample change in the crowded center of the telescope. The custom CAD-designed part is depicted in Figure 8.7, does not obstruct DUT movement and introduces rigidity against the stress of cables. It therefore allows a repeatable, exact DUT positioning by the DUT motion stage with a $\mathcal{O}(50\,\mu\text{m})$ and $\mathcal{O}(0.02°)$ precision.

8.2.3. Data Acquisition

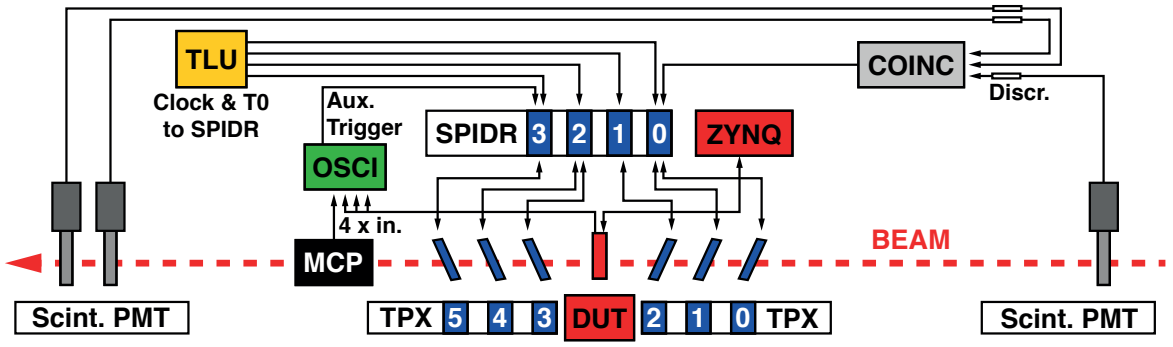

Figure 8.8: The telescope DAQ scheme for test beam measurements with FASTPIX. The color code identifies the different detector types and their associated readout solution. The Timepix hybrid pixel detector planes and SPIDR system in blue, the FASTPIX DUT and Caribou system in red, the oscilloscope in green, the TLU in yellow, the MCP-PMT in black and Scintillator-PMTs in shades of grey.

Figure 8.8 illustrates the data acquisition scheme that is applied during test beam measurements of FASTPIX samples inside the CLICdp beam telescope. The data acquisition for the Timepix3 hybrid pixel detector reference planes utilizes the SPIDR data acquisition system [104]. Especially in the test beam environment the SPIDR system is essential in managing the high-rate data streams from the telescope planes, operating in a data-driven, zero-suppressed readout mode.

Data is read continuously during as well as outside of the 4.8 s pion spills, ensuring comprehensive data capture with minimal loss. Each reference detector plane inside the telescope enclosure is connected via an FMC cable to a slot on one of four SPIDR boards mounted on top of the telescope frame. High speed data from SPIDR is sent through 10 GB optical links to network interfaces of the measurement server that is installed in close proximity to the telescope setup. The control and configuration of SPIDR boards is possible via 1 Gb E network and serial USB connections between the server and the FPGA development boards.
Based on preliminary hitmaps built around FASTPIX events, a region-of-interest (ROI) mask is defined by modifying the pixel configuration of each Timepix3 reference detector. The mask is loaded with the detector configuration at the beginning of each series of measurements and causes the Timepix3 chips to only send data from pixel hits within the ROI. The telescope acceptance is thereby reduced to the dimensions of the FASTPIX chip, including a safety margin of typically 10 pixels, in combination with a reduction of the total acquired telescope data volume per given amount of recorded FASTPIX hits.

The FASTPIX DUT receives power, bias and control from the Caribou readout system, introduced in Section 6.1. In a similar fashion, the ZYNQ board is placed on top of the telescope box above the DUT assembly and connects to the inside Carboard via FMC cable. Placing the development boards on top of the telescope enclosure reduces the ingress of excess heat from FPGAs, processors and micro chips and keeps them accessible in reconfiguration or debugging scenarios.
An Agilent DSO9254A oscilloscope [85] with 2.5 GHz analog bandwidth and a sampling rate of $10\,\mathrm{GS\,s^{-1}}$ is used to record the three digital channel signals. ZYNQ board and oscilloscope are connected to the local area network. Control commands for the Carboard and oscilloscope are issued by a Peary server instance running on the ZYNQ board. The recorded measurement data is directly saved to the measurement server as soon as the local oscilloscope hardware buffer size is reached. During the transfer of measurement data, the oscilloscope readout is subject to a dead time, typically 5 µs per 4000 events, that reduces the duty cycle of the DUT data acquisition.
The MCP-PMT timing reference detector is connected to the fourth channel of the oscilloscope. The FASTPIX fast-OR signal is set to trigger the oscilloscope acquisition of waveforms from all connected signals. The auxiliary trigger output is fed to a time-to-digital converter (TDC) on one of the telescopes DAQ boards and is used to synchronize the data streams from Timepix3 reference planes and DUT in track reconstruction.

The analog signals from the Scintillator-PMT planes are discriminated and combined by a coincidence unit. The coincidence signal is as well fed to a TDC channel and is used for debugging and monitoring during data taking.

The telescope TLU provides a global 40 MHz clock as well as a time synchronization signal called T_0 [105]. Both signals synchronize individual subsystems and the beginning of the collective data taking.

Detector control and data acquisition facilitated by the oscilloscope, Caribou and SPIDR is integrated into a custom telescope DAQ software that coordinates the telescope operation

and runs on the local measurement server. A frequent interaction with the telescope run control software entails the definition of time periods (runs) test-beam data is recorded in, the setup of paths for data storage and the scheduling of run lists that scan detector configuration parameters across consecutive measurements. The software synchronizes readout and data storage for each detector within the test beam setup. Binary pixel data recorded by each reference plane as well as FASTPIX binary waveform data recorded by the oscilloscope is stored on disk for offline processing and analysis.

9

Test-Beam Reconstruction and Analysis

In test-beam measurements FASTPIX is exposed to a beam of charged high-momentum particles that allow to characterize its performance in an environment that closely resembles the forseen spectrum of applications. The test beam enables to study the sensor response to ionizing particles in reference to particle track information provided by a beam-telescope setup.
The following chapter will present the applied methods that translate the data acquired from reference detector planes into reconstructed track information, which is finally compared against the observations made by the device under test in test beam data analysis.

9.1. Corryvreckan

Offline reconstruction and significant parts of the analysis of the test-beam data are performed as a multi-step process using the software framework Corryvreckan [106].
The software is engineered in a modular and configurable architecture, that offers significant flexibility and adaptability to address the complexity of test beam setups. At its core, the framework is managing fundamental operations such as parsing configuration files, managing the central event loop, and facilitating coordinate transformations. On top, various modules are dedicated to specific tasks in the data reconstruction and analysis process and can be configured in a process chain tailored to specific data sets and analysis goals. The individual steps include event building, clustering, track reconstruction, the association of reference track and DUT, detector-alignment procedures and detector-specific analysis techniques. The sequence of framework modules and the assignment of module-specific parameters is defined in a human-readable key-value based configuration file.
The data reconstruction starts with the parsing of raw or pre-processed data files for each detector plane, in order to identify pixel hits with their coordinates in space and time. The clipboard, a central storage mechanism within the framework, stores event objects that represent a specific time slice of the input data around a trigger or in a predefined time window. The events are then processed in series.
Neighboring hit pixels are aggregated into clusters, leveraging charge sharing, to attribute adjacent pixel hits to individual incident particles. The reconstruction of particle trajectories uses these clusters to form reference particle tracks that are then associated with signal responses from the DUT. The accuracy and reliability of clustering, tracking, and DUT

cluster-track association algorithms is enhanced by position and time cuts that allow to reduce the combinatorial complexity and the impact of noise.
The precision of an initial mechanical alignment of reference planes and the DUT inside the measurement setup is enhanced by algorithms based on the reconstructed track fits and the minimization of spatial residuals, respectively. Crucial for accurate data interpretation, a high degree of precision in alignment is achieved in an iterative application of these modules. The alignment is represented by detector geometry files that as well obey the structure of the framework configuration.
Data and analysis outputs are generated by every module as histograms, which are essential tools in identifying and addressing issues and for evaluating both the reconstruction process as well as the performance of the DUT.

9.2. Test-Beam Data Reconstruction

The beam telescope reference setup used to acquire all test-beam measurements within the scope of this thesis was introduced in Section 8.2. The Corryvreckan alignment and data reconstruction setup for the Timepix3 reference detector planes of the CLICdp beam telescope is based on previous work [107, 79]. During data taking the software framework is used for online data-quality monitoring and preliminary offline alignments of the telescope. The final telescope geometry and DUT alignment for measurement samples is then computed and checked for consistency offline, in parallel with data taking.

9.2.1. Adaptation for FASTPIX campaigns

DAQ, integration, setup and analysis for test beam measurements with FASTPIX were previously introduced in [13]. The extensions of the framework for the time-based decoding of position and pulse height as well as the proper treatment of the hexagonal pixel geometry have since been developed further.

The large amount of singular measurement runs that cover the extent of the FASTPIX process modification and sensor optimization parameter space calls for an adaptation of the manual run-by-run execution of the analysis framework to an automated approach. While Corryvreckan supports the parallel submission of jobs to computing clusters, a local serial processing of runs was implemented.
FASTPIX houses multiple detector matrices in one single chip, an arrangement that unifies all its matrices to a singular orientation in the telescope coordinate system. The alignment of a given run within e.g. a matrix scan can benefit from the finalized alignment of the previous runs, even if a different matrix was measured. Python code accesses the previous iteration of alignment, evaluates its success or uses previous alignment results as a starting point for the alignment of a new matrix of the same pitch. Based on good-run lists in web-based spreadsheets, the chip configuration is related to a run number, the state of alignment, reconstruction and the progress of analysis.
The sequence of Corryvreckan modules used for track reconstruction as well as the association and analysis of FASTPIX measurement data is illustrated in Figure 9.1.
The following sections discuss the individual steps and modules in the sequence.

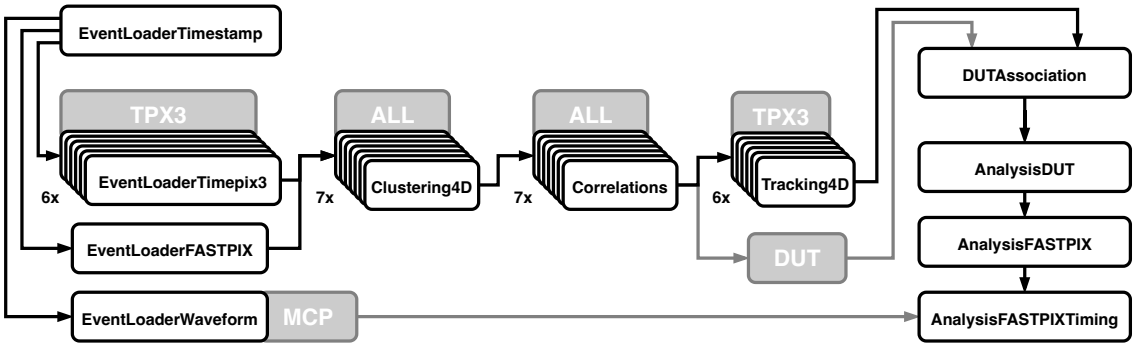

Figure 9.1: Sequence of modules in the Corryvreckan reconstruction and analysis chain.

9.2.2. Event Building

The reference telescope planes provide spatial as well as temporal information for pixel hits and are read out continuously and independent of FASTPIX. The telescope data stream therefore lacks an intrinsic definition of the time frame of an event. Information used to locate an event in the readout telescope data is either provided by a time stamp from an additional detector in the setup or by dividing the recorded data stream into same-length time intervals. Figure 9.2 illustrates the scheme applied during the assembly of events from the measured data for the case of 5 µs fixed time intervals centered around FASTPIX time stamps.

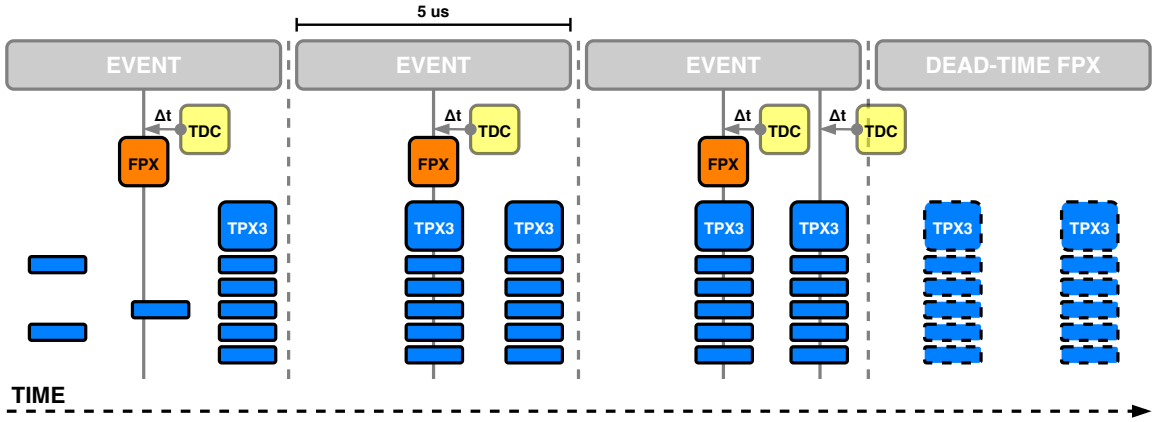

Figure 9.2: Schematic illustration of the event building logic for FASTPIX.

The schematic shows the auxiliary trigger input to the SPIDR board TDC in yellow, the derived FASTPIX timestamp FPX in orange as well as hit times on the Timepix3 reference planes TPX3 in blue. Events are created and filled based on a set of data assembled by four different EventLoader modules within the Corryvreckan framework.

Timestamps
During measurements with FASTPIX, the oscilloscope triggers on a fast logic OR combination of all pixels in a given matrix, providing the auxiliary time-stamp information through the SPIDR TDC which is used to synchronize FASTPIX and telescope planes.

The module EventLoaderTimestamp loads and sorts the trigger data recorded from the TDC input on the SPIDR board receiving the auxiliary trigger. Each trigger signal is processed to construct new 5 µs-long events centered around a trigger (FPX) or to add trigger information to an already existing event. External delays are compensated by a module-specific time offset parameter Δt to ensure the correct association of TDC triggers and TPX3 hits into events. For FASTPIX data taking, the applied Δt changes throughout the three years of measurement campaigns with values between 155 ns and 236 ns, depending on the cabling of the setup.

Metronome
By using the module Metronome, all recorded telescope events are assigned to individual intervals in a sequence of 10 µs time intervals.The time intervals are sized to avoid large hit multiplicities leading to a large number of combinations that have to be processed during the calculations for subsequent reconstruction steps.

Timepix3
Raw data from Timepix3 reference planes is loaded and sorted in time by the EventLoader-Timepix3 module. For each Timepix3 detector, signals from the pixel matrix (TPX3) as well as auxiliary signals from inputs of the SPIDR readout board associated with a given reference plane are added to the clipboard.
Due to the continuous readout of Timepix3 detectors, the event loader relies on previously defined event start and end times on the clipboard or an instance of the Metronome module which provides similar timing information.

FASTPIX
For FASTPIX, the recorded raw waveforms require offline decoding (see Section 5.6) and are provided in pre-processed form to the EventloaderFASTPIX module. Decoded data is loaded synchronized with available trigger numbers on the Corryvreckan clipboard. Data without a matching trigger or incomplete events with missing triggers are discarded.
The later analysis of observables in the spatial and temporal domain is based on telescope events that are linked to a trigger on FASTPIX. For a study of detector efficiency, the telescope data stream is divided independent of FASTPIX triggers.

Oscilloscope
The module EventLoaderWaveform loads raw waveforms recorded by an oscilloscope and adds them to the event clipboard. Waveforms are matched to trigger numbers stored inside individual events and are later accessed for analysis by the AnalysisFASTPIXTiming module. Constant Fraction Discrimination (CFD) signal processing is used to determine the precise timing of the observed signal peak. In this approach, timing errors due to varying signal amplitudes are mitigated by identifying the point where the signal crosses a constant fraction of its peak value.

9.2.3. Clustering

Charge sharing between neighboring pixels can yield multiple recorded hits as a response of a singular impinging particle and necessitates the grouping of these impacted pixels into clusters.

For each individual detector, the module Clustering4D facilitates the clustering of recorded pixel hits, which are typically neighbors in space with signals close in time. Clusters are assembled from adjacent pixels that record hits within a 200 ns time window around the seed-pixel time. The time window was chosen such that time differences between all secondary pixels and the seed pixel are consistent within this range and the cluster size remains unaffected by the timing requirement [107]. The pixel with the earliest timestamp is used to set the cluster timestamp. Clusters get attributed a center position that corresponds to the hit position. In case of a single-pixel cluster, the hit position is obtained by using the pixel center. For cluster sizes > 1, a charge-weighted interpolation of the cluster geometry is applied, corrected for non-linear charge sharing using an η-correction algorithm [108, 109]. For FASTPIX this correction is conducted in radial coordinates (r,ϕ) to account for the different symmetry axes of the hexagonal pixel grid [110]. The methods applied for the reconstruction of the cluster position are described in Section 9.4. In further analysis, clusters can be treated as singular entities.

9.2.4. Noise

Noise predominantly occurs as single pixel clusters and during test beam operation is observed best in between spills.
Noisy pixels on the telescope planes are tracked by evaluation of hitmaps throughout all test beam campaigns and are masked during data taking based on previous studies [111]. In the process of the definition of a ROI for all Timepix3 reference detectors (Section 9.2.5), the enabled regions are confirmed to contain no masked Timepix3 pixels in overlap with FASTPIX matrices.
Since a masking of pixels on a hardware level is not implemented in the FASTPIX frontend, a veto is applied to noisy pixel candidates that are subsequently excluded from the alignment procedure.

9.2.5. Offline Pixel Masking

To ensure high hit-detection efficiency, the detection threshold is set to a value that accommodates a manageable noise rate. At this threshold, a limited number of noisy pixel cells predominantly contribute to the observed noise. Noisy pixels on FASTPIX have been identified by laboratory measurements presented in Section 7.3.2 and a threshold is chosen that yields a $O(\leq 10\,\text{Hz})$ noise rate on a given matrix.
Typically 3 pixels are masked on a given matrix, amounting to 5 % of the matrix and occasional cases with increased noise in closer to 15 % of pixels.
The mask file employs a syntax that is borrowed from rectangular pixel geometries, where either all pixels in a given column, all pixels in a given row, or a single pixel located at a specific column and row address can be selected. In the hexagonal grid the definition of a row, a series of pixels in horizontal orientation is analogues to the case of the rectangular grid. The column number describes the index of a given pixel in its row, counting from the left edge of the matrix, disregarding the fact that consecutive rows are offset by half a pixel pitch with respect to each other.
Noisy pixel candidates are excluded from the track reconstruction preceeding detector alignment (see Section 9.3.1), where they complicate the combinatorics of track finding, affect

the convergence of the track fit and increase computation times. With the final alignment in place, the noise floor in the analysis is reduced by strict association cuts that are backed by the high spatial and temporal tracking precision.

9.2.6. Correlations

Correlations are calculated by the Correlations module as the differences in cluster observables between a given detector plane and the predefined reference of the telescope system, the second downstream plane. They enable to evaluate the spatial and temporal displacement and serve as an in-situ feedback mechanism before comprehensive analytical tracking results are available. A time cut of 50 ns specifies the maximum absolute time difference between two clusters that are considered for correlation.
Spatial correlations evaluate the level of symmetry between the particle beam in close alignment with the telescope z-axis prior to track reconstruction. Correlations provide an appropriate starting point for the alignment procedure, prior to reconstructed tracks being available for reference. Exemplified in Figure 9.3a, the spatial correlation between FASTPIX and the reference plane typically displays a Gaussian core, with tails attributable to noise and combinatorial backgrounds. A shift of the peak away from the zero-position, as it can be observed for the x-axis data, is indicative of an offset in the physical displacement of a detector plane with respect to the reference plane.

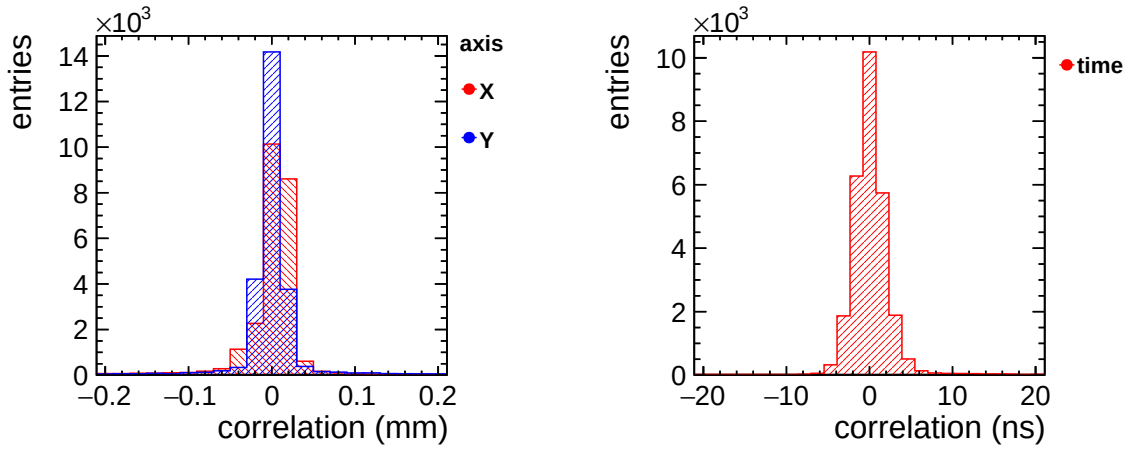

(a) Correlation in x-/y-dimension, $x_{\text{ref}} - x$ or $y_{\text{ref}} - y$, respectively.

(b) Correlation in time $t_{\text{ref}} - t$.

Figure 9.3: Correlations in space and time, calculated as difference between the measurement of a reference plane and the DUT measurement in global coordinates.

Temporal correlation evaluates the level of synchronization of the measurement system based on the global clock provided by the TLU. Figure 9.3b exemplifies the correlation in time between the FASTPIX and the telescope time reference plane. The distribution is plotted with a 1.5625 ns time binning, resembling the bin size of the on-chip TDC.
Furthermore, correlations are instrumental in setting appropriate cuts during track finding that exclude unlikely spatial and temporal coordinates in order to prevent misinterpretation an reduce computational load.

9.2.7. Track Reconstruction

The particle trajectories traversing the telescope setup are reconstructed by the module Tracking4D and provide the reference objects for the performance assessment of the DUT. The tracking process encompasses two main steps: track finding and track fitting.

Track Finding
Potential track candidates are identified by connecting clusters on the first and last telescope plane using a straight line. The track is refined as additional clusters from intermediate planes are incorporated. The clusters are selected based on spatial and temporal cuts that are adjusted based on the observed correlation widths and experimental conditions. Clusters on a given Timepix3 plane have to comply with $< 200\,\mu m$ absolute distance between the cluster center and track intercept as well as a time window of $\pm 20\,ns$ difference between track and cluster time stamp. The criteria for clusters are consciously stringent to enhance the reliability of track reconstruction. The DUT is systematically excluded to prevent analysis bias, treated instead as a passive element that at most contributes multiple scattering to the trajectory of the track.

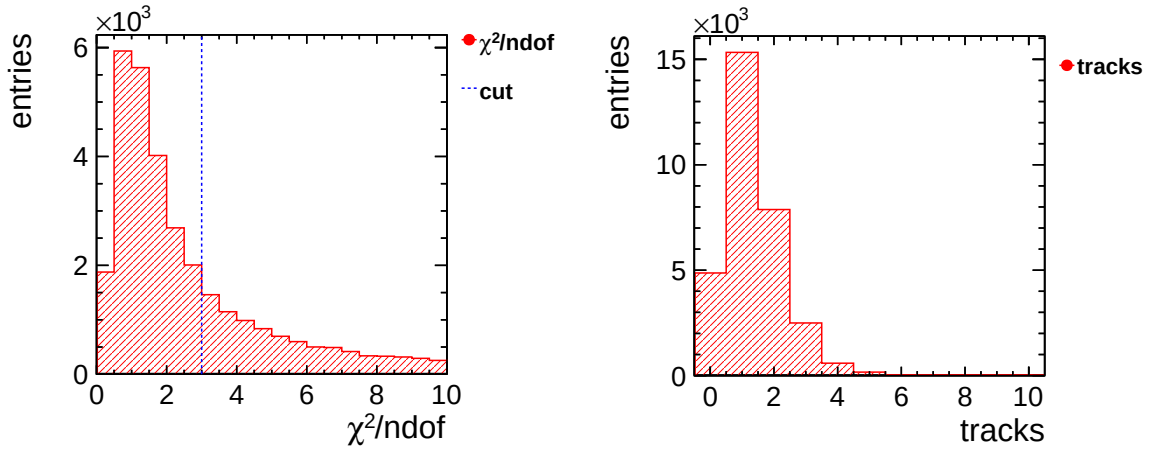

(a) χ^2 distribution with vertical marker at $\chi^2 = 3$. **(b)** Tracks per FASTPIX event.

Figure 9.4: Evaluation of the tracking process in form of fit quality and track multiplicity.

Track Fitting
The fitting process finalizes the particle trajectory using a straight-line track model adequate for the 120 GeV pion beam at the SPS North Area H6 beam line, where the effect of multiple scattering is small. The fitting process is quantified by minimizing the track chi-squared (χ^2), which is calculated by

$$\chi^2 = \sum_{i=0}^{n_{\text{meas}}} \left(\frac{(x_{t,i} - x_{c,i})^2}{\sigma_{x,i}^2} + \frac{(y_{t,i} - y_{c,i})^2}{\sigma_{y,i}^2} \right) \quad , \tag{9.1}$$

where $x_{t,i}$ and $y_{t,i}$ are the track intercepts on plane i, and $x_{c,i}$ and $y_{c,i}$ are the cluster positions on plane i that are part of the track. $\sigma_{x,i}$ and $\sigma_{y,i}$ represent the uncertainties of the cluster

positions, the single-plane spatial resolution. Figure 9.4a shows an exemplary distribution of χ^2 values from the fitted tracks of a single data taking run with 20 µm-pitch matrix 3 on sample W18S1-3. Each fitted track is required to intersect all 6 detector planes, incorporating uncertainties of cluster positions to refine the trajectory estimation. Only tracks with a $\chi^2/\text{ndof} < 3.0$ are considered, to exclude tracks comprising uncorrelated or spurious hits as well as tracks with multiple scattering. Figure 9.4b shows the number of tracks per processed FASTPIX event. The majority of those events encompass > 1 telescope track and about half of the events consist of a singular track. Events without tracks originate from e.g. excluded clusters on singular reference planes or imprecise track fits, both cause the track not to match the selection criteria.

9.2.8. Track-Cluster Association

The association between DUT cluster information and a given reference track is facilitated by the DUTAssociation module. The association process is central to the evaluation of DUT performance parameters like hit detection efficiency, the spatial resolution as well as the time resolution. Each track is interpolated to the z-position of FASTPIX, where the computed track intercept is gauged in its proximity to each reconstructed cluster. The cluster center closest to the track intercept is selected and validated by a predefined maximum distance in the spatial and temporal domain.
The selection cuts are derived from the widths of the 1-dimensional correlations including all clusters and all reconstructed reference tracks. A spatial cut of 20 µm in the x- and y-dimension probes the projected distance between the track intercept and the closest pixel of the cluster. An absolute difference in time of 15 ns between the reconstructed track and a given FASTPIX cluster cuts on fake noise hits from the DUT.

During the analysis, the module AnalysisFASTPIX addresses discrepancies at event boundaries. Tracks reconstructed close to the end of an event run the risk to loose their corresponding FASTPIX cluster to the beginning of the following event or inside a dead time of the oscilloscope readout. To mitigate the distortion of analysis observables such as hit detection efficiency, tracks are discarded if they occur less than 250 ns before the event edge and inside of the oscilloscope dead-time of 5 µs, while copying data from the readout buffer to the measurement server.
Figure 9.5 summarizes the time cuts applied for the selection of tracks and DUT clusters used for detector performance evaluation. Dashed areas represent the cuts around event edges, zig-zagged areas represent the oscilloscope dead-time. In both tracks (TRK) are discarded (dashed outline). The dotted area represents the time window in which a FASTPIX hit (FPX), a telescope track and a time reference signal (MCP) coincide, which arrives approximately 7 ns before the FASTPIX trigger.
In the spatial domain, the difference between cluster center and track impact position is enforced to be smaller than the pixel pitch of the investigated matrix. To avoid edge effects on the border of the pixel matrix, which are most likely for cluster sizes > 4 in the 4 x 16 pixel matrices, clusters with track intersect outside of the central 2 x 14 pixels are discarded.

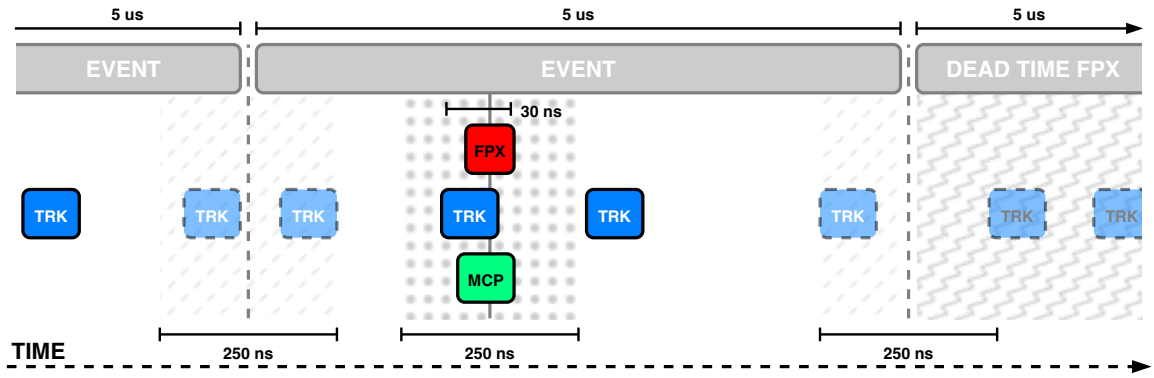

Figure 9.5: Schematic illustration of the applied time cuts for the FASTPIX performance evaluation.

9.3. Alignment

In addition to improvements of the mechanical alignment of the telescope setup presented in Section 8.2.2, the particle beam is used to further improve the alignment by calculating geometry offsets in translation and rotation with respect to the axes of the global telescope coordinate system. A precise knowledge of the detector plane positions relative to a common reference point is instrumental in reconstruction and analysis steps. The precision of the alignment impacts the quality of reconstructed tracks and ensures the correct association of a track with FASTPIX clusters. A reference spatial resolution at least an order of magnitude below the pixel pitch of the DUT is favorable to evaluate the spatial measurement performance of small-pitch matrices. Furthermore, in-pixel studies can reveal dependencies in observables on the particle intercept relative to the center of a pixel.

9.3.1. Alignment Sequence

The sequence of analysis modules used for the three applied alignment methods is illustrated in Figure 9.6. Precise plane position offsets in x-/y-direction are calculated in an iterative, multi-stage alignment procedure. Due to the geometry of the telescope setup, the data-driven alignment of positions along the z-axis (in direction of the beam) is not feasible. Manual measurements complete the geometry of the setup with an accuracy of ≈1 mm.
The alignment of the telescope planes in translation and rotation with respect to the reference plane is set within an individual geometry file for each data-taking run. A complete alignment of the telescope and its installed DUT is achieved through a pre-alignment step, followed by the telescope alignment and finally the DUT alignment.

9.3.2. Pre-Alignment

The initial translational pre-alignment of the telescope planes serves as a preparation for faster convergence in more complex, subsequent alignment steps. The pre-alignment adjusts the positions of the reference planes along the x- and y-axis by centering the spatial correlation mean at zero. The position offsets are calculated with respect to the first downstream Timepix3 detector plane, which itself remains stationary. Rotational misalignment is ignored

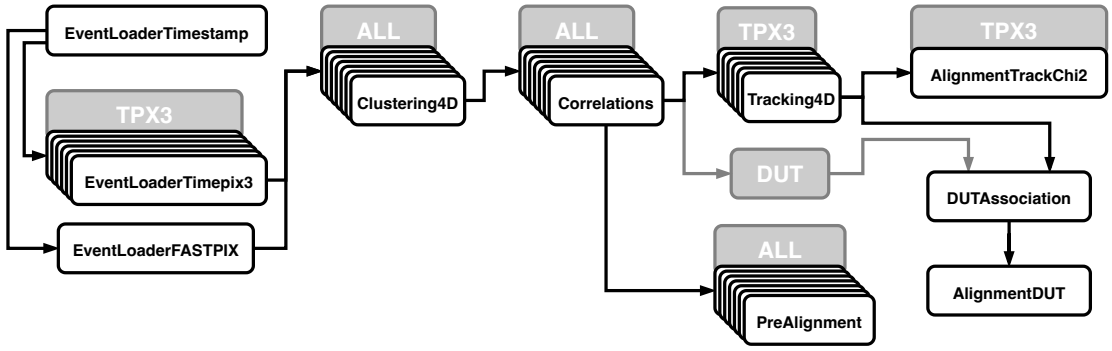

Figure 9.6: Sequence of modules in the Corryvreckan reconstruction and alignment chain.

during this step. In the final alignment the spatial correlations in x- and y-dimension reflect the actual physical displacement of the detector plane in relation to the reference plane. Approximating the shifts to be centered around zero is a functional estimation during the preliminary alignment.
The DUT is excluded during the initial telescope alignment e.g. after a reassembly of the telescope detector planes. It is included in the pre-alignment at the beginning of consecutive measurement campaigns between which only the DUT but not the telescope itself was changed. In this way, a change in x/y DUT position that is linked to a change in FASTPIX matrix between consecutive runs can be automatically pre-aligned based on the geometry of the preceding run.

9.3.3. Telescope Alignment

The telescope alignment process AlignmentTrackChi2 iteratively adjusts the positions and orientations of all telescope planes except the reference plane in x- and y-direction and around the x-, y-, and z-axes. In every iteration the chi-square (χ^2) value of the fitted tracks is minimized. The algorithm employs the Minuit2 package, which is specifically designed to determining a number of physical parameters and their errors through stages of function minimization [112]. The alignment process aims for a χ^2 per number of degrees of freedom (ndof) around 1.0, which is indicative of an optimal fit. The exemplary χ^2/ndof distribution in Figure 9.4a shows a pronounced peak at one, illustrating satisfactory alignment results.
Before the alignment has converged, the absolute spatial cut in Tracking4D is relaxed to a multiple of the 55 µm Timepix3 pixel pitch and is decreased incrementally down to the pixel pitch. Similarly, the χ^2/ndof cut is relaxed to 30 and progressively is decreased to a cutoff at 3. This allows to exclude significant outliers and select only the high quality tracks for the final high-precision alignment steps.

9.3.4. DUT Alignment

The DUT is similarly aligned in an iterative process that adjusts both its position and orientation. The algorithm minimizes the unbiased spatial residual width between the DUT and the reference tracks and runs until a stable convergence is achieved. The result is finalized after incremental adjustments < 0.0001 mm or $< 0.01°$ are reached by the previous iteration. An exclusive alignment of displacement precedes the combined position and

rotation alignment of the DUT. This strategy prevents from over-rotation or a potential misalignment arising from inadequate track fits. Similar to the telescope alignment, the spatial cuts are adjusted throughout multiple alignment iterations, starting at a factor of 3× down to 1× the pixel pitch of a given FASTPIX matrix. A cut of $\chi^2/\text{ndof} < 3$ selects high track quality during the alignment procedure, which is even lowered to 2 for 8.66 µm- and 10 µm-pitch matrixes. Only tracks with a single associated FASTPIX cluster are selected.
During this process, the alignment of the telescope remains unchanged, ensuring that the reference tracks are consistently reconstructed.

9.4. Cluster Position Reconstruction

The segmentation of the top sensor n-layer into a grid of pixels allows measurements of traversing particles in the spatial domain. Section 4.2 discusses the spatial measurement achieved with a grid of hexagonal pixels. Considering the entire area and assuming a uniform distribution of particle intercepts, the binary resolution provides a first estimation of spatial resolution based on the hexagonal pixel pitch.
The addition of information on the recorded signal amplitude per pixel enables a charge-weighted interpolation of the binary hit information in pixel clusters of size ≥ 2. The following section describe the position reconstruction techniques employed for the reconstruction and analysis of test beam data.

9.4.1. Charge-Weighted Position Reconstruction

Deposited charge that is shared among neighboring pixels results in a cluster of pixels with individual recorded signal height corresponding to their distance from the particle hit. These differences in recorded signal height can be incorporated into the calculation of the spatial hit coordinates.
A centre-of-gravity algorithm (CoG) determines the cluster centre x_c as the charge-weighted single pixel positions x_i divided by the total cluster charge:

$$x_c = \frac{\sum q_i x_i}{\sum q_i} \quad , \tag{9.2}$$

where x_i ist the single pixel position and q_i is the single-pixel charge of the i-th pixel in the cluster.
Figure 9.7 illustrates two exemplary clusters in a hexagonal grid with cluster size 2 and cluster size 3, both evaluated in radial coordinates. The algorithm is applied to the data from all detectors within the scope of this thesis. In addition to the CoG, the precision of the reconstructed cluster position is improved further in order to account for non-linear charge sharing effects.

9.4.2. Eta Correction for Non-Linear Charge Sharing

Equation (9.2) assumes a linear relationship between the distance from the collection electrode to the track intercept and the amount of charge registered by the frontend of a given pixel. However, the non-uniform field configuration of FASTPIX with strong lateral field components intentionally modifies the diffusion behavior of charge carriers and introduces non-linearities.

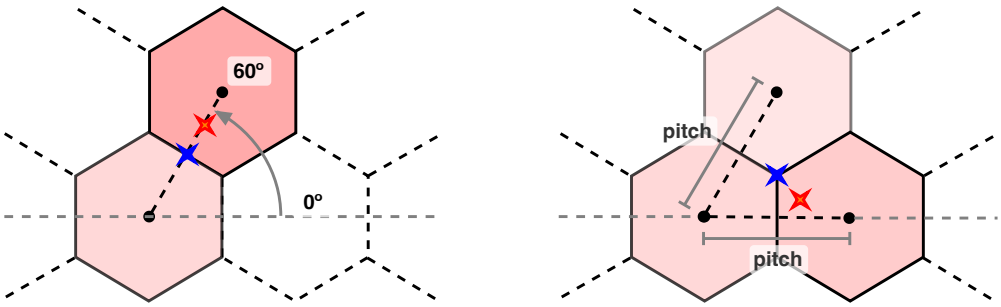

Figure 9.7: Illustration of pixel cluster in a hexagonal grid with examples for cluster size 2 and 3. The geometrical cluster center is marked in blue. The cluster position from the CoG algorithm is marked in red.

Since an overestimation/underestimation of the single-pixel share of charge introduces a bias to the interpolated cluster position towards/away from the pixel in question, a correction for the non-linear charge sharing is applied.

The η-algorithm [108, 109] is a method used to improve the accuracy of particle position measurements by modelling the impact of non-linear charge sharing at the pixel borders, which is corrected for 2- and 3-pixel clusters. For infrequent larger-size clusters, the η-algorithm looses its advantage to the increased number of terms in the charge-weighted position reconstruction. Delta rays (see Section 3.2.2) contribute to larger cluster size outside of the modeled charge-sharing effects.
The data-driven method compares between the cluster position reconstructed by the CoG algorithm and the more accurate position reconstructed at the intersect of the telescope reference track with the DUT.

Corryvreckan implements the η-correction in a two-step procedure. The module EtaCalculation obtains the correction coefficients based on all tracks and associated clusters that comply with the cuts introduced in Section 9.2.8. For cluster sizes 2 and 3, the telescope track position is plotted against the reconstructed cluster position for each axis of the detector coordinate system.
For FASTPIX this correction is conducted in radial coordinates to account for the different symmetry axis of the hexagonal pixel grid [110]. The initial cartesian coordinates (x, y) are transformed to ρ, ϕ and yield the exemplary η-distributions profiles shown in Figure 9.8 for 20 µm-pitch matrix 3 on sample W18S1-3.
In radius ρ (Figure 9.8a), two-pixel clusters yield a largely linear relationship between cluster and track coordinate. The reference pixel for the calculation is defined as the lowest, left-most pixel in the cluster which causes the absolute cluster positions of the distribution profile to extends from 0 µm to 20 µm, the pixel pitch of the matrix. The angular coordinate ϕ in Figure 9.8a exhibits three discrete cases, values -1 rad, 0 rad and 1 rad, which correspond to angles $-60°$, $0°$ and $60°$, respectively. In the pointy-topped hexagonal grid a singular pixel neighbor shares charge either along the lower-right, the right or upper-right edge. Here, a fit is redundant.
For the three-pixel case in Figure 9.8c, ρ exhibits a similar trend since an in-line cluster of size three is very unlikely for perpendicular track angles and diffusion-based charge sharing. The

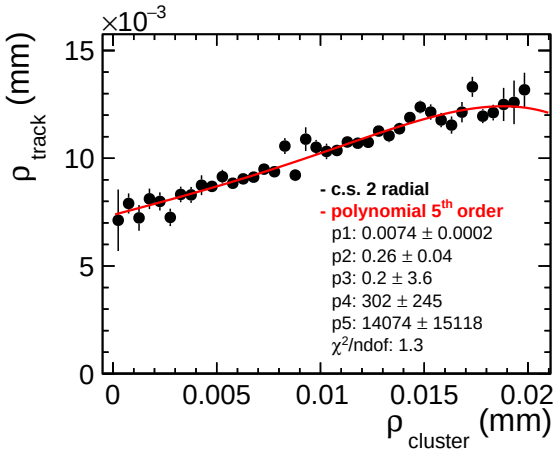

(a) ρ: 2-pixel clusters.

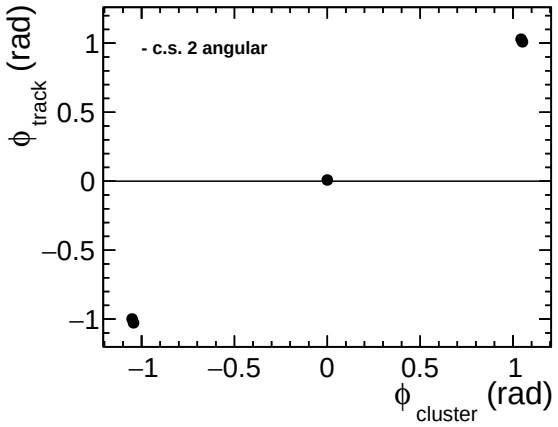

(b) ϕ: 2-pixel clusters.

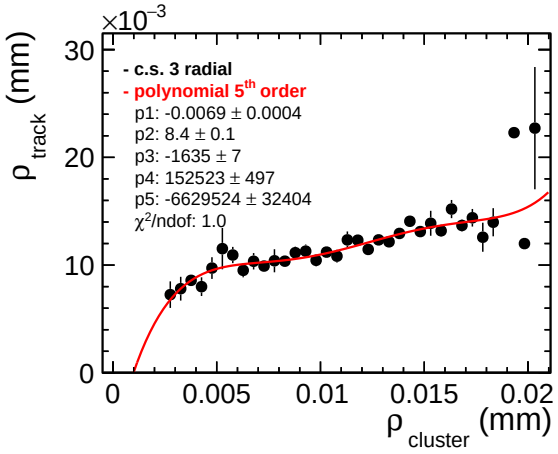

(c) ρ: 3-pixel clusters.

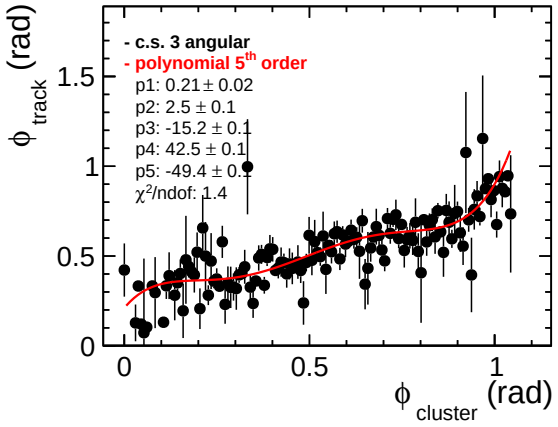

(d) ϕ: 3-pixel clusters.

Figure 9.8: η-distributions for 2- and 3-pixel clusters in radial coordinates (ρ, ϕ) from 20 µm-pitch matrix 3 on sample W18S1-3. A 5-th order polynomial is fitted to the distributions.

angular coordinate ϕ in Figure 9.8d now populates continuos intervals $[-60°, 0°]$ and $[0°, 60°]$ which can be combined into one quadrant due to the symmetry of the hexagonal grid.

The resulting eta distribution profiles are fitted with a 5th order polynomial function

$$y(x) = [0] + [1]x + [2]x^2 + [3]x^3 + [4]x^4 + [5]x^5 \quad , \tag{9.3}$$

with six fit parameters modeling every coordinate independent of the respective coordinate system. The fit result contains the correction parameters for the reconstructed cluster position. An η-correction configuration file is updated with eta correction parameters and formulas.

In the second step of the procedure, the module EtaCorrection applies the calculated correction to the run data before correlations. Similar to the η-calculation step, the correction is applied in the coordinate system of the calculation. In the case of the radial coordinate system used

for FASTPIX, the corrected cluster coordinates are transformed to the cartesian system for compatibility with the computation in the following framework modules.

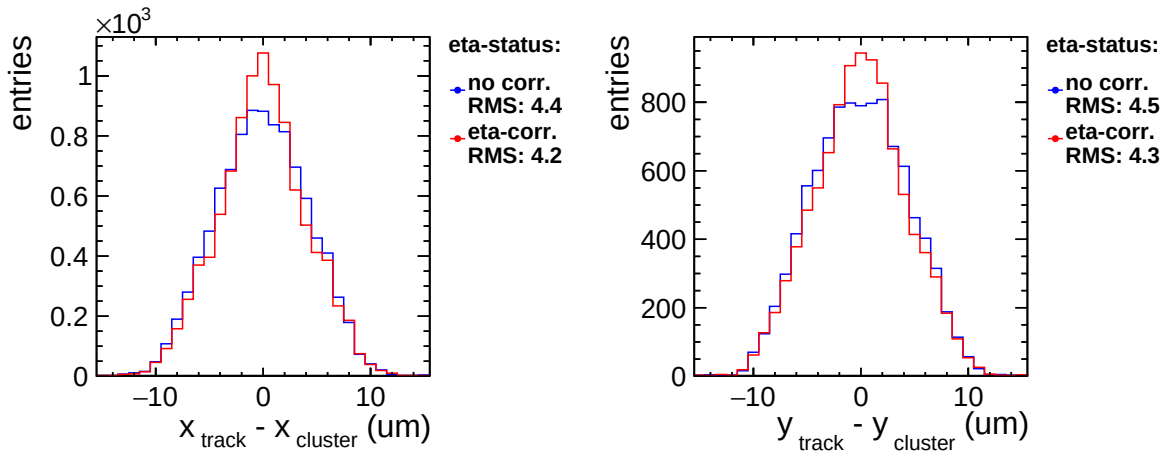

(a) Residuals along x-axis.

(b) Residuals along y-axis.

Figure 9.9: Local spatial residuals of 20 µm-pitch matrix 3 on sample W18S1-3 with and without η-correction.

Figure 9.9 illustrates the impact of the η-correction for non-linear charge sharing in the 20 µm-pitch pixel grid of matrix 3 on sample W18S1-3. The comparison of the spatial residuals before and after correction yields an ≈5 % improved RMS.

9.5. Observables

Reconstructed tracks are matched to FASTPIX clusters and provide a reference for the evaluation of its performance. The observables noise, cluster size, hit-detection efficiency, spatial resolution and time resolution are analyzed based on the reconstructed track information.

9.5.1. Noise

Figure 9.10 shows the timestamps of clusters recorded by FASTPIX during the first 280 s of a data taking run with 20 µm-pitch matrix 3.
The spill structure is visible by an increased number of entries per bin. The number of bin entries corresponds to the number of pixels that have seen signal above threshold in the single bin time window of 0.1 s. Noise causing a two pixel cluster is unlikely at the noise rates observed in test beam.
The beginning and end of a spill is found by measuring the time between the current and the previous multi-pixel cluster. A flag is used to track whether a cluster is part of a spill by evaluating the measured time difference to the previous "in-spill" candidate against a maximum allowed distance. Looping through the binned timestamps of events in sequential and in reversed order allows to catch both the beginning and end of a spill.
The red data set represents cluster timestamps during a spill which are framed by the the spill flag in blue, as detailed in Figure 9.10b. This separation into physics signals in spill and noise based on the timing and density of the observed clusters allows to count the total number of

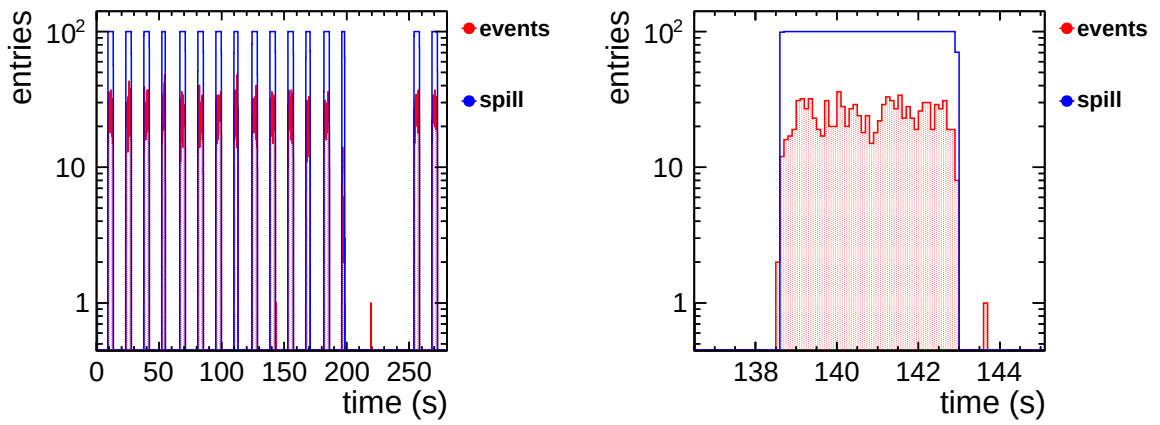

(a) First 280 s of measurement time.

(b) Zoom: spill/noise separation.

Figure 9.10: Cluster timestamps (red) and extracted spill envelope (blue).

clusters and the time duration in each category. The uncertainty in counting is $\Delta N = \sqrt{N}$, following a Poisson distribution.

9.5.2. Cluster Size

The extent of charge sharing across multiple pixel cells is quantified by the cluster size, defined as the number of pixels forming a reconstructed cluster. In the case of FASTPIX, the modified process variants and optimized lateral electric field of the sensor design optimizations are expected to exhibit variations in charge sharing between individual pixel matrices. Sub-threshold effects impact the observed cluster dimensions, as charge that does not induce a signal amplitude above the detection threshold remains undetected. Reduced signal form insufficient depletion of the epitaxial layer has a similar effect.
In addition, clusters are incorrectly identified due to spatial constraints of the 4×16 pixel grid of a given FASTPIX matrix. Cluster size is not resolved with total certainty as soon a two of its pixels are located along the border of the active area of the matrix. Energy depositions in matrix edge pixels share charge with inactive pixels in the matrix periphery and yield observed cluster sizes smaller than actual. To counter this, the local intercept position is determined and used to restrict cluster seed pixel locations to the central 2×14 pixels of the matrix. At the expense of half of the measurement statistics, the geometric bias in cluster size assessments is reduced by giving more margin for charge sharing within the sensitive volume of a matrix.

9.5.3. Hit-Detection Efficiency

The hit-detection efficiency ϵ is quantified by the ratio between the number of tracks linked to a FASTPIX cluster and the total number of tracks traversing the acceptance region of a given matrix. The total number of tracks is made available to the analysis by the Metronome module (Section 9.2.2) which assigns all recorded telescope hits to individual events in a sequence of

10 µs time intervals. The efficiency is calculated as

$$\epsilon = k/N \quad , \tag{9.4}$$

where k is the count of tracks associated with a cluster and N is the aggregated number of tracks considered. The evaluated acceptance encompasses the area of the active pixel matrix, omitting a single column and row along the peripheral edges. The spatial precision of the tracking system allows the analysis of efficiency variations across the area of the pixel cell. Efficiency evaluations obey binomial statistics

$$L(\epsilon \mid k, N) = \binom{N}{k} \epsilon^k (1-\epsilon)^{N-k} \quad , \tag{9.5}$$

where the binomial distribution serves as the likelihood function L. The arguments of the model comprise the mean efficiency ϵ and the terms k and $N - k$ as the count of successes and failures in detection, respectively. Confidence intervals for the calculated efficiency are computed using the Clopper-Pearson method [113], which provides exact binomial confidence intervals and was previously introduced in Section 6.4.3 in the context of threshold energy calibration.
Noise can inflate the observed efficiency,

$$\epsilon_{\text{measured}} = \epsilon_{\text{true}} + (1 - \epsilon_{\text{true}}) \cdot \epsilon_{\text{noise}} \quad , \tag{9.6}$$

where ϵ_{noise} denotes the probability of falsely associating a track to a noise hit. As confirmed in Section 7.4, a noise rate of <10 Hz is to be expected at the foreseen test beam detection threshold. Consequently, $\epsilon_{\text{noise}} \simeq 0$ due to the 15 ns association cut between track and possible noise hit.

9.5.4. Spatial Resolution

The spatial resolution of FASTPIX is extracted from the spatial residual width in local detector coordinates. For every track candidate that meets the cuts introduced in Section 9.2.8, the analysis calculates the difference in position between the reconstructed track intercept on the sensor and the observed cluster position from the CoG algorithm with corrections for non-linear charge sharing.

$$x_{\text{residual}} = x_{\text{track}} - x_{\text{cluster}} \quad , \tag{9.7}$$

Since the cluster is not part of the track formation, it does not impact the measurement outcome and acts as an independent observable.
Assuming a Gaussian distribution, the DUT resolution σ_{FPX} is unfolded from the calculated residual values through a quadratic subtraction of the telescope resolution $\sigma_{\text{telescope}}$ from the overall measured distribution width σ_{measured}.

$$\sigma_{\text{FPX}} = \sqrt{\sigma^2_{\text{measured}} - \sigma^2_{\text{telescope}}} \quad . \tag{9.8}$$

The telescope pointing resolution at the DUT position in the center of the setup can be estimated using the Telescope Optimizer [114]. The calculator uses the GBL formalism to

take multiple scattering in the telescope planes and the surrounding air into account. The 120 GeV c^{-1} pions and a close arrangement of the reference planes, which are optimized for low-material-budget tracking, reduce the impact of multiple scattering. This is reflected by a very small impact from changes in material budget on the simulated tracking resolution in the beam and geometry parameter set of the telescope setup. An intrinsic single-plane spatial resolution of 2.7 ± 0.2 µm is assumed for telescope plane [97]. The biased residuals exemplified in Figure 9.11 are the distances between the measured hit and the biased track fit. The squared biased residual width r_b^2 can be calculated by subtracting in quadrature the intrinsic resolution σ_{int} of the sensors from the telescope track resolution $\sigma_{t,b}$:

$$r_b^2 = \sigma_{int}^2 - \sigma_{t,b}^2 \quad , \tag{9.9}$$

at the position of a given telescope plane [115]. The measured biased residuals for tracks with $\chi^2/\text{ndof} < 3$ are exemplified in Figure 9.11 for the telescope reference plane 4.

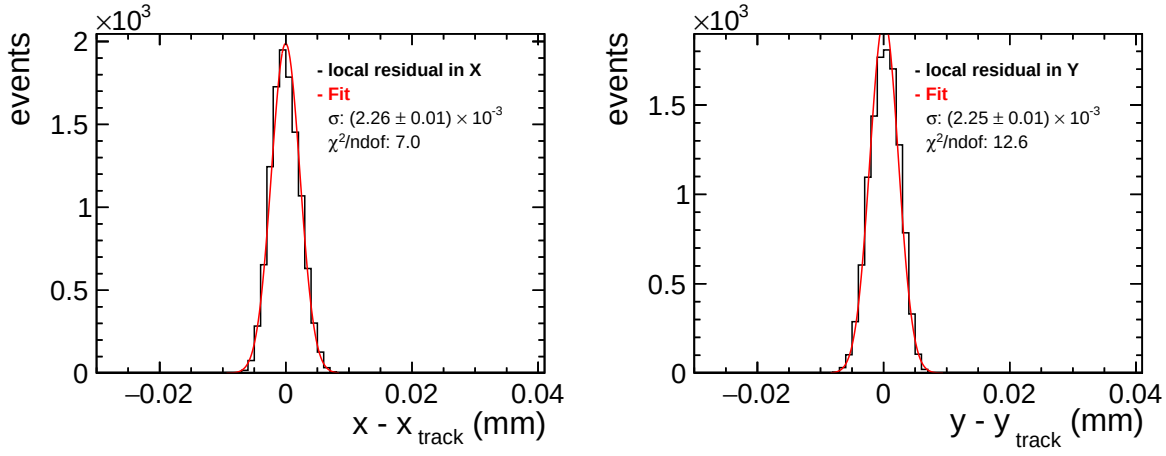

(a) In x direction.

(b) In y direction.

Figure 9.11: Biased local residuals of telescope plane 4, the reference plane for reconstruction and analysis of telescope data.

The exemplified distribution yields a width of 2.26 ± 0.10 µm along the x-axis and 2.25 ± 0.10 µm in y direction, both obtained as the standard deviation of a Gaussian fit.
Based on the telescope geometry listed in Table 8.2 and the material budget in Section 6.2.1, the Telescope Optimizer yields the biased tracking resolution. Agreement between measured and calculated values was found for an assumed intrinsic resolution of 2.9 ± 0.2 µm. This correspond to a tracking resolution at the position of the DUT of 1.25 ± 0.10 µm.

9.5.5. Time Resolution

For studies of time measurement precision, the time associated with the fastest-signal pixel in a cluster is used to calculate the time residual with respect to the reference track time t_{track}

$$t_{\text{residual}} = t_{\text{track}} - t_{\text{FPX cluster}} \quad . \tag{9.10}$$

As discussed in Section 4.4.2, better temporal resolution is expected with larger signal sizes and/or lower detection thresholds due to faster rise times, enhancing comparator sensitivity against jitter.

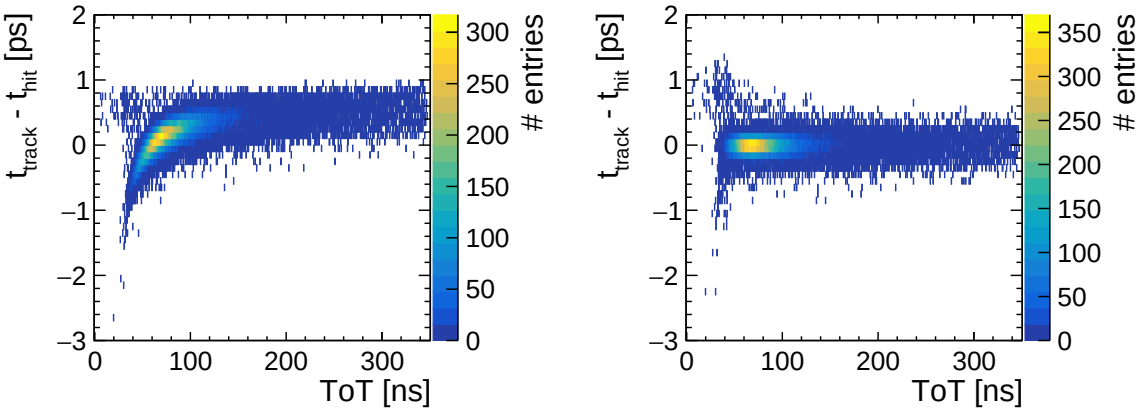

(a) Without correction.

(b) With timewalk correction.

Figure 9.12: Time residuals as function of seed signal for all pixels in the inner 2 x 14 pixel region of a 20 µm pitch matrix.

Figure 9.12a shows the residuals over seed-pixel ToT for all pixels in the inner 2 x 14 pixel region of 20 µm-pitch matrix 3 on sample W18S1-3. The data is indicative of a delayed hit timestamp with respect to the track timestamp and exhibits the expected timewalk behavior for small signal amplitudes (ToT).

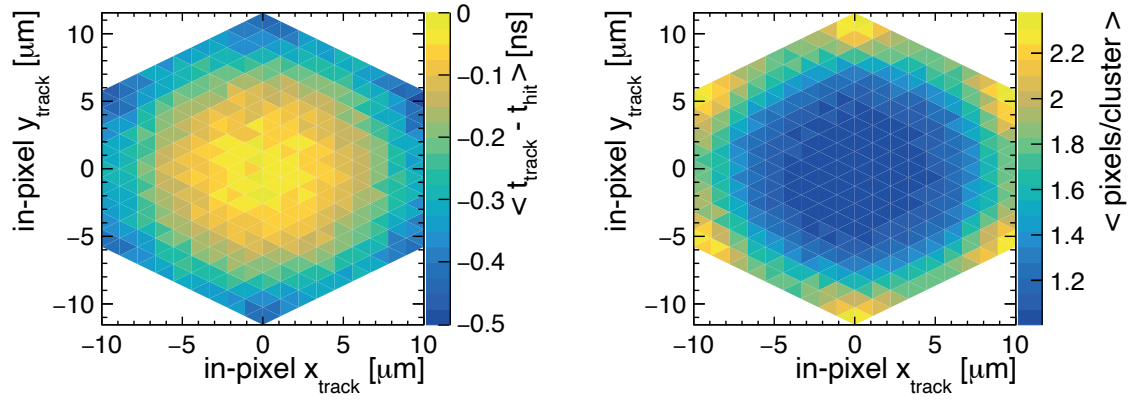

(a) Mean time residual in relation to in pixel track position.

(b) Mean number of pixels per cluster in relation to in pixel track position.

Figure 9.13: Time residual without time-walk correction and cluster-size maps for in-pixel track incidence positions in x-/y-plane of a 20 µm pixel pitch matrix. Hits from all pixels are projected into one hexagonal pixel area.

The equivalent in-pixel plot and a related in-pixel cluster-size distribution is shown in figure 9.13 and presents a dependency of the timing performance and correlated cluster size on the in-pixel particle incidence location. This suggests a time-walk correction approach

per cluster size applied on subsets of data. For each cluster size ≤5 an exclusive data set is assembled and used to evaluate the time residual in relation to ToT on a pixel-by-pixel level. Clusters >5 are grouped into a combined set to retain sufficient statistics for further analysis. A custom script corrects for the time-walk effect on independent halves of the data set.
The correction process is initialized with the creation of bins that hold the same accumulated number of data points, grouped such that each bin has to surpass a predefined count threshold before the next bin is created. The binning procedure aids in segregating similar events and allows for statistical corrections to be uniformly applied.
For each bin, the average deviation (Δt) is computed with respect to ideally expected zero-delay, representing the time offset for a given bin. Δt is calculated only for entries that fall within acceptable t_{residual} and ToT ranges, ensuring that outliers do not skew the correction factors.
The computed mean corrections are finally applied across the whole dataset by subtracting the corresponding bin's mean $\Delta t$from the opposite half of data, and vice versa.

Figure 9.12b exemplifies the residuals over seed-pixel ToT for all pixels in the inner region of the 20 µm-pitch matrix after time-walk correction, showing no significant dependence on signal height. The cluster-size-specific subsets have been rejoined after individual correction.

The temporal resolution is calculated by subtracting in quadrature the resolution of the track time τ_{track} from the τ_{measured} of a Gaussian fit of the time residual distribution:

$$\tau_{\text{FPX}} = \sqrt{\tau^2_{\text{measured}} - \tau^2_{\text{telescope}}} \quad (8.7) \tag{9.11}$$

The MCP-PMT time reference detector is used to provide tracks with high-precision timestamps. The peaks in a waveform are identified as the signal crosses a threshold of 15 mV and are detected as pairs of rising and falling edges. The baseline is the level from which the waveform deviates, as determined by the threshold crossings. For each pair of edges, the minimum value within the region is found and the CFD position is calculated as the point where the waveform crosses 1/5 of the peak minimum. The time of the CFD position is found using linear interpolation.

The time measurement precision at the settings applied during the FASTPIX test beam campaigns is characterized in measurements with three MCP-PMTs mounted onto the downstream telescope arm. Two similar HPK R3809U-50 devices MCP0 and MCP1 as well as MCP3, a Photek PMT240 device, are read out simultaneously by the oscilloscope readout, triggered by coincident signals in all three detectors. Telescope tracking allows to constrain the evaluation to a circular region of interest with a 4 mm diameter, which largely covers the positions of FASTPIX matrices projected onto the timing detector acceptance.
The convoluted time residual distributions between selected detector pairs can be related to the individual time measurement precisions, assuming the residuals obey a Gaussian distribution. The standard deviations of the convoluted time residual distributions are $\sigma_{01} = \sqrt{\sigma_0^2 + \sigma_1^2}$ (MCP0 and MCP1), $\sigma_{02} = \sqrt{\sigma_0^2 + \sigma_2^2}$ (MCP0 and MCP2) and $\sigma_{12} = \sqrt{\sigma_1^2 + \sigma_2^2}$ (MCP1 and MCP2), with individual standard deviations σ_0, σ_1 and σ_2

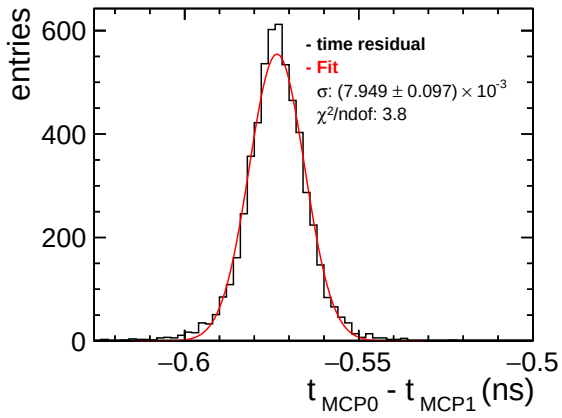

(a) T1742 & T1499.

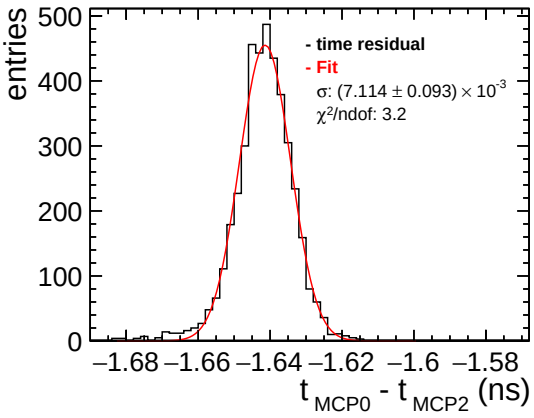

(b) T1742 & PMT240.

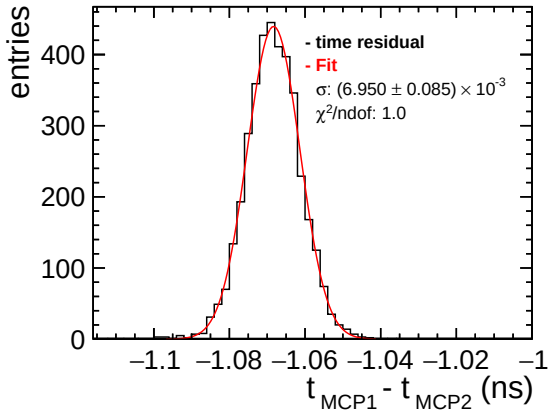

(c) T1499 & PMT240.

MCP-PMT	MCP0	MCP1	MCP2
HV (kV)	3.2	2.6	3.8
I (µA)	88.9	72.3	71.4
S (V/div)	0.1	0.05	0.05
τ_{MCP} (ps)	5.7 ± 0.1	5.5 ± 0.1	4.2 ± 0.1

(d) Deconvoluted resolution τ_{device} for set high voltage bias HV, measured current I and oscilloscope channel input gain S.

Figure 9.14: MCP-PMT time measurement precision based on measurements with three timing detectors.

These relationships are used to solve for the individual precisions.

$$\sigma_1 = \sqrt{\frac{\sigma_{01}^2 + \sigma_{12}^2 - \sigma_{02}^2}{2}} \quad , \quad \sigma_0 = \sqrt{\sigma_{01}^2 - \sigma_1^2} \quad \text{and} \quad \sigma_2 = \sqrt{\sigma_{12}^2 - \sigma_1^2} \quad . \tag{9.12}$$

The extracted time measurement precisions τ_{MCP} of MCP0, MCP1, and MCP2 are listed in Figure 9.14d. The statistical error on the width of the fit is propagated to the individual time measurement precisions. MCP1 is used for the time measurement observables in the following test-beam characterization of FASTPIX. The resulting 5.5 ± 0.1 ps represent the timing precision at a bias voltage of 2.6 kV.

10

Detector Performance in Test-Beam Measurements

During 12 week-long test beam campaigns between summer of 2021 and autumn of 2023, 3785 runs of measurement data were taken with the matrices on 4 FASTPIX samples, a test beam effort that is summarized by Table 10.1.

Table 10.1: Summary of Test Beam Campaigns

Campaign	Dates	Days	Runs	FASTPIX (GB)	Telescope (GB)
Jul. '21	06.08 - 11.08	6	905	91.97	4371.55
Sep. '21	02.09 - 13.09	11	330	146.21	1175.65
Oct. '21	06.10 - 20.10	15	765	285.46	5006.68
May '22	20.05 - 25.05	6	321	54.69	1429.96
Jun. '22	01.07 - 04.07	4	128	31.42	573.33
Nov. '22	11.11 - 14.11	4	105	53.05	410.14
May '23	22.05 - 24.05	3	88	103.45	307.63
Jun. '23	08.06 - 14.06	7	220	204.24	1113.40
Jul. '23	07.07 - 10.07	4	223	159.23	1249.80
Jul. '23	28.07 - 02.08	6	408	298.52	2530.92
Aug. '23	23.08 - 29.08	7	392	164.85	2184.02
Total		73	3785	1492.79	19753.08

The test beam results in this chapter open with an evaluation of observed rates of hits and fake hits during and outside of a spill, respectively. The following sections of the chapter attend to the performance observables charge sharing (Section 10.2), signal (Section 10.3), hit-detection efficiency (Section 10.4), spatial resolution (Section 10.5) and time resolution (Section 10.6). For each observable the effect of modification of the CMOS manufacturing process as well as the impact of optimized pixel design variants are discussed. The chapter aims to extract the performance gained by the large parameter space of improvements to the manufacturing process and pixel cell.

10.1. Noise

In order to avoid a bias from noisy pixels during the reconstruction of the test beam data, the detection threshold of FASTPIX samples is set to yield a noise rate more than an order of magnitude lower than the observed minimum hit rates on the smallest-pitch matrices. A significantly increased fake hit rate saturates the FASTPIX delay line logic, increases the occupancy of the readout system and complicates the pixel decoding.

10.1.1. Fake Hit Rate

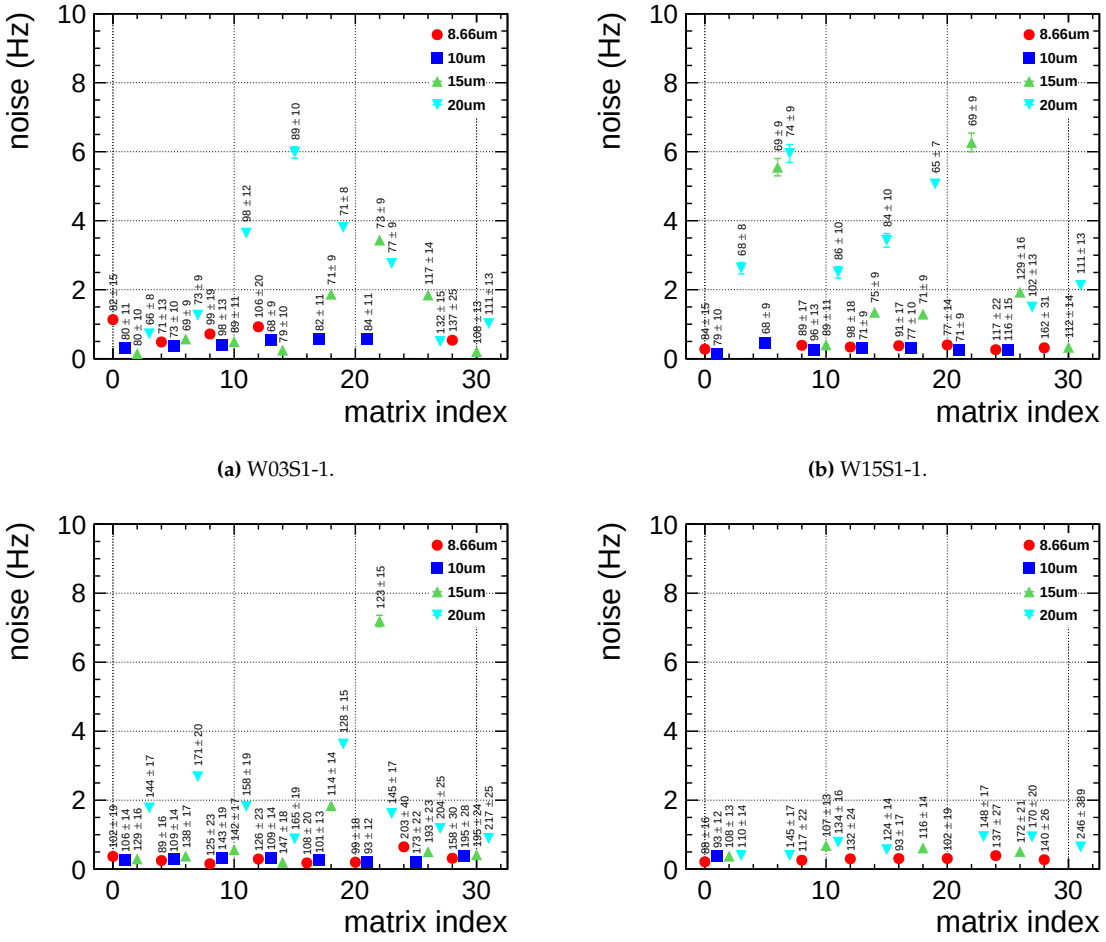

(a) W03S1-1.

(b) W15S1-1.

(c) W18S1-3.

(d) W18S1-4.

Figure 10.1: Noise rate at $i_{\mathrm{thr}} = 0.82\,\mathrm{V}$ for three FASTPIX samples W03S1-1,W15S1-1, W18S1-3 and W18S1-4. The superscript specifies the threshold in electrons for the respective matrix.

The noise rate is shown in Figure 10.1 for all tested matrices on standard-process sample W03S1-1, modified-process sample W15S1-1 as well as both most-modified-process samples W18S1-3 and W18S1-4. The rate is defined as the rate of single pixel events on the detector between spills and is a measure of detected fake hits during test beam data taking.

For all samples the typical recorded noise rate on a matrix at nominal threshold $i_{\text{thr}} = 0.82\,\text{V}$ is below 2 Hz with a few outliers at higher rates <10 Hz. The matrices that are found to be noisy in test beam match the matrices identified in Section 7.4, which reach a 10 Hz noise rate at a higher threshold (lower i_{thr}), compared to the majority of matrices.

10.1.2. Hit Rate

Figure 10.2 summarizes the observed hit rates during a spill, measured with all tested matrices on sample W18S1-3 at $i_{\text{thr}} = 0.82\,\text{V}$ and gives the mean values per pitch, which is equivalent to the rate per active matrix area.

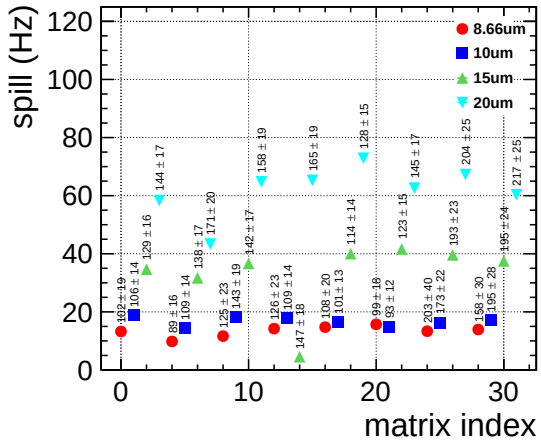

(a) Rate for all tested matrices. The superscript specifies the threshold in electrons for the respective matrix.

Pitch (µm)	Area (µm^2)	<Rate> (Hz)
8.66	16640	13 ± 1
10.0	22144	17 ± 1
15.0	49856	33 ± 4
20.0	88704	62 ± 3

(b) Mean spill rate and single-pixel area per pixel pitch.

Figure 10.2: Rates during spill measured with W18S1-3 at $i_{\text{thr}} = 0.82\,\text{V}$.

The nominal threshold was chosen as a compromise between detectable signal range and data taking efficiency. During the analysis of test beam measurements, fake hits are suppressed through the association of DUT clusters to a reference particle track in the telescope. With spill rates >10 Hz, a small rate of fake hits can be tolerated in favor of a lower detection threshold setting. The noise contribution to the measurement is negligible, especially in measurements from campaigns in 2023, where the beam line settings were improved to ≈4 times higher track rates.

10.2. Charge Sharing

Charge sharing is one of the central aspects considered in sensor design and is adapted to the requirements of a specific application, as discussed in Section 4.2. The geometry of the overall pixel cell with implant structures along its edges informs the field configuration and depleted region within the pixel volume and determines the charge sharing behavior in the pixel grid. As a measure of charge sharing, the observed cluster size is used to evaluate the impact of the process modifications and sensor design variations.

10.2.1. Pixel Level

Based on the concept introduced in Section 4.2.2, the impact position of a beam particle within the pixel cell is expected to inform the observed cluster size. Figure 10.3 shows the in-pixel representation of the mean total cluster size for the first four matrices of sample W18S1-3. For a given matrix, the plot combines all registered track positions relative to the center of the individual pixel, folded into one hexagonal pixel cell.

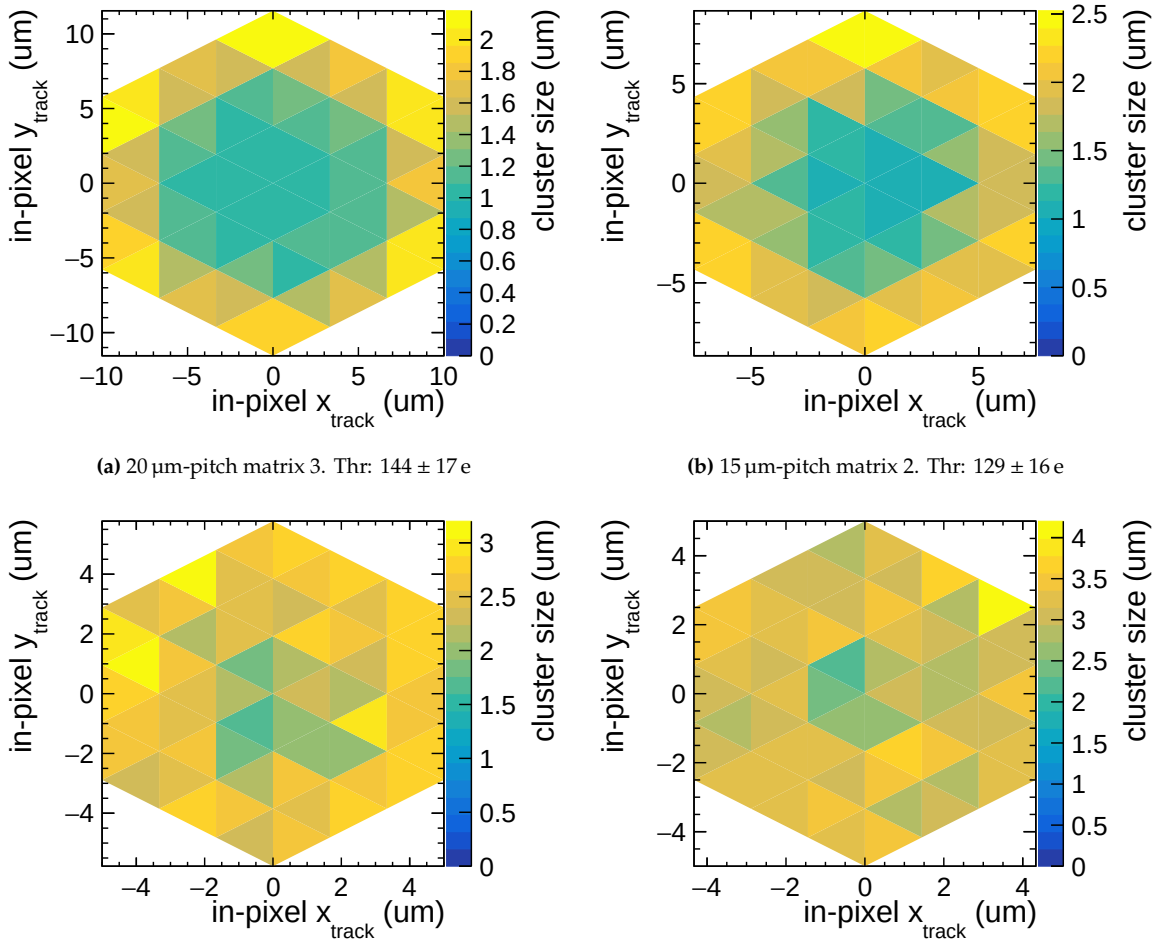

(a) 20 µm-pitch matrix 3. Thr: 144 ± 17 e

(b) 15 µm-pitch matrix 2. Thr: 129 ± 16 e

(c) 10 µm-pitch matrix 1. Thr: 106 ± 14 e

(d) 8.66 µm-pitch matrix 0. Thr: 102 ± 19 e

Figure 10.3: In-pixel mean cluster size distributions at $i_{\text{thr}} = 0.82\,\text{V}$ of the first four matrices on most-modified sample W18S1-3.

The dependency of cluster size on particle intercept position is most pronounced with larger pitch matrices and looses its definition as the pitch decreases. Single-pixel clusters predominantly occur as a result of a particle impinging on the center of a pixel cell. In this case the interaction mechanism generates charge carriers in the lateral vicinity of the collection electrode. The origin of the largest clusters is the pixel corner position, which holds the closest distance to the neighboring pixel and the furthest distance to the collection electrode. In combination with a weaker electric field, a particle impinging on the corner of a pixel results in a high contribution from charge carrier diffusion.

10.2.2. Matrix Level

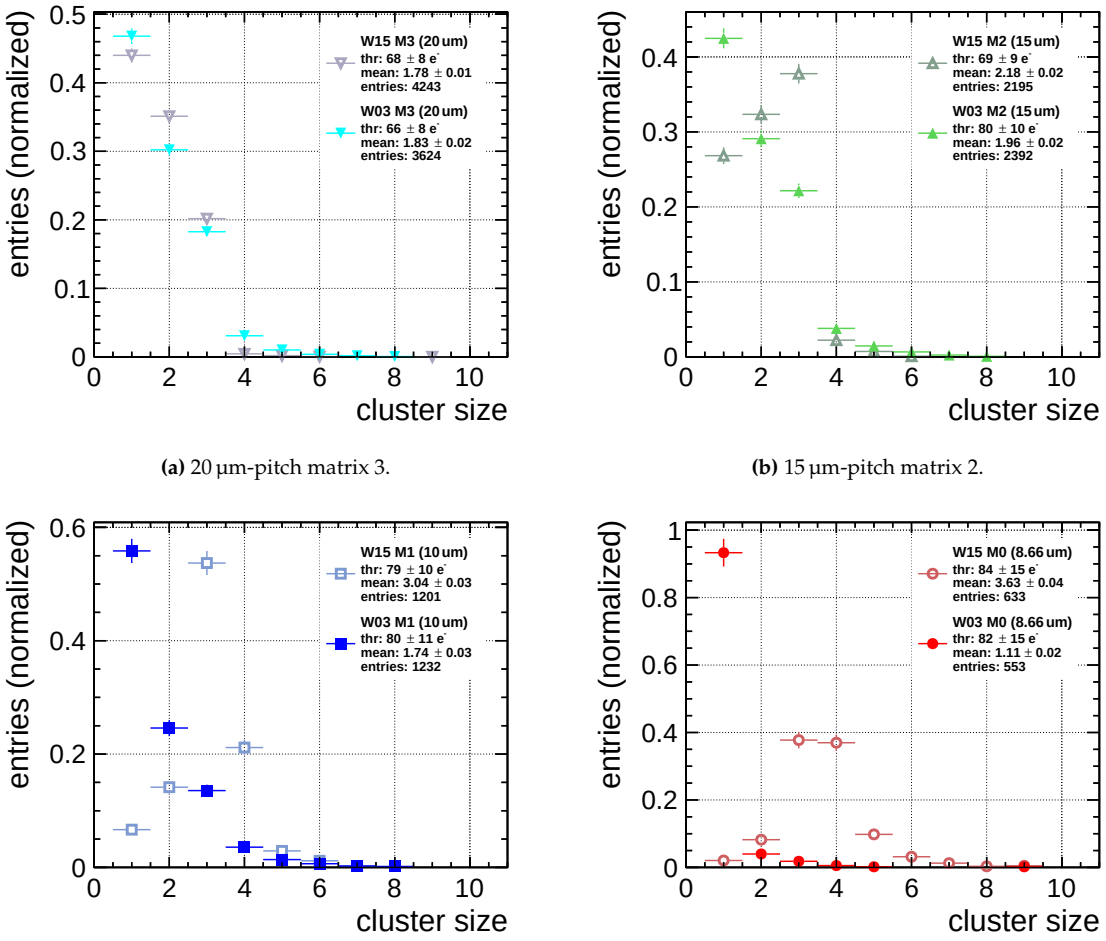

(a) 20 µm-pitch matrix 3.

(b) 15 µm-pitch matrix 2.

(c) 10 µm-pitch matrix 1.

(d) 8.66 µm-pitch matrix 0.

Figure 10.4: Cluster size distributions at $i_{\mathrm{thr}} = 0.82\,\mathrm{V}$ of the first four matrices on W03S1-1 andW15S1-1. The error bars represent statistical uncertainties.

Figure 10.4 compares normalized cluster size distributions measured with the first four matrices of standard process sample W03S1-1 and modified-process sample W15S1-1. For each plot, runs from the same test beam campaign have been combined to yield distributions based on similar statistic. The exemplary matrices cover all available pixel pitches (8.66 µm, 10 µm, 15 µm, 20 µm) and do not contain any additional structures in the pixel design, apart from the blanket deep n-implant and the extra-deep p-well that are both introduced with the modified process. On all wafers matrix 3 features pixels with a 0.86 µm collection electrode, 4.8 µm p-well opening and 16.03 µm deep p-well opening. The pixel edge of matrix 3 on W15S1-1 is lined by an uninterrupted deep n-implant and has an 18.8 µm extra-deep p-well opening. Both modifications accelerate charge collection by drift, reduce charge sharing and decrease cluster size.

The majority of observed clusters comprise more than one pixel. The share of charge carriers that spreads to neighboring pixels has a significant impact on the sensor response. The cluster

size distributions of the 20 µm-pitch matrices with index 3 are shown in Figure 10.4a and follow a similar trend. The mean cluster size measures 1.83 ± 0.02 pixels per cluster on W03 and 1.78 ± 0.02 pixels per cluster on W15S1-1, with statistical uncertainty.

The comparison of cluster size distributions of two 15 µm-pitch matrices with index 2 are shown in Figure 10.4b. The different mean cluster sizes measure 1.96 ± 0.02 pixels per cluster on W03 and 2.18 ± 0.02 pixels per cluster on W15S1-1, with statistical uncertainty, an increase in cluster size of 7 % and 22 % with respect to the 20 µm-pitch matrices.
In Figure 10.4c (10 µm-pitch) and Figure 10.4d (8.66 µm-pitch) the pitch decreases further and the difference in cluster size is more pronounced. While the cluster size of W15S1-1 matrices increases up to a mean of 3.63 ± 0.04 (8.66 µm pitch), the observed mean cluster size of W03S1-1 matrices switches its trend and decreases to 1.11 ± 0.02 for the 8.66 µm-pitch matrix 0. Matrices with index 0 feature pixels with a 0.86 µm collection electrode, 3.0 µm p-well opening and 4.8 µm deep p-well opening. On W15S1-1, pixels in the same matrix have a continuous deep n-implant and a 7.45 µm extra-deep p-well opening, with a similar effect as for the larger 20 µm pitch.
Compared to the mean cluster size of the respective 20 µm-pitch matrix, the 8.66 µm-pitch matrix yields an increase in cluster size of ≈100 % on W15S1-1, as opposed to a decrease of ≈40 % on W03S1-1. The cluster size distribution in Figure 10.4d shows a 3 times higher mean cluster size for the modified process sample W15S1-1, compared to the the standard process sample W03S1-1.

If both samples operate fully efficient as well as fully depleted at the same threshold, the standard process sample W03S1-1 is expected to yield larger cluster size compared to the modified process sample W15S1-1 due to the larger amount of charge sharing (see Section 5.3). If registered above threshold, large clusters, which are the expected main contributor to the standard process cluster size distribution, are more likely to be only registered by a small fraction of pixels surrounding the seed pixel. The rest of the pixels in the cluster get a small share of the deposited charge, causing their signal to stay below threshold and the observed cluster size to be reduced.

10.2.3. Threshold Dependence

An evaluation of the measured mean cluster size in dependance of different threshold settings is possible for modified process samples W15S1-1 and a small selection of set thresholds.
Figure 10.5 shows the change in cluster size with threshold for the first four matrices on sample W15S1-1. In each of the individual plots for the 20 µm-pitch, 15 µm-pitch, 10 µm-pitch and 8.66 µm-pitch matrix a linear fit models the decrease in cluster size with increasing detection threshold. The data in this limited threshold range shows an approximately linear decrease of mean cluster size with threshold. For higher thresholds outside of possible threshold settings, the mean cluster size is expected to converge to a value of 1, where only the highest-signal pixel (seed pixel) will remain above threshold.

The change in cluster size depends on pixel pitch and yields $-0.003 \pm 0.001/e$, $-0.005 \pm 0.001/e$, $-0.010 \pm 0.001/e$ and $0.014 \pm 0.001/e$ for matrix 3, 2, 1 and 0, respectively. In Figure 10.4, the signal threshold for the compared measurements is the same across the compared samples

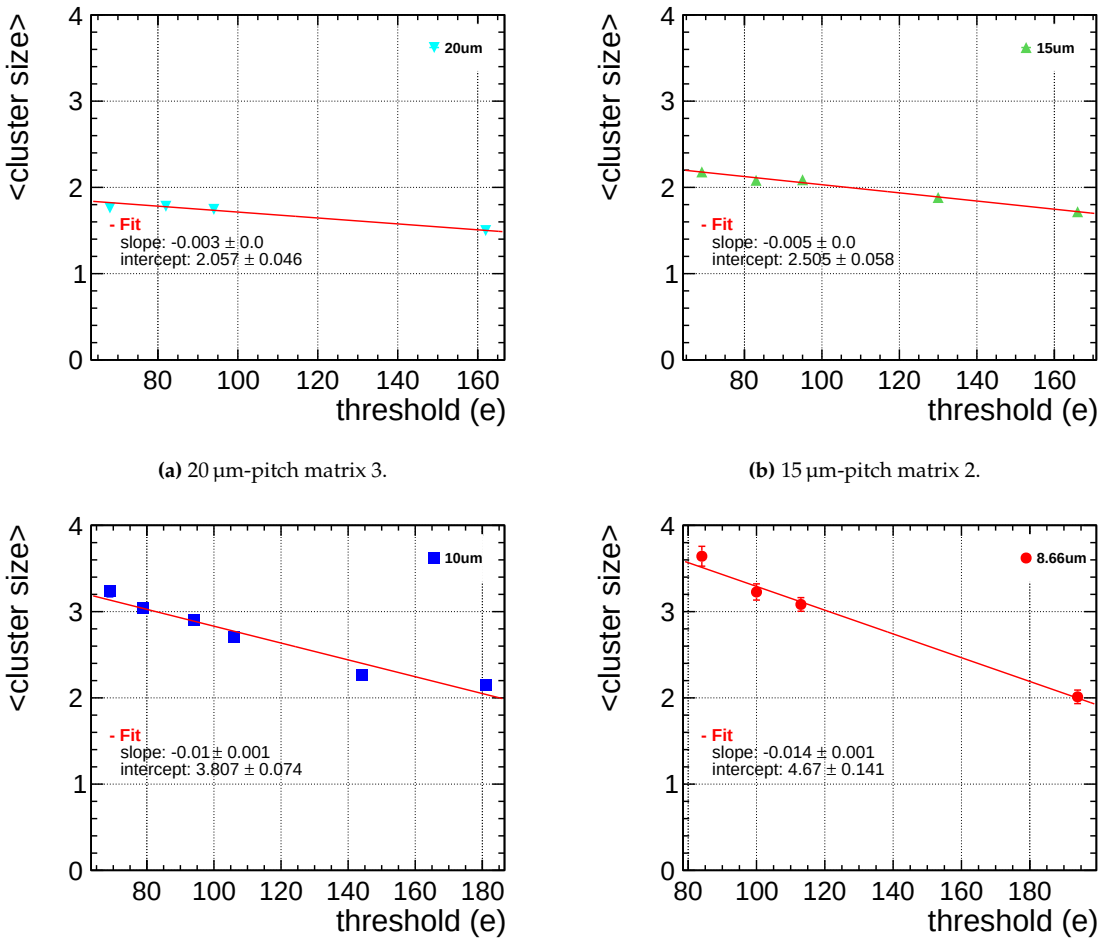

(a) 20 µm-pitch matrix 3.

(b) 15 µm-pitch matrix 2.

(c) 10 µm-pitch matrix 1.

(d) 8.66 µm-pitch matrix 0.

Figure 10.5: Mean cluster size over threshold for the first four matrices on W15S1-1. The error bars represent statistical uncertainties. A linear fit is shown in red.

(within errors), which are dominated by the error on the threshold calibration factor. An approximate error of 10 e on the set thresholds has an $\mathcal{O}(0.1)$ impact on the mean cluster size.

10.2.4. Sample Level

Figure 10.6 gives an overview of the observed mean cluster size for matrices on a standard sample, a modified sample and two samples from the most-modified process, at a common threshold setting of $i_{\mathrm{thr}} = 0.82\,\mathrm{V}$. For every group of four consecutive matrix indices a certain pixel design variation is implemented in each one of the four pixel pitches, which are indicated by the color scheme. The overview in Figure 5.14 illustrates the differences in design parameters and the combinations implemented for all 32 matrices, in each underlying CMOS process variant.

Figure 10.6a exhibits an overall smaller cluster size in comparison with the results from the

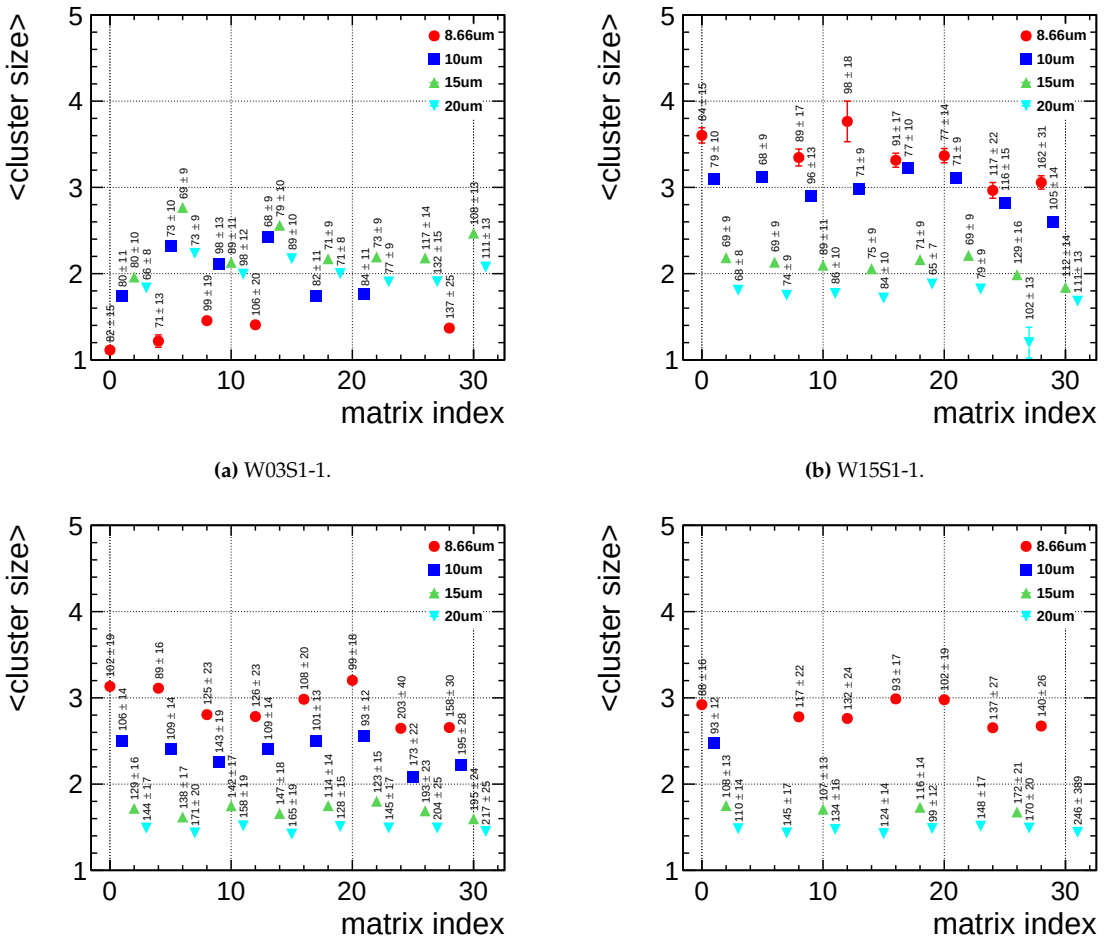

(a) W03S1-1.

(b) W15S1-1.

(c) W18S1-3.

(d) W18S1-4.

Figure 10.6: Mean cluster size at $i_{\mathrm{thr}} = 0.82\,\mathrm{V}$ for samples W03S1-1,W15S1-1, W18S1-3 and W18S1-4. The superscript specifies the threshold in electrons for the respective matrix.

modified sample in Figure 10.6b for comparable threshold levels. Due to the larger amount of charge sharing in the standard process (see Section 5.3), the result of the comparison is expected to be the opposite.
Within every group of four matrices the pixels share the same design variant and the collection electrode size is constant. In every complete group of standard-process sample W03S1-1 (four plotted data points), the observed mean cluster size agrees with the trends discussed in Section 10.2.2 and the 8.66 µm-pitch matrix yields the smallest cluster size. The 10 µm-pitch matrix yields values closer to the mean cluster size measured by the two larger pitches. The measurements with 15 µm-pitch matrix 2 result in the largest mean cluster size across all 8 pixel variants. The 20 µm-pitch matrix 3 yields smaller mean cluster sizes from charge collection below a larger pixel area than the 15 µm pitch.

The observed small cluster size in 8.66 µm-pitch matrices of the standard process sample is an effect of the very small pixel size. A decrease in pitch towards smaller pixel size distributes a

given amount of generated charge in the epitaxial layer to a larger number of pixels covering the area above the particle incidence. This results in an on average smaller signal on each pixel of a cluster, reducing the measured cluster size. The larger amount of charge sharing in the standard process adds to the smaller measured cluster size.
The geometry of the FASTPIX matrix introduces a cap on the observable cluster size in small-pitch matrices. The registered cluster size in the 8.66 µm pixel pitch matrices is cut as some clusters span or even extend beyond the 4 pixel height of the matrix. Figure 10.4d states largest shares from cluster size 3 and 4, a value that is found to be much smaller for matrices on the standard process sample. Clusters from tracks traversing a given matrix outside of the center line of the matrix experience edge effects. A fraction of their charge is deposited outside of the matrix, is not collected by active pixels and therefore not accounted for in a cluster size measurement. Consequently, a share of clusters get misidentified with a smaller size. To mitigate this effect the reconstructed local intercept position is used to only allow cluster seed pixel positions in the inner 2 x 14 pixels of a matrix.
A deficit in detection efficiency as a result of insufficient depletion is a possible causes for the deviation of the standard-process sample W03S1-1 from the expected behavior. The former will be covered by the results presented in Section 10.4.

As a result of the higher-doped blanket n-implant, the most-modified sample W18S1-3 in Figure 10.6c observes smaller mean cluster size than W15S1-1, across the chip. The impact of the overall higher signal thresholds on W18S1-3 at the same i_{thr} of 0.82 V can be estimated by applying the threshold dependence of cluster size that was previously discussed in Section 10.2.3. A difference in threshold of 20 e, 30 e, 60 e and 70 e results in a reduction of cluster size by 0.06, 0.1, 0.2 and 0.3, in case of the first four matrices 0, 1, 2, and 3. The increased concentration of dopants in the deep n-layer of W18S1-3 increases the electric field strength, accelerates the charge collection by drift and thereby reduces cluster size. Figure 10.6d exhibits a good sample-to-sample agreement in mean cluster size. The measured values differ between both samples by less than 0.2.

Across all 8 pixel-variant groups of W15S1-1 and W18S1-3, the mean cluster size follows the expectation and decreases with increasing pixel pitch. When switching from 8.66 µm to 10 µm, the mean cluster size of matrices on the most-modified sample is reduced by ≈20 %, the step from 10 µm to 15 µm yields a reduction of ≈30 %. The change in mean cluster size between matrices of 15 µm and 20 µm pixel pitch has a smaller impact on cluster size with a decrease of around 10 %.

The impact of variations in pixel design can be evaluated by comparing same-pitch matrices from the same quadrant of the W18S1-3 sample. Matrices with 8.66 µm and 10 µm pixel pitch are similar in dimensions and follow a similar trend in mean cluster size across the eight available pixel design variations. A detailed discussion of the 8.66 µm-pitch matrix 0 largely also applies to the 10 µm-pitch matrix 1, in the following the respective matrix index is added in parentheses.
The first design optimization is introduced with matrix 4 (5) in form of a hexagonal 2.6 µm gap in the pixel corners that gets added to the deep n-implant. Compared to the baseline pixel design in matrix 0, the cluster size is reduced by 5 %, which is more pronounced for 10 µm-pitch matrix 5. The gap increases the strength of the lateral electric field in the corner

regions of the pixel which accelerates charge collection by drift and reduces charge sharing. Matrix 16 (17) differs from matrix 0 in terms of p-well opening size. Reducing the area of the p-well benefits a uniform depletion over the full pixel area and improves charge collection. The smaller p-well area of matrix 16 with a 4.8 µm p-well opening instead of 3 µm yields a decrease of 5 % in cluster size, an effect that is comparable to the introduction of the hexagonal corner gap.
Matrix 8 (9) retains the additional deep n-implant corner gap as well as the larger p-well opening and features an enlarged 2.0 µm collection electrode. The combination results in a 10 % reduction of cluster size. An increased collection electrode size reduces the mean cluster size as a result of a stronger electric field and shorter charge drift path, but comes with a penalty for the signal-to-noise ratio and pixel power consumption. The change from PMOS to diode reset in matrix 12 (13) has no significant impact apart from the increase in threshold for the 10 µm-pitch matrix.
Similar to matrix 4 (5) but with a triangular geometry, a deep n-implant gap of 2.48 µm (3.8 µm) is placed in the pixel corners and increases the observed mean cluster size value with respect to the baseline matrix 0.
Matrix 24 (25) retains the design optimizations of matrix 16 (17) but features an enlarged collection electrode with similar effects to matrix 8 (9), with a full uninterrupted deep n-implant instead of the corner gaps. The change from PMOS to diode reset in matrix 28 (19) again has no significant impact apart from the increase in threshold for the 10 µm-pitch matrix.

In case of matrices with 15 µm and 20 µm pixel pitch, the pixel design optimizations only show minimal impact on cluster size. The observed reduction of cluster size is dominated by the pixel pitch and changes to the structure of the pixel cell only show relative changes below 5 % across the eight available variations.

10.3. Signal

A measurement of the signal equivalent to the energy deposited in the sensitive pixel volume from the interaction of a traversing particle is accessible through the time-over-threshold observable.

10.3.1. Matrix Level

The highest single-pixel signal in a cluster is the seed signal, shown in Figure 10.7 for the exemplary 8.66 µm-pitch matrix 0 and 20 µm-pitch matrix 3 of sample W18S1-3. The measured seed signal ToT is converted to physical units using the energy calibration in Section 7.2.1. The distributions are not expected to follow a Landau-Gauss model, as for cluster sizes >1 the total signal is shared in parts with neighboring pixels. In addition, the calibration result is based on a lower signal range and only allows a conversion with a relative error of ≈10 %. A Gaussian fit is used to approximate the peak region of the distribution and extract its position as a most-probable collected charge.
A large portion of matrices observe a cluster size close to 1, especially the 20 µm-pitch matrices on sample W18S1-3. The lower seed signal for the 8.66 µm-pitch matrix compared to the 20 µm-pitch matrix is expected, given the previously observed larger cluster size in the 8.66 µm-pitch pixel grid.

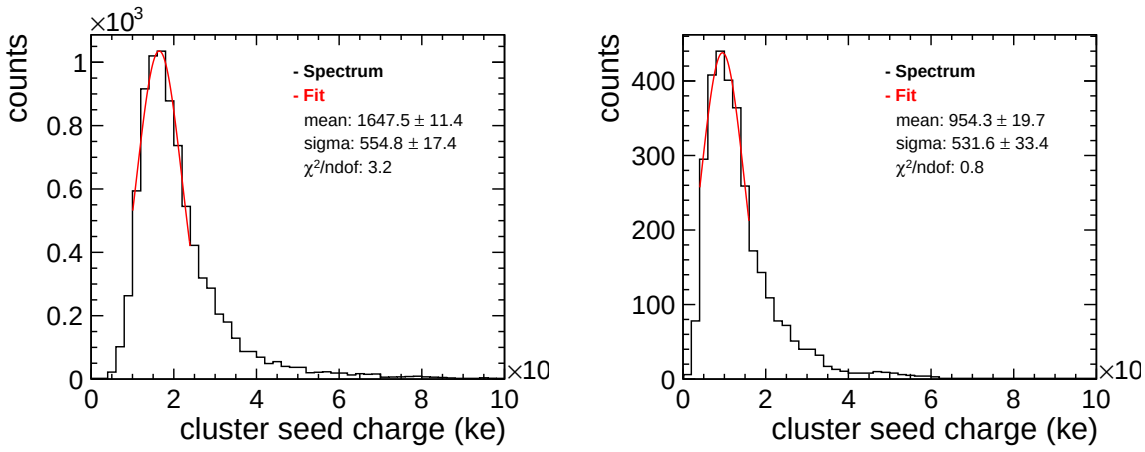

(a) 20 µm-pitch matrix 3.

(b) 8.66 µm-pitch matrix 0.

Figure 10.7: Cluster seed pixel charge at $i_{\mathrm{thr}} = 0.82\,\mathrm{V}$ for two matrices on W18S1-3. The Gaussian fit (red) approximates the peak position.

10.3.2. Sample Level

In comparison between Figure 10.8a and Figure 10.8b, which both show the most-probable observed ToT extracted for the individual matrix cluster seed charge distributions, the standard-process sample W03S1-1 exhibits an overall reduced collected signal due to the higher degree of charge sharing. While W15S1-1 shows a large spread of recorded signal, the most-modified sample W18S1-3 in Figure 10.8c was able to collect most-probable cluster seed charges that are in agreement with the expectation and the previously discussed charge sharing behavior across the chip (see Section 10.2.4). Figure 10.8d affirms the cluster seed charge observations on W18S1-3. For the majority of matrices the difference in signal stays below 100 e. Outliers are the result of a significant difference in detection threshold for the same matrix index on both samples.

An evaluation of the influence of variations in pixel design on the collected charge is only possible, to a limited extend, by comparing same-pitch matrices of the W18S1-3 sample. Small-pitch matrices with 8.66 µm and 10 µm pixel pitch show a raised cluster seed charge for the variations with increased collection electrode size and full blanket deep n-layer in matrix 24 (25) and 28 (29), compared to 16 (17). In case of 20 µm-pitch matrices, charge collection benefits from the switch to a larger collection electrode size while retaining the remaining design parameters, as exemplified by matrix 7 in comparison with 11 as well as matrix 19 in comparison with 27.

The results per pitch are consistent and the collected seed pixel charge increases with pitch, and thereby with decreasing amounts of charge sharing. The 20 µm-pitch matrices with a mean cluster size of 1.5 collect an average charge of 1600 e at an average detection threshold of 170 e. Threshold differences between matrices affect the sub-threshold charge loss, but are small compared to the observed differences. The possibility of sharing undetected charge to the two neighboring pixels that are closest to the track intercept, amounts to up to ≈300 e of generated charge that is not accounted for.

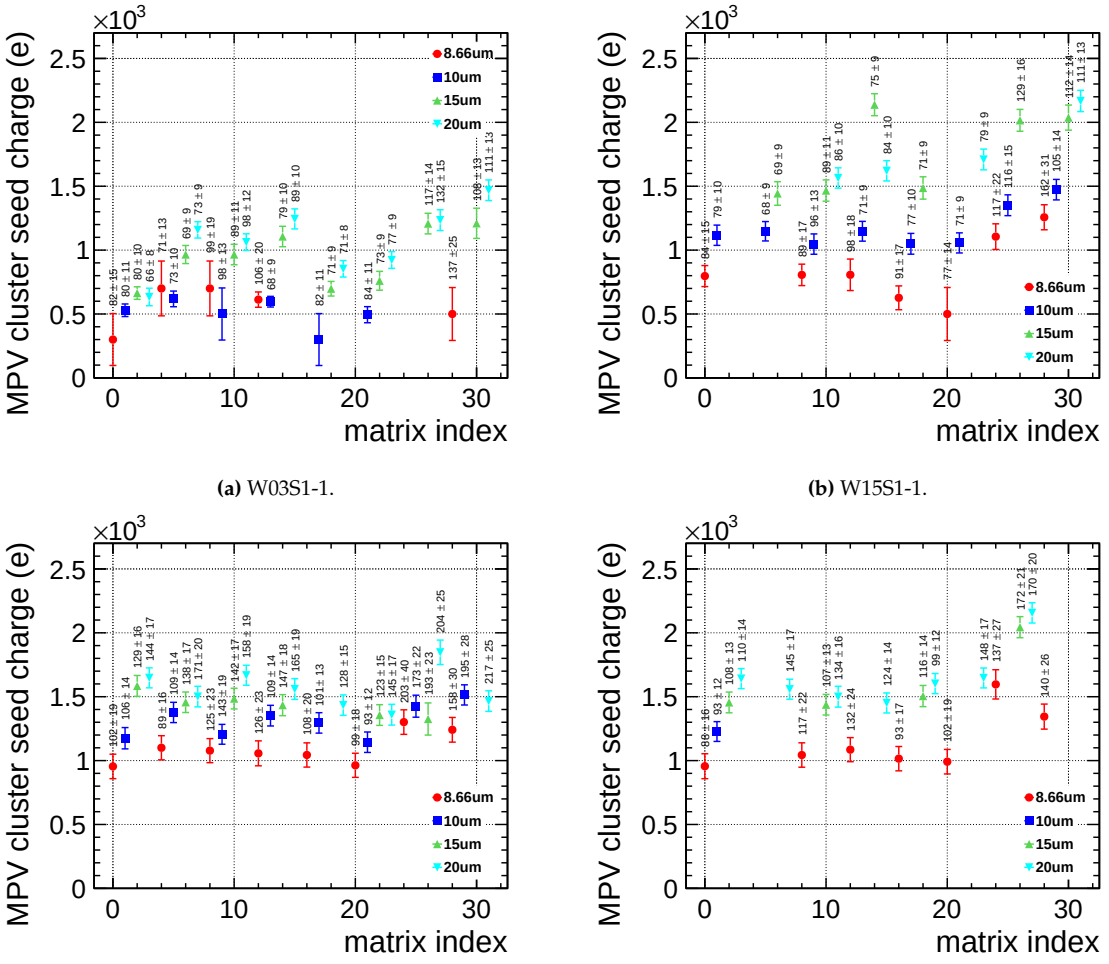

(a) W03S1-1.

(b) W15S1-1.

(c) W18S1-3.

(d) W18S1-4.

Figure 10.8: Most probable seed pixel charge at $i_{\mathrm{thr}} = 0.82\,\mathrm{V}$ for samples W03S1-1,W15S1-1, W18S1-3 and W18S1-4. The error bars represent the error on the fit result in Figure 10.7 and are exchanged for the larger bin width of the maximum bin in case of a fit failing to converge.

The discrepancy between the collected seed pixel charge of standard-process and modified-process matrices of a factor >2 suggests insufficient depletion.

10.4. Hit-Detection Efficiency

Hit-detection efficiency informs the reliability with which count-based observables like rates or probabilities can be extracted from the measurements of particle interactions in a pixel detector. As an indicator of the performance of a monolithic silicon sensor, hit-detection efficiency is investigated, initially to further indications of the previously observed difference in performance between the standard-process and modified-process samples well as to identify the impact of pixel design optimizations on detection efficiency.

10.4.1. Matrix Level

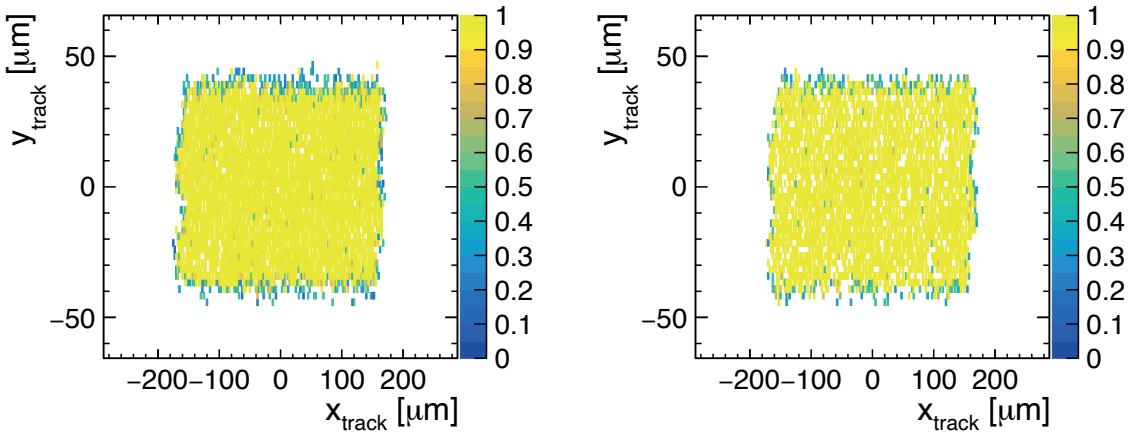

(a) W03, matrix 3, 20 µm pixel pitch, threshold 66 ± 8 e. **(b)** W15, matrix 3, 20 µm pixel pitch, threshold 68 ± 8 e.

Figure 10.9: Matrix efficiency maps from a standard process (left) and a modified process (right) sample. The color scale shows the efficiency for each track position bin on the x-/y-plane.

Figure 10.9 shows efficiency maps on W03S1-1 and W15S1-1. Matrix index 3 comprises a 0.86 µm collection electrode, 4.8 µm p-well opening and 16.03 µm deep p-well opening on both samples. The plots present a consistently efficient area of the matrix without visible structures introduced by characteristics of the chip or systematic features. A drop in efficiency along the edge is caused by charge sharing with inactive dummy-pixels surrounding the matrix edge making the sensitive area slightly larger than the 4 x 16 active pixels.

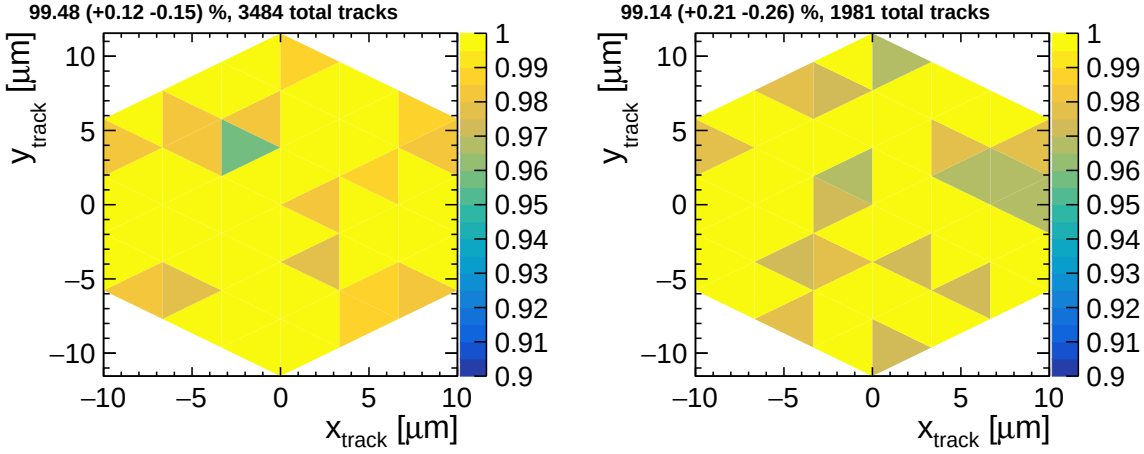

(a) W03S1-1, 20 µm-pitch matrix 3, threshold 66 ± 8 e. **(b)** W15S1-1, 20 µm-pitch matrix 3, threshold 68 ± 8 e.

Figure 10.10: In-pixel efficiency maps from a standard process (left) and a modified process (right) sample. Hits from all pixels are projected into one hexagonal pixel area. The color scale shows the efficiency for each triangular track position bin subdividing the hexagonal area on the x-/y-plane.

Figure 10.10 shows in-pixel efficiency maps of the same 20 µm-pitch matrices with no visible

characteristics of the pixel implant geometry or systematic features across the pixel area. On W03S1-1 as well as W15S1-1, matrix 3 is able to achieve fully efficient operation at a similar threshold of 66 ± 8 e and 68 ± 8 e without significant difference in cluster size or efficiency, respectively.

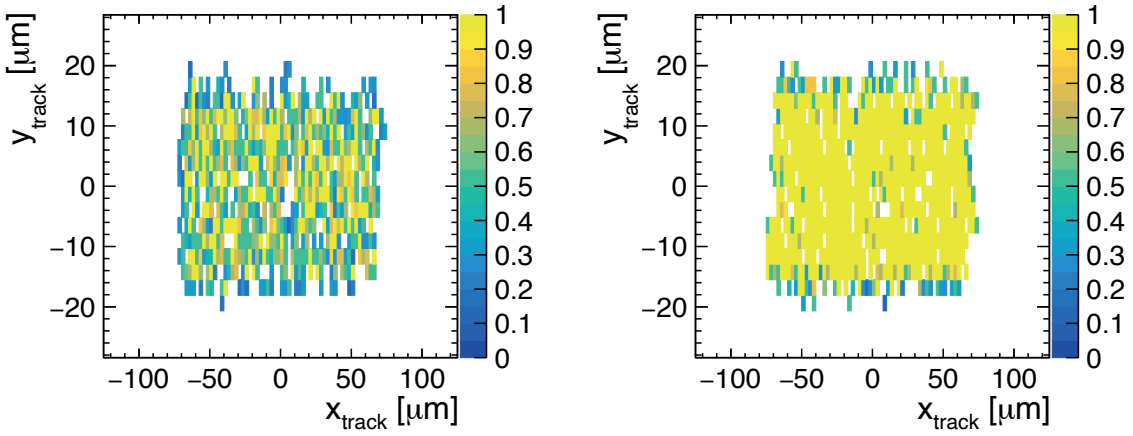

(a) W03S1-1, 8.66 µm-pitch matrix 0, threshold 80 ± 11 e. **(b)** W15S1-1, 8.66 µm-pitch matrix 0, threshold 84 ± 15 e.

Figure 10.11: Matrix efficiency maps from a standard process (left) and a modified process (right) sample. The color scale shows the efficiency for each track position bin on the x-/y-plane.

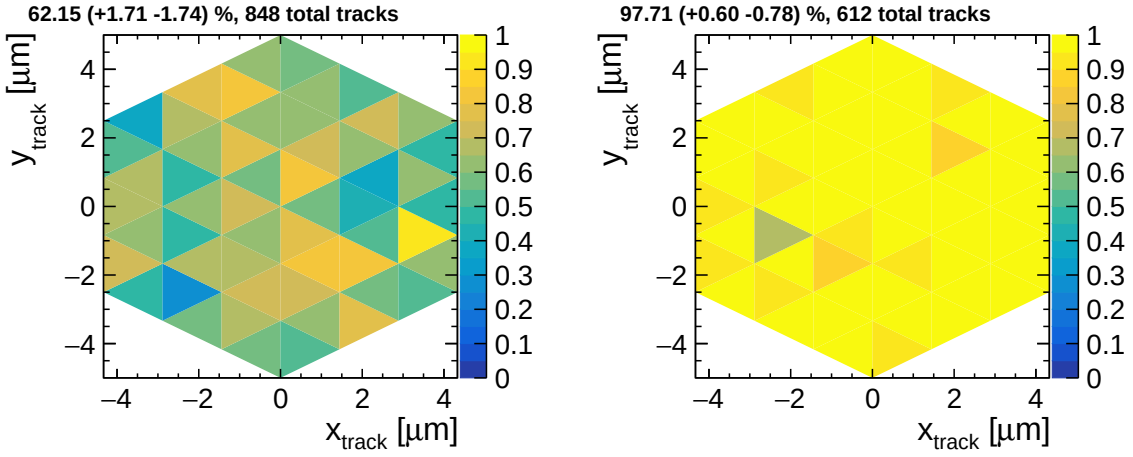

(a) W03S1-1, 8.66 µm-pitch matrix 0, threshold 80 ± 11 e. **(b)** W15S1-1, 8.66 µm-pitch matrix 0, threshold 84 ± 15 e.

Figure 10.12: In-pixel efficiency maps from a standard process (left) and a modified process (right) sample. Hits from all pixels are projected into one hexagonal pixel area. The color scale shows the average efficiency for each triangular track position bin subdividing the hexagonal area on the x-/y-plane.

However, this observation changes for the smallest pixel pitch. Figure 10.11 and Figure 10.12 show matrix and in-pixel efficiency maps of 8.66 µm-pitch matrix 0 from the standard process sample W03S1-1 and the modified process sample W15S1-1, respectively. Across all wafers matrix 0 features pixels with a 0.86 µm collection electrode, 3.0 µm p-well opening and 4.8 µm deep p-well opening. On W15 pixels in the same matrix have a continuous deep n-implant

and a 7.45 µm extra-deep p-well opening, two modifications that accelerate charge collection by drift, reduce charge sharing and decrease cluster size.

The efficiency plots present a consistently efficient area of the matrix as well as pixel area. With respect to the modified process sample W15S1-1, the standard process sample W03S1-1 experiences a decrease in efficiency of approximately 35 % for 8.66 µm pixel pitch matrix 0. Both matrices are operated at the same threshold within errors, W03S1-1 at 80 ± 11 e compared to a threshold value of 84 ± 15 e for sample W15S1-1.

10.4.2. Sample Level

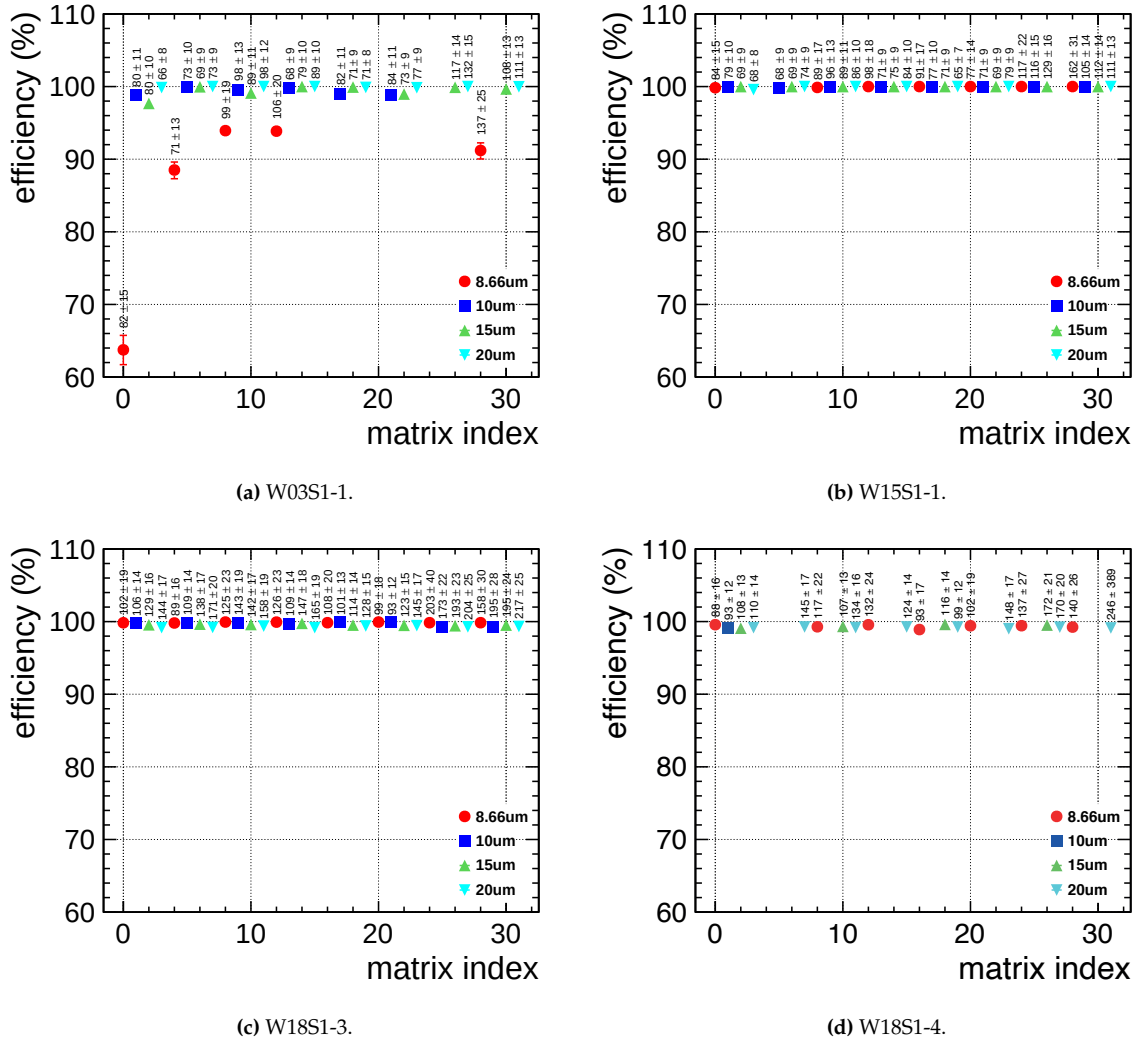

(a) W03S1-1.

(b) W15S1-1.

(c) W18S1-3.

(d) W18S1-4.

Figure 10.13: Detection efficiency at i_{thr} = 0.82 V for samples W03S1-1,W15S1-1, W18S1-3 and W18S1-4. The superscript specifies the threshold in electrons for the respective matrix.

Figure 10.13 gives an overview of the calculated efficiency for matrices on a standard sample, a modified sample and two samples from the most-modified process, at a common threshold

setting of $i_{\mathrm{thr}} = 0.82\,\mathrm{V}$. For every group of four consecutive matrix indices a given pixel design variation is implemented for each one of the four pixel pitches, as indicated by the color scheme. Figure 5.14 illustrates the differences in design parameters of the 32 matrices on a FASTPIX sample.

The modified-process sample W15S1-1 as well as both most-modified samples W18S1-3 and W18S1-4 exhibit >99 % hit-detection efficiency at the nominal threshold. Aso the 10 µm-, 15 µm- and 20 µm-pitch of standard-process sample W03S1-1 yield efficiencies close to 100 %. The fully efficient matrices show no significant dependency of efficiency on pixel design variations.

On W03S1-1 the matrices with 8.66 µm pixel pitch stand out with a reduced hit-detection efficiency. The larger p-well opening and an enlarged 2.0 µm collection electrode improves the 62 % efficiency of matrix 0 to a 94 % efficiency of hit detection for matrix 8 and 12. For matrix 12 the frontend is changed to a diode reset, while the pixel cells remains unchanged. A decrease in pitch towards smaller pixel size distributes a given amount of generated charge in the epitaxial layer to a larger number of pixels covering the area above the particle incidence. This results in an on average smaller signal on each pixel of a cluster, reducing both the measured cluster size and the efficiency. The larger amount of charge sharing in the standard process enhances this reduction of measured cluster size and efficiency.

In combination with the previous sections, the hit-detection efficiency results show how the process modifications of the modified process and most-modified process samples help to contain the charge within a single pixel and with that give more margin for efficient detector operation of the 8.66 µm-pitch matrices.

10.5. Spatial Resolution

The spatial measurement precision for the local intercept coordinates between a particle trajectory and the sensor surface is an essential performance indicator for vertex and tracking detectors. Apart from the pitch in the pixel grid of the sensor, its charge sharing behavior has a similarly important impact on the achievable spatial resolution.

10.5.1. Matrix Level

An observable closely linked to cluster size is the width of the spatial residual distribution, shown in local x- and y-direction for a 8.66 µm-pitch matrix 0 from modified process sample W18S1-3 in Figure 10.14.
The exemplary residual distributions of 8.66 µm-pitch matrix 0 on sample W18S1-3 are approximated with a Gaussian model and exhibit widths of 1.77 ± 0.05 µm and 1.83 ± 0.06 µm in x- and y-direction, respectively. Despite a small asymmetry in the distribution, the model approximates both data sets well. The extracted RMS and width σ match within errors and show no significant difference in width outside of the respective errors.

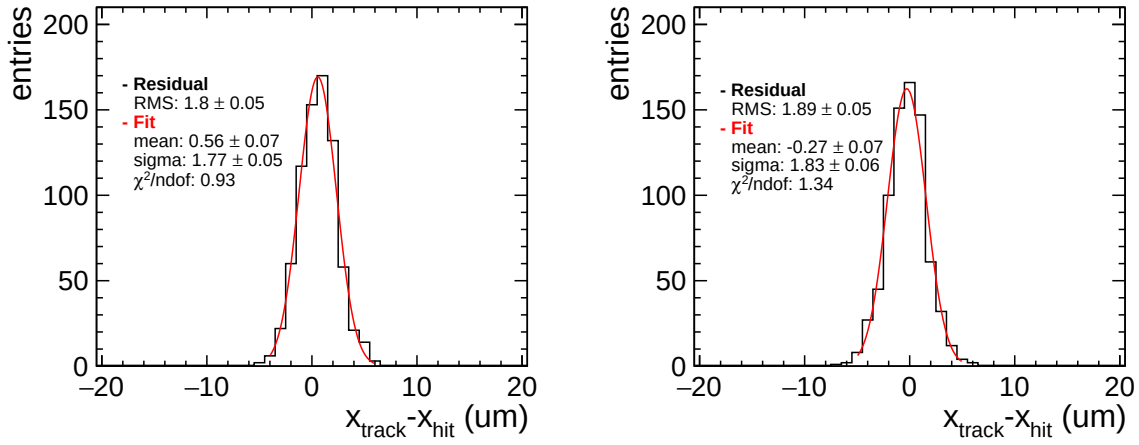

(a) Local x-direction.

(b) Local y-direction.

Figure 10.14: Spatial residuals along the x- and y-axis perpendicular to the beam, measured with 8.66 µm-pitch matrix 0 on the W18S1-3 sample, at a threshold of 102 ± 19 e.

10.5.2. Sample Level

An overview of the width of spatial residuals including all tested matrix variants on individual samples is shown by Figure 10.15 for the local x-direction of standard-process sample W03S1-1 and modified process sample W15S1-1.
The width of the residual distributions yields values between 2.1 µm and 3.1 µm with an average residual width of 2.6 µm, in case of W03S1-1. W15S1-1 yields narrower residuals from its small-pitch matrices between 1.6 µm and 3.1 µm.

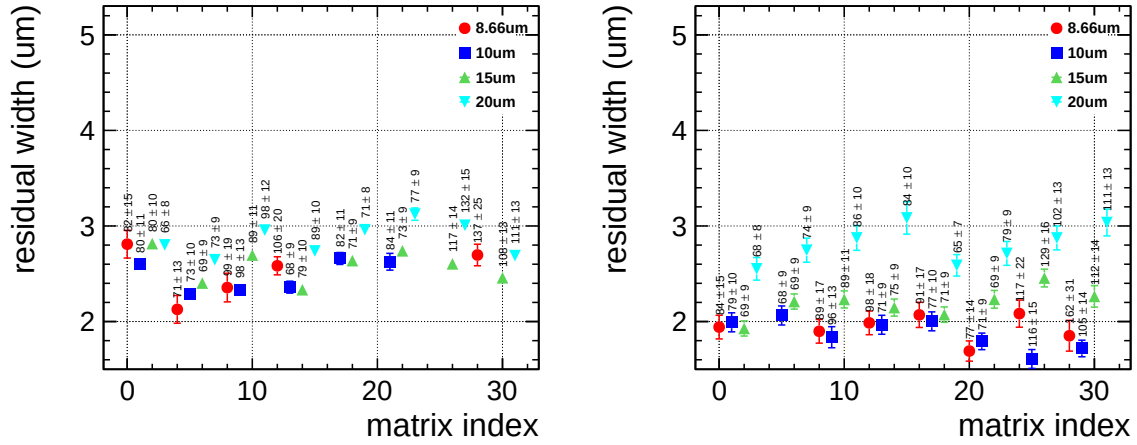

(a) W03S1-1.

(b) W15S1-1.

Figure 10.15: Overview of the width of spatial residuals in y-direction measured for the majority of matrices on a standard-process and a modified-process sample. The width corresponds to the sigma of the gaus fit with the associated fit error.

The modified-process outperforms the standard-process sample by an overall 15 % improvement in residual width. The spatial measurement results from the W03S1-1 are penalized by the impaired charge collection, reduced observed cluster size and detection efficiency, which indicate insufficient depletion of the epitaxial layer.

The higher-dose deep n-implant of the most-modified process sample W18S1-3 exhausts the available process modifications for improved depletion and electric field configuration, as discussed in Chapter 5. It has shown consistent results in charge sharing and charge collection, was tested extensively in test beam campaigns and will be predominantly used for a detailed discussion of performance in the spatial as well as temporal domain.
Figure 10.16 presents an overview of the width of spatial residuals in both dimensions of the sensor plane for all tested matrix variants on sample W18S1-3. Along the x-axis the width of the Gaussian fit of the residual distributions yields values between 1.7 µm and 3.8 µm. The measurement does not show significant differences between the residuals along x-axis vesus the residuals along the y-axis.

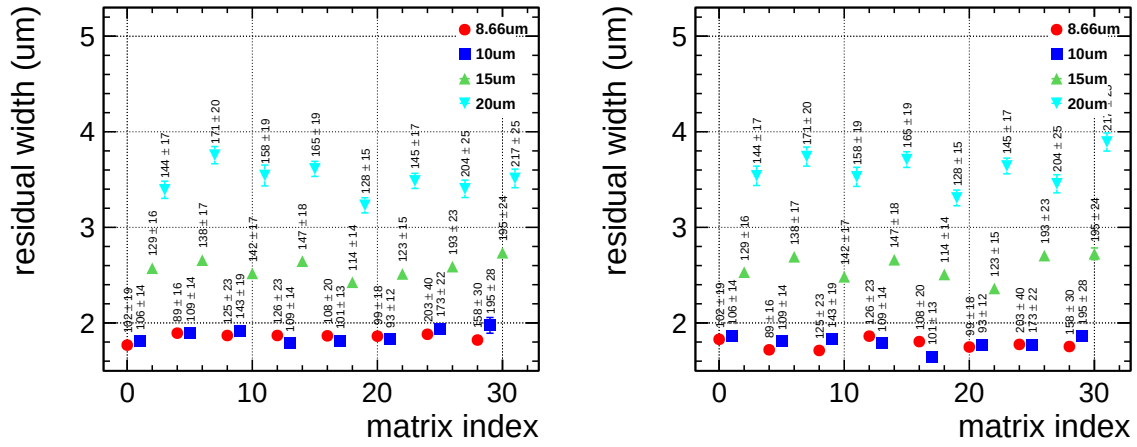

(a) Sigma in local x. **(b)** Sigma in local y.

Figure 10.16: Overview of the width of spatial residuals measured for all 32 matrices of the W18S1-3 sample at $i_{\mathrm{thr}} = 0.82\,\mathrm{V}$. The width corresponds to the sigma of the gaus fit with the associated fit error.

Smaller pitch matrices achieve lower sigma values due to the higher granularity and since larger mean cluster size and a tendency for lower electron thresholds allow for a more precise reconstruction of the DUT hit position with respect to the interpolated track intersect. 8.66 µm pixel pitch matrices only show little difference in spatial residual width compared to larger 10 µm pixel pitch. The average residual width of both pitch-groups differs by less than 5 %. The 8.66 µm-pitch matrix 0 achieves a spatial resolution down to 1.1 µm after unfolding the telescope tracking resolution (see Section 9.5.4).
The 15 µm pixel pitch matrices exhibit an average 40 % wider residual, compared to the smallest pixel pitch. The residuals of the 20 µm-pitch matrices widen on average by another 30 % and experience a further reduction of spatial resolution compared to the 15 µm pixel pitch. This trend agrees with the change in mean cluster size with pixel pitch that was previously observed in Section 10.2.4. As the cluster size decreases the charge-weighted calculation of particle intercept from the center positions of the pixels in a cluster looses its precision.

Within both sets of smaller-pitch matrices the impact of pixel design variations is small. Compared to the two sets of larger-pitch matrices, the change to the smaller pixel sizes itself has improved the spatial residual width such that the resolution of differences in pixel design variation is clouded by the telescope track resolution. The difference between pixel design variation is more pronounced for the measurements with 20 µm- and 15 µm-pitch matrices. Matching up with the trends established for the mean cluster size, the residual width increases as the charge sharing is reduced by a given change of the in-pixel implant structures. This is the case for the introduction of deep n-layer gaps in the corners of the pixel cells, which is exemplified in the comparison of matrix 3 (2) with 7 (6) as a ≈10 % increase in residual width. The impact of a larger collection electrode size is not apparent from the data as improvement in residual width as is observed between matrix 7 (6) and 11 (10), which has a 2.0 µm instead of a 0.86 µm collection electrode. Also in comparison of matrix 19 (18) with 27 (26), a ≈10 % increase in residual width, cannot be attributed to the increased collection electrode size, given the ≈80 e difference in threshold. Similarly, the small visible impact of a change in p-well opening size e.g. between matrix 3 (2) and 19 (18) is clouded by the errors and a difference in threshold.

10.6. Time Resolution

In a high track density and interaction rate environment, precision timing enables to resolve particle interactions that otherwise would pile up and be assigned to a singular timestamp. The time measurement precision of FASTPIX matrices is evaluated as the width of the time residual distribution. The following section discusses the observed residual widths and determines the impact of the process modifications and pixel design optimizations on the timing performance. The time measurement precision of the chip is a convolution of contributions from sensor and the front-end circuity jitter of 20 ps, simulated in [57].

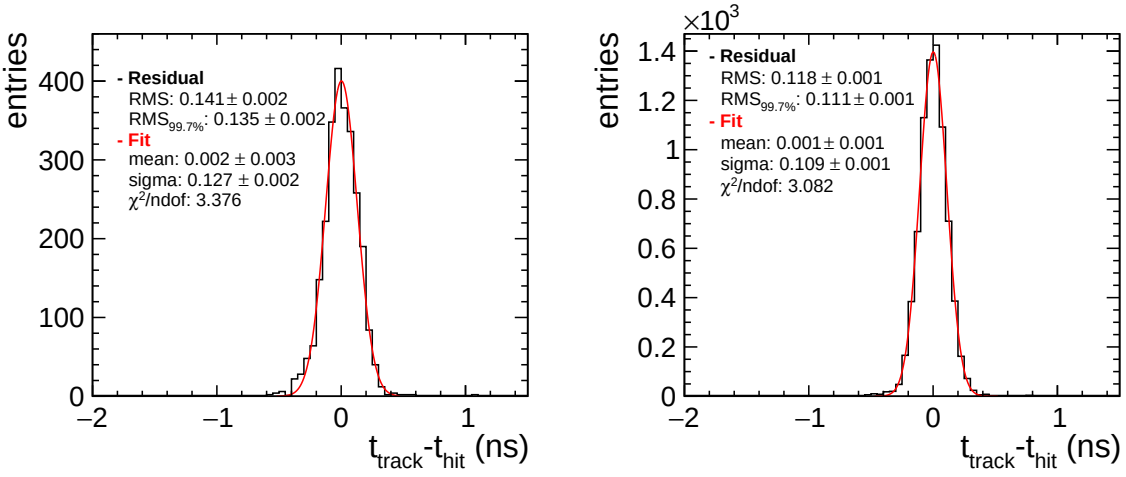

(a) Matrix 1, 10 µm pixel pitch, threshold: 62 e.

(b) Matrix 3, 20 µm pixel pitch, threshold: 80 e

Figure 10.17: Time residual from two matrices on sample W18S1-3 at i_{thr} = 0.82 V. A Gaussian fit models the observed distribution.

10.6.1. Matrix Level

Exemplary time residuals of a 10 µm-pitch matrix and 20 µm-pitch matrix on most-modified sample W18S1-3 are shown in Figure 10.17. The RMS yields 141 ± 2 ps and 118 ± 1 ps, a slightly higher value than the width of a Gaussian fit σ = 127 ± 2 ps and σ = 109 ± 1 ps, for the respective sets of data. The fit is in agreement with the $RMS_{99.7\,\%}$, for which the outmost 0.3 % of outliers are excluded, which yields 135 ± 2 ps and 111 ± 1 ps for the 10 µm-pitch and especially the 20 µm-pitch matrix, respectively.

10.6.2. Sample Level

The timing performance is evaluated for all tested matrices on four samples, comprising three manufacturing process variants and two most-modified-process samples.

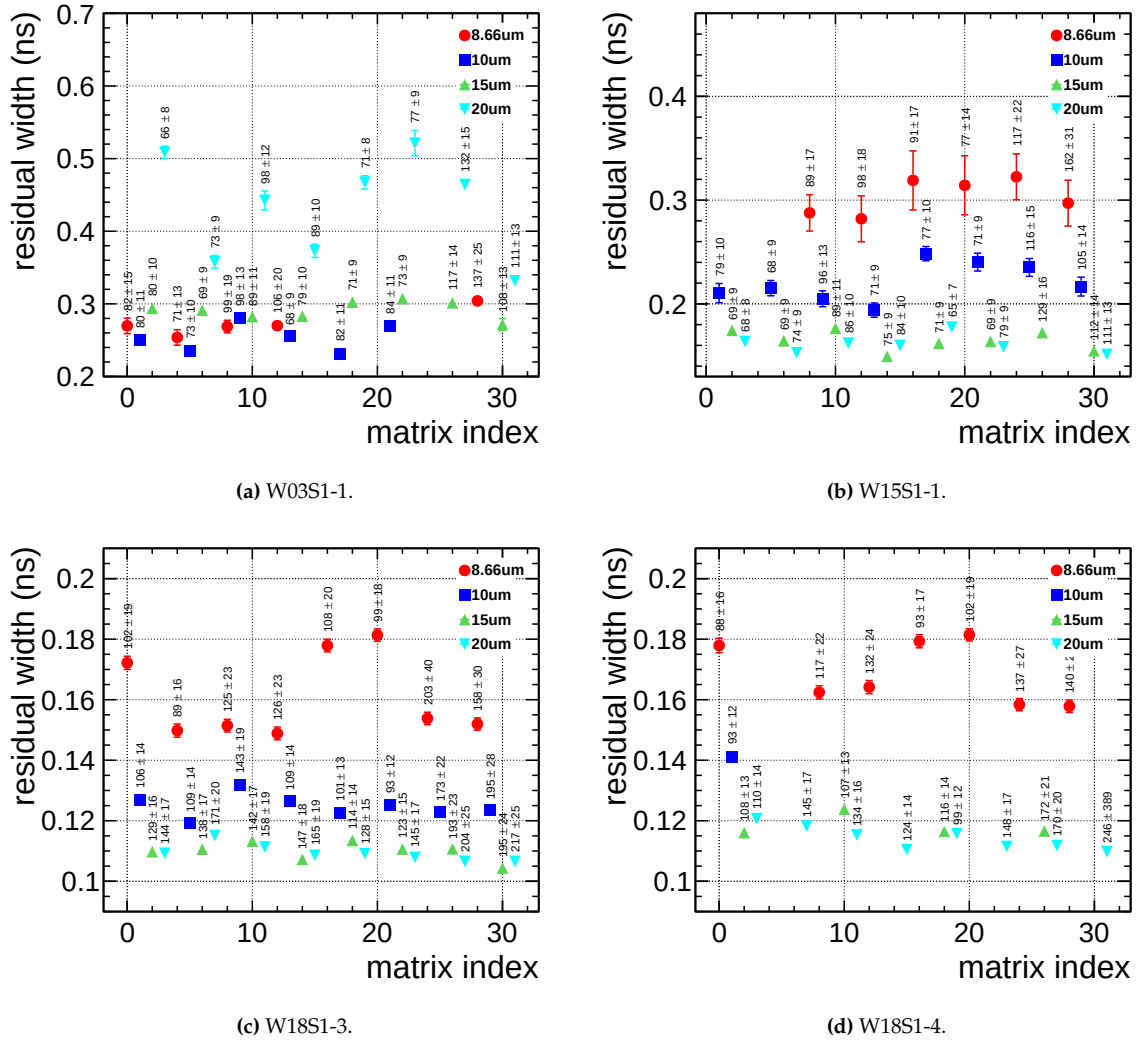

(a) W03S1-1.

(b) W15S1-1.

(c) W18S1-3.

(d) W18S1-4.

Figure 10.18: Overview of the width of time residual distributions for samples W03S1-1,W15S1-1, W18S1-3 and W18S1-4 at i_{thr} = 0.82 V. The superscript specifies the threshold in electrons for the respective matrix.

Figure 10.18 shows the time residual width for tested matrix variants on four individual

samples based on a statistic of ≈2000 tracks. The time resolution is plotted as the width σ of the Gaussian model fitted to the time-walk-corrected residual distribution. Time measurement precision is given without deconvoluting the track time resolution 5.5 ± 0.1 ps, which has an impact of less than 0.5 % on the best performing matrices close-to the 100 ps mark.

The standard manufacturing process yields residual distribution widths between 219 ps and 539 ps. W15S1-1 measures time with a higher precision and therefore narrower residual. Its matrices yield residual distribution widths between 146 ps and 325 ps. The error on sigma is extracted from the Gaussian fit result and is larger for matrices that show non-Gaussian tails on either side of the distribution.
The higher dose deep n-implant of the W18S1-3 sample accentuates the gradient in the doping profile and the lateral component of the field, driving charges from the pixel border towards the collection electrode, maximizing the seed pixel signal and reducing time-walk effects. The most modified sample yields a time measurement precision between 104 ps and 182 ps. A comparison of the same matrix indices on both most-modified samples yields an average sample-to-sample variation of approximately 10 ps.

The impact of different pixel design modifications can be discussed by isolating matrices of equal pitch from the overview of most-modified samples W18S1-3 in Figure 10.18c and W18S1-4 in Figure 10.18d.
In the subset of matrices with 20 µm pixel pitch the baseline is matrix 3, which achieves a time residual width of 109 ps. Following Figure 5.15, this matrix features pixels with a 0.86 µm collection electrode, 4.8 µm p-well opening, 16.03 µm deep p-well opening and 18.8 µm extra-deep p-well opening. The pixel edge is lined by an uninterrupted deep n-implant without modifications of the deep n-implant geometry.
For matrix 7 a hexagonal 2.6 µm corner gap gets added to the deep n-implant while the other parameters remain unchanged. The gap increases the strength of the lateral electric field in the corner regions of the pixel which accelerates charge collection by drift, reduces charge sharing and maximizes the seed pixel signal. Despite the introduced optimizations, the time residual width increases to 116 ps. On the other hand, W18S1-4 exhibits the expected improvement between matrix 3 and matrix 7, a decrease of from 121 ps to 118 ps. For the smallest two pixel pitches, the improvement is more pronounced. The jump from 10 µm-pitch matrix 1 to 5 yields a 6 % reduction and an 8 % improvement between the residual width of 8.66 µm-pitch matrix 0 and matrix 4.
Another variation of the deep n-implant is found in matrix 23 where the corner gap is changed to a 3.8 µm triangular geometry. The larger gap produces an even more pronounced pull away from the pixel corner towards the collection electrode and further narrows the spread in timing performance. On W18S1-3 as well as on W18S1-4 the measurement results in a time residual width of 111 ps and 108 ps, respectively, an improvement of approximately 10 % with respect to the baseline matrix.
Matrix 19 differs from matrix 3 in terms of p-well opening size, while the remaining parameters stay the same. Reducing the area of the p-well benefits a uniform depletion over the full pixel area, favors charge collection but also cuts into the area available for in-pixel circuitry and its complexity. The smaller p-well area of matrix 19 with a 6.0 µm p-well opening achieves a time residual width of 109 ps. While here the change in p-well opening did not decrease the residual width, on W18S1-4 an improvement of 5 % can be observed between the same two

matrix indices.
The collection-electrode size is another parameter that is changed throughout these eight matrices. Increasing the size of the collection electrode has similar beneficial effects as the change in p-well opening but comes with a penalty for signal-to-noise ratio and power consumption. Comparing matrix 19 (109 ps) and 27 (107 ps) shows the small impact of a change in collection electrode size from 0.86 µm to 2.0 µm with an uninterrupted deep n-implant geometry. Comparing matrix 7 (116 ps) with 15 (109 ps), yields a larger gain in timing performance from the same difference in collection electrode size with a hexagonal 2.6 µm corner gap. W18S1-4 exhibits a similar trend.

In comparison with the baseline matrices 3, 2, 1 and 0, an approximate doubling of the collection electrode size and a ≈50 % increase in p-well opening size brought improvements in timing performance of ≈7 % and ≈10 %, respectively. The largest improvement can be observed with the addition of corner gaps, especially the triangular corner gaps could yield a decrease in time residual width of ≈17 % compared to the baseline matrix.

10.6.3. High-Statistic Data Set

For a selection of FASTPIX matrices on sample W18S1-3 a high-statistic set of data is available, which exhibits less contribution of non-Gaussian tails and asymmetries in the time residual. With ≈30 times more entries than in e.g. Figure 10.17 the impact of pixel pitch is illustrated by Figure 10.19.

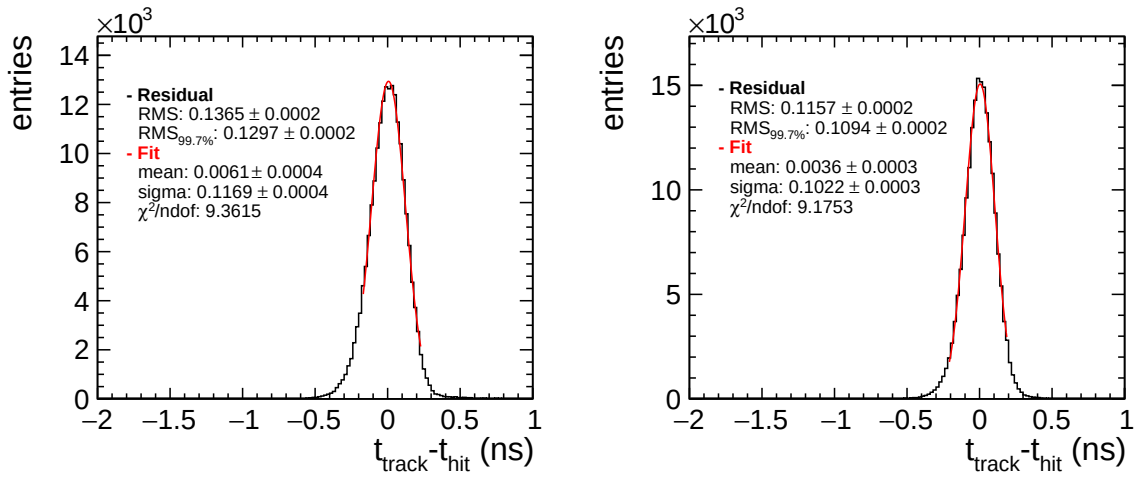

(a) Matrix 1, 10 µm pixel pitch at a threshold of 62 e.

(b) Matrix 3, 20 µm pixel pitch at a threshold of 80 e.

Figure 10.19: Time residual distributions for two matrices of modified process sample W18S1-3. The errors represent statistical uncertainties and errors on the fit parameter.

Apart from pixel pitch, the remaining pixel design modification parameters are equal, except the deep p-well and extra-deep p-well opening. The latter two dimensions of the pixel cell have a specific size for each pixel pitch, or per quadrant of the FASTPIX chip (see Figure 5.15). The 20 µm pixel pitch matrix achieves 15 % better timing performance compared to the 10 µm pixel pitch.

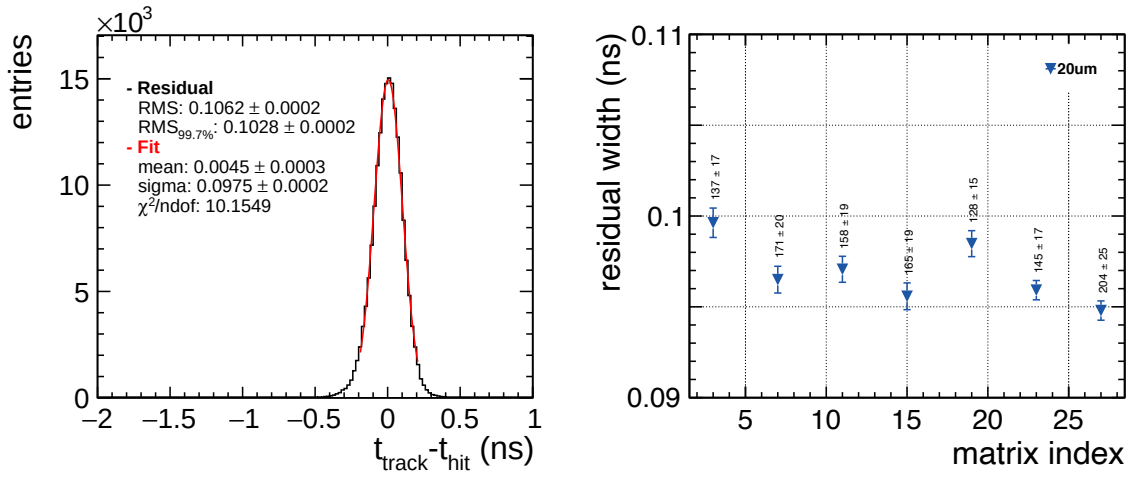

(a) Matrix 15, 20 µm pixel pitch, threshold: 165 ± 19 e.

(b) Residual width for all 20 µm-pitch matrices. The superscript specifies the threshold in electrons for the respective matrix.

Figure 10.20: Time residuals for 20 µm-pitch matrices on modified process sample W18S1-3. The errors bars represent the error on the fit result.

Figure 10.20 presents high-statistic time residuals for seven 20 µm-pitch matrices on modified-process sample W18S1-3. The exemplary residual for matrix 15 reaches a residual width of 96 ± 2 ps which is similar to the 95 ± 1 ps of matrix 27.

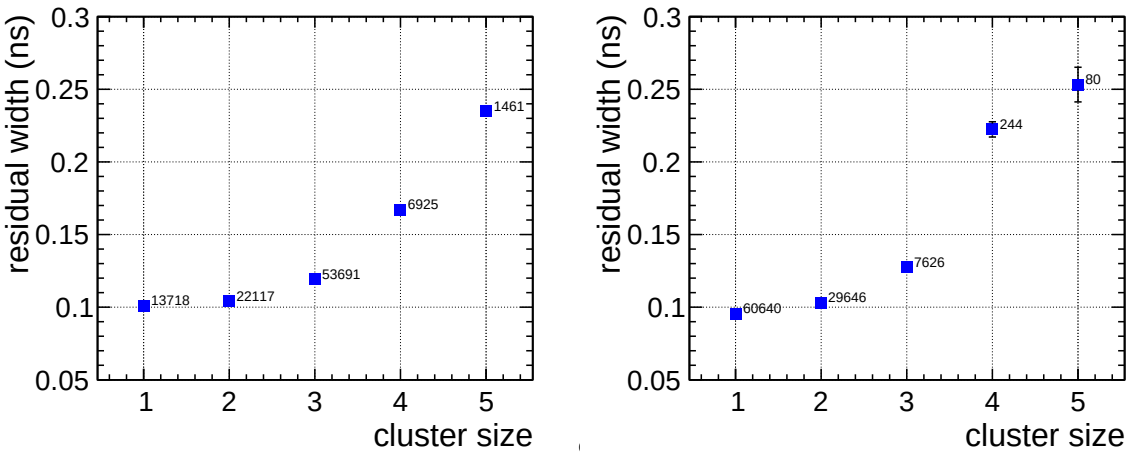

(a) Matrix 1, 10 µm pixel pitch at a threshold of 106 ± 14 e. The distribution for single-pixel clusters yields: 102.1 ± 0.1 ps $RMS_{99.7\,\%}$

(b) Matrix 3, 20 µm pixel pitch at a threshold of 102 ± 19 e. The distribution for single-pixel clusters yields: 95.9 ± 0.1 ps $RMS_{99.7\,\%}$

Figure 10.21: Time residual width ($RMS_{99.7\,\%}$) per cluster size for two matrices of modified process sample W18. The error bars represent the statistical uncertainties. The superscript of each data point gives the number of entries in the subset of the underlying time residual distribution.

The time-walk-correction approach introduced in Section 9.5.5 enables an investigation of the contribution of seed pixel signals of different size clusters to the time measurement precision of the chip. In case of a cluster size >1 less signal is collected by the seed pixel, giving way to

larger time-walk effects. Moreover, for large cluster size it is more likely that a particle hit falls on the corner of the pixel, where charge collection is slower and exhibits more spread in collection speed.
Figure 10.21 shows the width of time residuals from subsets of data sorted by cluster size. Time difference values $\Delta t = t_{DUT} - t_{MCP}$ for cluster sizes ≤5 are sorted in exclusive data sets while clusters >5 are grouped in a combined set. In both cases, independent of pitch, single pixel clusters reach the best performance with a higher probability of collecting the majority of deposited charge in a singular pixel. Doubling the pixel pitch yields an improvement of 6 %, from an $RMS_{99.7\,\%}$ of 102 ps for the 10 µm pixel pitch matrix to 96 ps in case of the 20 µm pixel pitch matrix. Large pixel pitch is in favor of timing performance as a large part of the signal charge is collected by the seed pixel, reducing time-walk effects. In this way matrices 15 and 27 reach single-pixel time measurement precisions down to 91 ps.

10.7. Summary

The large amount of test beam data enabled to conclude on the effects of modifications of the CMOS manufacturing process as well as the impact of optimized pixel design variants.
Initially, the operational parameters of the test beam as well as the FASTPIX readout setup have been confirmed to be sufficient for successful data taking without a bias introduced on the measurements or impaired data taking efficiency.

The observed cluster size was used to discuss the charge sharing behavior within the sensor with regard to the process modifications and sensor design variations. A dependency of cluster size on in-pixel particle intercept position was found to be most pronounced with larger pitch matrices. The addition of an uninterrupted deep n-implant with the modified CMOS process in combination with an extra-deep p-well results in reduced charge sharing and decreased cluster size.
For the larger-pitch matrices the pixel design optimizations had only a minimal impact on the observed cluster size. Smaller pitches have shown to be more sensitive to the variations of the pixel cell implant structures. Gaps added to the deep blanket n-implant in the pixel corners as well as the reduction of the p-well area were found to result in a similar ≈5 % decrease in cluster size. An additionally enlarged collection electrode strengthens the electric field, shortens the charge drift path and arrived at a total ≈10 % reduction of cluster size.

In case of the standard process sample the cluster size measurements provided first indications of insufficient depletion at the nominal −6 V substrate and p-well bias. In comparison with the modified samples, the cluster size was observed to be drastically reduced for <20 µm-pitch matrices on W03S1-1, as opposed to the expected larger cluster size from an increased amount of charge sharing.

The evaluation of hit-detection efficiency could present a consistently efficient area of the matrix as well as pixel. Samples manufactured in the modified and most-modified process yield >99 % detection efficiency across all matrices. With respect to the modified-process sample W15S1-1, the standard-process sample W03S1-1 was found to experience a decrease in efficiency of up to 35 % for the smallest-pitch matrices.

A decrease in pitch towards smaller pixel size distributes the generated charge in the epitaxial layer to a larger number of pixels. On average, a smaller signal is induced on each pixel of a cluster, reducing the measured cluster size, a mechanism that is enhanced by the larger amount of charge sharing in the standard process. In addition, edge effects cause a share of clusters get misidentified with a smaller size.

An evaluation of the most-probable signal collected in test beam measurements could confirm the charge collection deficit of the standard-process sample W03S1-1. The modified-process and most-modified-process samples yielded most-probable signals that are consistent with the expected charge deposition from minimum-ionizing particles.
The discrepancy in charge collected by standard-process and modified-process matrices of a factor 1.5 - 2 suggests insufficient depletion in the standard manufacturing process. The depletion deficit impacts detection efficiency and charge sharing as the pixel pitch decreases to the smallest-possible size for a monolithic pixel in the underlying CMOS technology node. The measurements confirmed that process modifications and pixel design optimizations provide additional margin for efficient detector operation in a $(O)(10\,\mu m)$ regime of pixel sizes and below.

In terms of spatial resolution, the modified-process outperforms the standard-process sample by an overall 15 %. The results from standard-process sample W03S1-1 are penalized by the impaired charge collection. The modified and most-modified FASTPIX samples show a spatial resolution down to 1 µm. The effect of pixel design variations on spatial measurement precision was found to be most prominent for the two larger pixel pitches with dependencies that were already discussed in relation to charge sharing.
A timing precision of $(O)(100\,ps)$ was reached by the 20 µm-pitch matrices of W18S1-3, the modified-process sample with higher-dose deep n-implant. The largest relative improvement was observed for additional triangular corner gaps, followed by improvements from a change in collection electrode and p-well opening size.

11

Summary and Prospects

The advancement of particle physics through both current and future collider facilities pushes the boundaries of technology in present HEP instrumentation. Experiments, operating at the energy and intensity frontier, are motivated by high-precision measurements of Standard Model physics as well as the search for physics beyond the Standard Model. The anticipated physics goals and demanding operational conditions require sophisticated improvements in all detector subsystems.
Focused on the advancement of silicon vertex and tracking detectors, this dissertation has demonstrated the performance of a new pixel detector technology for future high-energy physics collider detectors at the next-generation of particle accelerators.

The addition of a high-precision time measurement to the spatial measurement capabilities of pixel detectors is at the core of future trackers. The key characteristics to be considered are adequate spatial and time resolution, low-power and low-noise readout electronics as well as a detector layout with minimized material budget. Recent developments in monolithic sensors place modified industry-standard CMOS imaging processes as viable options for the production of future pixel detectors. An investigation into the potential of targeted sensor process modifications and design optimizations for the detector performance is essential in the pixel detector R&D cycle and has important implications for future sensor designs.

Detectors placed in the inner layers of future experiments face stringent requirements that call for the ability to detect single ionizing particles using small $< 25\,\mu m$ pixels with significant in-pixel functionality generating low-noise, large amplitude signals while achieving $< 3\,\mu m$ spatial resolution, $< 100\,ps$ time resolution, minimal material budget and extreme radiation tolerance. Furthermore, innovative detector design has to be able to cover large areas, obey cost limitations and engineering constraints as well as anticipate future technology developments.

The monolithic silicon pixel sensor demonstrator FASTPIX has been developed in a modified 180 nm CMOS imaging process technology that is targeting such performance figures. The chip allows to evaluate the suitability of its small collection electrode design on a 25 µm-thin sensitive detection layer in combination with small pixel pitches ranging from 8.66 to 20 µm. A large parameter space of 32 mini matrices assesses manufacturing process modifications and sensor design variations optimized in simulations. The sensor design encompasses hexagonal pixels with collection electrodes capacitances of a few femto-farad and large signal-to-noise

ratios, in favor of detection efficiency and precise timing. Low-field regions, non-uniform electric field configurations and space requirements for complex in-pixel circuits introduce timing variation depending on the in-pixel particle incidence location. In order to face a tradeoff between pixel size and non-uniform timing, 8 design variations are explored per pixel pitch, aiming at accelerating the charge collection and making the timing of the charge collection more uniform over the pixel area.

The conducted research presented in this thesis comprises laboratory and test beam characterization measurements as well as the associate development of hardware and software for the employed test systems.
The working state of the sensor and its expected electrical properties were confirmed in initial laboratory-based studies. Current-voltage characterizations of individual samples confirmed the operation of the chip at the nominal bias voltage of $-6\,\mathrm{V}$ for p-well and substrate at a stable current and sufficient margins.
The ToT response to electrically injected signal pulses was found to feature a minimum detectable ToT value of approximately $175 \pm 25\,\mathrm{e}$ as a characteristic of the FASTPIX front-end design. A calibration of the electrically injected signal was achieved through a comparison of signals from X-ray photons with the pulse-injection voltage at common most-probable ToT values. The calibration factor and associated test-pulse injection capacitance are calculated per pitch. The ToT observable was used to cross-check laboratory calibrations with test beam measurements using minimum ionizing particles. The nominal discriminator detection threshold was subsequently calibrated using the confirmed signal-to-energy conversion factors and ranges between $60\,\mathrm{e}$ and $160\,\mathrm{e}$, depending on process modification and pixel design variation.
Samples with modifications of the manufacturing process exhibited approximately 15 % smaller gain as a result of the introduction of a blanket deep n-layer across the pixel cell. The dependency of the gain on the pitch is inverted for the modified-process sample with increased deep n-layer doping concentration, with respect to the base-value doping concentration of the modified process. The tested FASTPIX matrices exhibit a gain between $120\,\mathrm{e/V}$ and $260\,\mathrm{e/V}$. Across all samples, the dominant thermal noise of the frontend yields values between $5\,\mathrm{e}$ and $15\,\mathrm{e}$ with clear trends following pixel pitch and collection electrode size. For samples with increased deep n-type implant doping levels, increased pitch or enlarged collection electrode, the input capacitance as well as the rate of fake hits increases as an effect of increased gain.

Comprehensive test-beam data sets from measurements in charged particle beams assess the performance gain of modifications of the CMOS manufacturing process as well as the impact of pixel design optimizations.
The charge-sharing properties are represented by the observed cluster size within the sensor and were evaluated with regard to the process modifications and sensor design variations. The modification of the manufacturing process with an uninterrupted deep n-implant in combination with an extra-deep p-well results in reduced charge sharing and decreased cluster size. The effect of the hexagonal grid was directly observed in larger-pitch matrices where ≈99 % of cluster were observed with a size < 3, indicative of the three neighboring pixels at a given pixel corner. Larger-pitch matrices have shown a reduced impact of pixel design optimizations on the observed cluster size, as the border region occupies a smaller share of the total pixel area, compared to the smaller pixel pitches. In case of smaller-pitch matrices,

gaps added to the deep blanket n-implant in the pixel corners as well as the reduction of the p-well area were found to result in a similar ≈5 % decrease in cluster size. An additionally enlarged collection electrode amounts to at a total ≈10 % reduction of cluster size.

The cluster size measurements provided first indications of insufficient depletion of the standard process sample at the nominal sensor bias. While the evaluation of hit-detection efficiency could present values >99 % across all matrices of samples with deep blanket n-implant, a decrease in efficiency of up to 35 % was observed for the smallest-pitch matrices on the standard-process sample. An evaluation of the most-probable signal collected in test-beam measurements could confirm the charge collection deficit of the standard-process without the added deep n-layer. The depletion deficit impacts detection efficiency and charge sharing as the pixel pitch decreases to the smallest-possible size for a monolithic pixel in the underlying CMOS technology node.
The modified-process and most-modified-process samples yielded most-probable signals that are consistent with the expected charge deposition from minimum-ionizing particles. The measurements confirmed that process modifications and pixel design optimizations provide additional margin for efficient detector operation in a $(O)(10\,\mu m)$ regime of pixel sizes and below.

The spatial resolution of samples with deep blanket n-implant outperformed standard-process samples by an overall 15 % due to the impaired charge collection of the standard process. The modified and most-modified FASTPIX samples did show a spatial resolution down to 1 µm, influenced most-prominently by pixel design variations in combination with larger pixel pitches.

A timing precision of $(O)(100\,ps)$ was reached by the 20 µm-pitch matrices on the sample with highest-dose deep n-implant. The largest relative improvement in time measurement precision was observed for additional triangular corner gaps, followed by a change in collection electrode and p-well opening size.

While the FASTPIX sensor matches or even surpasses most of the sensor performance requirements for future pixel detectors, the chip lacks in pixel-matrix size, the integration of the full front-end into the pixel cell and added functionality for the digitization, concentration and transmission of measurement data as well as chip-to-chip powering and communication. The implemented front-end circuitry design prioritizes signal quality and integrity over low power consumption or the implementation of a fully developed data digitization and reduction/concentration stage. The main limitation for a fully-developed front-end in a large-scale production of a monolithic pixel detector based on the FASTPIX sensor is imposed by the limited transistor count per unit area in the 180 nm CMOS technology node.
Developments in 65 nm feature-size CMOS processes provide the necessary logic density and significant advantages in signal speed for sophisticated readout architectures in small (< 25 µm) pixels. Such technologies will allow readout circuitry in the matrix as well as at the periphery that feature fast front-end and clock distribution blocks with high-rate serial outputs at a low power consumption [10].
Independent of the leap towards smaller CMOS feature-size, the characterization of the FASTPIX sensor technology demonstrator contributes to the development of CMOS manufacturing process modifications as well as the application-specific choice of pixel design optimizations

in a small collection-electrode pixel layout. The simulation of the observed effects can further refine the underlying simulation approach, which in-turn is used for the validations and optimizations of the next iteration of monolithic pixel detector developments.
The general principles extracted from measurements with FASTPIX similarly apply to other applications of monolithic CMOS image sensors. To this extend, the conducted detector R&D advances not only applications in high energy physics, but also other fields such as imaging Time-of-Flight Mass Spectroscopy, Fluorescence Life-Time Imaging Microscopy, electron microscopy, even commercial Light Detection and Ranging systems.

References

[1] Oliver Sim Brüning et al. *LHC Design Report*. CERN Yellow Reports: Monographs. Geneva: CERN, 2004. DOI: 10.5170/CERN-2004-003-V-1. URL: https://cds.cern.ch/record/782076.

[2] Andrea Dainese et al. *Report on the Physics at the HL-LHC, and Perspectives for the HE-LHC*. Tech. rep. Geneva, Switzerland, 2019. DOI: 10.23731/CYRM-2019-007. URL: https://cds.cern.ch/record/2703572.

[3] *High-Luminosity LHC*. Accessed: 2024-05-05. URL: https://home.cern/science/accelerators/high-luminosity-lhc.

[4] *2020 Update of the European Strategy for Particle Physics (Brochure)*. Tech. rep. Geneva, 2020. DOI: 10.17181/CERN.JSC6.W89E. URL: https://cds.cern.ch/record/2721370.

[5] The Future Circular Collider Collaboration. "FCC Physics Opportunities". In: *The European Physical Journal C* 79.6 (2019), p. 474. DOI: 10.1140/epjc/s10052-019-6904-3. URL: https://doi.org/10.1140/epjc/s10052-019-6904-3.

[6] The Future Circular Collider Collaboration. "FCC-ee: The Lepton Collider". In: *The European Physical Journal Special Topics* 228.2 (2019), pp. 261–623. DOI: 10.1140/epjst/e2019-900045-4. URL: https://doi.org/10.1140/epjst/e2019-900045-4.

[7] The Future Circular Collider Collaboration. "FCC-hh: The Hadron Collider". In: *The European Physical Journal Special Topics* 228.4 (2019), pp. 755–1107. DOI: 10.1140/epjst/e2019-900087-0. URL: https://doi.org/10.1140/epjst/e2019-900087-0.

[8] The Compact Linear Collider Collaboration. *The Compact Linear Collider (CLIC) - 2018 Summary Report*. Ed. by P.N. Burrows. Vol. 2. CERN Yellow Reports: Monographs. 2018. DOI: 10.23731/CYRM-2018-002. URL: https://cds.cern.ch/record/2652188.

[9] CERN. *CERN Annual report 2022*. Tech. rep. Geneva: CERN, 2023. DOI: 10.17181/AnnualReport2022. URL: https://cds.cern.ch/record/2857560.

[10] Martin Aleksa et al. *Strategic R&D Programme on Technologies for Future Experiments*. Tech. rep. Geneva: CERN, 2018. DOI: 10.17181/CERN.5PQI.KDL2. URL: https://cds.cern.ch/record/2649646.

[11] Markus Nordberg Roy Pennings Pablo Tello. *The ATTRACT Programme*. 2018. URL: https://attract-eu.com/wp-content/uploads/2021/04/ATTRACT-1.pdf.

[12] Walter Snoeys et al. *FASTPIX - Sub-nanosecond radiation tolerant CMOS pixel sensors*. 2019. URL: https://phase1.attract-eu.com/showroom/project/sub-nanosecond-radiation-tolerant-cmos-pixel-sensors-fastpix/.

[13] Justus Braach et al. "Performance of the FASTPIX Sub-Nanosecond CMOS Pixel Sensor Demonstrator". In: *Instruments* 6.1 (2022). ISSN: 2410-390X. DOI: 10.3390/instruments6010013. URL: https://www.mdpi.com/2410-390X/6/1/13.

[14] Justus Braach et al. "Test-beam performance results of the FASTPIX sub-nanosecond CMOS pixel sensor demonstrator". In: *Nuclear Instruments and Methods in Physics Research Section A: Accelerators, Spectrometers, Detectors and Associated Equipment* 1056 (2023), p. 168641. ISSN: 0168-9002. DOI: https://doi.org/10.1016/j.nima.2023.168641. URL: https://www.sciencedirect.com/science/article/pii/S0168900223006319.

[15] Mark Thomson. *Modern Particle Physics*. Cambridge University Press, 2013.

[16] David Galbraith and Carsten Burgard. *Diagram of the Standard Model of particle physics*. Accessed: 2024-05-11. URL: https://texample.net/tikz/examples/model-physics/.

[17] Andrei D Sakharov. "Violation of CP invariance, C asymmetry, and baryon asymmetry of the universe". In: *Soviet Physics Uspekhi* 34.5 (May 1991), p. 392. DOI: 10.1070/PU1991v034n05ABEH002497. URL: https://dx.doi.org/10.1070/PU1991v034n05ABEH002497.

[18] Edvige Corbelli and Paolo Salucci. "The extended rotation curve and the dark matter halo of M33". In: *Monthly Notices of the Royal Astronomical Society* 311.2 (Jan. 2000), pp. 441–447. ISSN: 0035-8711. DOI: 10.1046/j.1365-8711.2000.03075.x. eprint: https://academic.oup.com/mnras/article-pdf/311/2/441/2881340/311-2-441.pdf. URL: https://doi.org/10.1046/j.1365-8711.2000.03075.x.

[19] Richard Massey, Thomas Kitching, and Johan Richard. "The dark matter of gravitational lensing". In: *Reports on Progress in Physics* 73.8 (July 2010), p. 086901. DOI: 10.1088/0034-4885/73/8/086901. URL: https://dx.doi.org/10.1088/0034-4885/73/8/086901.

[20] P. J. E. Peebles and Bharat Ratra. "The cosmological constant and dark energy". In: *Rev. Mod. Phys.* 75 (2 Apr. 2003), pp. 559–606. DOI: 10.1103/RevModPhys.75.559. URL: https://link.aps.org/doi/10.1103/RevModPhys.75.559.

[21] The Super-Kamiokande Collaboration. "Evidence for Oscillation of Atmospheric Neutrinos". In: *Phys. Rev. Lett.* 81 (8 Aug. 1998), pp. 1562–1567. DOI: 10.1103/PhysRevLett.81.1562. URL: https://link.aps.org/doi/10.1103/PhysRevLett.81.1562.

[22] The Daya Bay Collaboration. "Observation of Electron-Antineutrino Disappearance at Daya Bay". In: *Phys. Rev. Lett.* 108 (17 Apr. 2012), p. 171803. DOI: 10.1103/PhysRevLett.108.171803. URL: https://link.aps.org/doi/10.1103/PhysRevLett.108.171803.

[23] The KamLAND Collaboration. "First Results from KamLAND: Evidence for Reactor Antineutrino Disappearance". In: *Phys. Rev. Lett.* 90 (2 Jan. 2003), p. 021802. DOI: 10.1103/PhysRevLett.90.021802. URL: https://link.aps.org/doi/10.1103/PhysRevLett.90.021802.

[24] Mauro Mezzetto and Francesco Terranova. "Three-Flavor Oscillations with Accelerator Neutrino Beams". In: *Universe* 6.2 (2020). ISSN: 2218-1997. DOI: 10.3390/universe6020032. URL: https://www.mdpi.com/2218-1997/6/2/32.

[25] Masahiro Ibe, Alexander Kusenko, and Tsutomu T. Yanagida. "Why three generations?" In: *Physics Letters B* 758 (2016), pp. 365–369. ISSN: 0370-2693. DOI: https://doi.org/10.1016/j.physletb.2016.05.025. URL: https://www.sciencedirect.com/science/article/pii/S0370269316301721.

[26] Michael Dine. *Supersymmetry and String Theory: Beyond the Standard Model*. Cambridge University Press, 2007.

[27] *LHC site plan*. Accessed: 2024-05-11. URL: https://www.weltmaschine.de/service_material/mediathek/lhc/.

[28] *CMS conventional coordinate system with LHC and other detectors*. Accessed: 2024-05-11. URL: https://tikz.net/axis3d_cms/.

[29] O. Aberle et al. *High-Luminosity Large Hadron Collider (HL-LHC): Technical design report*. CERN Yellow Reports: Monographs. Geneva: CERN, 2020. DOI: 10.23731/CYRM-2020-0010. URL: https://cds.cern.ch/record/2749422.

[30] H. Kolanoski and N. Wermes. *Particle Detectors: Fundamentals and Applications*. Oxford University Press, 2020. ISBN: 9780198858362. URL: https://books.google.ch/books?id=7-4-zQEACAAJ.

[31] The ATLAS Collaboration. "The ATLAS Experiment at the CERN Large Hadron Collider". In: *Journal of Instrumentation* 3.08 (Aug. 2008), S08003. DOI: 10.1088/1748-0221/3/08/S08003. URL: https://dx.doi.org/10.1088/1748-0221/3/08/S08003.

[32] The CMS Collaboration. "The CMS experiment at the CERN LHC". In: *Journal of Instrumentation* 3.08 (Aug. 2008), S08004. DOI: 10.1088/1748-0221/3/08/S08004. URL: https://dx.doi.org/10.1088/1748-0221/3/08/S08004.

[33] The ALICE Collaboration. "The ALICE experiment at the CERN LHC". In: *Journal of Instrumentation* 3.08 (Aug. 2008), S08002. DOI: 10.1088/1748-0221/3/08/S08002. URL: https://dx.doi.org/10.1088/1748-0221/3/08/S08002.

[34] The LHCb Collaboration. "The LHCb Detector at the LHC". In: *Journal of Instrumentation* 3.08 (Aug. 2008), S08005. DOI: 10.1088/1748-0221/3/08/S08005. URL: https://dx.doi.org/10.1088/1748-0221/3/08/S08005.

[35] *Technical Design Report for the ATLAS Inner Tracker Pixel Detector*. Tech. rep. Geneva: CERN, 2017. DOI: 10.17181/CERN.FOZZ.ZP3Q. URL: https://cds.cern.ch/record/2285585.

[36] *The Phase-2 Upgrade of the CMS Tracker*. Tech. rep. Geneva: CERN, 2017. DOI: 10.17181/CERN.QZ28.FLHW. URL: https://cds.cern.ch/record/2272264.

[37] *Technical Design Report: A High-Granularity Timing Detector for the ATLAS Phase-II Upgrade*. Tech. rep. Geneva: CERN, 2020. URL: https://cds.cern.ch/record/2719855.

[38] Collaboration CMS. *A MIP Timing Detector for the CMS Phase-2 Upgrade*. Tech. rep. Geneva: CERN, 2019. URL: https://cds.cern.ch/record/2667167.

[39] ALICE collaboration The. *Technical Design Report for the Upgrade of the ALICE Inner Tracking System*. Tech. rep. 2014. DOI: 10.1088/0954-3899/41/8/087002. URL: https://cds.cern.ch/record/1625842.

[40] ALICE collaboration The. *Technical Design report for the ALICE Inner Tracking System 3 - ITS3; A bent wafer-scale monolithic pixel detector*. Tech. rep. Co-project Manager: Magnus Mager, magnus.mager@cern.ch. Geneva: CERN, 2024. URL: https://cds.cern.ch/record/2890181.

[41] The International Linear Collider Collaboration. *ILC Reference Design Report Volume 1 - Executive Summary. ILC Reference Design Report: ILC Global Design Effort and World Wide Study*. Tech. rep. 2007. arXiv: 0712.1950. URL: https://cds.cern.ch/record/1075077.

[42] Emilie Ter Laak. "Schematic of an 80-100 km long circular tunnel. Schéma d'un tunnel circulaire de 80 à 100 km de long". In: (2014). General Photo. URL: https://cds.cern.ch/record/1646785.

[43] Frank Zimmermann. "High-energy physics strategies and future large-scale projects". In: *Nuclear Instruments and Methods in Physics Research Section B: Beam Interactions with Materials and Atoms* 355 (Apr. 2015). DOI: 10.1016/j.nimb.2015.03.090.

[44] Michelangelo L Mangano et al. *Conceptual design of an experiment at the FCC-hh, a future 100 TeV hadron collider*. Tech. rep. 2022. DOI: 10.23731/CYRM-2022-002. URL: https://cds.cern.ch/record/2842569.

[45] Andrzej Smykiewicz. *Tracking performance with the HL-LHC ATLAS Detector*. Tech. rep. Geneva: CERN, 2019. URL: https://cds.cern.ch/record/2686542.

[46] D.A. Neamen and Inc. Staff MathSoft. *Semiconductor Physics and Devices: Basic Principles*. McGraw-Hill Higher Education, 2011. ISBN: 0073529583.

[47] Leonardo Rossi et al. *Pixel detectors: from fundamentals to applications*. Particle acceleration and detection. Berlin: Springer, 2006. DOI: 10.1007/3-540-28333-1. URL: https://cds.cern.ch/record/976471.

[48] U Fano. "Ionization yield of radiations. II. The fluctuations of the number of ions". In: *Phys. Rev.* 72.1 (1947), pp. 26–29. URL: https://cds.cern.ch/record/425303.

[49] "56 - ON THE ENERGY LOSS OF FAST PARTICLES BY IONISATION". In: *Collected Papers of L.D. Landau*. Ed. by D. TER HAAR. Pergamon, 1965, pp. 417–424. ISBN: 978-0-08-010586-4. DOI: https://doi.org/10.1016/B978-0-08-010586-4.50061-4. URL: https://www.sciencedirect.com/science/article/pii/B9780080105864500614.

[50] R. L. Workman et al. "Review of Particle Physics". In: *PTEP* 2022 (2022), p. 083C01. DOI: 10.1093/ptep/ptac097.

[51] W. Shockley. "Currents to Conductors Induced by a Moving Point Charge". In: *JAPIAU* 9 (Oct. 1938), pp. 635–636. DOI: 10.1063/1.1710367.

[52] *Currents Induced by Electron Motion*. Vol. 27. IEEE, Sept. 1939, pp. 584–585. DOI: 10.1109/JRPROC.1939.228757.

[53] Walter Snoeys et al. "First beam test results from a monolithic silicon pixel detector". In: *Nuclear Instruments and Methods in Physics Research Section A: Accelerators, Spectrometers, Detectors and Associated Equipment* 326.1 (1993), pp. 144–149. ISSN: 0168-9002. DOI: https://doi.org/10.1016/0168-9002(93)90344-H. URL: https://www.sciencedirect.com/science/article/pii/016890029390344H.

[54] *Horizon 2020*. Accessed: 2023-12-21. URL: http://wayback.archive-it.org/12090/20220124075100/https:/ec.europa.eu/programmes/horizon2020/.

[55] W. Snoeys. *Private communication*. 2021–2023.

[56] W. Snoeys et al. "A process modification for CMOS monolithic active pixel sensors for enhanced depletion, timing performance and radiation tolerance". In: *Nuclear Instruments and Methods in Physics Research Section A: Accelerators, Spectrometers, Detectors and Associated Equipment* 871 (2017), pp. 90–96. ISSN: 0168-9002. DOI: https://doi.org/10.1016/j.nima.2017.07.046. URL: https://www.sciencedirect.com/science/article/pii/S016890021730791X.

[57] Thanushan Kugathasan et al. "Monolithic CMOS sensors for sub-nanosecond timing". In: *Nuclear Instruments and Methods in Physics Research Section A: Accelerators, Spectrometers, Detectors and Associated Equipment* 979 (2020), p. 164461. ISSN: 0168-9002. DOI: https://doi.org/10.1016/j.nima.2020.164461. URL: https://www.sciencedirect.com/science/article/pii/S0168900220308585.

[58] Magdalena Munker. "Fast charge collection in small collection electrode monolithic CMOS sensors. Fast charge collection in small collection electrode monolithic CMOS sensors". In: (2021). URL: https://cds.cern.ch/record/2750682.

[59] S. Agostinelli et al. "Geant4—a simulation toolkit". In: *Nuclear Instruments and Methods in Physics Research Section A: Accelerators, Spectrometers, Detectors and Associated Equipment* 506.3 (2003), pp. 250–303. ISSN: 0168-9002. DOI: https://doi.org/10.1016/S0168-9002(03)01368-8. URL: https://www.sciencedirect.com/science/article/pii/S0168900203013688.

[60] J Allison. "Geant4 developments and applications". In: *IEEE Trans. Nucl. Sci.* 53 (2006), p. 270. DOI: 10.1109/TNS.2006.869826. URL: https://cds.cern.ch/record/1035669.

[61] J. Allison et al. "Recent developments in Geant4". In: *Nuclear Instruments and Methods in Physics Research Section A: Accelerators, Spectrometers, Detectors and Associated Equipment* 835 (2016), pp. 186–225. ISSN: 0168-9002. DOI: https://doi.org/10.1016/j.nima.2016.06.125. URL: https://www.sciencedirect.com/science/article/pii/S0168900216306957.

[62] Simon Spannagel et al. "Allpix^2: A Modular Simulation Framework for Silicon Detectors". In: *Nucl. Instrum. Methods Phys. Res. A* 901 (2018), pp. 164–172. DOI: 10.1016/j.nima.2018.06.020. arXiv: 1806.05813. URL: https://cds.cern.ch/record/2315456.

[63] R Cardella et al. "MALTA: an asynchronous readout CMOS monolithic pixel detector for the ATLAS High-Luminosity upgrade". In: *JINST* 14.06 (2019), p. C06019. DOI: 10.1088/1748-0221/14/06/C06019. URL: https://cds.cern.ch/record/2691881.

[64] Jacobus Willem van Hoorn. "Study and Development of a novel Silicon Pixel Detector for the Upgrade of the ALICE Inner Tracking System". Presented 24 Nov 2015. TU Vienna, 2015. URL: https://cds.cern.ch/record/2119197.

[65] Tomas Vanat. "Caribou – A versatile data acquisition system". In: *Proceedings of Topical Workshop on Electronics for Particle Physics - PoS(TWEPP2019)*. Vol. 370. 2020, p. 100. DOI: 10.22323/1.370.0100.

[66] *ZC706 Evaluation Board for the Zynq-7000 XC7Z045 SoC*. Accessed: 2023-11-29. URL: https://www.xilinx.com/support/documentation/boards_and_kits/zc706/%20ug954-zc706-eval-board-xc7z045-ap-soc.pdf.

[67] *AMD Kintex 7*. Accessed: 2023-11-29. URL: https://www.xilinx.com/products/silicon-devices/fpga/kintex-7.html.

[68] *Cortex-A9*. Accessed: 2023-11-29. URL: https://developer.arm.com/Processors/Cortex-A9.

[69] *AXI Basics 1 - Introduction to AXI*. Accessed: 2023-11-29. URL: https://support.xilinx.com/s/article/1053914?language=en_US.

[70] *Yocto Project*. Accessed: 2023-11-29. URL: https://www.yoctoproject.org/development/technical-overview/.

[71] Chris M. Lonvick and Tatu Ylonen. *The Secure Shell (SSH) Protocol Architecture*. Jan. 2006. DOI: 10.17487/RFC4251. URL: https://www.rfc-editor.org/info/rfc4251.

[72] Raj Seelam. *I/O Design Flexibility with the FPGA Mezzanine Card (FMC)(WP315)*. Aug. 2009. URL: https://docs.xilinx.com/v/u/en-US/wp315.

[73] *I2C-bus specification and user manual*. Oct. 2021. URL: https://www.nxp.com/docs/en/user-guide/UM10204.pdf.

[74] *SEARAY^{TM} high speed, high density open-pin-field array connector*. Accessed: 2023-11-29. URL: https://www.samtec.com/connectors/high-speed-board-to-board/high-density-arrays/searay.

[75] Karl Sauter Sr. "PCB Laminates". In: *Lead-Free Soldering*. Ed. by Jasbir Bath. Boston, MA: Springer US, 2007, pp. 199–220. ISBN: 978-0-387-68422-2. DOI: 10.1007/978-0-387-68422-2_8. URL: https://doi.org/10.1007/978-0-387-68422-2_8.

[76] *Staystik 571 - Silver Filled Electrically Conductive Film*. Accessed: 2023-11-29. URL: https://www.macdermidalpha.com/sites/default/files/2021-08/STAYSTIK-571-EN-19Sep19-TDS.pdf.

[77] *LEMO Interconnect Solutions*. Accessed: 2023-11-29. URL: https://www.lemo.com.

[78] Particle Data Group. "Review of Particle Physics, 2012-2013. Review of Particle Properties". In: *Phys. Rev. D* 86.1 (2012), p. 010001. DOI: 10.1103/PhysRevD.86.010001. URL: https://cds.cern.ch/record/1481544.

[79] Katharina Dort. "Simulation Studies and Characterisation of Monolithic Silicon Pixel-Detector Prototypes for Future Collider Detectors & Unsupervised Anomaly Detection in Belle II Pixel-Detector Data". Presented 07 Jun 2022. 2022. URL: https://cds.cern.ch/record/2813457.

[80] J. Prabket et al. "Resistivity profile of epitaxial layer for the new ALICE ITS sensor". In: *Journal of Instrumentation* 14.05 (May 2019), T05006. DOI: 10.1088/1748-0221/14/05/T05006. URL: https://dx.doi.org/10.1088/1748-0221/14/05/T05006.

[81] *Ultimaker ABS - Technical data sheet*. Accessed: 2023-11-29. Apr. 2020. URL: https://ultimaker.my.salesforce.com/sfc/p/%5C#j0000000HOnW/a/5b000004UWOb/mqEDmbBEqiM6dfNicGFkHQEgcV9T8W762bqwplt4bxo.

[82] *Ultimaker ABS - Safety data sheet*. Accessed: 2023-11-29. dez 2022. URL: https://ultimaker.my.salesforce.com/sfc/p/%5C#j0000000HOnW/a/5b000005DOwE/LhTYq_QGnim.F6ivZbZq3cGgpimHby7MtHksWVv3QRE.

[83] *Tenma - Single Channel Programmable DC Power Supply*. Accessed: 2023-11-29. URL: https://www.farnell.com/datasheets/3743267.pdf.

[84] *Keithley 2400 Graphical Series SMU instruments*. Accessed: 2023-11-29. URL: https://www.tek.com/en/products/keithley/source-measure-units/2400-graphical-series-sourcemeter.

[85] *DSO9254A - Infiniium 9000 Series Oscilloscope*. Accessed: 2023-11-29. URL: https://www.keysight.com/de/de/assets/7018-02091/data-sheets/5990-3746.pdf.

[86] *DG535 — Digital delay and pulse generator*. Accessed: 2023-11-29. URL: https://www.thinksrs.com/downloads/pdfs/catalog/DG535c.pdf.

[87] *BME280 - Digital humidity, pressure and temperature sensor*. Accessed: 2024-03-20. URL: https://www.bosch-sensortec.com/media/boschsensortec/downloads/datasheets/bst-bme280-ds002.pdf.

[88] Fons Rademakers et al. *root-project/root: v6.26/04*. Version v6-26-04. June 2022. DOI: 10.5281/zenodo.3895852. URL: https://doi.org/10.5281/zenodo.3895852.

[89] *NuDat 3*. Accessed: 2024-03-18. URL: https://www.nndc.bnl.gov/nudat3/.

[90] J H Hubbell and Stephen M Seltzer. *Tables of X-ray mass attenuation coefficients and mass energy-absorption coefficients 1 keV to 20 MeV for elements Z=1 to 92 and 48 additional substances of dosimetric interest*. Tech. rep. 1995. URL: https://cds.cern.ch/record/353989.

[91] *EMPYREAN PW3373/10 Ceramic X-ray Tube*. Accessed: 2024-03-18. URL: https://www.malvernpanalytical.com//en/assets/empyrean_tube_tcm50-52050.pdf.

[92] M. Munker et al. "Simulations of CMOS pixel sensors with a small collection electrode, improved for a faster charge collection and increased radiation tolerance". In: *Journal of*

Instrumentation 14.05 (May 2019), p. C05013. DOI: 10.1088/1748-0221/14/05/C05013. URL: https://dx.doi.org/10.1088/1748-0221/14/05/C05013.

[93] *Accelerator complex*. Accessed: 2024-01-07. URL: https://home.cern/science/accelerators/accelerator-complex.

[94] *Secondary Beam Areas of the PS, SPS machines*. Accessed: 2024-01-03. Feb. 2019. URL: http://sba.web.cern.ch/sba/.

[95] *CERN Geographic Information System - GIS Portal - EHN1/R*. Accessed: 2024-01-03. URL: https://gis.cern.ch/gisportal/planotheque.htm?share=76701600-3f44-44e0-a94c-d6f0c9c00dc4.

[96] Kazu Akiba et al. "LHCb VELO Timepix3 Telescope". In: *JINST* 14.05 (2019), P05026. DOI: 10.1088/1748-0221/14/05/P05026. arXiv: 1902.09755. URL: https://cds.cern.ch/record/2668670.

[97] Niloufar Alipour Tehrani. "Test-beam measurements and simulation studies of thin pixel sensors for the CLIC vertex detector". Presented 13 Mar 2017. 2016. URL: https://cds.cern.ch/record/2270788.

[98] A. C. Abusleme Hoffman et al. *CERN Yellow Reports: Monographs, Vol 1 (2019): Detector Technologies for CLIC*. Tech. rep. CERN-2019-001. 2019, p. 152. DOI: 10.23731/CYRM-2019-001. arXiv: 1905.02520. URL: https://bib-pubdb1.desy.de/record/429703.

[99] HAMAMATSU Photonics K.K. Electron Tube Division. *Microchannel Plate - Photomultiplier Tube (MCP-PMT) R3809U Series*. 2023. URL: https://www.hamamatsu.com/content/dam/hamamatsu-photonics/sites/documents/99_SALES_LIBRARY/etd/R3809U_TPMH1067E.pdf.

[100] J. Bortfeldt et al. "Timing performance of a Micro-Channel-Plate Photomultiplier Tube". In: *Nuclear Instruments and Methods in Physics Research Section A: Accelerators, Spectrometers, Detectors and Associated Equipment* 960 (2020), p. 163592. ISSN: 0168-9002. DOI: https://doi.org/10.1016/j.nima.2020.163592. URL: https://www.sciencedirect.com/science/article/pii/S0168900220301613.

[101] *GTS70 - Motorized Linear Stage*. Accessed: 2024-01-07. URL: https://www.newport.com/p/GTS70.

[102] *GTS30V - Motorized Vertical Stage*. Accessed: 2024-01-07. URL: https://www.newport.com/p/GTS30V.

[103] *URS50BCC - Motorized Rotation Stage*. Accessed: 2024-01-07. URL: https://www.newport.com/p/URS50BCC.

[104] J Visser et al. "SPIDR: a read-out system for Medipix3 & Timepix3". In: *JINST* 10.12 (2015), p. C12028. DOI: 10.1088/1748-0221/10/12/C12028. URL: https://cds.cern.ch/record/2159188.

[105] Elena Dall'Occo. "The Timepix3 Telescope and Sensor R&D for the LHCb VELO Upgrade". In: (2018). URL: https://cds.cern.ch/record/2651308.

[106] D. Dannheim et al. “Corryvreckan: a modular 4D track reconstruction and analysis software for test beam data”. In: *Journal of Instrumentation* 16.03 (Mar. 2021), P03008. DOI: 10.1088/1748-0221/16/03/P03008. URL: https://dx.doi.org/10.1088/1748-0221/16/03/P03008.

[107] Jens Kroeger. “Characterisation of a High-Voltage Monolithic Active Pixel Sensor Prototype for Future Collider Detectors”. Presented 13 Oct 2021. 2021. URL: https://cds.cern.ch/record/2784385.

[108] E. Belau et al. “Charge collection in silicon strip detectors”. In: *Nuclear Instruments and Methods in Physics Research* 214.2 (1983), pp. 253–260. ISSN: 0167-5087. DOI: https://doi.org/10.1016/0167-5087(83)90591-4. URL: https://www.sciencedirect.com/science/article/pii/0167508783905914.

[109] Kazuyoshi Akiba et al. “Charged particle tracking with the Timepix ASIC”. In: *Nuclear Instruments and Methods in Physics Research Section A: Accelerators, Spectrometers, Detectors and Associated Equipment* 661.1 (2012), pp. 31–49. ISSN: 0168-9002. DOI: https://doi.org/10.1016/j.nima.2011.09.021. URL: https://www.sciencedirect.com/science/article/pii/S0168900211017736.

[110] F. Feindt, S. Spannagel, and H. Wennloef. *Private communication*. 2023.

[111] Morag Jean Williams. “Evaluation of Fine-Pitch Hybrid Silicon Pixel Detector Prototypes for the CLIC Vertex Detector in Laboratory and Test-Beam Measurements”. Presented 12 Feb 2021. University of Glasgow, 2020. URL: https://cds.cern.ch/record/2766510.

[112] F. James and M. Roos. “Minuit - a system for function minimization and analysis of the parameter errors and correlations”. In: *Computer Physics Communications* 10.6 (1975), pp. 343–367. ISSN: 0010-4655. DOI: https://doi.org/10.1016/0010-4655(75)90039-9. URL: https://www.sciencedirect.com/science/article/pii/0010465575900399.

[113] C. J. Clopper and E. S. Pearson. “The Use of Confidence or Fiducial Limits Illustrated in the Case of the Binomial”. In: *Biometrika* 26.4 (1934), pp. 404–413. ISSN: 00063444. URL: http://www.jstor.org/stable/2331986 (visited on 05/14/2024).

[114] *The Telescope Optimiser V1.0*. Accessed: 2024-05-15. URL: https://mmager.web.cern.ch/telescope/tracking.html.

[115] Hendrik Jansen et al. “Performance of the EUDET-type beam telescopes”. In: *EPJ Techniques and Instrumentation* 3.1 (2016), p. 7. DOI: 10.1140/epjti/s40485-016-0033-2. URL: https://doi.org/10.1140/epjti/s40485-016-0033-2.